Numerical Modelling and Interaction of Crack and Aeroelastic Behaviour of Composite Structure for Aerospace Applications

By:

Nur Azam bin Abdullah

A thesis submitted in partial fulfilment of the requirements for the degree of Doctor of Philosophy

The University of Sheffield
Faculty of Engineering
Department of Mechanical Engineering

May 2018

Abstract

Aeroelasticity and fracture mechanics are two fields that commonly known will result in a structural failure. However, small attention is given in assessing the structural integrity of any flying object in aerospace application subjected to aerodynamic or aeroelastic loads especially the aircraft wing. The current research in the aircraft industry is focusing on the development of advanced composite wing structure, which there are still not well explored widely. Due to the higher strength of composite materials, a stronger wing could be designed to sustain the aerodynamic loads or any gust turbulence during flying at high altitude. This situation will be severely dangerous in the event of having a crack or damage on the surface of the cruising wing structure. This research aims at investigating the structural integrity of composite plate, either undamaged or with damage (with crack) subjected to the aerodynamic loads. The purpose of this study is to provide a novel numerical modelling in predicting the application of aerodynamic loads, by observing the flight maneuver safety margin including the flutter speed determination. Initially, the flutter speed was computed based on the coupled of finite element method (FEM) for the structural modelling and the doublet lattice method (DLM) in MSC Nastran for the unsteady aerodynamic modelling. Both structural and aerodynamic models were connected by interpolation using spline. In the end, the safety flight envelope for the composite plate was plotted based on the regulations provided by the Federal Aviation Regulations (FAR) 23. The numerical predictions of crack propagations of the damaged composite structure were determined by implementing the extended finite element model (XFEM), subjected to the aerodynamic loads intercorrelated through Fourier Series Function (FSF). Significantly, the aerodynamic loads were predicted by the implementation of gust, which produced the same level of maximum deflection analysed via aero-static analysis. The results show that the fibre orientation of the composite plate contributes significant crack propagations under the cruising aerodynamic loads. The same procedures were repeated to the wing box prototype developed under the joint program of Indonesian Aerospace, National Institute of Aeronautics and Space of Indonesia and Agency for Assessment and Application of Technology of Indonesia. For this work, the wing fracture was investigated by the influence of turbulence, called discrete 'gust loads'. From here, FSF was used to combine the wingtip deflection under the gust load influence, and hence applied XFEM to model the crack propagations. The results show that the crack propagated at the lower-front skin near to the wing root.

Acknowledgment

> *”The whole problem with the world is that fools and fanatics are always so certain of themselves, and wiser people so full of doubts.”*
> *- Bertrand Russell (British philosopher, mathematician, historian, and Nobel laureate, 1872-1970).*

I would like to express my full gratitude to my supervisor, Dr. Jose L. Curiel Sosa for his consistent encouragement, and extraordinary guidance throughout this research work. I am sincerely grateful to my second supervisor, Dr. Zeike A. Taylor for his help and support in this research. It was an honour for having such a proficient and supportive team to guide me and propel me throughout the highs and lows of these couple of years. The knowledge, skills, and attitudes I learnt from them have helped me in developing my professionalism.

Huge appreciations to the Ministry of Education Malaysia and the International Islamic University Malaysia for their sponsorship on my Ph.D. study. I would like to address a big appreciation to The National Space Agency Malaysia (ANGKASA) and National Institute of Aeronautics and Space Indonesian (Lembaga Penerbangan dan Antariksa Nasional/LAPAN) especially to Mr. Nanda Wirawan (Team Leader, Aerostructure Division, Aeronautics Technology Center, LAPAN) for their facilities and supports given in conducting this research.

My personal thanks to my friends, Computer-Aided Aerospace and Mechanical Engineering Team research group members, Mahesa Akbar, Meor Iqram, Dr. Behrooz Tafazzolimoghaddam, Dr. Joaquin Navarro-Zafra, Dr. Chao Zhang (Jiangsu University, China) and Dr. Juan Luis Martinez Vicente (Universidad de Castilla-La Mancha, Spain) for their continuous supports given to me since I started my Ph.D. journey. Not to forget, my military mentor Lieutenant Colonel Parvez Mohamed Yusuf RMAF for his continuous powerful motivations. All your guidance and supports in assisting me finishing this research will always be in my heart.

Deep admiration for my family members, my lovely mother, Marnilai Masriah and my father, Abdullah, siblings (Nur Ilham, Nur Fitri, Nur Aizzah, Nur Muhamad Firdaus, and Nur Abdul Hakim) for bringing me up to be someone who I am now. Last but not least I would like to give the highest gratefulness to my beloved wife, Azira bt Mat Zin and my daughters, Nur Aisyah Humaira’ and Nur Hawa Syakila for their sacrifices towards my responsible as a student.

Contents

List of Figures

List of Tables

Nomenclature

$\boldsymbol{A}^{MT}$	Mori-Tanaka concentration tensor
$\boldsymbol{I}$	Identity tensor
$\boldsymbol{S}$	Stress tensor matrices
Δ	Change in amount
η	Crack ratio
Λ	Swept angle
σ	Stress
θ	Angle
ξ_c	Crack location
a	Crack length
C_L	Lift coefficient
E	Modulus of elasticity
g	Structural damping
G_c	Critical fracture toughness
$H(x)$	Heaviside function
K	Stress intensity
k	Reduced frequency

L	Lift
r	Radius
R_n^α	Residual force
t	Time
V	Speed/ velocity
V_∞	Freestream velocity
V_c	Cruise speed
V_d	Dive speed
V_F	Flutter speed
V_R	Reference speed
2D	Two-dimensional
3D	Three-dimensional
ALE	Arbitrary-Eulerian method
CASR	Civil Aviation Safety Regulations
CFRP	Carbon fibre reinforced polymer
DLM	Doublet lattice method
FAA	Federal Aviation Administration
FAR	Federal Aviation Regulations
FEM	Finite element method
FSF	Fourier series function
FSI	Fluid-structure interactions
GA	General aviation

KEAS	Knot equivalent airspeed
KTAS	Knot true airspeed
MFH	Mean field homogenisation
mph	Miles per hour
n	Load factor
NASA	National Aeronautics and Space Administration
NSVs	Non-synchronous vibration
NTSB	National Transportation Safety Board
RVE	Representative volume element
SERR	Strain energy release rate
SFVs	Separated flow vibrations
SIF	Stress intensity factor
SV	Synchronous vibration
VCCT	Virtual crack closure technique
VIV	Vortex-induced vibration

Chapter 1

Introduction

"If history repeats itself, and the unexpected always happens, how incapable must Man be of learning from experience."
- George Bernard Shaw (Irish playwright, critic and polemicist, 1856 – 1950).

This chapter presents a brief introduction to the investigations conducted in this study. An overview is provided to capture the attention of studying the interrelation between aeroelasticity and fracture mechanics of composite structure. A brief discussion to show the significance of this research is included.

1.1 Field of Study in Aeroelasticity

"Aeroelasticity" is defined as one field of study that related to the interaction of structural elasticity and the resultant aerodynamic forces from the freestream [1]. Aeroelasticity is a field of study that investigates the interactions between inertia, elasticity, and aerodynamics. There are several phenomena that are known in this region, such as flutter, buffeting, galloping, and vortex-induced vibration (VIV).

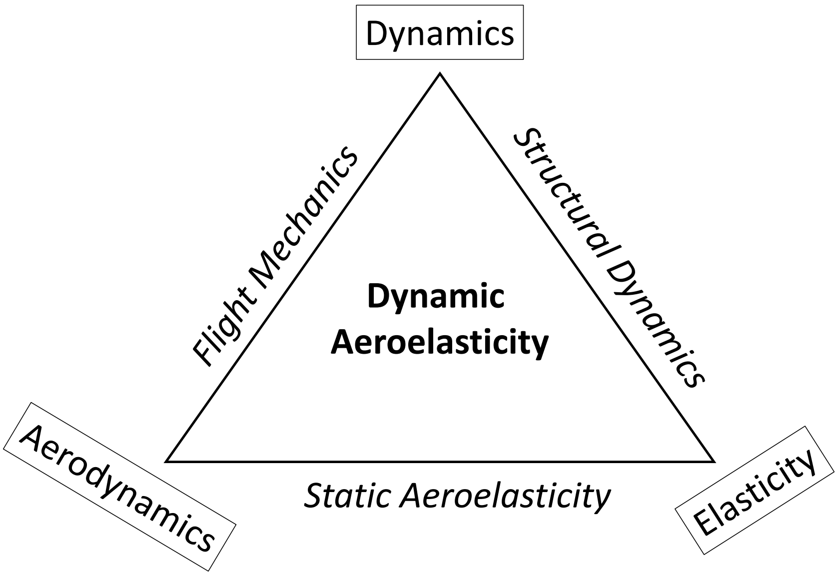

Figure 1.1: Field in aeroelasticity by Hodges and Pierce [1]

Based on Figure 1.1, when the dynamics and the aerodynamics fields are combined, the combination appears to the development of dynamics stability field called as flight mechanics. The same development goes for the study of mechanical vibrations which is called as structural dynamics when dynamics and elasticity are combined. When the study concerns about aerodynamics and elasticity, the static aeroelasticity field of study are established. Some examples of static aeroelasticity phenomenon are the aeroelastic effect on static stability, load distributions, control effectiveness, divergence and control system reversal.

Flutter and galloping are instability problems. Technically, flutter is a self-excited phenomenon in which the structural vibration exerted by the aerodynamic loads due to the movement of the air relative to the structure. Flutter commonly occurs at least if there are influences of two modes coalescent at a particular speed, so-called critical flutter speed. While galloping usually induced by an internal turbulence of the fluid or other initial disturbance [2]. Different with flutter, galloping usually is a one-degree-of-freedom case, i.e., transversal galloping or torsional galloping.

In contrast, buffeting and VIV classified as resonance problems. Buffeting differs with galloping phenomenon, where the secondary structure oscillates due to the turbulence flow extracted by the adjacent structure. Buffeting phenomenon mostly is seen when the open space freestream flows exciting an array of electrical cables due to the wake of upstream cables. While VIV is exerted by the oscillating vortex behind a structure exposed to an airflow [3].

All types of aeroelastic phenomenon are categorised into static and dynamics aeroelasticity which are presented in Figure 1.2.

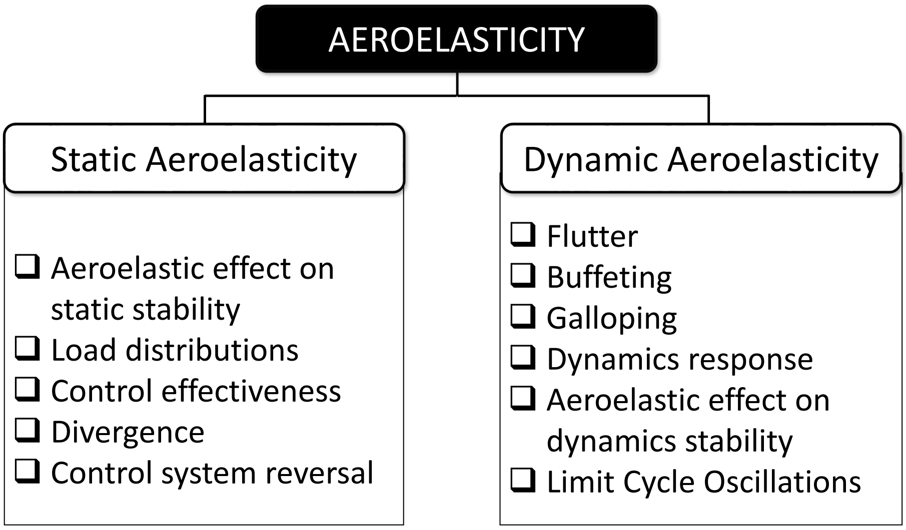

Figure 1.2: Example of static and dynamics aeroelasticity

1.1.1 A brief history of aeroelasticity failure

Flutter can deform an aircraft due to dynamics instability [4]. The flutter phenomenon was first time discovered in 1916 where a twin-engine biplane bomber called Handley Page 0/400 in Lanchester, England [5] has crashed. For that reason, several aircraft crash incidents subjected to flutter failures are listed in Table 1.1 to explore the causes of this event.

Table 1.1: List of aircraft flutter crash incidents

No.	Model - (Type)	Year	Type of flutter	Highlights	Refs.
1	Braniff Airways Lockheed Electra L-188A - (GA)	1959	Whirl flutter	Harmonic coupling cause ever larger wing vibrations	[6]
2	A Northwest Orient Lockheed L-188 Electra - (GA)	1960	Wing flutter	A design flaw caused an oscillation known as a mode to transfer propeller wobble to the outboard nacelles	[7]
3	GAF N24 Nomad Aircraft - (GA)	1976	Tail flutter	Aicraft crashed	[8]
4	Grob Aerospace/ G180A - (Business)	2006	Elevator flutter	1 fatal	[9]
5	Aveko S.R.O. VL3A1 Flamingo - (Light Sport)	2010	Wing flutter	Left wing failed during descent, 2 fatals	[10]
6	P-51D Mustang - (Light Sport)	2011	Elevator flutter	10 fatals, 64 injuries	[11]

The same phenomenon was identified in the incident of Tacoma Narrows Bridge. Figure 1.3 is taken from [12] illustrates the collapse of Tacoma Narrows Bridge at flutter condition. This phenomenon was recorded on 7th November of 1940 where the wind frequency had coincided with the natural frequency of the bridge, thus has excited the bridge to catastrophic vibrations.

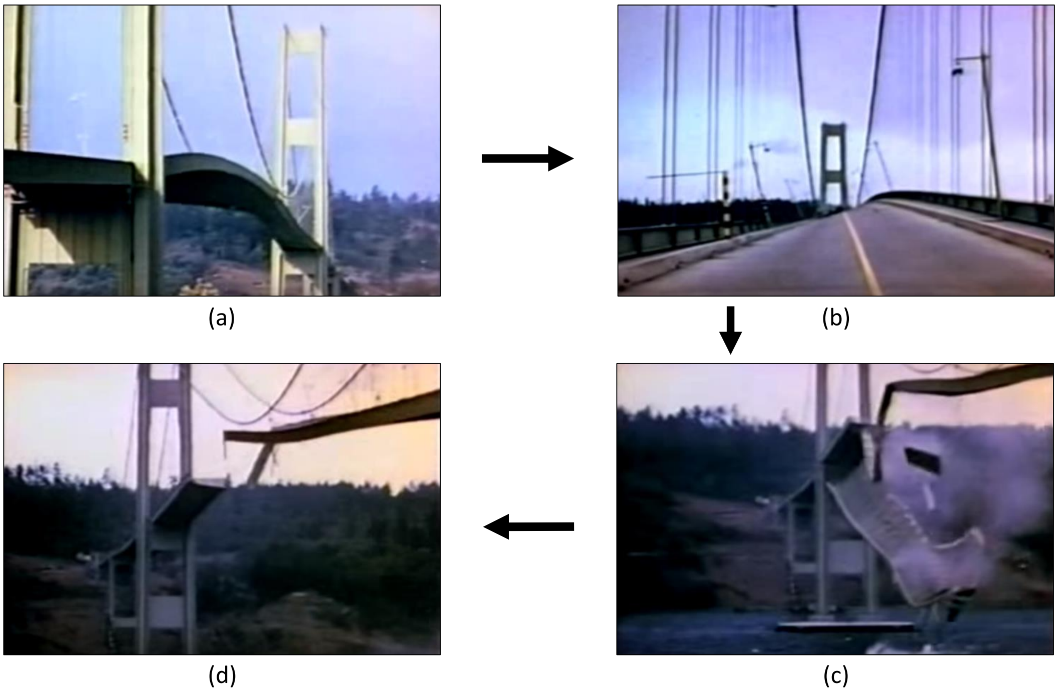

Figure 1.3: Tacoma Narrows Bridge failure due to flutter excitation where (a) the bridge began to the interacts with the free stream air flow, (b) the vibration amplitude has increased with the increment of aerodynamic load, (c) the bridge structural damping could not stand the load and began to crack, and (d) the bridge has completely broken due to the excitation

There are four images denoted as (a), (b), (c) and (d) in Figure 1.3, which present the fracture mechanism of Tacoma Narrows Bridge under aerodynamic load. In (a), the airflow from a perpendicular direction to the bridge is interacting with the bridge structure. The bridge began to vibrate due to the self-exciting mechanism when the flow frequency coincides with the natural frequency of the bridge shows in (b). The vibration amplitude is then kept increasing with the incrementation of the dynamic load. When the structural damping could not endure the bridge large vibration amplitude subjected to the excitation frequency, a crack began to appear on the bridge structure. With the increment of time which also increased the loads acting on the bridge, the bridge has broken due to the excited loads as depicted in (c). Thus, the splitting of the bridge to the flutter phenomenon is presented in (d), which has brought the bridge collapsed.

1.1.2 Flight flutter test techniques

In verifying an aircraft safety before it is permitted to fly, several tests are required such that ground vibration test, fatigue test, stress analysis, drop test and flutter test. In this section, the flutter test procedure is described. The vibration and the flutter flight test procedures reported by Wolfe [13] and FAA [14] are presented here.

The aircraft is accelerated during flying until it reaches the extreme region of the flight envelope which is until dive region. The plane should be redesigned if it has proven to be in a dangerous situation. However, the flutter flight testing is considered to be a success if it is still safe in that region.

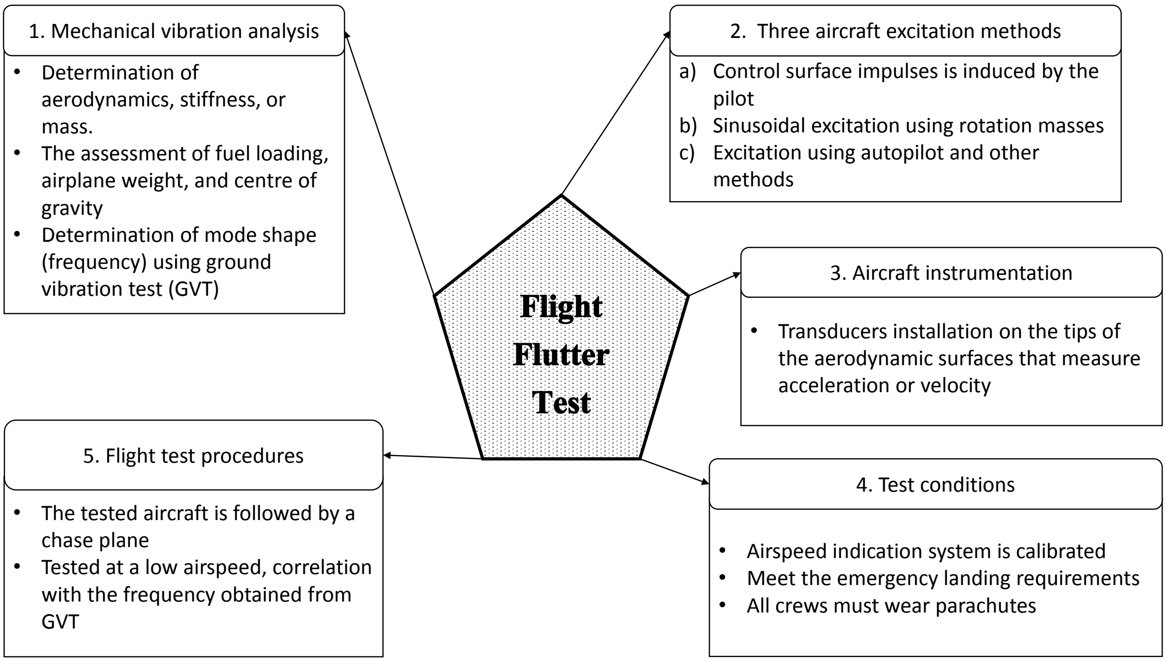

1. Mechanical vibration analysis
- Determination of aerodynamics, stiffness, or mass.
- The assessment of fuel loading, airplane weight, and centre of gravity
- Determination of mode shape (frequency) using ground vibration test (GVT)

2. Three aircraft excitation methods
a) Control surface impulses is induced by the pilot
b) Sinusoidal excitation using rotation masses
c) Excitation using autopilot and other methods

3. Aircraft instrumentation
- Transducers installation on the tips of the aerodynamic surfaces that measure acceleration or velocity

4. Test conditions
- Airspeed indication system is calibrated
- Meet the emergency landing requirements
- All crews must wear parachutes

5. Flight test procedures
- The tested aircraft is followed by a chase plane
- Tested at a low airspeed, correlation with the frequency obtained from GVT

Figure 1.4: Flight flutter test procedure listed by Wolfe [13] and FAA [14]

1.2 Problem Statement & Its Significance

Flutter is defined as the unsteady aerodynamic and structural interaction event in which it can cause a structural failure. Numerically, the flutter speed of a wing aircraft depends mostly on several factors such as mass matrices, stiffness matrices, and aerodynamics matrices. For that reason, several relationships can be linked to these fields of study. In general, the fracture mechanism is expected to give influence in the aeroelasticity investigation based on these relationships.

1.2.1 Research motivation

From the overview discussed in Section 1, several areas of studies are interconnected to strengthen the reason for conducting this research. For that reason, several challenges are highlighted based on the historical data and events that happened in the past.

1.2.1.1 *Related case study*

The most recent airplane crash due to aerodynamics flutter was reported in 2011. The crash of the North American P-51D Mustang named as The Galloping Ghost happened during the National Championship Air Races in Reno/Stead Airport (RTS), Reno, Nevada shown in Figure 1.5. The incident has caused fatalities to the pilot and other ten people on the ground. At least 64 people were accidentally injured.

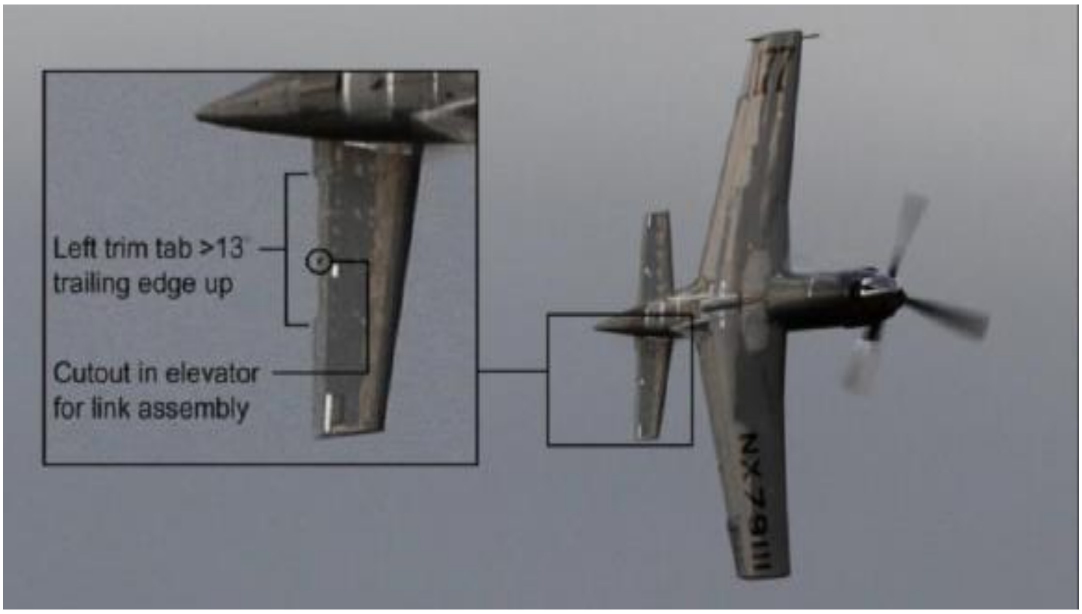

Figure 1.5: P-51D Mustang by NTSB [11]

The National Transportation Safety Board (NTSB) released the causes of the incident in the Aircraft Accident Brief report [11]. The statement was mentioned below:

> *"The reduced stiffness of the elevator trim tab system might be the cause that triggered aerodynamics flutter to happen at racing speed. A deteriorated locknut inserts made the trim tab attachment loosen and the fatigue crack in one screw initiated. Both factors had reduced the stiffness before the crash happened. The failure*

of the left trim tab assembly, elevator movement, high flight loads, and out of control were caused by an aerodynamics flutter. Undocumented and untested major modification of the flying aircraft further made the causes of the accident worst.”

From this aircraft accident report, it is shown that the relationship between fracture mechanics and aeroelasticity could be deeply interrelated. From the view of aeroelasticity, the flutter boundary region of the aircraft has changed due to several factors. Before the plane was permitted to fly, the flutter speed has been determined, and several tests have been performed. However, based on the report, it is mentioned that the stiffness of the material has been reduced due to the loose of screw attachment and fatigue crack which led to an aeroelastic failure which is called flutter. When the flutter happened less than the expected speed as determined at the initial place, it is meant that the flutter boundary region has shifted less than expected in the first place.

The other thing that the organization did not mention is about the crack propagations that led to the failure of the aircraft. This present research is investigating the relationship between crack initiation that could trigger the structural failure, then influence the flight boundary diagram by reducing flutter speed. This investigation is in the attempt to model crack propagations of composite structures using a numerical method called XFEM.

1.3 Aims and Objectives of This Study

The research aims to establish a platform to interface the crack modelling of composite structure using XFEM with the aeroelastic modelling using Nastran for iterative analysis. The present research embarks on the following objectives:

- **To model transversal crack and delamination of laminates using XFEM.** The scope in this part will focus on the validation of experimental results on crack and delamination from previous literature. A modelling technique called XFEM is used to solve the discontinuity of element in modelling the crack. Besides that, there is also an investigation on the size effect of the presented laminates.

- **To develop and validate the flutter solution, and at the same time**

investigate the effect of cracked composite plates of different lay-up on flutter speed.

For this objective, a previous study concerning the damage effect on flutter that was by previous literature is studied. The historical results for the modelling are compared with this presented technique of coupling FEM-DLM using *pk*-method for the flutter solution. Several flutter responses are expected to be plotted in order to explain the effect of damage to the flutter solution.

- **To investigate the crack propagation subjected to gust loads at several specific flight regions before flutter is expected to occur.**

  This objective is the most original work that expected to be accomplished in this research. At this state, several aircraft crash incidents that happened due to fracture under dynamics loads are supposed to be investigated at this point. Some modelling technique of coupling between XFEM and the computed aerodynamic loads will be performed to support the hypothesis.

- **To develop a fracture mechanism on wing box subjected to aeroelastic gust loads.**

  Gust is known as the one type of aeroelastic loads that can cause a disturbance on a flying aircraft. Here, a discrete gust of '1-cosine' is computed to investigate the weakest spot on the wing box that could lead to destruction when it associates with gust loads. XFEM is used to examine the crack propagations on the wing surface which depends on the energy release rate of the aluminum wing.

1.4 Research flow

The research flow is presented in Figure 1.6 to achieve all objectives described in Section 1.3. Herein, two big fields of studies which are fracture mechanics and aeroelasticity are combined to investigate the fracture mechanism under the generated aerodynamic loads.

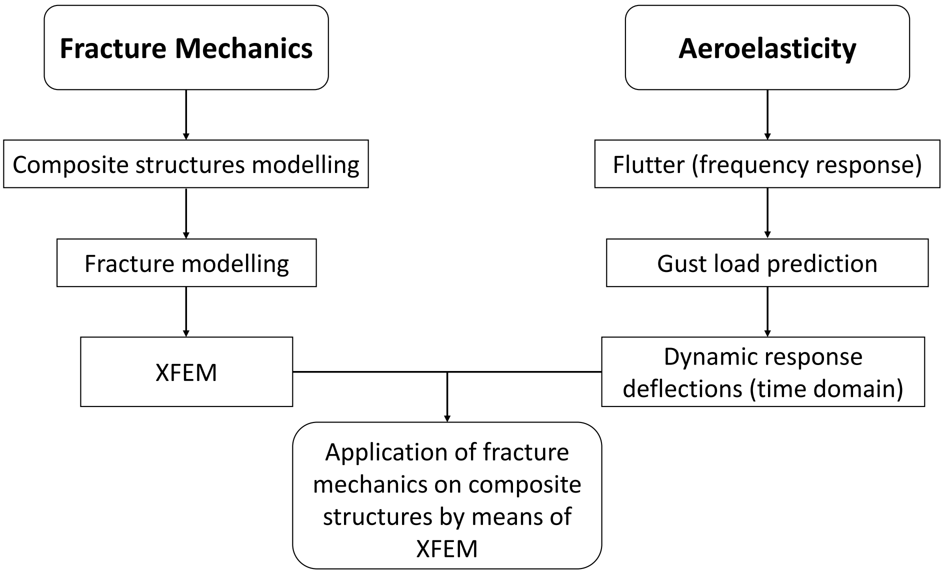

Figure 1.6: Contribution to knowledge: presented research flow

The study is focused on the attempt of modelling crack propagations by means of XFEM under aerodynamic loads. However, there are few challenges face in developing the computational procedure to achieve this objective. For example, there is a limitation in fracture modelling using XFEM since the analysis is applicable for linear static loads and implicit [15]. For that reason, several modifications are needed since the aerodynamics, and aeroelastic loads will be used in modelling the fracture. Thus, it is a crucial state to be pointed out since the computed aerodynamics loads, such that pressure distributions are mostly described in real and imaginary form.

Doublet lattice method (DLM) [131] is applied to evaluate the unsteady aerodynamic loads. The DLM is a panel-based unsteady aerodynamic approach for a planar lifting surface. The aerodynamic forces, i.e., lift, are calculated as a function of airspeed, frequency, and mode shape. Coupling between the aerodynamic panels and the finite structural elements is implemented to provide the flutter instability analysis. This flutter analysis is used as verification of the structural and aerodynamic models of the lifting structure prior to performing the gust analysis. To perform the gust analysis, the aerodynamic forces are transformed from the frequency function into time function. This is due to in the present work, the objective is to obtain the response of the structure with respect to the time. Furthermore, the crack propagation is done in the time domain via XFEM. The flutter and gust response analyses without crack propagation are conducted by using the MSC Nastran Aeroelasticity module. The crack propagation evaluation due to the gust response via XFEM is performed via Abaqus XFEM module.

1.5 Thesis Outline

A summary of this study is reported here.

Chapter 1 introduces the essential background of the flutter mechanism. Here, several cases of flutter incident of Tacoma Narrows Bridge is discussed for further explanation. The other case of flutter that is the crash incident of the North American P-51D Mustang also been explored. This case is a related case to the current investigation and highlighted as the motivation for conducting this research.

Chapter 2 presents the literature reviews that arranged based on the relationship between fracture and aeroelasticity. Several works in fracture modelling are discussed and proposed for this research.

Chapter 3 presents the strategy of transversal crack and delamination of laminates composite. Here, the implementation of fracture modelling technique called Extended Finite Element Modelling is introduced.

Chapter 4 shows the flutter assessment conducted on the cracked composite plate. The investigation is divided into two parts, the effect of crack ratio to flutter speed and the effect of crack location to flutter speed.

Chapter 5 presents the investigation of structural integrity of cracked composite plates ($\theta = 0°$ and $\theta = 135°$ $(-45°)$) under the aerodynamic loads influence.

Chapter 6 presents a novel insight of fracture mechanism on commuter aircraft wing box under aeroelastic-gust loads using XFEM.

Chapter 7 presents the conclusions of this research. Most of the novelties are featured in this chapter.

Chapter 2

Aeroelasticity - Fracture Literature

> *"Failure is so important. We speak about success all the time. It is the ability to resist failure or use failure that often leads to greater success. I've met people who don't want to try for fear of failing."*
> *- J.K. Rowling, CH, OBE, FRSL, FRCPE (British novelist, screenwriter, and producer, 1965).*

This chapter presents discussions of some studies and investigations that related to the present work. The arrangement of the literature is constructed based on the interrelation between fracture mechanics and flutter modelling that stresses the originality of this research.

2.1 Relevant Fracture Modelling

Fracture mechanics is one of the topics that contribute to the development of structural integrity field. Several fracture computational techniques on composite structures are reviewed in this section. In this part, some factors that could affect a structural fracture are studied. The discussions include some relevant challenges and problems that explained in other research which are related to present investigation.

2.1.1 Type of fracture

Several types of fracture behaviour are explained in exploring the fundamental of this field of study. The reason is that the kind of fracture depends on the type of loads acting on the structure. There are three types of well-known fracture modes as shown in Figure 2.1.

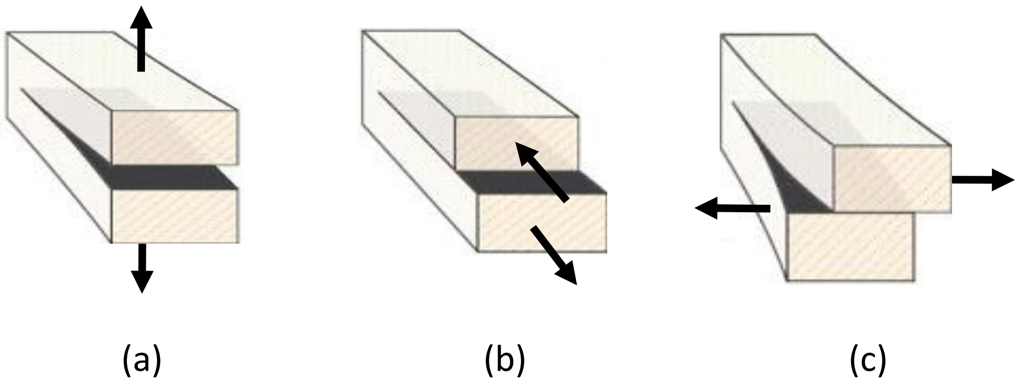

Figure 2.1: Type of fracture crack separation modes where (a) Fracture Mode I: crack opening, (b) Fracture Mode II: in-plane shear, and (c) Fracture Mode III: tearing mode

Fracture Mode I as shown in Figure 2.1 (a) is a fracture mode that happened when two loads are acting in the opposite direction, 180° to each other. This condition has triggered the crack opening. The Fracture Mode II is a condition where the structure experience in-plane shear while the Fracture Mode III is a tearing mode where the shear stress is acting parallel to both the plane of the crack and the crack front. In this thesis, it is intended to apply a computational technique in developing the Fracture Mode I. In another hand; several works have computationally modelled the Mode I fracture by using a virtual crack closure technique (VCCT) for a composite structure. [16, 17]. This technique not only can be used to model 2D crack but also 3D crack. Rathinasabapathy [18] has applied VCCT to model and validate the 2D and 3D crack of Mode I in 3 points bending experiment of the composite plate. The interlaminar crack, called as delamination is defined as a degradation occurrence that causes a separation between bonded layer which reduce the stiffness and the strength of the composite structure [19]. A great deal of previous research into the interlaminar crack which has focused on the delamination growth modelling under static loads by eliminating the buckling effect performed by Allix and Ladevèze [19].

In other hand, a free edge delamination of carbon-epoxy laminates was modelled and experimentally validated by Schellekens and Borst [20]. Here, further analysis of size effect also been investigated. The matrix crack and delamination strength are found to be decreased as the thickness of the laminates are increased. Interlaminar stresses are the major factor that contributes to triggering the lamination of composite laminates near the free edges, for example, the composite plate edge. There are also some works that analysed stress on interlaminar crack; under uniform axial extension [21], out-of-plane shear/bending [22], anticlastic bending deformation [23], and combined thermo-mechanical loading [24].

From Figure 2.2 [25], the interlaminar stress shows a stable value from a free edge. The interlaminar stress value tends to diverge as it nears to the free edge, leads to an infinite value. Thus, this is also called as the singularity stress field where a point at which a function takes an infinite value. This matter is the reason that any estimation of interlaminar stresses at a free edge is mesh dependent. The interlaminar stress at the free edge will continue to increase as the mesh is refined. Technically, the singularity stress fields of anisotropic composites near the free edges are one of the factors accountable for delamination under static loading. For instance, the singularity order of stress field depends on the geometric angles of the bonded wedges, which form a half plane in this case, and the composite material properties which include the stiffness and orientation of the fibres. In this case, the singularity is solved by manipulating the wedge angle and the fibre orientation in a full circular region [26].

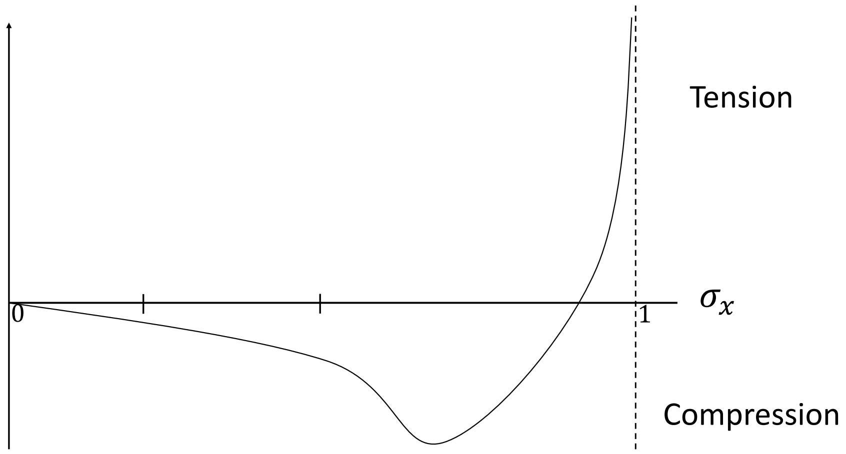

Figure 2.2: Free edge singularity plot [25]

2.1.2 Challenges in modelling fracture under dynamics load

Over the past few decades, researchers began to investigate the effect of aerodynamic loading acting on a flying surface if the loads could trigger the crack propagation. For instance, an experimental has been carried out by Schijve et al. [27] on sheet aluminum specimen with central notch and two fatigue cracks, to assess the crack propagation under lower and higher gust loads. Based on the fractographic inspection, there was a fracture surface transition from the bending (tensile) mode to the torsional (shear) mode during the crack growth. In the state of this condition, flight simulations for the crack assessment have been done to validate the results [28]. Several effects on the crack propagation rate have been studied by the implementation of a gust load.

2.1.2.1 *Discontinuity problem in fracture modelling*

The difficulty that is mostly confronted by researchers in fracture modelling is the discontinuity. There are two types of discontinuity which are the strong discontinuity and the weak discontinuity. The strong discontinuity is presented as a jump of displacement shown in Figure 2.3.

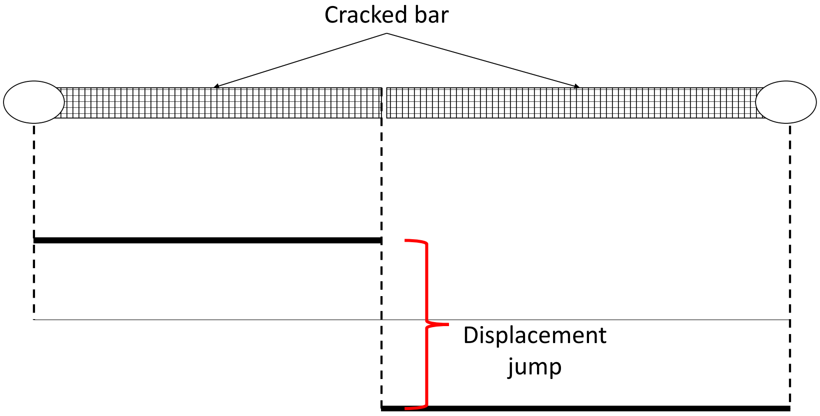

Figure 2.3: Discontinuity problem: cracked bar

There is also a problem of discontinuity that happens when modelling a fracture of two combined material called bimaterial in Figure 2.4. This concern involves a discontinuity of kink in displacement.

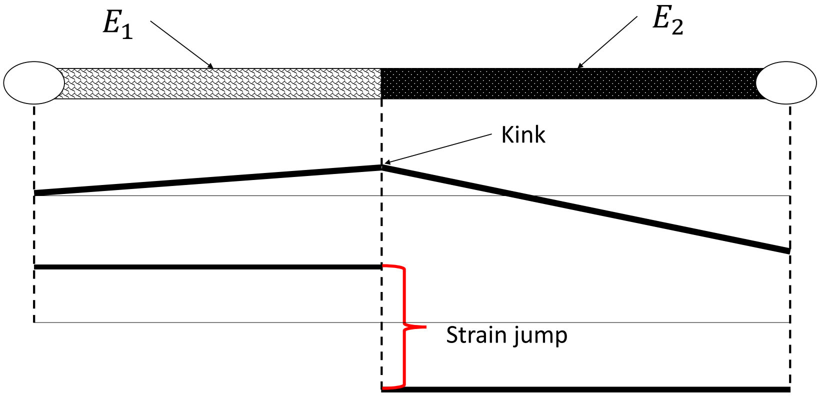

Figure 2.4: Discontinuity problem: bimaterial bar

The geometry must be explicitly represented the mesh when modelling the fracture using standard FEM. To do this, the nodes are significantly located on the crack tip and across the crack. Thus, mesh refinement is very important to be implemented near the crack tip. The reason is that the mesh refinement will represent the asymptotic fields associated with the crack tips. However, a process of remeshing is necessary to be performed as the crack propagates along the structure. This circumstance has led to the disadvantage of modelling fracture in FEM where the computational time and cost are increased due to the remeshing process.

2.1.2.2 *Structural fracture due to vibration motion*

As mentioned in Hodges and Pierce [1], flutter is an elastic-aerodynamic failure that is caused by self-excitation mechanism. The flutter speed is determined by examining the structural damping and frequency point of view [14]. There is research that was conducted by Odahara et al. [29] which studied the hydrodynamics self – oscillation phenomenon on a nuclear reactor which triggered micro level fatigue fracture. This is the only research that is showing the nearest approach to the present work here. The current practice is concerns in modelling the crack or split of the composite plate under aerodynamics load using XFEM.

When there is a vibration that drives to the increment oscillations in a system at specific frequency due to the existence of an external force, the system is in the state of resonance. Also, there are some concerns about in the event of aerodynamic load can cause vibrational forces. A crack identification on rotor was done by Dong and Chen [30], which managed to predict the possibility of having another cracks development once the pre-existing open crack has undergone a vibrational mode. Also, there is an exciting approach that was established by Magi et al. [31] to model the transversal crack and delamination of laminated carbon fibre reinforced polymer (CFRP) under vibration fatigue by applying the Virtual Crack Closure Technique (VCCT). In another hand, the VCCT was used to calculate the Strain Energy Release Rate (SERR) at the crack tip of an opening delamination under vibration conditions.

This event is supported with several occurrences in some research such as long-span suspension bridges interaction with freestream flow [32], transient load and tornado effect on buildings investigation [33] and aerodynamic load control using blade on wind turbine [34]. In the state of this condition, the aerodynamic loads will deform the structure, or increase the structural deflections which are expected could lead to the crack propagation.

From this point of view, it is suggested that different type of dynamic load applied in fracture mechanics should be modelled based on the application. The novel idea that is presented in this work relies on the unexpected fracture mechanics failure of fractured structure that happens under dynamic load i.e. at dive condition in a safe region (based on the V-n diagram) before flutter speed is achieved. In the present investigation, this is the first time that aerodynamics load is coupled with XFEM to model the crack propagations.

2.2 Fundamentals of Aeroelasticity

In general, flutter will cause a catastrophic fracture of the structure subjected to aerodynamic loads. When it is referred to the flight envelope in Figure 2.5, flutter speed is always beyond the safe flight regime.

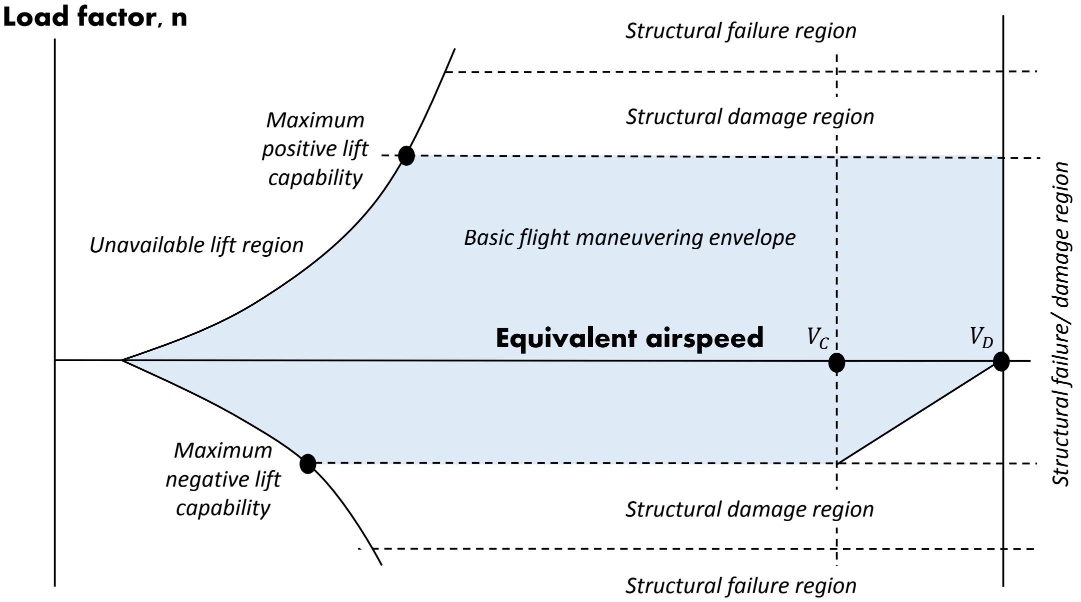

Figure 2.5: Flight envelope by FAA [14]

One of the destructive aeroelastic phenomena is known as flutter. Flutter phenomenon occurs when there is an interaction between the structural elasticity, aerodynamic loads, and the inertia forces. When a structure is excited near to the flutter speed, the structure begins to vibrate. In the case of horizontal planform structure such as wing or bridge that deals with the proportional direction of freestream flow, the structure will vibrate and begin to oscillate. In severe condition, when the structure deforms, the aerodynamic distribution on the structure will increase, and subsequently, raise the oscillating rate. If the structural damping could not sustain the load, the structure will fail.

However, due to several reasons, it has cast doubt on the failure potential when there is existing damage such as a crack in the structure when it interacts with the aerodynamic loads. In this case, there is a curiosity on either the flutter will come first or the cracked structure will fail due to the fracture circumstance. The flutter computational results on cracked unidirectional composite plates by Wang et al. [35], where the structures were modelled as beam elements. The flutter results were computed using Galerkin method, where the structures were coupled with strip theory for the aerodynamic modelling. Nevertheless, only a few references are given in this study that successfully models the fracture of composite structures subjected to aerodynamic and flutter loads. For this judgement, this study intends to model a fracture under this type of dynamic load.

2.2.1 Flutter mechanism

There are two types of vibrations, synchronous vibrations (SV) and non-synchronous vibration (NSVs) [36] as shown in Figure 2.6. This type of vibration is the same with separated flow vibrations (SFVs) except NSVs are well order flow that happen at one dominant frequency, also can happen at stalled condition [37]. Separated flow vibrations (SFVs) are likely buffeting developed when an unsteady, separated flow is generated over the structures and lead to the structural vibration. There are three types of self-excited vibration which are acoustic resonance, self-excited rotating instability and flutter.

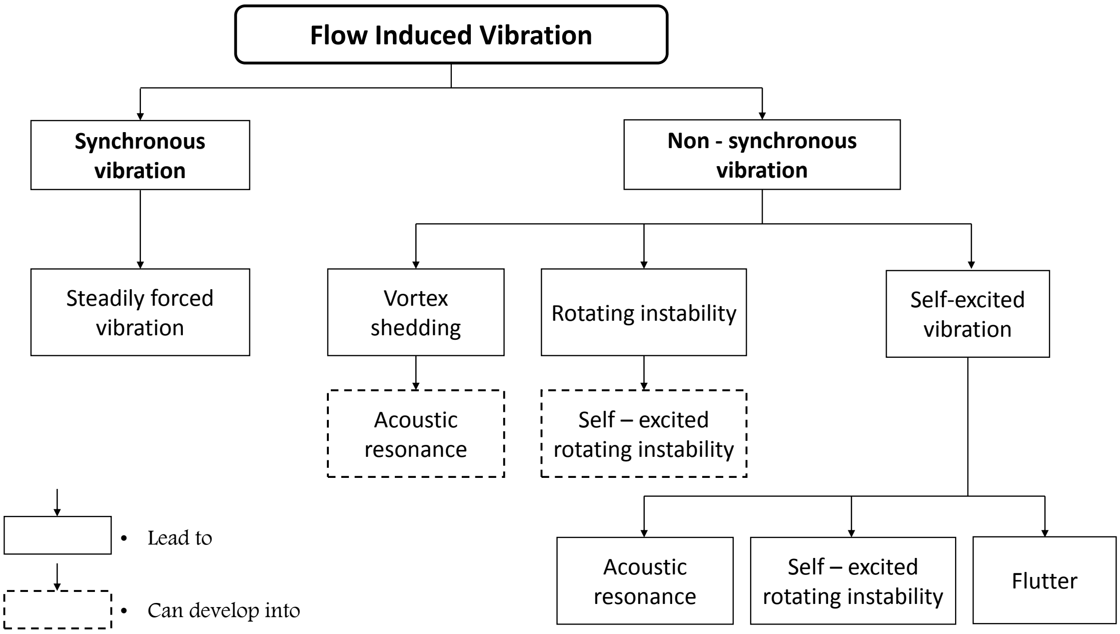

Figure 2.6: Field in flow induced vibration [36]

All structures have their own natural vibration modes depending on the mass distribution, stiffness and material composition. When the structures are excited at a certain frequency, the structures will experience a rapid periodic motion. Flutter happens because of the self-excitation phenomenon as shown in Figure 2.7.

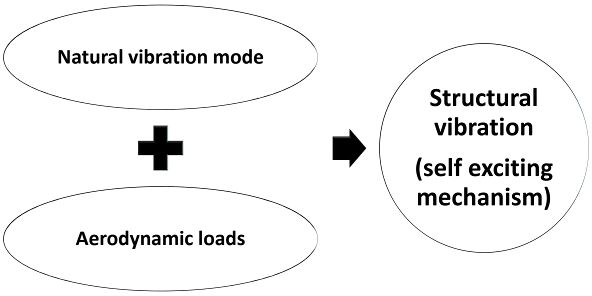

Figure 2.7: Flutter self-excited mechanism

It is a result when aerodynamic load interacts with the properties of the structural components. This is also called as self-sustaining motion, where it can be in the bending mode, torsion mode or combination of both modes. Thus, the structure will vibrate when the streamlined stacking at the time is intercepted with a natural vibration mode. The vibrating structure will then increase the streamlined load - where at the same time will increase the vibration amplitude in a severe situation. This self-sustaining mechanism can lead to the structural self-destruction failure if the structural damping is insufficient. In other hand, Figure 2.8 manifests the conventional flow diagram to estimate the flutter speed based on frequency response mode.

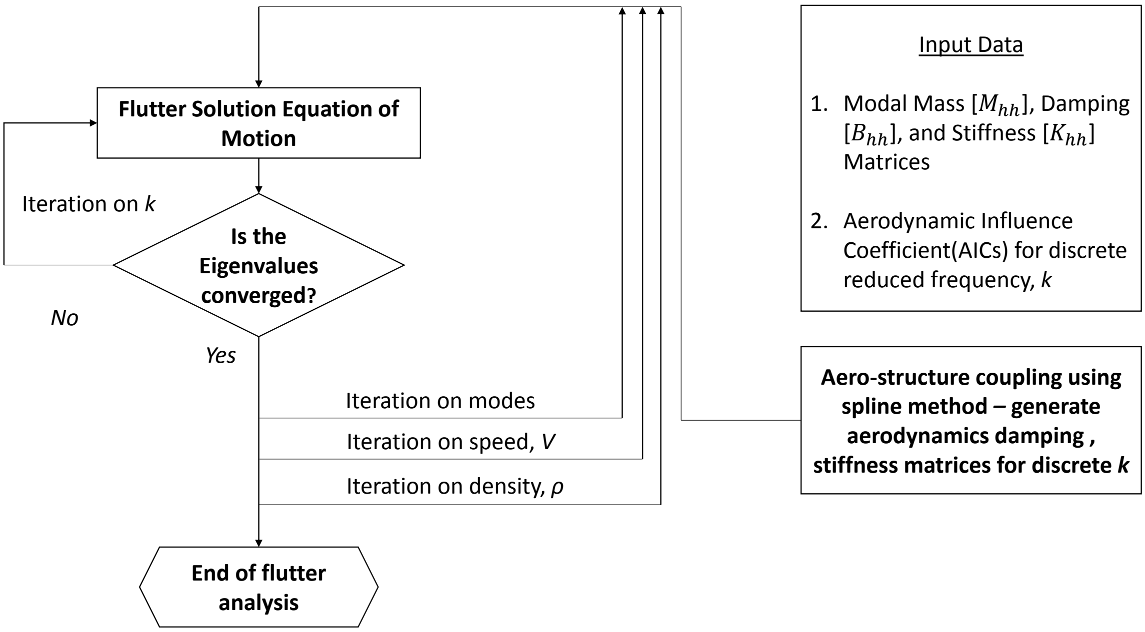

Figure 2.8: Typical flow diagram for prediction of flutter

As illustrated in Figure 2.8, the input data from modal mass matrices, damping matrices and stiffness matrices are required to calculate the flutter speed. For instance, the reduced frequency, k is iterated until the computed eigenvalue has found to converge. The computational of flutter speed is satisfied when the input data are utilised for several iterations process of vibration modes, speed and density.

2.2.2 Flutter problem solution

Several techniques that are implemented to solve flutter speed problem are discussed in this section. There are some significant issues that are necessary to be explored before the flutter solution could be reached. As the discussion in the Section 1.2, the flutter speed estimation depends on the mass, stiffness, damping and the external load. By changing these parameters, some ideas could be developed to improve the flutter speed or region.

The most popular technique that is used widely to enhance the flutter speed region is mass balancing. Theoretically; to implement this technique, center of gravity also known as the center of mass must be located ahead (forward) of the aerodynamic center of the wing or control surface. A mass or weight might be added at the front of the structure, considering the mass not too heavy. A theoretical report by Moxon [38] suggested the implementation of mass balancing using mass-balance arm flexibility to improve the control surface flutter.

There is also another technique that implemented to improve the flutter speed. By changing the shape of the structure, the aerodynamic loads acting on it can be altered, and thus change the flutter boundary. The implementation of this technique can be seen in an aerospace application where a finite rectangular wing could be altered with a swept angle at the wing root.

There are three sweptback wings with the angle of 0°, 35° and 50° presented by Molyneu [39] to study the flutter effect of sweptback angle of the wing. The same investigation performed by Barmby et al. [40]. The other work concerning aerodynamics on wing using ground-launched rocket [41]. The cause of the flutter speed has been delayed due to sweptback angle is presented in Figure 2.9.

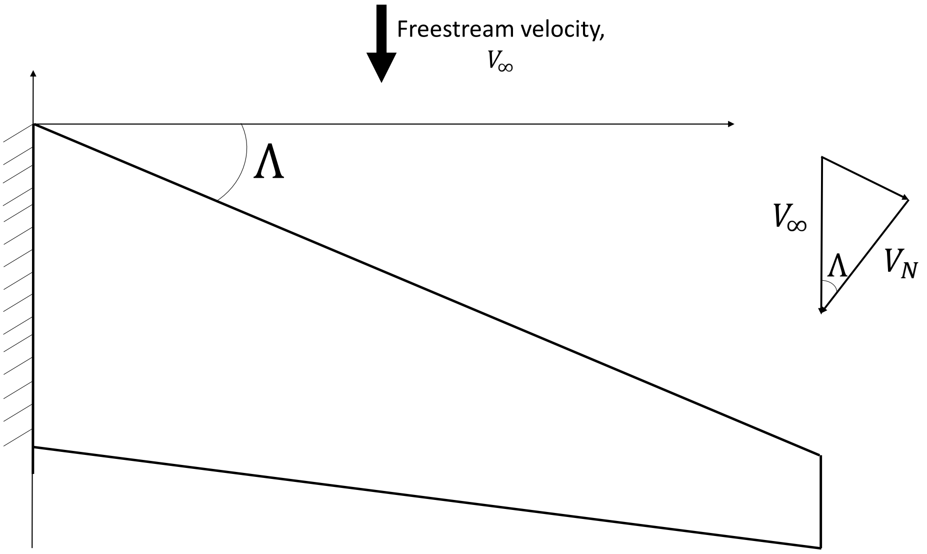

Figure 2.9: Sweptback wing designed in reducing flutter speed

In Figure 2.9, the stream velocity of airflow is reduced due to the sweptback effect. The stream velocity that is normal to the wing surface relationship is shown in Equation 2.1 where Λ is the swept angle, such that 'cos' as a function of trigonometry.

$$V_N = V_\infty cos\Lambda \tag{2.1}$$

Consequently, the actual free stream Mach number can be increased as the critical Mach number, in this case, the designed flutter speed is now reduced. However, it is a different situation when the wing is swept forward, where Λ has become more prominent, thus led to a negative normal stream velocity. A twisting force developed by the aerodynamic lift will rotate the wing leading edge upward and cause the increment of the angle of attack. As the angle of attack increases, the lift force also increases which has continuously twisted the wing. This will result in a broken catastrophic failure called divergence.

This is one of the reason that for some decades, the application of swept forward wing on jet fighter aircraft could not be developed due to high-speed maneuver that might cause the wing suddenly breaks. From the view of aerodynamics, there is the beneficial side of having forward swept wing. The maneuverability and controllability of forwarding swept wing remain stable and unstalled at high angles of attack because the air flows inboard on the forward swept wing, which shows a different attribute when compared with the backswept wing [42].

Then, a novel technique was found, which is by changing the isotropic material to anisotropic. This technique has been proposed by Krone [43]. By doing this, the stiffness of the structure is altered since the elasticity of the composite material is higher compared to the isotropic material. The applications of aeroelastic tailoring were used to improve the bending-torsion mode of swept-forward wing [44, 45, 46]. Consequently, since the density of composite is lower than the metal, thus composite structure attributes to a lighter weight. Several optimization techniques for aeroelastic tailoring have been proposed to reduce the structural weight such that Evolutionary Algorithms [47], FE analysis, and gradient-based optimization modules within the Nastran package [48] and Steepest Descent Method [49], Master-Slave parallel real-coded genetic algorithm (GA) [50] by using composite laminates as the wing structure. The flutter speed is altered by changing the laminates ply angle [49] to increase the flutter speed. Aeroelastic tailoring also has been used to optimise the wing design by reducing the angle of attack of the rear wing at higher speed [51]. The optimization has constraint the tractions at low speeds.

For some reasons, the knowledge of factors that could efficiently affect the flutter boundary could be exploited to obtain some benefits. For example, the application of energy harvesting technique due to flutter vibration has benefit in transforming from mechanical energy due to self-oscillation to the generation of electrical energy [52, 53, 54, 55].

2.3 Disturbance effect on flight performance

2.3.1 Instability and structural failure due to gust loads

In common, most of the aircraft will encounter aeroelastic loads called gust loads during the flight. A critical aspect of predicting the gust loads is by knowing the gust flow behaviour. According to Wright and Cooper [56], the turbulence can be described into two types; the first one is discrete gust and the second one is continuous turbulence. The illustrations of both turbulences conditions are shown in Figure 2.10.

For instance, the wind data collection at NASA's 150-meter Meteorological Tower

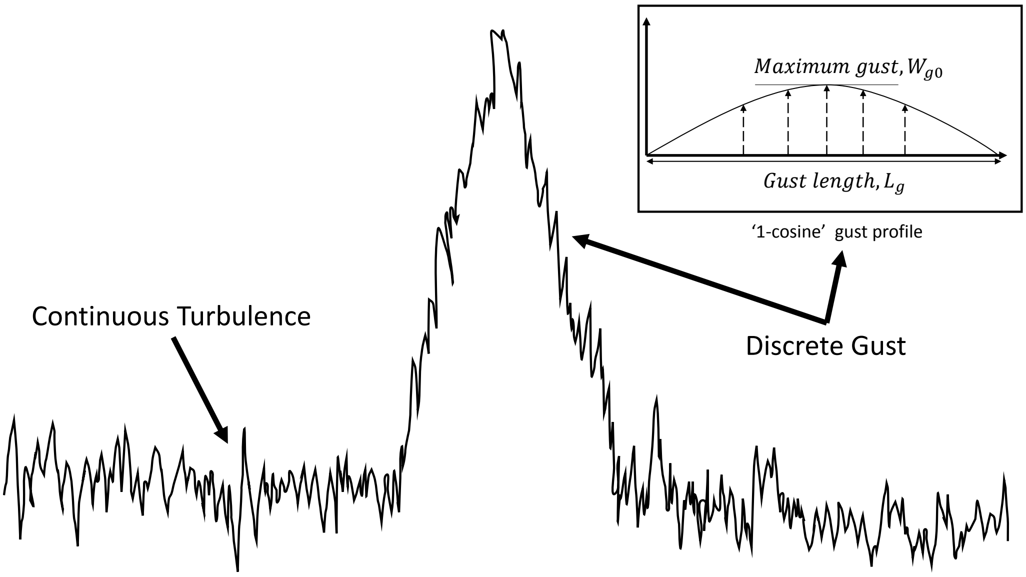

Figure 2.10: Continuous and discrete turbulence [56]

Facility located in the Merritt Island Launch Area at the Kennedy Space Center, Florida [57] and wind speed time series measured at the meteorological mast at Cabauw, The Netherlands [58] have benefited in determining several gust shape dependencies within the gust duration. Here, it can be defined that the discrete gust happens when the gust velocity caries in a deterministic manner, prior known in the form of a '1-cosine' shape described in Figure 2.10. It is different to the continuous turbulence since the gust is assumed to differ in a random behaviour, which can be estimated through a power spectral density technique. Hence, most of the researchers used this approach to estimate gust loads distribution in their works.

The practical way of solving the discrete gust is in the time domain while the continuous turbulence always been assessed in the frequency domain. In this day, gust loads can be numerically predicted by using some provided regulations. Knigge and Raasch [59] has provided a fascinating insight into improving and establishing of 1D and 2D discrete gust models by applying a large-eddy simulation model. The presented approach is applicable in designing the aircraft and wind turbine that should expose to the gust loads.

Nevertheless, the gust existence will affect the load distributions on the flying surface, hence affecting the structural strength. In that state, if the load found to be higher than the structure strength, the structure might be damaged. Kim and Hwang

[60] applied the probability distribution of bending moment in examining the composite wing reliability subjected to gust loads. They figured out that an aerospace vehicle could experience a critical structural failure when it is exposed to random air turbulence. In that case, the stress concentration on the structure has been increased when an aircraft encounters gust loads during the flight. It is supported by the research conducted by Wang et al. [61], where they suggested that the gust response might affect the flight performance and the structural stress. The gust response on helicopter rotor was examined in their study, where they concluded that the gust had caused the loss of thrust force by increasing the rotors deflection. In that sense, it is a critical issue to be dealt when gust loads interact with a flying object.

In examining the flexibility factor on the roof structure in wind tunnel, Zhou et al. [62] pointed out that the flexibility of the structure to adapt the external loads, especially by gust is significant. Since the bending stiffness influences the flexibility, the structure might deform if the bending stiffness is small. Hence, the structure could show a distinct geometric nonlinearity, which could lead to a fracture. Extensive research has shown that the flexibility of aerospace vehicles could be designed by considering the aeroelastic and gust loads to sustain a safe flight [63, 64, 65]. In the event the designed aircrafts got an approval to fly in the standard safety margin, some researchers took advantage of that situation. A so-called energy harvesting technique due to the induced vibration subjected to the gust loads that can generate electric power by attaching piezoelectric elements inside the wing structure [66, 67, 68, 55].

For most cases, the wing can be structurally altered through several mechanisms to achieve good controllability and maneuverability when encounters gust. For instance, Guo et al. [69] analysed the gust alleviation on a wing box by designing a passive twist wingtip to exploit the gust loads acted on the wing and the whole aircraft. Over the past decades, Wanhill [70] has investigated the effect of gust spectrum that could lead to the crack propagations on the skin materials, with consideration of fatigue crack. The fatigue loading is commonly known as the primary factor that triggers the crack propagations to the aircraft structures [71].

For example, Georgiou et al. [72] managed to model the composite wing aeroelastic behaviour with uncertain damage severity using a probabilistic approach. Besides, they applied the probabilistic procedure in the attempt of predicting the severity of the composite wing subjected to the gust loads. It is therefore likely that such connections exist between the aeroelastic response and fracture. The implementation of this field benefits in allocating the weak spot or any critical point that could lead to the fracture when the structure interacts with the aerodynamic loads. For sure, the fracture behaviour caused by an extreme flow such as gust or turbulence also can be explored.

2.4 Time domain versus frequency domain response

The different ways of analysing the flutter response from time domain and frequency domain are shown in Figure 2.11 [73]. In Figure 2.11 (a), the time domain responses are categorised into 3 states; stable, neutral and unstable. In the stable region [A], the motion amplitude is decreasing with the increment of time. Means, the system is underdamped. At this state, the system is facing a decaying in vibration which is the system is stable. This circumstance signifies due to the corresponding of the negativity of the complex root real parts.

In a neutral state [B], the amplitude motion is maintained to be constant since the system has no damping influence. The unstable state is shown in [C] where the motion amplitude is kept increasing with time. Here, the system becomes unstable since it is getting bigger until the system fails. The vibration amplitude is increased corresponding to the positive real parts of the complex roots. The flutter speed is determined when the unstable system is achieved with the time increments.

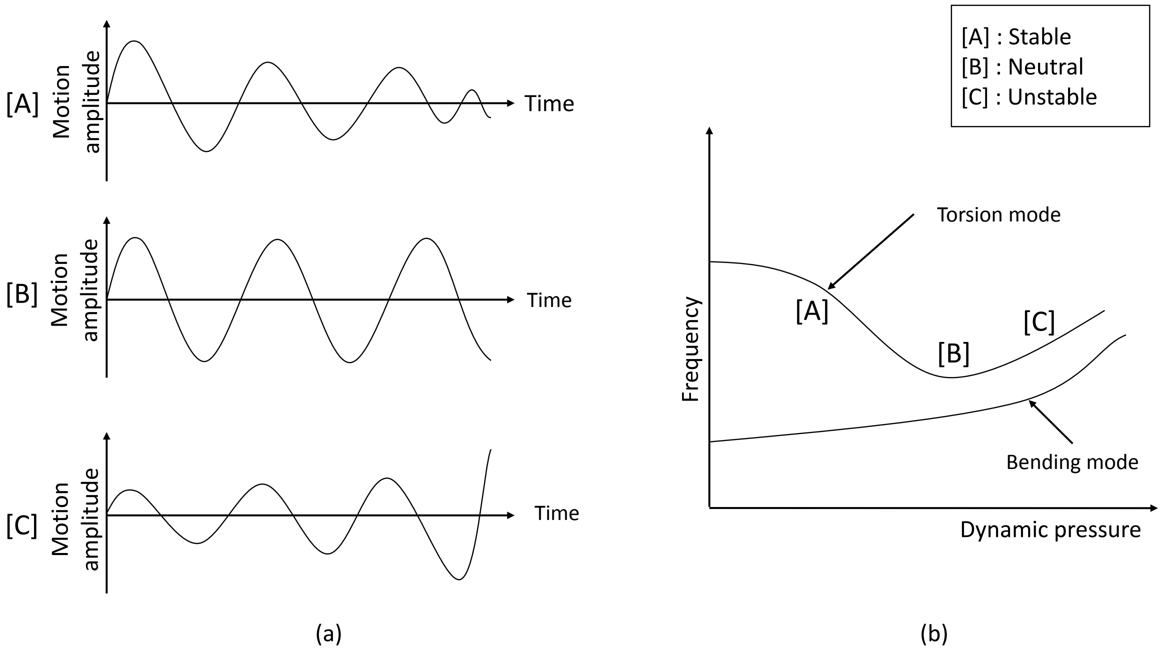

Figure 2.11: Time dependent versus modal coupling flutter assessment where (a) time histories, and (b) modal coupling

However, it is a different strategy when the flutter speed is assessed through frequency domain. In Figure 2.11 (b), the modal coupling is used to show the frequency instability where the two expected mode, especially when the bending-torsion mode is intercepted.

2.4.1 Fluid-structure interaction (FSI)

One of the methods to evaluate the structural response, in a stable or unstable state is by using a numerical method called fluid-structure interactions (FSI). Hou et al. [74] have reviewed several approaches to solve FSI problem, which is monolithic approach and partitioned approach. The monolithic approach [75, 76, 77, 78] tends to solve the governing equations of flow and displacement of the structure simultaneously by using a single solver. In their review article, Hou et al. [74] pointed out that the interfacial states are implicit in the solution procedure. A better accuracy could be achieved by this computational approach in multidisciplinary problems, but it needs more resources and expertise in developing a specialised code programming.

It is contradicting to the partitioned approach [79, 80, 81, 82] where the flow governing equations and the structural displacement are solved separately by applying two different solvers. In that case, the interfacial states are explicit in solving the fluid-structure interaction. Figure 2.12 shows the standard computational flow of fluid-structure interactions in ANSYS Fluent Software, which is one of the partitioned approach used to solve FSI.

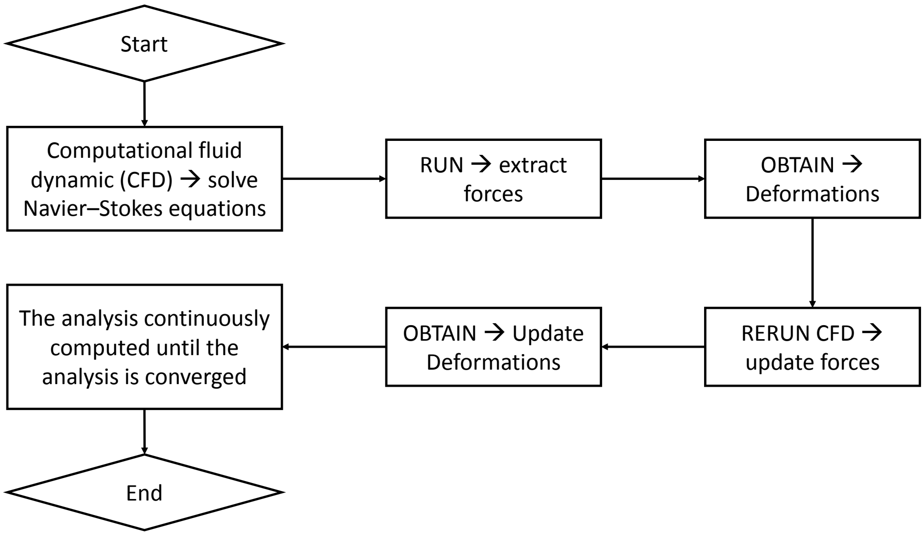

Figure 2.12: Fluid structure interaction flow in ANSYS Fluent

In FSI, the most critical part is the level of fidelity. In general, the high degree fidelity in FSI could be achieved via Arbitrary-Eulerian Method (ALE). ALE-based finite element computation can alleviate several weaknesses that attributed to the conventional Lagrangian-based and Eulerian-based finite element simulations. For that reason, Donea et al. [83] mentioned that Lagrangian algorithms mostly used in structural mechanics have a weakness where it is incapable to follow massive distortions of the computational domain without recourse to conventional remeshing operations. The same goes for Eulerian algorithms that are likely applicable in fluid dynamics. However, description large distortions in the continuum motion can be managed with relative ease, but generally at the expense of precise interface definition and resolution of flow details. In that sense, the best features of both the Lagrangian and the Eulerian approaches were combined to establish a new FSI approach, called ALE. ALE Finite Element Techniques not only restricted in the computational of FSI combination of pure Eulerian mesh, pure Lagrangian mesh and ALE mesh in different regions. ALE also can be applied in manufacturing technology (e.g., metal forming/cutting, casting) and coupling of multi-physics fields with multi-materials (moving boundaries and interfaces).

However, the computational cost of this approach using FSI is high. However, to inspect the crack visually via FSI might require FSI to be coupled with damage model, which is requires a high fidelity numerical solution. For example, a novel FSI model of the physiological aortic root simulating its function throughout the entire cardiac cycle that was conducted by Sturla et al. [84]. They have revealed that the computational cost might be increased to solve complicated coupling procedure such that transient dynamics(for Aorta valve model) and fluid dynamics (for Valsalva sinuses model). For that reason, they suggested that linear elements with reduced integration were preferred to limit the computational cost of the simulation. Even the analysis was performed for biomechanics application, the same consequence might be faced if FSI is used for fracture mechanics modelling. The only work that really working on the dyanmic fracture using FSI is presented by [85]. In their study, the FSI was coupled with XFEM and Deletion Element (DE) technique in assessing the dynamic fracture of preflawed aluminum pipes driven by gaseous detonations, the explosion of an air-backed aluminum cylinder submerged in water, and the underwater implosion induced by an explosive loading of a tapered aluminum tube with bulkheads.

The evidences presented thus far support the argument that the computational cost to complete the objectives of this present research will be very high if the fluid structure interaction is coupled with XFEM. Furthermore, XFEM is intended to be used as a method in modelling the fracture mechanism of composite plate. For that reason, in this thesis, a novel computational scheme to observe the aeroelastic response with crack propagations is proposed with a combination of unsteady aerodynamics using doublet lattice method (DLM) and extended finite element method (XFEM) for crack propagations.

2.5 Effect of Fracture on Flutter Speed

2.5.1 Stiffness effect on fracture

It is believed that the existence of a crack will affect the stiffness of the structure [86]. There is a work that investigates the stiffness effect on symmetric laminates with arbitrary sequence [87]. The reduction in transverse and shear stiffness of the laminate as a function of the crack density in one ply was estimated by deriving an analytical solution. Thus, the accuracy in predicting the stress redistribution, from a cracked ply to the rest of the laminate has been achieved. Hence, it is a logical reason to investigate the flutter speed of cracked composite structures since one of the parameters that could affect the flutter speed estimation is the stiffness.

Flutter is an instability problem due to structural vibration exerted by the aerodynamic load. Flutter often categorised as a self-excitation phenomenon, as the aerodynamic load is a function of the structural dynamic responses. A critical speed in which the structural vibration could lead to a catastrophic failure is called 'critical flutter speed'. One of the most well-known examples of flutter vibration leading to a catastrophic failure is well presented in the incident of the Tacoma Narrows Bridge collapse on the 7^{th} of November 1940 [88].

It was reported that 42 mph speed of wind had excited several vibration modes on that day [89]. The dominant mode was moving vertically with a node at midspan and thus changed to torsional motion with a node at midspan abruptly. Within 4 seconds, the vibration amplitude has twisted the bridge about 45° before it collapses.

The existence of crack would affect the stiffness distributions as discussed in the literature. It is also a requirement to determine the flutter boundary by considering the structural stiffness. Castravete and Ibrahim demonstrated that the stiffness significantly affects the flutter boundary [90]. This evidence has attracted attention to investigating the flutter boundary when there is an existence of crack on the structure.

In studying the circumstance, one of the aircraft crash incidents of North American P-51D Mustang that related to the event is mentioned as an example. The racing aircraft which also known as "The Galloping Ghost" crashed at the National Championship Air Races in Reno/Stead Airport, Nevada, USA. The technical investigation report by National Transportation Safety Board revealed that the existing fatigue crack in one screw caused the reduction of elevator trim tab stiffness [11]. This situation had triggered aerodynamics flutter to occur at racing speed.

2.5.2 Previous work: flutter and crack

There are some works reported regarding supersonic flutter on composite panels such that shear deformable laminated composite flat panels by Birman and Librescu [91], microstructural continuum damage by Pidaparti [92] and, Pidaparti and Chang [93]. The coupling between two-dimensional static aerodynamic technique and a higher order transverse shear deformation theory for the structural plate model were performed in [91]. The laminated composite rectangular flat panel was analysed subjected to hypersonic speed, such that Mach number 2. The plate was modelled symmetrically, assigned as orthotropic elastic layers. However, no indication of crack appeared mentioned in this work when the plate deformed due to the shear condition.

In another study, skew cracked composite thin plate models were developed [92, 93] based on tensorial mathematics using thin shell theory, classical lamination theory, and linear potential flow aerodynamic theory. For instance, the edge crack on the plate surface was modelled by deleting several nodes. In that case, the crack tip should be ended at the element node. The adopted approach might be applicable for modelling a straight crack direction since it will be difficult to model an inclined crack initiation. Since the objective was to evaluate the flutter performance on the cracked thin plate, aerodynamic models of Piston theory were applied, providing the square panels were modelled based on the damage mechanics theory with an internal state variable to mark damage characteristic in the material [92, 93]. The flutter speed of the cracked thin composite was evaluated based on several fibre angle directions from 0° to 90°.

Meanwhile, Natarajan et al. [94] studied the flutter behaviour of simply supported square Functionally Graded Material (FGM) plates immersed in a supersonic flow. FGM is known as a material that consists of variation in composition and structure gradually over volume, modified for a specific performance or function [95]. Technically, the modification of FGM could contribute in designing a material that requires high hardness and high toughness in wear-resistant coatings, especially when a structural component has diverse and contradictory property requirement. Thus, FGM is considered as an advanced composite material. For this work [94], FGM that made of a mixture of ceramic and metal was modelled and tested for flutter evaluation. In their work, two cases were considered for the modelled FGM plate, cantilevered plate with a side crack and simply supported plate with a center crack. Based on their numerical study, they concluded that the critical pressure and the frequency were decreased with the increment of both gradient index and the crack length.

Viola et al. [96] presented the recent investigation of the interaction between cracks on flutter. The numerical flutter analysis was performed on a multi-cracked Euler-Bernoulli beam under subtangential force as the non-conservative dynamic load. In general, subtangential force is known as a produced force subjected to the combination of a dead load of the tip rigid body and the pure follower thrust induced by a rocket motor [97]. Several works can be explored in the sense to have more understanding about the subtangential force. For example, the combined action of rocket thrust and the rocket weight motor itself could develop a subtangential force [98], which influence the vibration and stability of the structure. For that reason, the research conducted by Viola et al. [96] focused on the instability behaviour concerning double cracked beams subjected to nonconservative forces. Here, the finite element formulation with an approach based on fracture mechanics was combined. In addition, the cracks' intensity effect and their locations on the buckling or flutter load were investigated.

Some researchers applied the probabilistic approach to assess the flutter failure of a composite structure with a crack in subsonic flow. The application of Monte Carlo simulation in [99] and Polynomial Chaos Expansion method in [72] show the statistical studies of flutter with the presence of multiple damage uncertainties. However, the probabilistic approach might not be significantly applicable in determining the crack propagations when there is an interaction between a structure and aerodynamic loads since it involves the complexity of fluid dynamics and structural deflection. In that sense, a direct approach to the numerical solution is crucial to be implemented in assessing this kind of failure condition.

Based on the overview, it can be seen that there is a lack of publication on the flutter of cracked composite structures. Moreover, at the subsonic regime, to the author's knowledge, only Wang et al. [35] studied it by means of an analytical/semi-computational model. As a concluding remarks, it is observed that most researchers put the interest in evaluating the vibrational, flutter and instability responses, instead of the mechanical failure due to crack propagation presented in this research. As most transport and light aircraft are operating in subsonic regime, thus it is considered a great benefit to investigate the influence of crack on flutter for the cracked composite within this airspeed regime.

2.6 Fracture modelling techniques

2.6.1 Fracture mechanics modelling using XFEM

The computational modelling of the fracture study of crack and delamination of composite structures is still under development. Several assumptions and techniques have been developed in this field of study to obtain numerically accurate damage predictions. To simulate an accurate crack propagation, the modelling method requires a reliable calculation of the stress intensity factor (SIF) to be able to apply fracture criteria [100]. Al-ansari et al. [101], Lecheb et al. [102] and Zhou et al. [103] studied the stress intensity factor for 2-dimensional (2D) form composite structure. FEM's and meshfree method were compared to calculate the SIF for the Mode I fracture [101].

However, in recent years, a numerical method called extended finite element method (XFEM) was developed by Ted Belytschko and collaborators in 1999 to solve structural crack propagation problems without continuous or minimum re-meshing [104]. To that extend, XFEM was used to estimate the SIF in Modes I and II crack problems [102]. One of the reported advantages of XFEM is that XFEM allows both Mode I and Mode II modelling straightforwardly through convenient criteria. The study found that the composite crack angle imposed a minimal SIF.

In general, the development of XFEM in are still in progress as highlighted by Huynh and Belytschko [105]. In their work, the material interfaces where the crack tip enrichments and computational meshes were assigned. The method applied is used to solve both 2D and 3D composite structure cracks [105]. In the standard FEM, the element edges coincide with the material interfaces and the required crack surfaces, whereas XFEM has eliminated this restriction. The fracture modelling using XFEM began to evolve in several recent years including fracture development on 3D structure using XFEM. For example, Mode II fracture propagation modelling using XFEM in concrete with the additive material of siliceous fly-ash was presented by Golewski et al. [106]. Based on the result, the 2D crack numerical modelling using XFEM showed good agreement with the experimental data.

Parallel to that development, several works were conducted to explore the fracture mechanism that could be established by using XFEM, with more advanced applications. At the instance, XFEM not only restricted in developing an interlaminar crack but also can be applied to develop an intralaminar crack, know as delamination. For example, the fracture mechanism of glass reinforced aluminum (GLARE) presented by Curiel-Sosa and Karapurath [100] has opened a new dimension in delamination modelling using XFEM. Some research that related to the crack propagation of 3D composite structures using XFEM in Abaqus, such that the work demonstrated by Moreno et al. [107] and Navarro-Zafra et al. [108]. Both studies presented the modelling procedure of intralaminar cracks without any interlaminar crack involved.

Some works that related to the modelling of delamination in composite structures used integrated XFEM and cohesive elements [109, 110, 111, 112]. Grogan et al. [109] applied a combination of XFEM and cohesive elements to simulate microcrack nucleation in composite structures. The random microcrack and propagation (intralaminar failure) were computed based on XFEM while the delamination between plies was computed based on a mixed mode surface cohesive zone model (SCZM). Yazdani et al. [110] applied the XFEM to model the composite mixed-mode delamination. The adhesive contacts were modelled between each layer with cohesive elements. The computation interlaminar stresses were established based on a first-order shear deformation theory. The interlaminar stresses increment was triggered by the Poisson's ratios mismatch and interaction which led to the delamination initiation. Prior to that evidence, it is clear that the combined crack and delamination modelling is still under development.

In another work, Hu et al. [111] defined three cases to establish the matrix-fracture and delamination migration based on a progressive damage model. For each case, laminates were tested with distinct staking sequences. Crack initiation was based on the expected crack angle path (pre-allocation) for each layer of composite. The delamination by cohesive elements was not triggered until the matrix crack touched the interface, which is a step forward with respect to Hallet et al. [113], in which every crack was initially pre-allocated.

Significantly, a crack detection of a 2D flat membrane subjected to the time-harmonic vibration was demonstrated by Rabinovich et al. [114] in establishing an XFEM-based crack detection scheme using a genetic algorithm. The procedure was presented to develop a frequency-response where it applied the estimated amplitudes of a scattered single-frequency signal to locate the crack existence. Even the results showed a good correlation with the results gained by non-destructive testing (NDT), ultrasonic NDT practice nowadays relies more on time-dependent pulse technique to detect the crack. For that reason, Rabinovich et al. [115] purposed another crack identification scheme using XFEM subjected to the time-harmonic excitation with a single frequency, but with a transient procedure based on arrival time. The computational framework was established to identify any flaw exists in 2D structures. Based on their observation, the crack detectability is more efficient with a transient procedure based on time as discussed in [115] compared to the frequency-response procedure explained in [114]. The results from both approached were validated by the obtained crack detection results via NDT process.

Based on the discussions, it is figured out that small attention is given when there is a possibility to model crack propagations subjected to time-harmonic motion using XFEM. For that reason, this research intends to establish a novel scheme that could be used in modelling crack propagations subjected to aerodynamic loads using XFEM. However, this scheme also extended for modelling the crack propagations under the influence of aeroelastic loads called discrete gust.

2.7 Summary

In this chapter, several related research to the present investigations were discussed. The first part of this chapter described the fracture studies, including the basic understanding of the fracture mode. However, the current work not only concerning the fracture study but also several factors that contribute to another type of failure, which is aeroelasticity. Thus, some relevant research that managed to link between both kinds of failures were explored. In overall, the contributed findings from all cited literature were reviewed, including the proposed fracture numerical solver called XFEM. The discovery of the research gap is propelled as the motivation and the originality of this research.

Chapter 3

Transversal crack and delamination of laminates using XFEM

"You look closely enough, you'll find that everything has a weak spot where it can break, sooner or later."
- Sir Philip Anthony Hopkins CBE (Welsh film, stage, and television actor).

This chapter offers a new insight into the computational modelling of crack and delamination of carbon fibre composite. Both transversal cracks (intralaminar) and delamination (interlaminar) are modelled with Extended Finite Element Method (XFEM). Constitutive and fracture laws are integrated to model the initiation of crack or delamination, and their subsequent evolution. The study includes the size effect assessment of composite due to the increment of composite thickness. The results are in close agreement between the experimental and analytical data of each specimen modelled based on the size of the carbon fibre composite volume.

3.1 Extended Finite Element Modelling

In the present investigation, an advanced computational modelling technique in fracture mechanics, called the extended finite element method (XFEM) has been applied to model the crack and delamination. This technique proposes that the nodes enrichment by the Heaviside function in establishing the enrichment function on the element in the interface. Here, the solid elements are considered, that have been encountered to the splitting by the mentioned enrichment function. The crack propagations mechanism upon this method relies on the initiation criteria such that the evolution criteria, which is depends on the material energy release rate.

3.1.1 Crack propagation using the Level Set Method

XFEM has been developed based on level set method. To solve the fracture problem using this approach has brought into a difficulty in constraning the evolution of the signed distance function when the crack propagates, while at the same time to uphold the previous emerging crack surface in a frozen state [116]. Ever since the implementation of level set method in open curve interfaces such as crack, several adjustments or adaptations have been introduced. Rather than only one set level which is marked as ϕ, the second set level, denoted as ψ is also required at the tip of the crack.

Basically, the zero-level set of function $\psi(x,t)$ is used to simplify a 1D crack growth. The intersection of the zero-level set of function $\psi(x,t)$ with the zero-level set of function $\phi^k(x,t)$ is set at the end point of the crack where k is the number of tips at the defined crack. An assumption is made for a condition where ψ is orthogonal to ϕ. The nodes are only used as storages for level set function values.

$$\phi_{,i}\psi_{,i} = 0 \tag{3.1}$$

Using the similar finite element shape function, the functions are interpolated over the mesh in which the function can now be written as in Equation 3.2 and Equation 3.3.

$$\phi^k(x,t) = \sum_{j=1}^{n} N_j(x)(\phi^k(x,t)_j) \tag{3.2}$$

$$\psi(x,t) = \sum N_j(x)(\psi_j(x,t)) \tag{3.3}$$

However, the zero level set of ψ is cut through the entire domain even when the crack is actually embedded inside a domain. An assumption of the part is fixed without changing any shape or moving once the crack has emerged. The iteration updates of ϕ^k and ψ functions lead to the recalculation of the ϕ function, which are used to model the crack growth. The crack growth direction of θ is the factor of ϕ^k and ψ evolutions. The velocity vector $\mathbf{v} = (\mathbf{v}_x, \mathbf{v}_y)$, which is always normal to the interfaces, is determined for every step with the displacement of the crack tip.

The procedure of level set function of ϕ_n^k and ψ_n evolutions in the n- step was simplified [117]. The level set rotation of ϕ_n^k is expressed by $\phi_n^{k,r}$ and computed based on Equation 3.4 and $\psi_{(n+1)}$ in Equation 3.5;

$$\phi_n^{k,r} = (x - x_k)\frac{\mathbf{v}_x}{\|\mathbf{v}\|} + (y - y_k)\frac{\mathbf{v}_y}{\|\mathbf{v}\|} \tag{3.4}$$

where x is the nodal coordinate and x_k is the crack tip coordinate.

$$\psi_{n+1} = \left|(x - x_k)\frac{\mathbf{v}_x}{\|\mathbf{v}\|} + (y - y_k)\frac{\mathbf{v}_y}{\|\mathbf{v}\|}\right| \tag{3.5}$$

Next, the updated crack tip location is calculated based on Equation 3.6.

$$\phi_{n+1}^k = \phi^{k,r} - \Delta t \, \|\mathbf{v}\| \tag{3.6}$$

Abaqus/Standard commercial software does not estimates the exact and real time of the test to be performed as it is a Newton - Raphson solver. For this reason, the iterations are computed without time step. This is the reason where the implementation of velocity in Equation 3.6 was introduced [118]. The velocity is multiplied with the time difference (Δ t) to calculate the increment iteration in this simulation. Therefore, the velocity parameter is used to estimate the displacement (crack propagation) on the surface of the composite.

Equation 3.7 is used for more than one crack tip.

$$\phi(x, t) = \max_k(\phi^k) \tag{3.7}$$

Lastly, the intersection of zero level sets of ϕ_{n+1}^k and ψ_{n+1} is computed to solve the location of new crack tip of k. Figure 3.1 shows the crack tip deformation field coordinates and typical contour Γ [119]. The polar coordinates of r and θ with respect to the tangential of crack tip at a point x can be written as shown in Equation 3.8 and Equation 3.9.

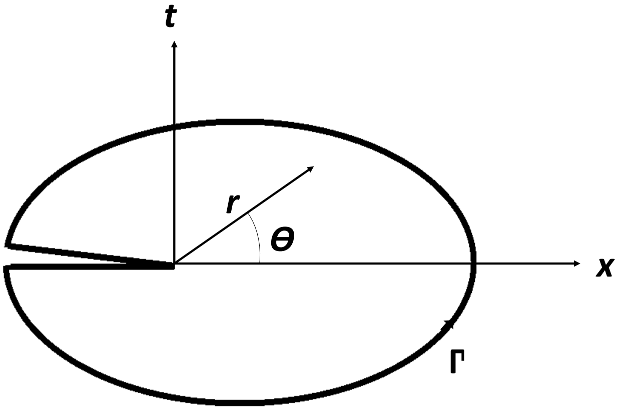

Figure 3.1: Crack tip deformation field coordinates and typical contour Γ

$$r = \sqrt{\phi(x,t)^2 + \psi(x,t)^2} \tag{3.8}$$

$$\theta = tan^{-1}[\frac{\psi(x,t))}{\phi(x,t))}] \tag{3.9}$$

By implementing the local coordinate in this analysis, XFEM is used to estimate the crack propagation in the contour region.

3.1.2 Enrichment Function

The enrichment function is used to solve the discontinuity within the element by providing an additional shape function. Equation 3.10 shows the approximate displacement applied in the most standard finite element methods, where $N(x)$ is the shape function and d is the change of displacement in every node.

$$u(x) = \sum_{j=1}^{n} N_j(x) d_j \tag{3.10}$$

To calculate the crack propagation path, some enrichments might be added as shown in Equation 3.11. The shape function in the second term is added as the enrichment for solving the extra degree of freedom node, which is expressed as a_j with m as the nodes enriched by the Heaviside function. However, for solving the crack at the crack tip, a third notation is required. As the last point of the crack tip is in a singular point form, the $F(x)$ function is used in terms of the singular point radius, where mt is the number of nodes enriched by crack tip asymptotic field enrichments and mf is the number of crack tip enrichment functions.

Several assumptions and techniques have been developed in this field of study to obtain the accurate damage prediction numerically.

$$u^h(x) = \sum_{j=1}^{n} N_j(x) d_j + \sum_{j=1}^{m} N_h(x) H(x) a_j + \sum_{k=1}^{mt} N_k(x) \left[\sum_{l=1}^{mf} F(x) b_k \right] \tag{3.11}$$

3.1.3 Damage Initiation

In this work, maximum principal stress failure criteria are used to predict intralaminar damage initiation as shown in Equation 3.12;

$$\sigma_{1,2} = \frac{\sigma_x + \sigma_y}{2} \pm \sqrt{\frac{(\sigma_x - \sigma_y)^2}{2} + \tau_{xy}^2} \tag{3.12}$$

$$tan 2\theta_p = \frac{2\tau_{xy}}{\sigma_x - \sigma_y} \tag{3.13}$$

A damage occurs if any of these stress components such as σ_1,σ_2,τ_{12} in the principal material axis meet the criteria as given in Equations 3.14, 3.15 and 3.16.

$$\sigma_1 \geq \left(\begin{smallmatrix} \sigma_1^{T*} (\sigma_1 > 0) \\ -\sigma_1^{C*} (\sigma_1 < 0) \end{smallmatrix} \right) \tag{3.14}$$

$$\sigma_2 \geq \left(\begin{smallmatrix} \sigma_2^{T*} (\sigma_2 > 0) \\ -\sigma_2^{C*} (\sigma_2 < 0) \end{smallmatrix} \right) \tag{3.15}$$

$$\tau_{12} \geq \tau_{12}^{*} \tag{3.16}$$

where σ_1^{T*} is the longitudinal tensile strength, σ_1^{C*} is the longitudinal compressive strength, σ_2^{T*} is the transverse tensile strength, σ_2^{C*} is the transverse compressive strength and τ_{12}^{*} is the in-plane shear strength.

The standard formulation in Equation 3.12 is modified for anisotropic mixed mode crack maximum principal of stress as presented in Equation 3.17 [120].

$$\sigma_{max} = \frac{\sigma_{11} + \sigma_{22}}{2} \pm \sqrt{\frac{(\sigma_{11} - \sigma_{22})^2}{2} + \tau_{12}^2} \tag{3.17}$$

The ply failure depends on the material properties assigned for each case, either under tension or under compression, following the maximum stress failure envelope. For the present investigation, if the ply meets any of the above mentioned conditions during the tensile loading simulation, the ply will fail.

3.1.4 Damage Evolution

The mixed mode in crack propagation leads to the formation of cracks and delamination. The non-zero K_I and K_{II} stress intensity factors are established because of the inclined or curvilinear propagations from multiaxial loadings. These two stress intensity factors emerged when a notch or a crack was subjected to in-plane loading [120].

Both stress intensity factors for an inclined crack can be written as in Equation 3.18 and Equation 3.19, where a is the crack length and θ_0 is the angle between the crack inclination and the existing crack.

$$K_I = \sigma \sin^2 \theta_0 \sqrt{a\pi} \tag{3.18}$$

$$K_{II} = \sigma \sin \theta_0 \cos \theta_0 \sqrt{a\pi} \tag{3.19}$$

The relationship between the stress intensity factors and the strain energy release rate based on the crack growth is defined in Equation 3.20:

$$G = G_I + G_{II} = \frac{{K_I}^2}{E'_I} + \frac{{K_{II}}^2}{E'_{II}} \tag{3.20}$$

where E'_I and E'_{II} are generalised elastic modulus.

Nucleation is not intended, rather an initiation via Equation 3.14 and Equation 3.15 together with delamination evolution through energy release criterion is used. For this reason, Equation 3.21 is provided where G_c is the critical fracture toughness.

$$G \geq G_c \tag{3.21}$$

Based on the maximum energy release rate, both these stress intensity factors can be expressed in θ from Figure 3.1 as given in Equation 3.22 and Equation 3.23.

$$K_I(\theta) = g(\theta)K_I cos\theta + \frac{3}{2}K_{II} sin\theta \tag{3.22}$$

$$K_{II}(\theta) = g(\theta)K_{II} cos\theta + \frac{3}{2}K_I sin\theta \tag{3.23}$$

where,

$$g(\theta) = (\frac{4}{3 + cos^2\theta})(\frac{1 - \frac{\theta}{\pi}}{1 + \frac{\theta}{\pi}})^2 \tag{3.24}$$

3.2 Fracture Model

This section aims to accomplish two objectives in fracture modelling. For the first part, it is desirable that the fracture modelling could be established using XFEM to demonstrate the transversal crack propagation alongside the delamination of laminates. The second part is to study the size effect of the presented carbon fibre composite laminates using XFEM, where the same ply orientation blocked together.

For the first objective, the experimental sampling of carbon fibre composite laminates provided by Hallet et al. [113] is investigated. In this reference, the laminates fracture due to tensile loading has been presented. To validate the fracture result, the laminated composite is modelled in Abaqus/Standard commercial software. The computational result is compared with the experimental result published in [113] as to validate the XFEM fracture modelling technique based in the maximum principal stress criterion and energy release rate evolution.

The second part of this section investigate the size effect of the presented composite laminates, as experimentally presented by Wisnom et al. [121]. The specimen laminates volume thickness have been increased, where the same ply orientation blocked together. As the results in this reference [121] were done experimentally, this part aims to compare the results obtain via computational method by means of XFEM.

3.2.1 Transversal crack and delamination by using XFEM

In this section, the laminated carbon fibre composite developed by Hallett et al. [113] is studied, where the specimen has been tested under tensile load. Based on the experimental procedure in [113], the objective is to estimate the fracture strength under the tensile load. In the present work, the material properties of the carbon fibre laminates used is presented in Table 3.1. As the lay-up of the laminates provided in [113], this work applied the same laminate configuration of $(45/90/-45/0)_s$ for modelling the carbon fibre composite specimen.

Table 3.1: Carbon fibre composite's elastic properties used in the XFEM analysis

Parameter	Value
E_1	161 GPa
$E_2 = E_3$	11.38 GPa
$G_{12} = G_{13}$	5.17 GPa
G_{23}	3.98 GPa
$v_{12} = v_{13}$	0.32
v_{13}	0.436

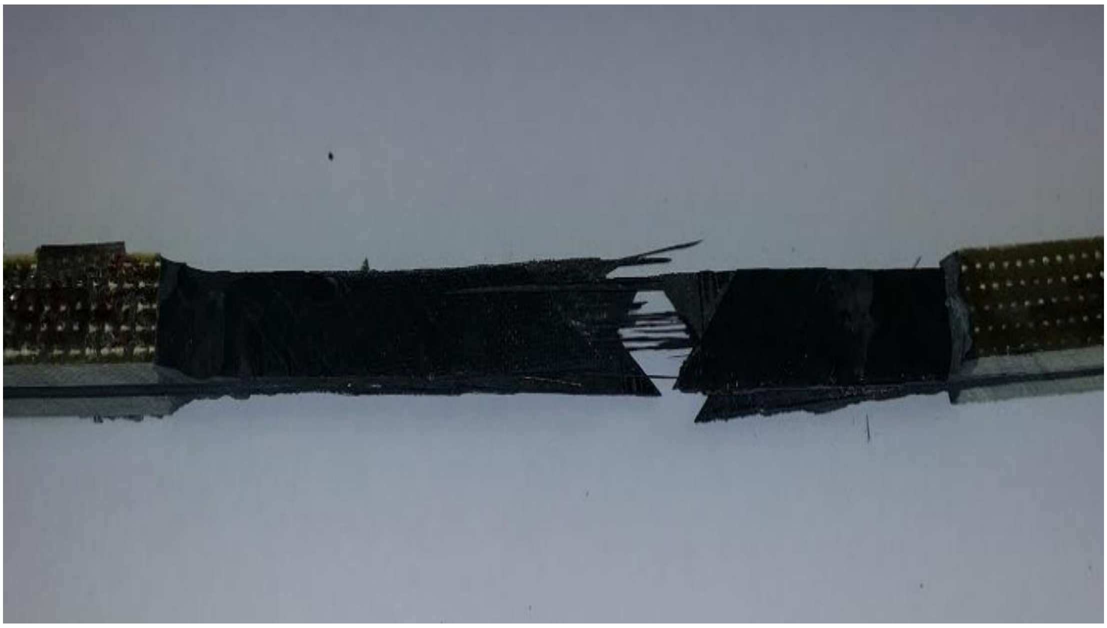

Figure 3.2: Experimental results of crack and delamination

There are a good correlation between the experimental result and the simulation results done by Hallett et al. [113]. This is due to the pre-allocations of fracture propagation. To clarify, a similar experimental tensile test has been performed, as the experimental setup presented in [113] to assess the fracture behaviour on the composite plate. The fracture mechanism shown in Figure 3.2 observed is similar to the one assesed in [113], i.e transversal crack eventually triggering delamination.

In this research, the specimen of Case 1 is modelled symmetrically with the neutral axis (mid-plane) of the composite structure as the symmetrical plane. Each ply with thickness of 0.125 mm of the laminate is modelled as solid element subjected to splitting in the corresponding loading condition. In this work, the symmetrical axis is defined on the top of 0° ply at the instance to optimise the structural thickness ratio with the thin crack initiation. The modelling specimen illustration for this analysis is presented in Figure 3.3. The crack initiation for this model is defined in the middle of the specimen at the bottom at 45° inclination. This crack initiation is shown in Figure 3.3, where it is represented as the rectangular black inside the red dotted line. Boundary conditions are such force motion in traction direction is allowed and transversal motion is not impeded. The crack will propagate based on the damage model and the boundary condition assigned, with no crack path assigned manually.

The length of the specimen in Case 1 is modelled without the grip to reduce the

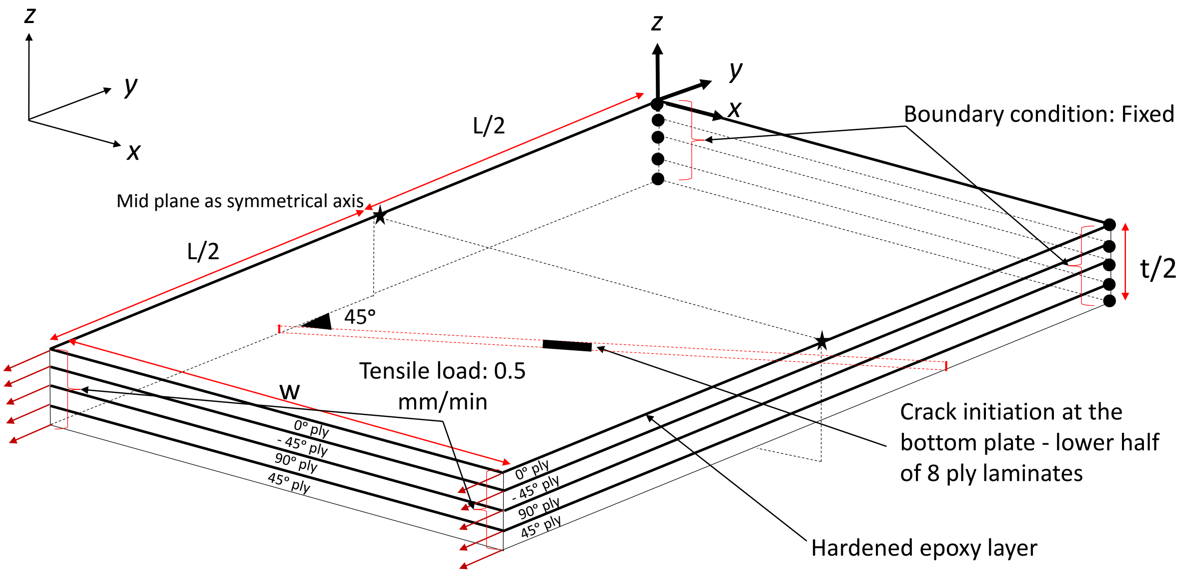

Figure 3.3: Specimen modelling of Case 1

calculation time required for a larger size specimen. The tensile load of 0.5 mm/min and fixed boundary conditions are applied directly to the end nodes. The maximum stress criterion and the energy damage evolution are specified as the damage model for this static analysis. All composite layers with different ply angles and epoxy matrix damage criteria modelling data presented in Table 3.2, Table 3.3, and Table 3.4 are obtained from [122, 123, 124]. The element meshing applied in this investigation is based on linear elastic solid element demonstrated in Figure 3.4 for each number of nodes.

Table 3.2: Yield stress used in XFEM analysis taken from Corum et al. [122] and Ibtihal-Al-Namie et al. [124]

Material	Angle	Maximum principal stress (MPa)
Carbon fibre	0	476
Carbon fibre	45	149
Carbon fibre	90	476
Carbon fibre	-45	149
Epoxy	Nil	50.2

Table 3.3: Carbon fibre ply ultimate stress taken from Corum et al. [122] and Ibtihal-Al-Namie et al. [124]

Type of ultimate stress	Value (MPa)
Ultimate tensile strength 0°, X_t	600
Ultimate compressive strength 0°, X_c	570
Ultimate tensile strength 90°, Y_t	600
Ultimate compressive strength 90°, Y_c	500
Ultimate in-plane shear strength, S	90

Table 3.4: Fracture toughness value of carbon fibre composite laminate by Pinho et al. [123] and Ibtihal-Al-Namie et al. [124]

Layer	G_{lc} (kJ/m^2)
Carbon fibre	91.6
Epoxy matrix	1.7

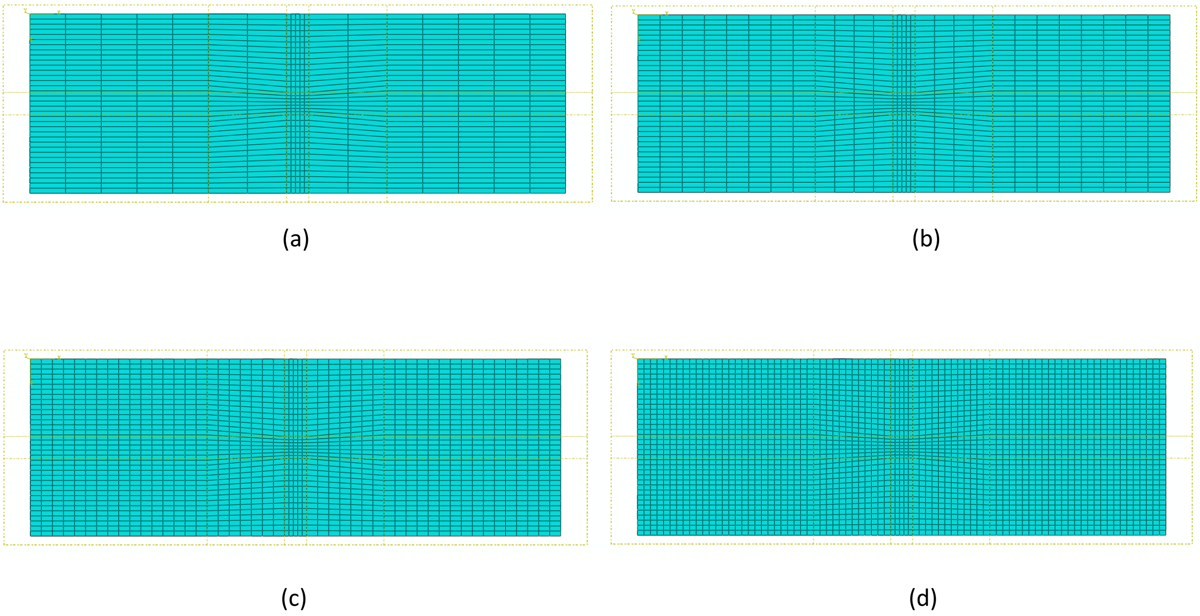

Figure 3.4: Element meshing for Case 1 where (a) 6300 nodes, (b) 9450 nodes, (c) 19845 nodes, and (d) 26460 nodes

To demonstrate a crack model with delamination, the epoxy matrix used in the model is assumed to be hardened as a layer (with thickness of 0.001 mm) between each attaching carbon fibre ply. This assumption is very important as the XFEM always exhibits a crack behaviour based on the damage model of a solid isotropic material.

In this analysis, if the crack appears between the composite lamina and causes an interlaminar crack, then the crack is called as delamination.

Figure 3.5 shows the strain contour for the presented composite plate where the transversal crack (intralaminar) and delamination (interlaminar) fracture had propagated simultaneously after the crack occurrence. The composite structure is considered a complete failure when the elastic region of the stress-strain relation is at the breaking point.

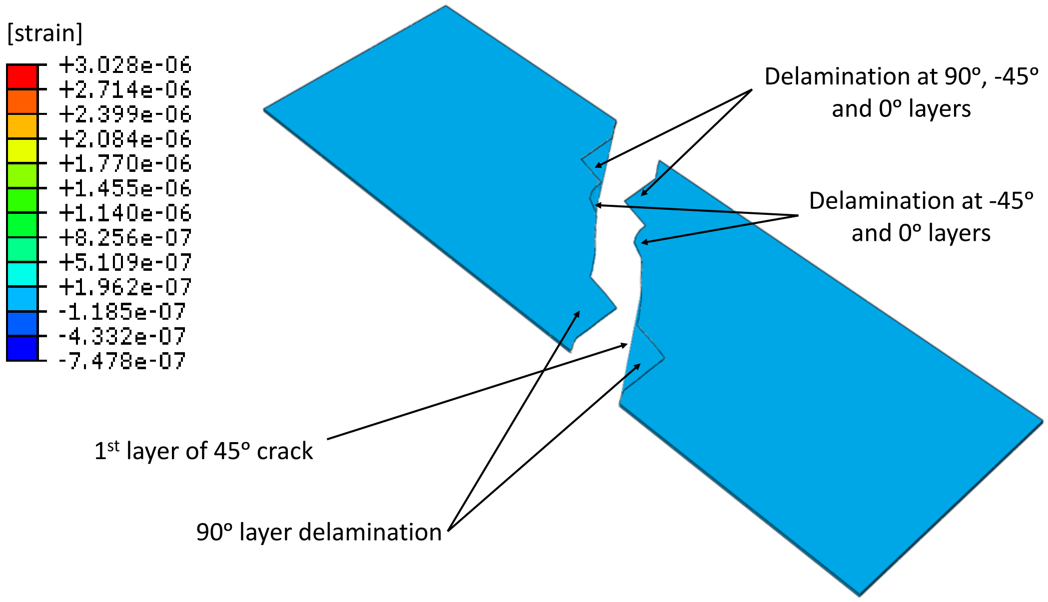

Figure 3.5: Case 1 - Crack and delamination simulation result

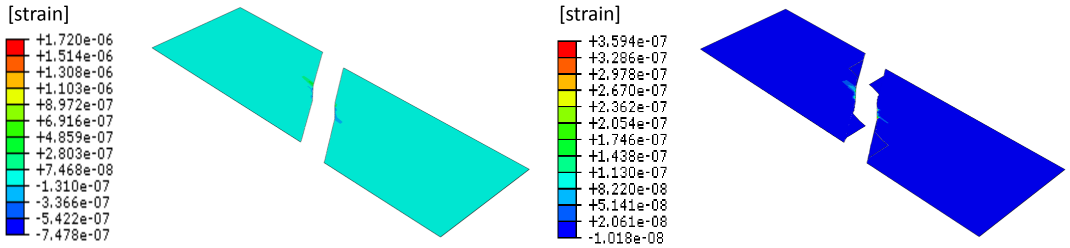

a. Carbon fiber composite ply : 45°

b. Carbon fiber composite ply : 90°

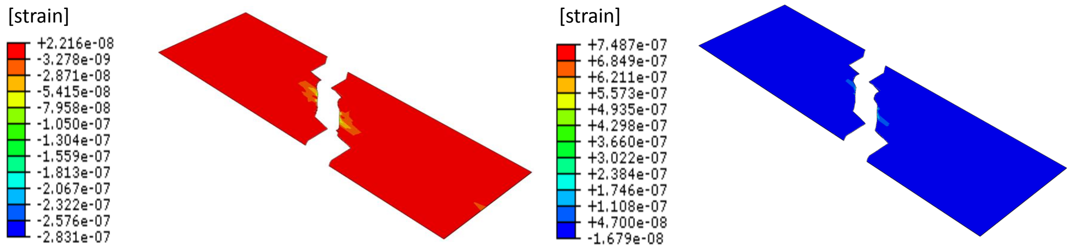

c. Carbon fiber composite ply : -45°

d. Carbon fiber composite ply : 0°

Figure 3.6: Case 1 - Crack and delamination strain contour for each ply

Figure 3.6 shows the strain contour extracted after the crack occurrence for each carbon fibre composite ply as the crack and delamination are presented. Figure 3.6 (a) shows the transversal crack for the ply inclined at 45° where the crack is initiated in the middle of the ply. As the transversal crack propagates along the ply, the crack also propagates to the upper side and triggers the next layer. The resulting situation is shown in Figure 3.6 (b), where the 90° ply consists of some delaminations, and the crack constantly propagates to the next composite layer until the simulation ends.

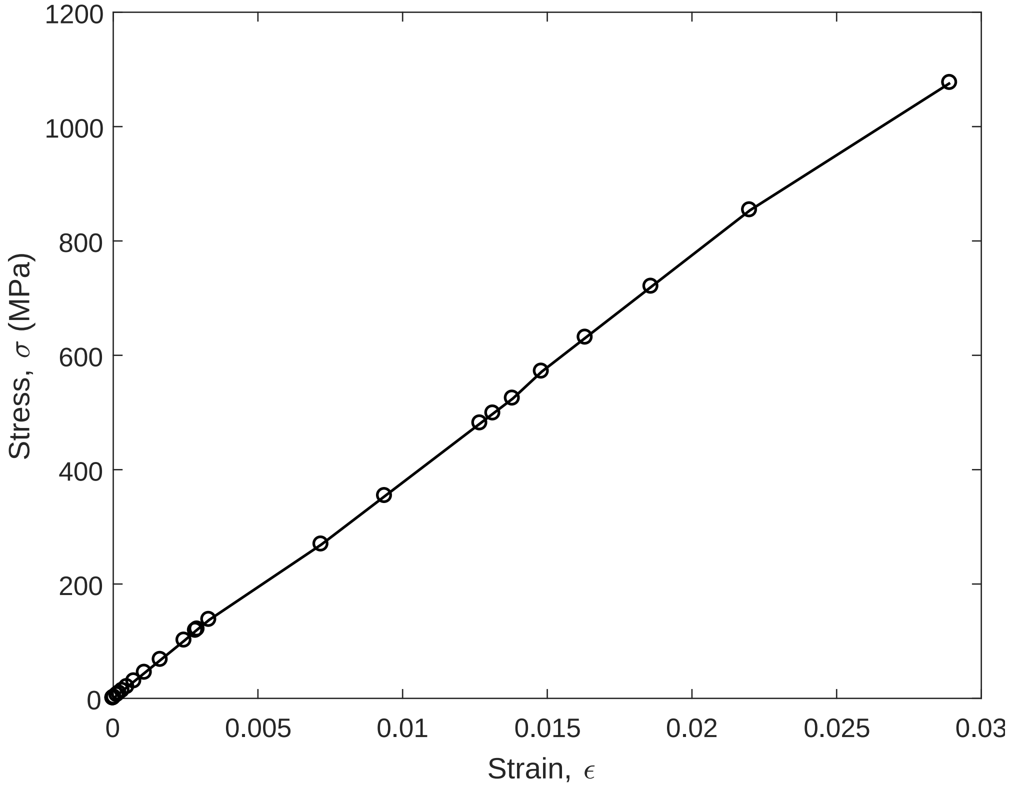

Figure 3.7: Case 1 - Stress-strain plot

Figure 3.7 shows the stress-strain plot for Case 1 until the structure fails. A mesh sensitivity analysis is performed to ensure that the number of elements used in this analysis is acceptable without any convergence problem. Figure 3.8 shows the mesh sensitivity analysis for Case 1. The number of elements selected is 6080 (number of nodes: 6300), for which the failure stress occurred at 1076.36 MPa. The number of elements is selected in such a way that the analysis requires only less computational time. It was observed that the computational failure stress corresponded with the experimental data result consistently, with minimal error.

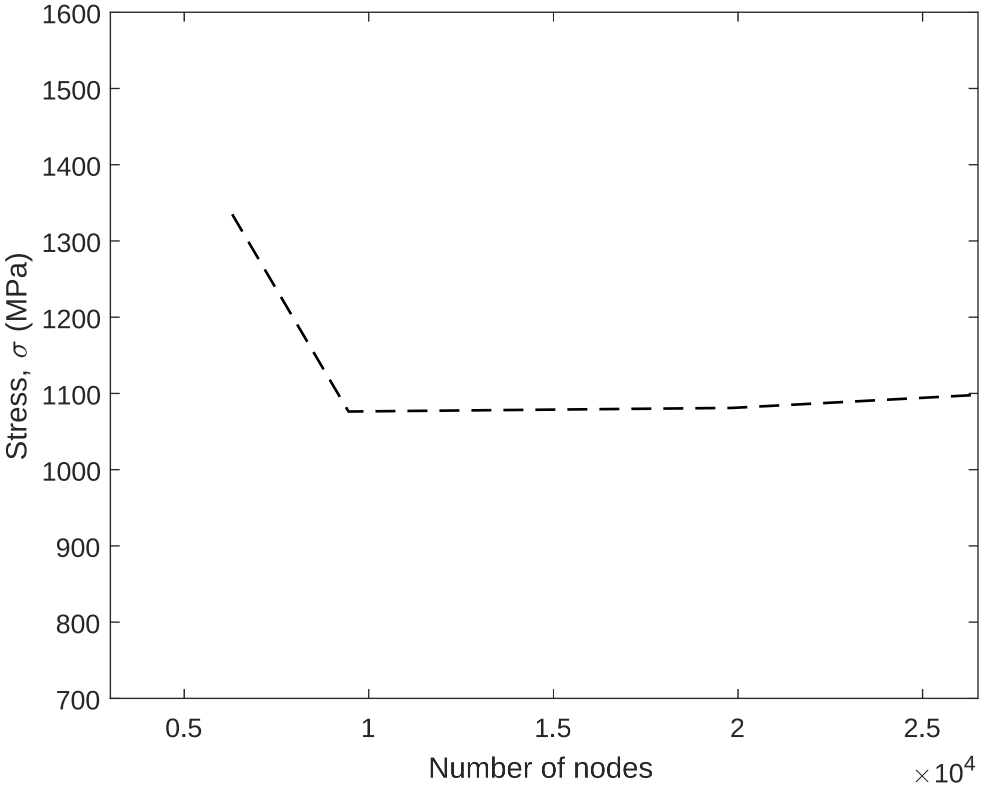

Figure 3.8: Case 1 - Sensitivity analysis plot

Figure 3.9 presents the strain contour of Case 1 for the bottom view where the transversal crack and delamination have developed. The bottom view of the transversal crack and delamination is shown in Figure 3.10, in which the region of both intralaminar and interlaminar crack can be seen clearly. The transversal crack and delamination are in a non-linear form, as the composite structure consists of different orientation angles for each ply. The behaviour of crack propagation for the laminate composite is successfully modelled and is presented in Figure 3.10 for the bottom view of the composite plate.

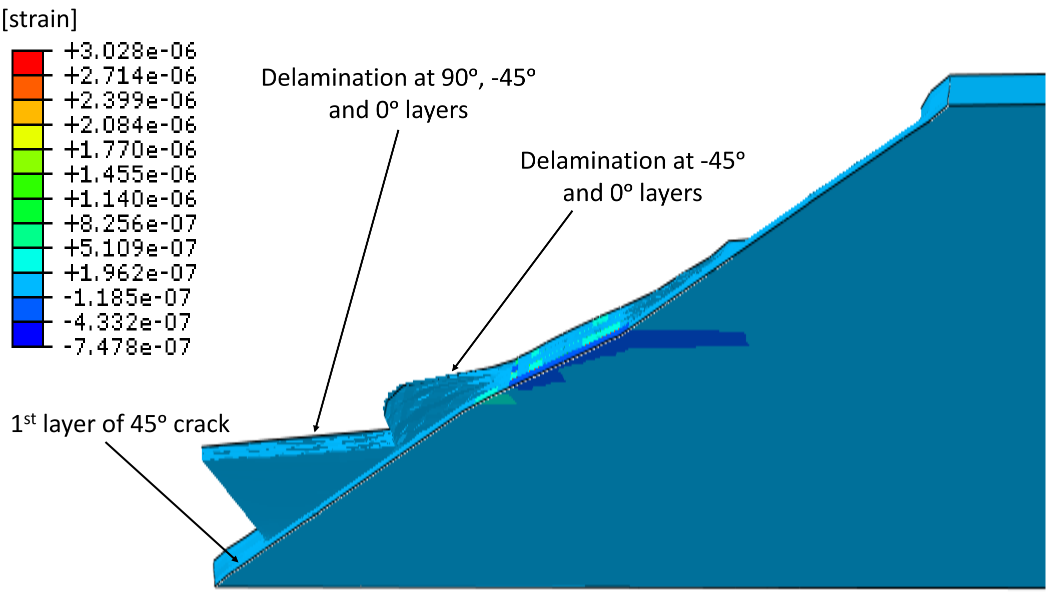

Figure 3.9: Case 1 - strain contour: Bottom view of transversal crack and delamination at focus area

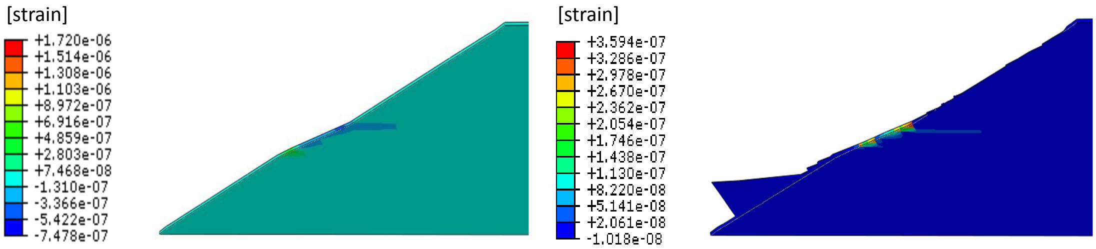

a. Carbon fiber composite ply : 45°

b. Carbon fiber composite ply : 90°

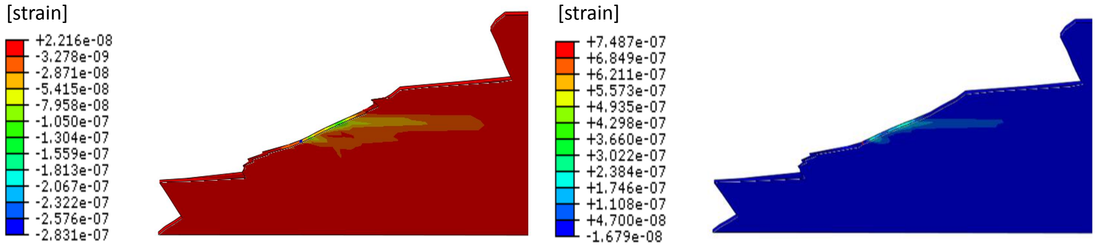

c. Carbon fiber composite ply : -45°

d. Carbon fiber composite ply : 0°

Figure 3.10: Case 1 - strain contour: Bottom view of transversal crack and delamination per ply at focus area

3.2.2 Size effect modelling study on the same ply orientation blocked together

The same material properties of carbon fibre are studied in this section. Wisnom et al. [121] have conducted experiments for investigating the size effect modelling study on the same ply orientation blocked together in carbon fibre composite. $(45_m/90_m/-45_m/0_m)_{ns}$ composite lay-ups are used, where m is the number of same ply orientation blocked together = 1, 2 and 4 and n = 1. These results are termed as the validation for the simulation. Table 3.6 shows the experimental results presented in [121] to validate the analytical calculation data. The results are used as a benchmark for the present work.

The objective of this section is to study the size effect on the addition of same ply orientation blocked together using a numerical computational technique. The specimen models geometry for this investigation are listed in Table 3.5. The reason is based on [121]; where they found that the strength of carbon fibre composite became lower when the tensile test was performed on larger volume of carbon fibre composite plate. The strategy was performed by applying some additional plies as shown in the carbon fibre composite lay-up in Table 3.6, Table 3.7 and Table 3.8. Thus; the application of same ply orientation blocked together was the reason that the composite plate strength was reduced even the composite plate volume was bigger.

Table 3.5: Specimen models geometry for size effect investigation by Wisnom et al. [121]

Case	Lay-up	Gauge length (mm)	Width (mm)	Ply thickness (mm)
1	$(45/90/\text{-}45/0)_s$	30	8	0.125
2	$(45_2/90_2/-45_2/0_2)_s$	60	16	0.125
3	$(45_4/90_4/-45_4/0_4)_s$	120	32	0.125

Table 3.6: Percentage difference of expected strength and experimental results by Wisnom et al. [121]

Case	Lay-up	Expected strength (MPa)	Experimental (MPa)	Difference %
1	$(45/90/\text{-}45/0)_s$	1074	842	21.6
2	$(45_2/90_2/-45_2/0_2)_s$	642	660	2.8
3	$(45_4/90_4/-45_4/0_4)_s$	454	541	19.2

Table 3.7 shows the difference in the present work simulation results with the analytical expected strength for each case. The percentage difference increases with a rise in the size of the modelled composite specimen. The present work also compares the results with an experimental data as shown in Table 3.8.

Table 3.7: Percentage difference between the expected strength and failure stress - present work

Case	Lay-up	Expected strength (MPa) [121]	Failure stress-present work (MPa)	Difference %
1	$(45/90/\text{-}45/0)_s$	1074	1076.36	0.2
2	$(45_2/90_2/-45_2/0_2)_s$	642	692.47	7.86
3	$(45_4/90_4/-45_4/0_4)_s$	454	546.59	20.39

The stress contours at the 1st ply that result due to the tensile load for Case 2 and Case 3 are demonstrated in Figure 3.12 and Figure **??**, respectively. As the crack propagations occur at the bottom layer of the laminates (45° ply), the stress concentration has triggered the crack to propagate to the upper layer of the laminates. Hence, the crack transversely splits the laminates.

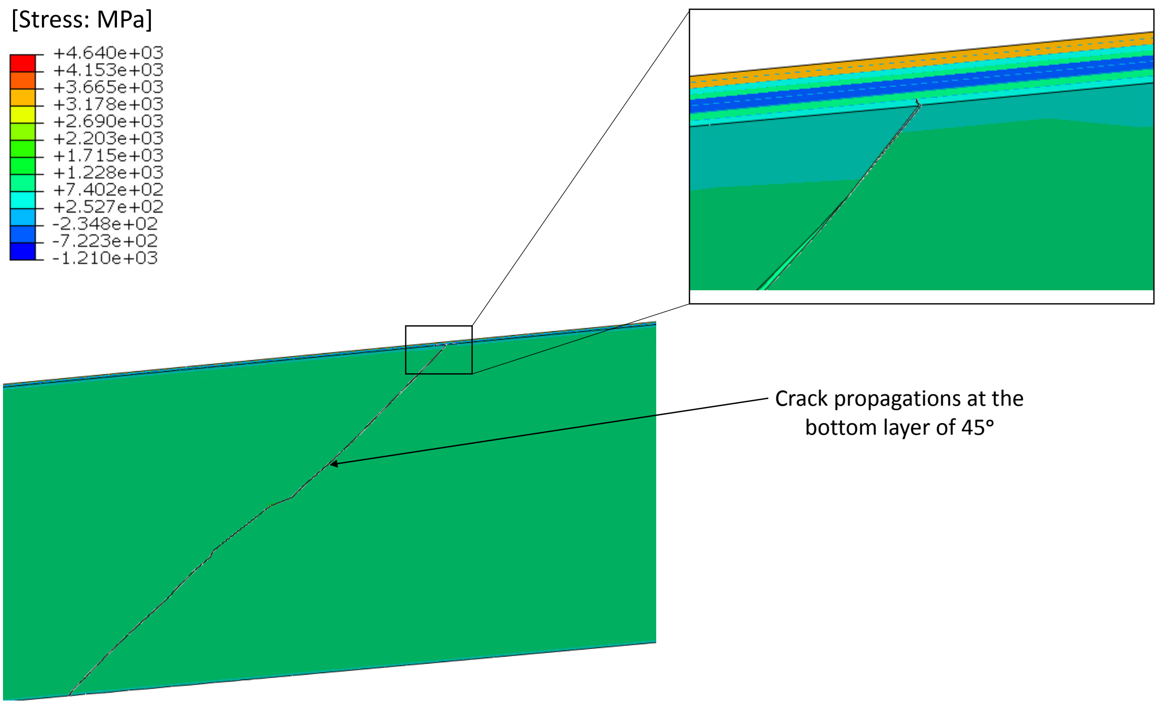

Figure 3.11: Case 2 - Stress contour at the bottom ply of 45°

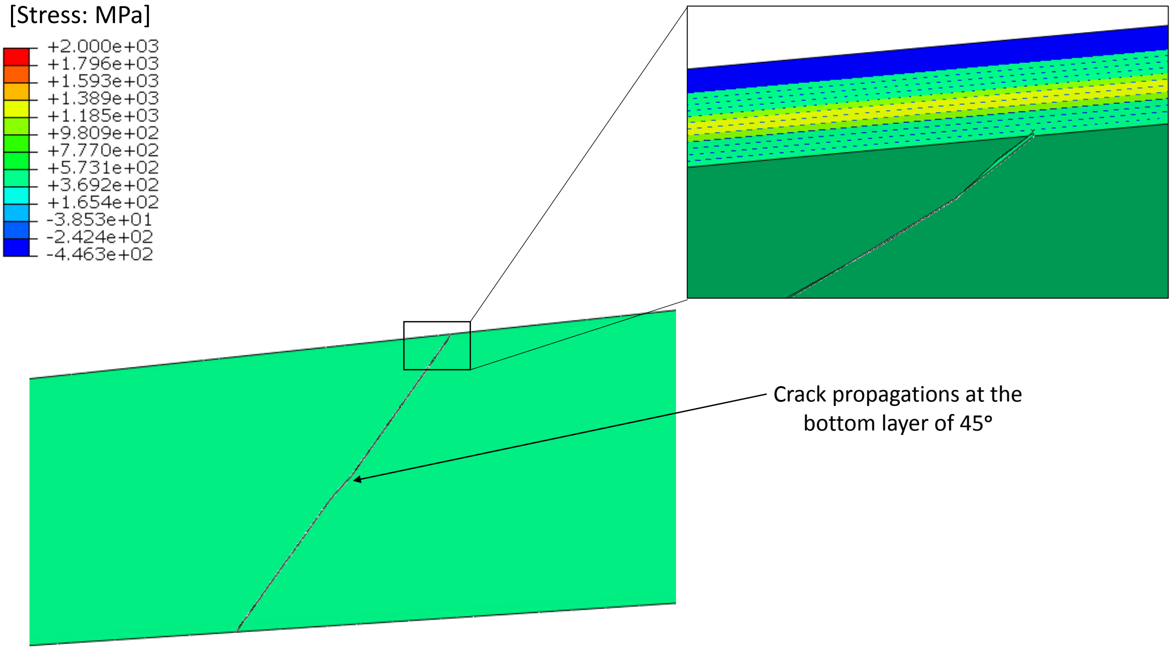

Figure 3.12: Case 3 - Stress contour at the bottom ply of 45°

These results indicate that the size effect assessment of the same ply orientation blocked together in carbon fibre composite is different if it is compared to an isotropic material such as metal. Carbon fibre composite is one of the anisotropic materials. The mechanical properties are dependent on the fibre angle orientation. In this case, the failure stress decreases as the volume of the carbon fibre composite increases.

Table 3.8: Percentage difference of experimental and failure stress-present work

Case	Lay-up	Experiment (MPa) [121]	Failure stress-present work(MPa)	Difference %
1	$(45/90/\text{-}45/0)_s$	842	1076.36	27.83
2	$(45_2/90_2/-45_2/0_2)_s$	660	692.47	4.92
3	$(45_4/90_4/-45_4/0_4)_s$	541	546.59	1.03

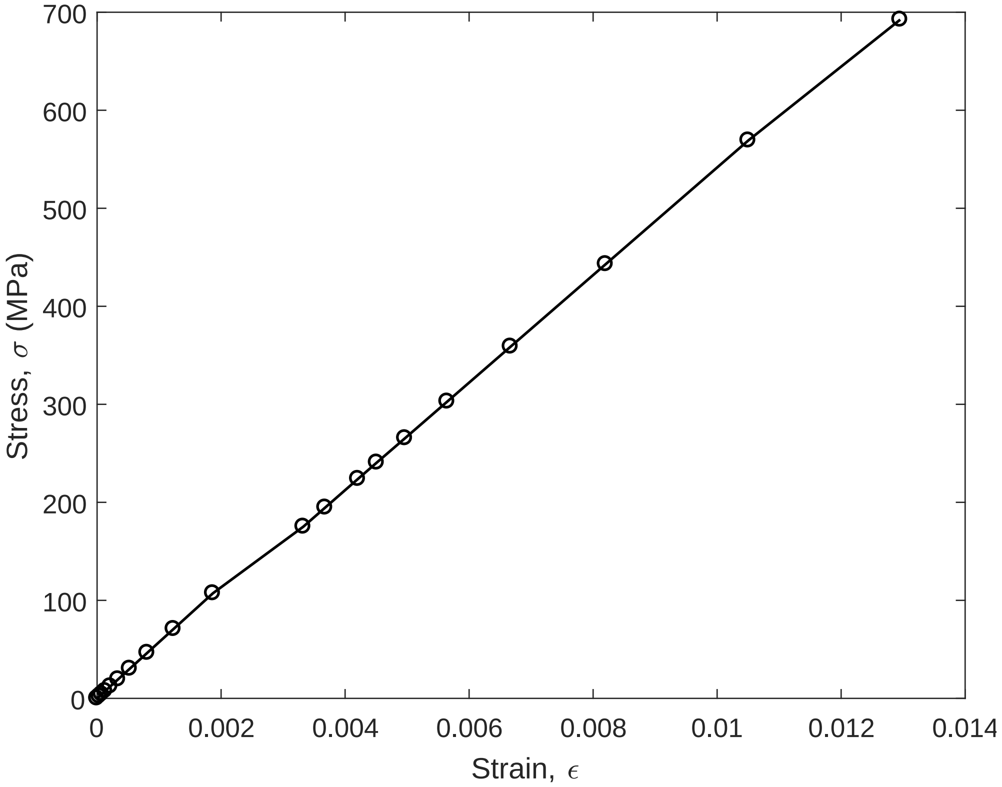

Figure 3.13: Case 2- stress-strain plot

Figure 3.13 and Figure 3.14 show the stress-strain plot of Case 2 and Case 3 respectively; where the volume of the composite structures are bigger than the composite structure of Case 1. As the volume of composite structure in Case 3 is larger than the composite structure of Case 2, the failure stress of Case 3 specimen is found to be lower than the specimen of Case 2.

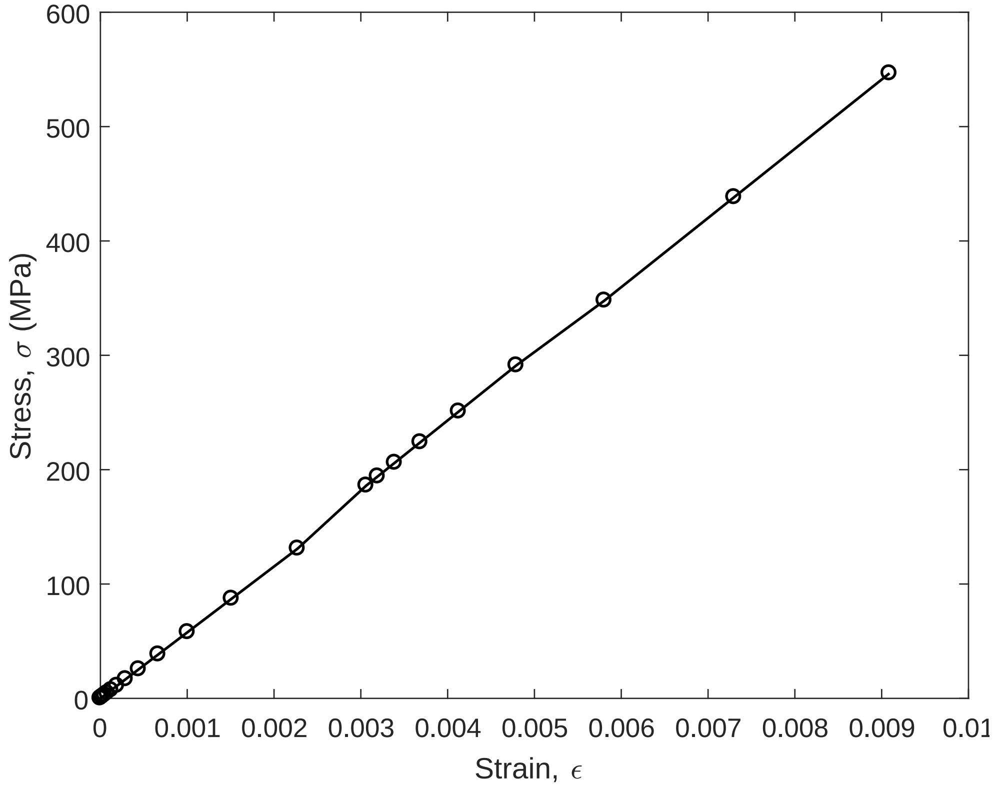

Figure 3.14: Case 3- stress-strain plot

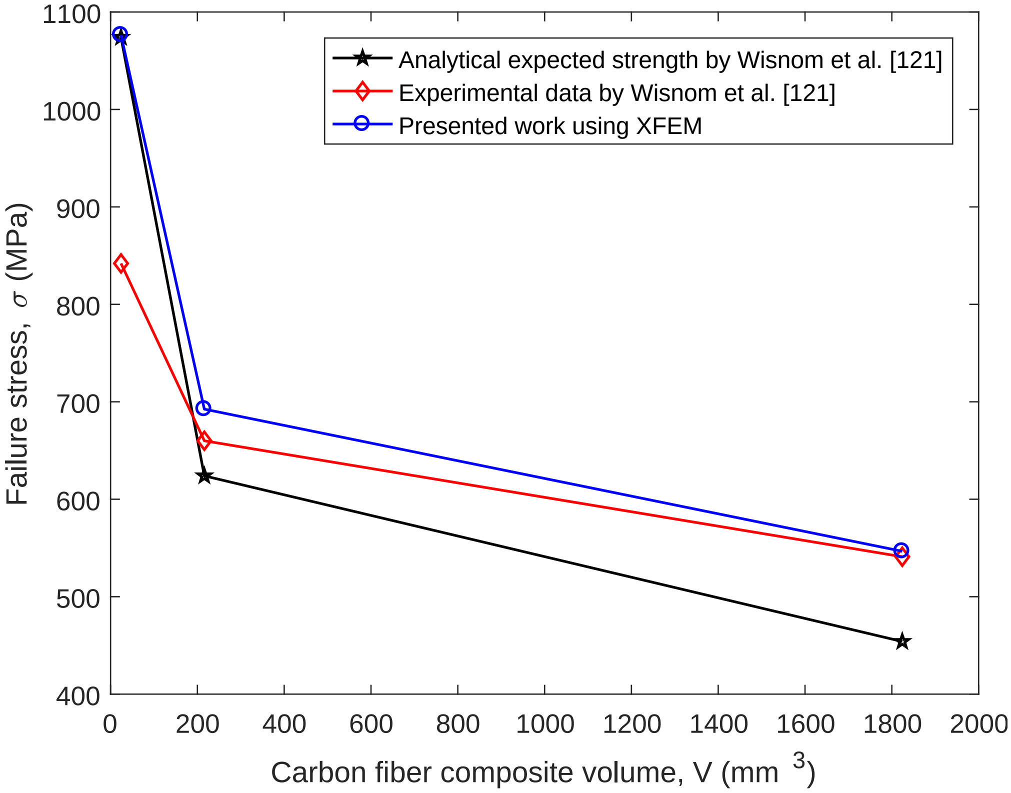

Figure 3.15: All cases- size effect strength plot

Graph in Figure 3.15 shows the comparison of results between the analytical calculation of the failure stress and the experimental data of the failure stress along with the simulation results performed in this report. It is clearly shown that the trend of failure stress nonlinearly reduces with the increment in carbon fibre composite plate volume and failure stress, as presented in Figure 3.15. The approximate linear of strength reduction in Figure 3.16 is plotted to examine the effectiveness of XFEM in predicting the size effect phenomenon. From this graph, the size effect modelling of composite using XFEM renders a slightly higher approximation compared to the experimental and expected strength provided in [121].

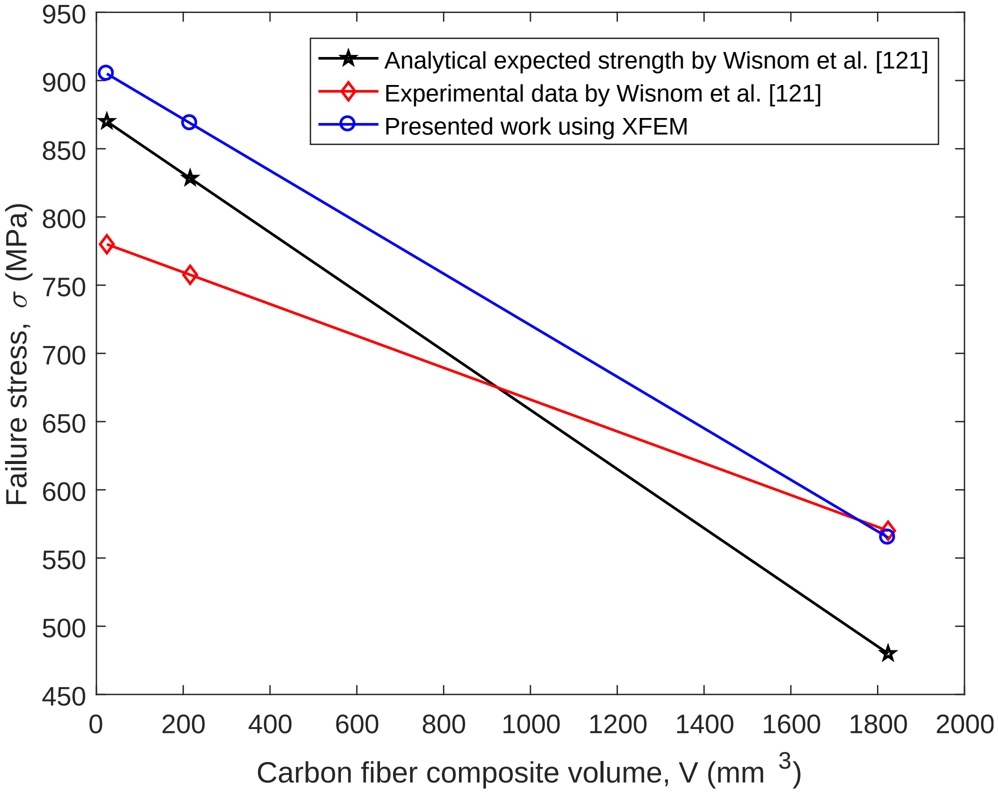

Figure 3.16: All cases- linear approximation of size effect strength plot

As the composite structure is an anisotropic material, its behaviour is different from the isotropic material where the increment in the size of the isotropic structure increases the failure strength. The trend for simulation results shows a good agreement with the analytical as well as the experimental data.

3.3 Summary

This chapter presents the numerical modelling of transversal crack and delamination of carbon fibre laminates using extended finite element method (XFEM). Energy release rate of the material was used to predict the crack propagations. The same procedure was applied to study the size effect on the same ply orientation blocked together in carbon fibre composite. In this chapter, a step forward has been given in the simulation by doing both intralaminar and interlaminar fracture by XFEM. The numerical computational presented in this chapter was implemented to develop the transversal crack and delamination of carbon fibre composite. Since it is the maximum stress was measured at the crack tip in the same way as a thin plate, the true failure may be caused by the interlamina stress between the plies which has different fibre orientation and excessive large stiffness (not recommended in practice rather than the stress inside the ply). This matter should be further investigated with improved interface modelling between plies.

Chapter 4

Aeroelastic assessment of cracked composite plate by means of fully coupled FE and DLM

> *"We are like butterflies who flutter for a day and think it is forever."*
> *- Dr. Carl Sagan (American Astronomer, Writer and Scientist, 1934-1996).*

This chapter presents an investigation of the flutter on cracked composite plates. This work is divided into two sections: (a) variation of crack length at a fixed location on the plate, and (b) variation of crack location on the plate with a fixed crack length, modelled as a unidirectional composite for 0°, 90° and 135° ($-45°$) orientation.

4.1 Flutter Speed Determination

Flutter is defined as a state or phenomenon of flight instability which can cause structural failure due to the unfavourable interaction of aerodynamics, elastic, and inertia forces [125]. In that sense, flutter can deform an aircraft, especially the wing due to the dynamics instability. In practice, structural damping, g versus velocity, V for each vibration mode shape is plotted to determine the flutter speed graphically. Based on the Federal Aviation Administration Regulations in [14], the required structural damping, (g) value for plotting Figure 4.1 must exceed more than 3%, $g > +0.03$ in the unstable region so that the plot can be stated as in flutter speed.

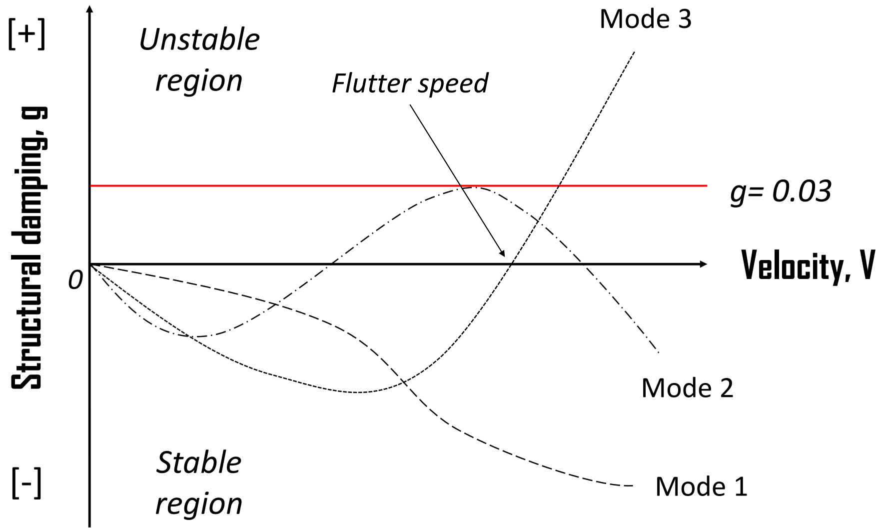

Figure 4.1: Structural damping graph guided by FAA [14]

As reported by Nissim and Gilyard [126], an experiment was conducted to estimate the flutter speed by using the parameter identification technique. Based on the experimental procedure, it is highlighted that there is significant issue of complexity when the 'exact' analytical scheme applied to solve the flutter solutions. An assumption has been made where the system is assumed to be an undamped structural system on account of the damping only merged with aerodynamic terms. To that end, the system excitation at zero damping resulting in the zero dynamic pressure, and hence will trigger the responses at resonance become infinite values. For this reason, the 3% of structural damping is assumed and at the same time, the responses of the 'exact system' is calculated. When this procedure objective is achieved, the flutter speed can be determined at zero structural damping.

To be more specific, the graphical presentation to determine to flutter mode is presented in Figure 4.1. Referring to the figure, vibration Mode 1 moves freely in the stable region and not showing any tendency to crossed the $g = 0$ axis where the mode will enter an unstable region. It is an interesting motion of vibration Mode 2, where it crossed the velocity axis which refers to the zero structural damping. However, even vibration Mode 2 plot has crossed the $g = 0$ axis, it still not not exceeding $g = 0.03$. With the time increment, the motion seems to moves towards the stability region, where the structure is now in a safe zone. Unfortunately, this type of mode motion behaviour would likely causing the instability motion which lead to an aeroelastic phenomenon called 'limit cycle oscillation'. It is a different kind of graphical presentation for vibration Mode 3 where the plot has crossed the velocity axis where the structural damping is zero and has surpassed the limitation of $g = 0.03$, and never returns back to the stable region. In this case, this mode tends to cause a dangerous vibration motion in the instability region where the aeroelastic flutter phenomeneon is expected to happen.

Based on the explanation, this methodology is used to determine the flutter speed in frequency domain. Several vibration modes have been assessed at certain frequencies in modal analysis. From here, the coupling between structural and aerodynamic factors will be implemented to estimate the flutter speed and flutter frequency. In the present investigation, the flutter speed for each composite structure is determined by using this technique. The same procedure has been repeated in assessing the flutter speed of each cracked composite plate. Several parameters are concerned to be investigated; the unidirectional composite angle, θ, crack ratio, η and the dimensionless crack location, ξ_c.

4.2 Mean Field Homogenisation (MFH)

This study used the composite structure composition of Graphite Polyimide as the composite material used by Wang et al. [35]. The fibre and matrix composition are equally divided (fibre 50 %, polyimide 50 %), hence the simple rule of mixture to represent the composite structure is becoming complicated. In this part, a process called homogenisation which is considered to represent the composite material properties is performed. Representative volume element (RVE) is used to represent the microscale of the structure that would simplify the material properties in simple form of material stress tensor matrices.

The objective of applying this process is to estimate the stresses and strains as the matrix and the fibres are entirely mixed. In this study, the homogenisation of composite structures is carried out by applying the Eshelby method. Figure 4.2 shows the schematic diagram of homogenisation based on the Eshelby method presented in

[127] and [128].

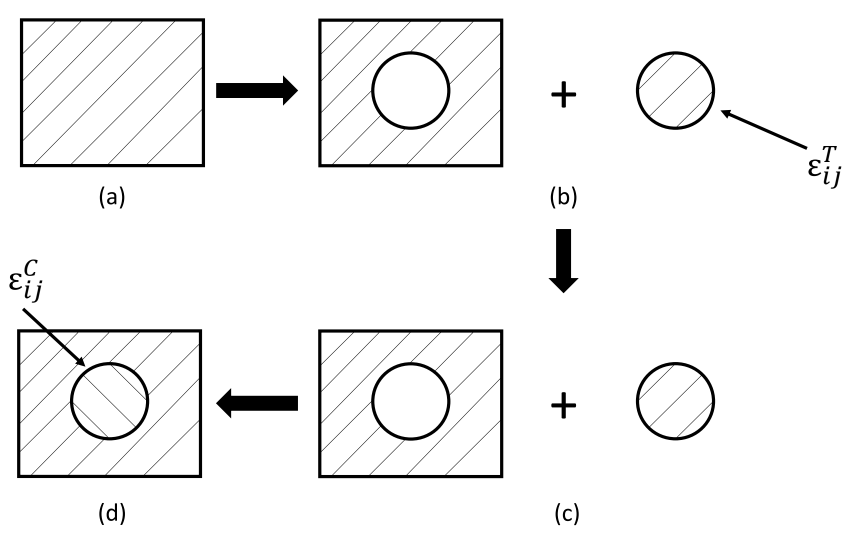

Figure 4.2: Schematic diagram of homogenisation based on the Eshelby method

Figure 4.2 (a) shows an initial unstressed elastic homogeneous material. A visualization of a cutting section called as inclusion is assumed to this structure, presented as the circle. The inclusion is presumed encounters a shape change free behaviour; causing the transformation strain $\boldsymbol{\varepsilon}_{ij}^{T}$ in Figure 4.2 (b) from the constraining matrix.

Assuming the strain is uniform within the inclusion, the stress in the inclusion, $\boldsymbol{\sigma}_{ij}^{I}$ is estimated using Equation 4.1.

$$\boldsymbol{\sigma}_{ij}^{I} = \boldsymbol{C}_{ijkl}^{M}(\boldsymbol{\varepsilon}_{kl}^{C} - \boldsymbol{\varepsilon}_{kl}^{T}) \tag{4.1}$$

The constraining strain can be determined in the form of transformation strain, ε_{kl}^{T} as shown in Equation 4.2.

$$\boldsymbol{\varepsilon}_{ij}^{C} = \boldsymbol{S}_{ijkl}\boldsymbol{\varepsilon}_{kl}^{T} \tag{4.2}$$

The Equation 4.2 is substituted in Equation 4.1 to compute the stress in the inclusion. The equation is simplified in Equation 4.3.

$$\boldsymbol{\sigma}_{ij}^{I} = \boldsymbol{C}_{ijkl}^{M}(\boldsymbol{S}_{klmn} - \boldsymbol{I}_{klmn})\boldsymbol{\varepsilon}_{mn}^{T} \tag{4.3}$$

The 4-th rank identity tensor of $\boldsymbol{I}_{klmn}$ in Equation 4.3 is given in Equation 4.4.

$$\boldsymbol{I}_{klmn} = \frac{1}{2}(\delta_{km}\delta_{ln} + \delta_{kn}\delta_{lm}) \tag{4.4}$$

Equation 4.3 is transformed in vector and matrices form as in Equation 4.5, where the braces and brackets are indication of vector and matrices, respectively.

$$\boldsymbol{\sigma}^I = \boldsymbol{C}^M(\boldsymbol{S} - \boldsymbol{I})\boldsymbol{\varepsilon}^T \tag{4.5}$$

As the fibre is assumed as infinite long cylindrical, the expressions of Eshelby tensors are estimated in form of matrix Poisson's ratio as in Equation 4.6 to Equation 4.14.

$$S_{1111} = S_{2222} = \frac{5 - \upsilon_m}{8(1 - \upsilon_m)} \tag{4.6}$$

$$S_{3333} = 0 \tag{4.7}$$

$$S_{1122} = S_{2211} = \frac{-1 + 4\upsilon_m}{8(1 - \upsilon_m)} \tag{4.8}$$

$$S_{1133} = S_{2233} = \frac{\upsilon_m}{2(1 - \upsilon_m)} \tag{4.9}$$

$$S_{3311} = S_{3322} = 0 \tag{4.10}$$

$$S_{1212} = S_{1221} = S_{2112} = S_{2121} = \frac{3 - 4\upsilon_m}{8(1 - \upsilon_m)} \tag{4.11}$$

$$S_{1313} = S_{1331} = S_{3113} = S_{3131} = \frac{1}{4} \tag{4.12}$$

$$S_{3232} = S_{3223} = S_{2332} = S_{2323} = \frac{1}{4} \tag{4.13}$$

Otherwise,

$$S_{ijkl} = 0 \tag{4.14}$$

Eshelby tensors of the inclusion as the function of matrix material properties and inclusion geometry or shape are applied. The assumption made in this case where the shape is an infinite long cylinder as shown in Equation 4.15.

$$\boldsymbol{S}_{MnAb} = f(\boldsymbol{C}_m, l \rightarrow \infty) \tag{4.15}$$

In this study, the effective composite properties of the composite plates are obtained by using Mori-Tanaka method as shown in [129] and [130].

The effective material properties via Mori-Tanaka of composite $\boldsymbol{C}_{comp}$ is expressed in Equation 4.16, where V, $\boldsymbol{C}$ and $\boldsymbol{A}^{MT}$ are the volume fraction, the material properties constitutive equation and the concentration tensor based on Mori-Tanaka method with respect to fibre, f and matrix, m, respectively.

$$\boldsymbol{C}_{comp} = V_m \boldsymbol{C}_m \boldsymbol{A}_m^{MT} + V_f \boldsymbol{C}_f \boldsymbol{A}_f^{MT} \tag{4.16}$$

The Mori-Tanaka tensor equation is shown in Equation 4.17 where $\boldsymbol{A}^{di}$ is the dilute concentration tensor and $\boldsymbol{I}$ is the identity matrix. The dilute tensor equation is expressed in Equation 4.18.

$$\boldsymbol{A}_f^{MT} = \boldsymbol{A}_f^{di}[V_m I + V_f \boldsymbol{A}_f^{di}] \tag{4.17}$$

$$\boldsymbol{A}_f^{di} = [\boldsymbol{I} + \boldsymbol{S}_{MnAb} \boldsymbol{C}_m^{-1}(\boldsymbol{C}_f - \boldsymbol{C}_m)]^{-1} \tag{4.18}$$

The properties are calculated as the function of fibre and matrix material properties, volume fractions and Eshelby tensors as summarised in Equation 4.19.

$$\boldsymbol{C}_{comp} = f(\boldsymbol{C}_m, \boldsymbol{C}_f, V_m, V_f, \boldsymbol{S}_{MnAb}) \tag{4.19}$$

Figure 4.3 shows the transformation of composite volume fraction to the homogenised composite using Mori-Tanaka method.

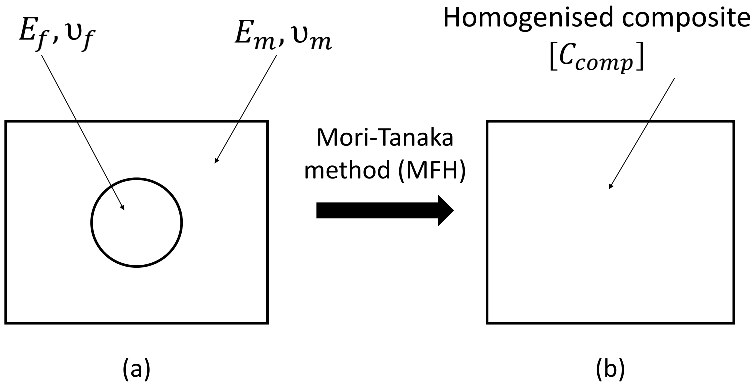

Figure 4.3: Mean field homogenisation by Mori-Tanaka method

4.3 Aerostructural coupling

In this section, the Doublet Lattice Method (DLM) is used to predict the unsteady aerodynamic distributions on the composite plate. Doublet Lattice Method has been developed by Albano and Rodden [131] to calculate the lift distributions in subsonic flow region.

The same coupling procedure between DLM and structural modelling using modified higher order shear deformation theory was performed by Abbas et al. [132] to estimate the flutter speed. There is another finite element that can be used, e.g. beam element, based on [133] but it is unattempted this time.

4.3.1 Finite element model

The 4-noded quadrilateral shell elements are implemented in the finite element model. The finite element model with 105 nodes for this specimen is presented in Figure 4.4. The boundary condition is fixed displacement on the root. The load used in the finite element model, is the aerodynamic load obtained via Doublet lattice method (DLM) in MSC Nastran. This procedure allows for a coupling between the structure (finite element) and the aerodynamics (DLM).

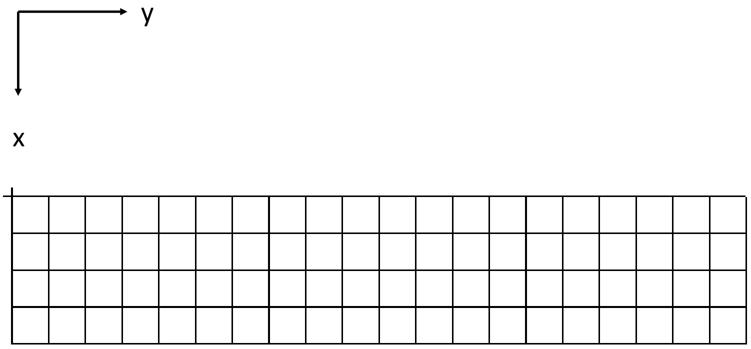

Figure 4.4: Present specimen modelled with 4-noded quadrilateral shell elements that consists of 105 nodes

The edge crack is modelled using double nodes in the chordwise direction. Two sets of nodes are assumed along the opposite face of the crack interface. The displacement fields of these two separated sets of nodes are independent to account the discontinuity along the crack interface.

4.3.2 Doublet lattice method

The specification of boxes along span and chord direction is required for coupling of FE-DLM using spline technique as shown in Figure 4.5. To compute the unsteady aerodynamics modelling using DLM, a set number of elements called aerodynamics box is specified.

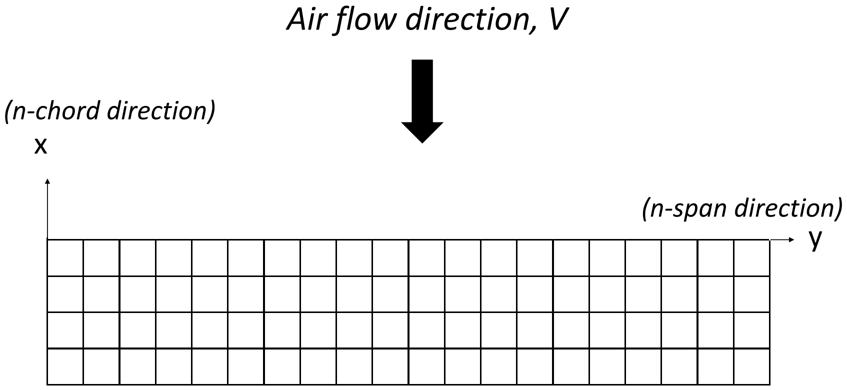

Figure 4.5: Aerodynamics modelling for coupling FE-DLM

The number of box, n and the constant force per unit length of the 1/4 chord line,

f for each box is visualised. The strategy starts with the definition of doublet strength amplitude of the $j-th$ division as in Equation 4.20; where l_j and $d\mu$ are the division line length and changes of length increment, respectively. In the present work, the size of the panels are constructed as close as possible following the structural meshing to provide simple interpolation between aerodynamic forces on the panels to the structural grids, i.e., the panels of a rectangular plate coincide with the quadrilateral elements. Based on MSC Nastran [134], the chord length of the boxes should be less than 0.08 times the velocity divided by the greatest frequency (in Hz) of interest, i.e., $\Delta x <$ 0.08V/f.

$$\frac{\bar{f}_j}{4\pi\rho}\int_{lj} d\mu \tag{4.20}$$

The normal wash amplitude generated at point (x_i,s_i), on the surface by $j-th$ number of doublet line is given in Equation 4.21.

$$\bar{w}_j(x_i,s_i) = (\frac{\bar{f}_j}{4\pi\rho}U^2)\oint_{lj} K[x_i s_i; x_i(\mu), s_j(\mu)]d\mu \tag{4.21}$$

By summing the normal wash developed by $n-th$ doublet lines, the total normal wash at point (x_i, s_i) is calculated. This relationship is presented in Equation 4.22.

$$\bar{w}(x_i,s_i) = \sum_{j=1}^{n}(\frac{\bar{f}_j}{4\pi\rho}U^2)\oint_{lj} K[x_i s_i; x_j(\mu), s_j(\mu)]d\mu \tag{4.22}$$

$\bar{f}_j$ is evaluated by exerting Equation 4.21 at n downwash points on the total surface of boxes. Equation 4.23 is the pressure difference across the boxes surface; where the box area is calculated as $\Delta x_j cos\lambda_j$. The denotions of Δx_j and λ_j are the box average chord and doublet line sweep angle, respectively.

$$\bar{P}_j = \frac{\bar{f}_j}{\Delta x_j cos\lambda_j} \tag{4.23}$$

Thus, the new expression of parameters from Equation 4.20 is shown in Equation 4.24, considering the sweep angle of doublet line.

$$\frac{\bar{f}_j}{4\pi\rho}U^2 = \frac{1}{8}\pi\bar{p}_j\Delta x_j cos\lambda_j \tag{4.24}$$

Based on [131], the normal wash velocity can be estimated by implying the Kutta condition. The Kutta condition meets the requirement when each downwash point is the 3/4 chord point at a box midspan. By applying this specification, Equation 4.21 is simplified in form of pressure distribution as expressed in Equation 4.25 where D_{ij} is the aerodynamic influence matrices and $\bar{p}_j$ is the pressure on lifting element.

$$\bar{w}_i = \sum_{j=1}^{n} D_{ij}\bar{p}_j \tag{4.25}$$

where,

$$D_{ij} = (\frac{1}{8}\pi)\Delta x_j cos\lambda_j \oint_{lj} K[x_i, s_i; x_j(\mu), s_j(\mu)]d\mu \tag{4.26}$$

In this study, the composite plate is considered as a thin plate where the panel is divided into several boxes for aerodynamics modelling. The thin composite panel is divided equally into 20 boxes in the spanwise direction and 5 boxes in the chordwise.

4.3.3 Generalised aerodynamic matrices

Referring to Equation 4.25, it can be rewritten as shown in Equation 4.27 where $\boldsymbol{A}$ is the aerodynamic influence matrices and P is the pressure on lifting element. Technically, aerodynamic influence matrices depend on the structural geometry, operating Mach number and reduced frequency.

$$w_i = \boldsymbol{A}_{ii}P \tag{4.27}$$

In that case, Equation 4.25 is rewritten as the substantial differentiation matrices of the deflections in Equation 4.28, where $\boldsymbol{D}^1_{ik}$ is the real part of the aerodynamic influence coefficient matrices, $\boldsymbol{D}^2_{ik}$ is the imaginary part of the aerodynamic influence coefficient matrices and u_k is the displacement at aerodynamic grid points.

$$w_i = [\boldsymbol{D}^1_{ik} + ik\boldsymbol{D}^2_{ik}]u_k \tag{4.28}$$

Meanwhile, the pressure on the lifting element can be estimated by the multiplication of transpose matrices of the aerodynamic influence coefficient, $\boldsymbol{A}^{-1}$ with the downwash which is expressed in Equation 4.29.

$$P = \boldsymbol{A}^{-1} w_{ii} \tag{4.29}$$

The integration of the pressure is presented in Equation 4.30 to obtain the lifting forces, F where $\boldsymbol{S}$ is the integration matrices.

$$F = \boldsymbol{S} P \tag{4.30}$$

Equation 4.30 is expanded by consideration of pressure from Equation 4.29 as shown in Equation 4.31.

$$F = \boldsymbol{S}\boldsymbol{A}^{-1}[\boldsymbol{D}^1 + ik\boldsymbol{D}^2]u_k \tag{4.31}$$

Technically, the three matrices of Equations 4.27, 4.28 and 4.30 can be combined to present the aerodynamic influence coefficient matrices in Equation 4.32.

$$\boldsymbol{Q}_{kk} = \boldsymbol{S}\boldsymbol{A}^{-1}[\boldsymbol{D}^1 + ik\boldsymbol{D}^2] \tag{4.32}$$

F can be simplified in term of aerodynamic matrices in Equation 4.33 by substituting Equation 4.32 into Equation 4.31. Thus, the lifting force for each aerodynamic element (k x k) is computed via this relation.

$$F = \boldsymbol{Q}_{kk} u_k \tag{4.33}$$

A modal reduction has to be implemented to obtain the matrices in generalised form. Those transformations are expressed in Equation 4.34 where $\boldsymbol{Q}^*_{ii}$ is the generalised aerodynamic matrices, $\boldsymbol{G}_{ka}$ is the spline matrix reduced to i-set.

$$\boldsymbol{Q}^*_{ii} = \boldsymbol{G}^T_{ka}\boldsymbol{Q}_{kk}\boldsymbol{G}_{ka} \tag{4.34}$$

In the aeroelastic analysis, the h-set is defined as a-set (from structural) normal modes. Thus the i-matrix of a-set from the normal mode vector (modeshape) in the physical a-set is denoted by $\boldsymbol{\phi}_{ah}$. The generalised aerodynamic matrices in h-set are computed through Equation 4.35.

$$\boldsymbol{Q}_{hh} = \boldsymbol{\phi}_{ah}^{T} \boldsymbol{Q}_{ii}^{*} \boldsymbol{\phi}_{ah} \tag{4.35}$$

Finally, the calculated lifting forces from Equation 4.33 can be expressed in the h-set of the aeroelastic solution as presented in Equation 4.36 for solving the problem involved in flutter or gust.

$$F^{*} = \boldsymbol{Q}_{hh} u_{k} \tag{4.36}$$

4.4 Flutter solution of *pk*-method

Here, the coupling of finite element model for structural and doublet lattice method for unsteady aerodynamics has been performed using spline technique. To estimate the flutter speed/ boundary in this study, the flutter solution based on *pk*-method shown in Equation 4.37 is applied [56], where $\boldsymbol{M}_{hh}$ is the mass matrices, $\boldsymbol{B}_{hh}$ is the damping matrices, $\boldsymbol{Q}_{hh}^{R}$ is the real aerodynamic matrices, $\boldsymbol{Q}_{hh}^{I}$ is the imaginary aerodynamic matrices and $\boldsymbol{K}_{hh}$ is the stiffness matrices.

$$\boldsymbol{M}_{hh} p^{2} + \left(\boldsymbol{B}_{hh} - \frac{\frac{1}{4}\rho \bar{c} \boldsymbol{Q}_{hh}^{I}}{k}\right) p + \left(\boldsymbol{K}_{hh} - \frac{1}{2}\rho V^{2} \boldsymbol{Q}_{hh}^{R}\right) = 0 \tag{4.37}$$

The term *pk* is referring to two parameters which are used to predict the flutter speed. p is the root of the quadratic equation and k is the reduced frequency in Equation 4.37. To solve the reduced frequency of k, Equation 4.38 is used where ω is the natural vibration mode frequency, $\bar{c}$ is the average chord length and V is the computed velocity.

$$k = \frac{\omega \bar{c}}{2V} \tag{4.38}$$

As the solution in Equation 4.37 is in quadratic form of p, structural damping of g can be estimated as mentioned in Equation 4.39.

$$p = \omega(2g + i) \tag{4.39}$$

To simplify the Equation 4.38 and Equation 4.39, the natural frequency that is obtained from modal analysis denoted by ω is eliminated. The relationship between g and V based on pk-method is now shown in Equation 4.40.

$$p = \frac{2kV}{\bar{c}}(2g + i) \tag{4.40}$$

In the final solution of Equation 4.40, this relationship is used to plot the structural damping, g versus airflow velocity, V to obtain the flutter speed. As mentioned in Section 4.1, the flutter speed is obtained at $g = 0$ where the structure begins to fail.

4.4.1 FE-DLM Coupling procedure

By using an interpolation technique, both structural and aerodynamic grids are associated. Thus, using this procedure allows the selection of both structural and aerodynamic of the lifting surfaces become independent to be performed in any particular theory of the fluid- structure interaction. An interpolation method called as 'splining' technique is used to interconnect both structural and aerodynamic model. The structure of the body can be modelled in one-, two- or three-dimensional array of grid points. For aerodynamic model, a lifting surface theory or strip theory might be used to model the aerodynamic boxes.

In this work, the composite plate is analysed with the existence of edge crack as shown in Figure 4.6. Thus, it triggers the separation of the plate surface into subregions that has led to the discontinuous slope. For this reason, the aerodynamic degrees of freedom depends on the structural degrees of freedom. To make a relation between both models, a spline matrix is derived.

In general, the spline matrix that interpolates the displacements at the grid points of the structural finite element to the control points of aerodynamic boxes to resolve the data transferral problem. In Equation 4.41, the total spline matrix of $\boldsymbol{G}_{ka}$ is expressed based on the generation of spline matrix by surface spline method, where u_k is the interpolated displacement vector at aerodynamic boxes, including the translational displacements and their slopes with respect to the components of the structural grid point deflections, u_g.

$$u_k = \boldsymbol{G}_{kg} u_g \tag{4.41}$$

Any grid components can be defined to describe the structural degrees of freedom. In this case, two transformations are required. The first one is the interpolation from the structural deflections to the aerodynamic deflections. The second one is the interpolation of the relationship between the aerodynamic loads and the structural equivalent loads acting on the structural grid point. From here, the aerodynamic degrees of freedom is correlated to be depending on the structural degrees of freedom. Further details about the aero-structure coupling of 'splining' technique can be explored in [134].

4.5 Cantilever unidirectional composite plate model

The unidirectional composite plate (1 ply) of graphite - fibre reinforced polyimide that is used in this study was developed in [135]. The unidirectional composite specimen model is presented in Figure 4.6. It is modelled as a cantilever plate where the length, L is 0.5 m; the width, b is 0.1 m and the height, h is 0.005 m. As the crack development in this study is qualitatively measured, the crack ratio is defined as $\eta = a/b$ where a is the crack length. In the present work, this specimen is modelled by using shell element. The dimensionless crack location for this study is denoted by $\xi_c = l/L$. The material properties of graphite - fibre reinforced polyimide is shown in Table 4.1.

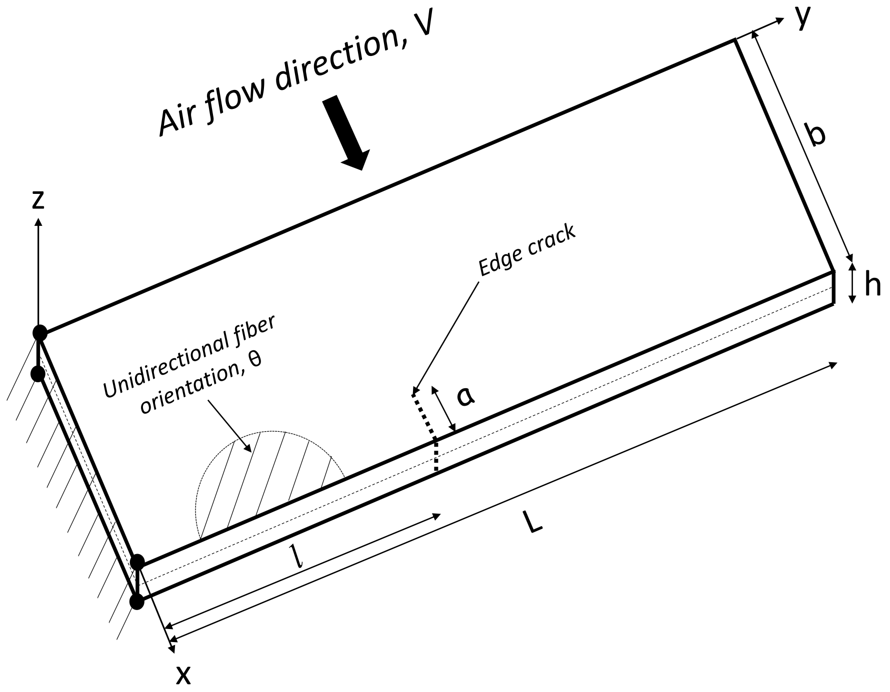

Figure 4.6: Specimen modelling of the unidirectional composite plate

Table 4.1: Material properties of graphite - fibre reinforced polyimide composite

Modulus of elasticity	$E_m = 2.76$ GPa	$E_f = 275.6$GPa
Poisson's ratio	$\nu_m = 0.33$	$\nu_f = 0.2$
Shear modulus	$G_m = 1.036$ GPa	$G_f = 114.8$ GPa
Mass density	$\rho_m = 1600\ kg/m^3$	$\rho_f = 1900\ kg/m^3$
Fibre volume fraction	$V = 0.5$	

4.5.1 Mean field homogenisation (MFH) from Mori - Tanaka method

A code is developed to estimate the stiffness and the constitutive matrices based on Mori-Tanaka method for the presented composite structure. By using Chan-Unsworth model, the numerical properties calculated are compared with Mori-Tanaka method developed in this section. Figures 4.7 and 4.8 present the compliance matrices estimation of the present material. Figures 4.9 and 4.10 show the constitutive matrices estimation of the material.

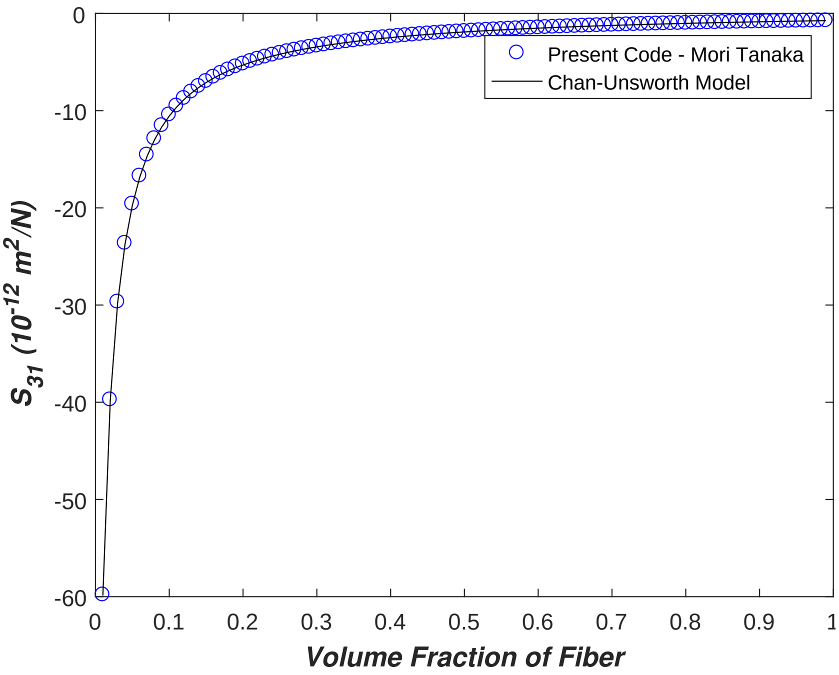

Figure 4.7: Compliance matrix component of S_{31}

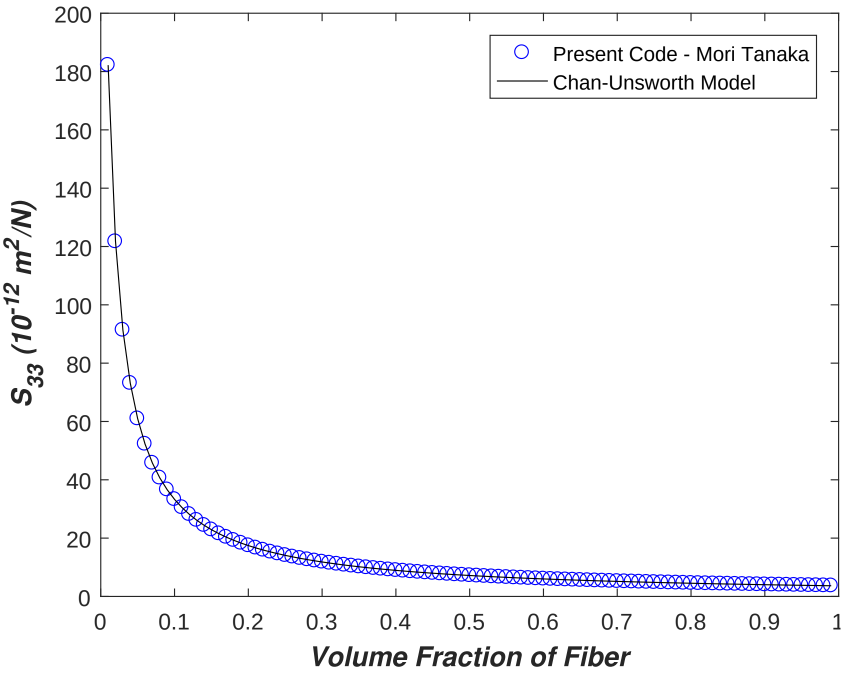

Figure 4.8: Compliance matrix component of S_{33}

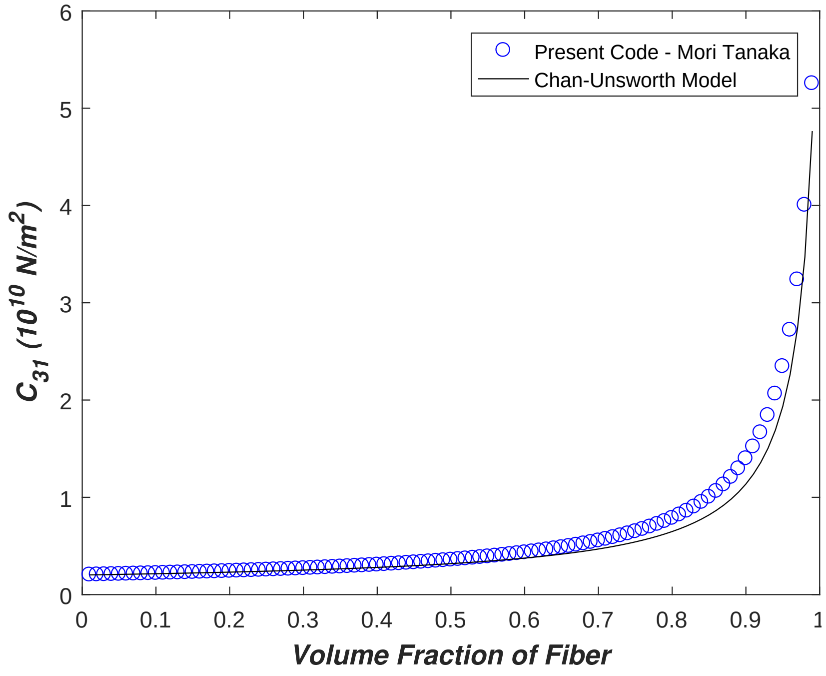

Figure 4.9: Effective stiffness matrix component of C_{31}

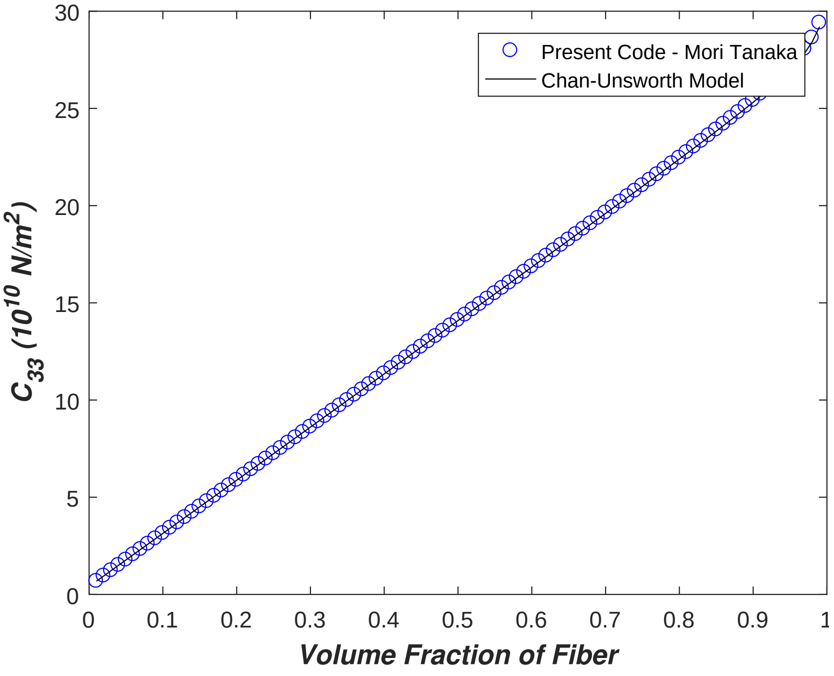

Figure 4.10: Effective stiffness matrix component of C_{33}

As the Mori - Tanaka micromechanical model is implemented in this study, the constitutive equation in Plane Stress form $\boldsymbol{C}_{comp}$ [unit: Pa] is shown in Table 4.2:

Table 4.2: Constitutive values in plane stress form based on Mori-Tanaka method

$\boldsymbol{C}_{comp}$	Value (Pa)
$C_{11} = C_{22}$	6.8503 x10^9
$C_{12} = C_{21}$	3.1437 x10^9
$C_{13} = C_{23} = C_{31} = C_{32}$	0
C_{33}	2.646 x10^9

4.5.2 Comparison of modal analysis results

Modal analysis is performed to validate the procedure used in this work. In this section, the composite plate specimen without crack is used as the baseline to other cracked composite plates. The benchmark results of vibration modes are compared with the results presented by Wang et al. [35]. In Table 4.3, the results of the modal analysis for a unidirectional composite of $\theta = 0$ using the presented method are shown and are compared with the results established in [35].

Table 4.3: First four bending modes and first four torsion modes vibrational frequencies for $\theta = 0°$

Wang et al.	Mode	1st (Hz)	2nd (Hz)	3rd (Hz)	4th (Hz)
	Bending	6.94	43.47	121.71	238.49
	Torsion	62.81	197.45	329.08	460.71
Present work	Mode	1st (Hz)	2nd (Hz)	3rd (Hz)	4th (Hz)
	Bending	5.87	36.59	102.87	203.02
	Torsion	60.54	184.23	315.74	460.00
Relative error	Mode	1st (Hz)	2nd (Hz)	3rd (Hz)	4th (Hz)
	Bending	15.35 %	15.83 %	15.48 %	14.87 %
	Torsion	3.61 %	6.69 %	4.05 %	0.15 %

As the results of the modal analysis are validated, the procedure is applied to other specimens with existing crack. All eight vibrations modes (four bending modes and four torsion modes) that are presented in Table 4.3 are plotted in Figure 4.11. As the calculated relative errors between the present work and Wang et al. [35] in bending mode are higher mostly due to the structure mesh definition to the composite structure. As the structure will demonstrate a bending mode when it is excited at a particular frequency, the mesh should be refined in the spanwise and chordwise direction to prevent and to minimise the shear locking. In another hand, this error also might occur due to the less meshing definition through thickness which has led to the distortion or hour glassing problem. In that sense, more mesh refinements are needed to be implemented to reduce the relative error in bending mode.

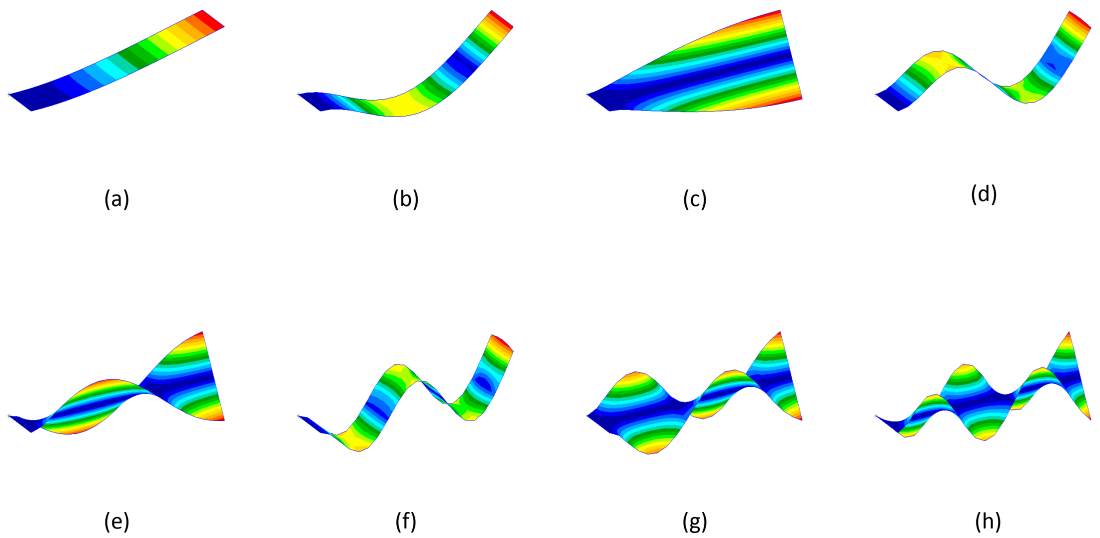

Figure 4.11: First eight vibration modes for $\theta = 0°$ where (a) 1st mode: 5.87 Hz, (b) 2nd mode: 36.59 Hz, (c) 3rd mode: 60.54 Hz, (d) 4th mode: 102.87 Hz, (e) 5th mode: 184.23 Hz, (f) 6th mode: 203.02 Hz, (g) 7th mode: 315.74 Hz, and (h) 8th mode: 460.00 Hz

It is a different modelling technique in observing the modal vibration modes. Thus, in this case, the finite element modelling has been applied to the unidirectional cracked composite panel instead of a cracked beam presented in [35]. In the reference, an analytical model was used to determine the natural frequencies/ mode shapes. Furthermore, a function of mode shapes was assumed to satisfy the boundary condition at the crack location. However, in the present chapter, a full finite element model is used to obtain the mode shapes and the natural frequencies. Thus, for the plate with crack, the crack also modelled directly in the finite element model. Therefore, there will be discrepancies with the results compared to the reference. Further flutter analyses are presented in the next sections.

4.5.3 Section a: Influence of crack ratio on flutter speed

The objective of this section is to study the effects of the flutter speed while the crack location is fixed and the crack length is changed. Several analyses are performed to the unidirectional composites of 0°, 90° and 135° (−45°) orientations. The same procedures are repeated and applied for crack ratio denoted by $\eta = a/b$ as η is increased from 0 to 0.75.

The flutter analyses are performed to the undamaged (without crack) composite plates for 0°, 90° and 135° orientations in the first place. The flutter speed for this situation is considered as the reference for other cases which is denoted as V_R. The flutter speed estimation for unidirectional composite without crack for 0°, 90° and 135° orientations are shown in Figure 4.12.

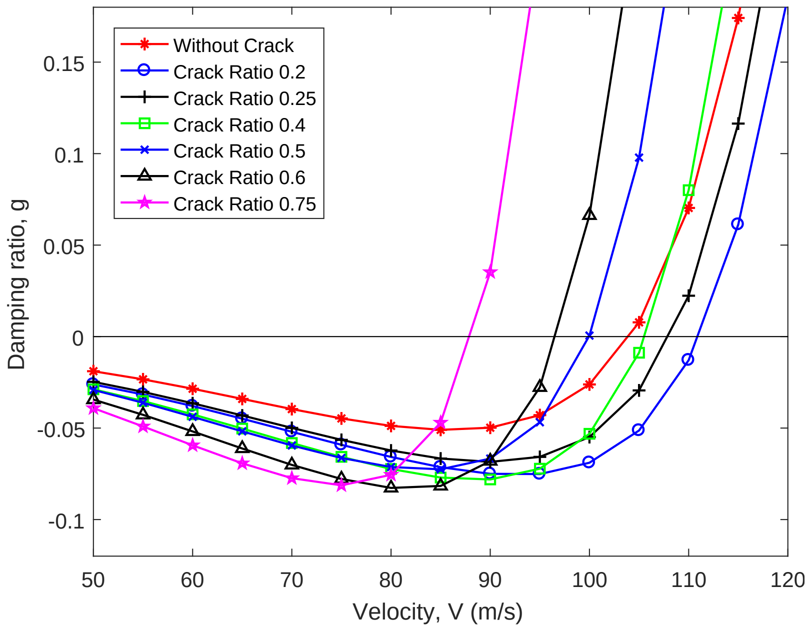

Figure 4.12: Flutter speed determination for $\theta = 0°$

In this work, the frequency of vibrational mode interacting with the speed increment is presented in Figure 4.13 for an oscillating composite plate at unidirectional of 0°. Based on the plot, the flutter frequency is found to be 37.37 Hz, where the structural damping is zero. Technically, the V-g plots in Figure 4.12 are based on the 2nd bending mode that has led to the flutter mode as discussed in [35] for several crack ratios. Using FEM-DLM approach in MSC Nastran, the flutter frequency for $\eta = 0.2$ is found to be a bit higher than the undamaged specimen.

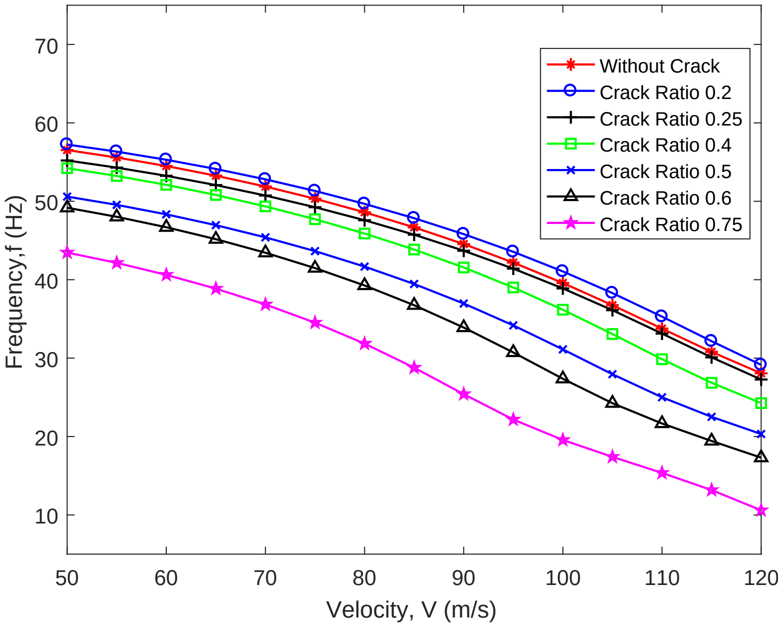

Figure 4.13: Flutter frequency reduction for $\theta = 0°$

As the flutter speeds of undamaged unidirectional composite plates at angle 0°, 90° and 135° have been determined, the flutter analyses with crack planform are performed. The flutter speed, V_F is determined for several cases of crack ratio, $\eta = a/b$ which are 0.2, 0.25, 0.4, 0.5, 0.6 and 0.75. The normalised flutter speeds of V_F/V_R versus the crack ratio which are compared with results in [35] as shown in Figure 4.14.

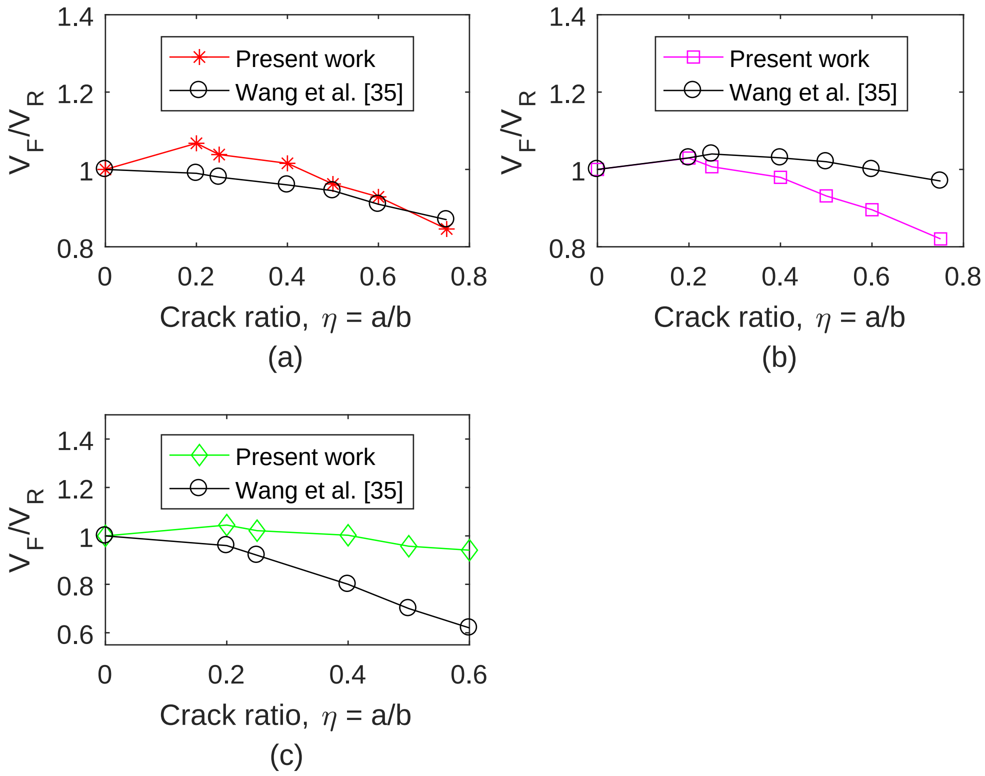

Figure 4.14: Normalised flutter speeds with respect to the crack ratio for case (a) $\theta = 0°$, (b) $\theta = 90°$ and (c) $\theta = 135°$

The results show that the flutter speeds are increasing for all presented composite angle when the crack ratio is 0.2 compared to the flutter speed of undamaged composite plates. The trends of flutter speed begin to decrease but are still above the reference flutter speed when $\eta = 0.25$. The same pattern is seen for crack ratio 0.4, but the flutter speed for this case is almost near to the flutter speed of the undamaged composite plate. At $\eta = 0.5$, the normalised flutter speeds of V_F/V_R for $\theta = 0°$ and $90°$ begin to decrease about 1.84 % and 8.67 %, respectively. The same trend is found for $\theta = 135°$ with $\eta = 0.5$ with a difference of 36.77%.

Based on these facts, the existence of crack ratio, η more than 0.4 makes the structure weaker from the undamaged plate ($\eta = 0$). As a result, the structure vibration amplitude tends to increase with the increment of crack ratio. This explanation shows an agreement with the work done by Song et al. [136] where the crack opening increment has weakened the cantilevered composite when it deals with dynamics loading. The results are almost similar to the results published in [35] where the flutter speed had found to be increased when the crack was initiated, but it began to decrease gradually when the η has reached 0.35. The same trend for present work is seen when the unsteady aerodynamics is modelled using strip theory as in Figure 4.15.

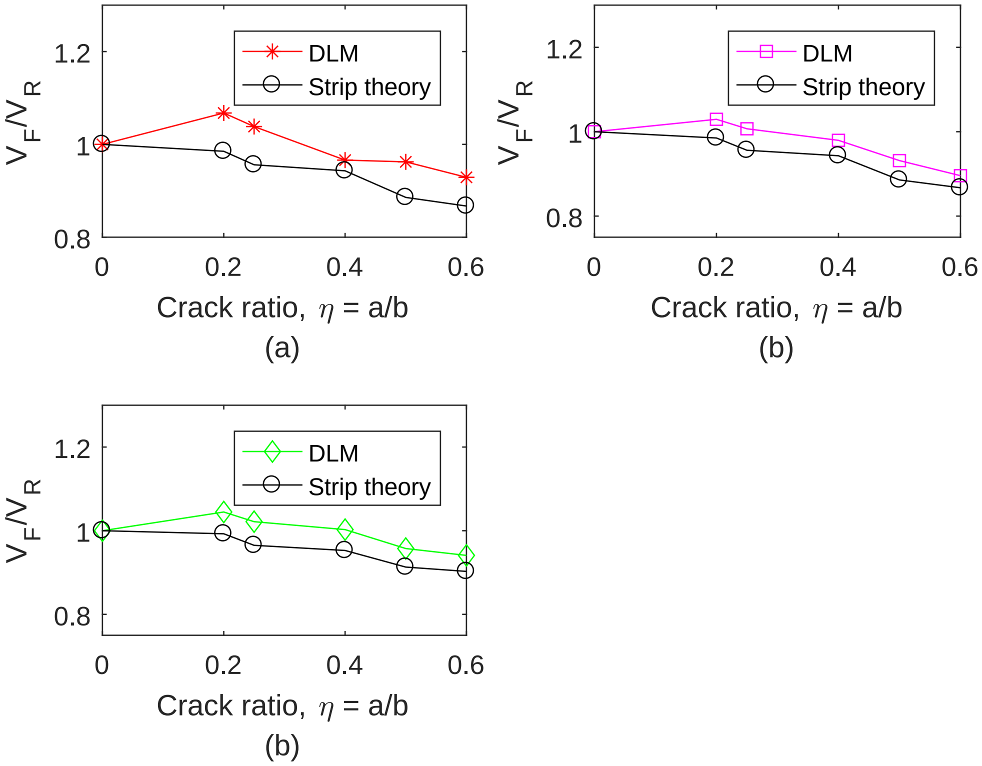

Figure 4.15: Comparison of DLM and Strip theory for normalised flutter speeds with respect to the crack ratio for case (a) $\theta = 0°$, (b) $\theta = 90°$ and (c) $\theta = 135°$

To gain a deeper understanding of this phenomenon, flutter response modes are plotted in Figure 4.16. This part aims to study the changes of the mode from without any crack until the specimen almost breaks where f_F is the flutter frequency for each case. In Figure 4.16 (a) where $\eta = 0$, the flutter response mode is a first torsion mode, with $f_F = 37.37$ Hz. With the existence and increment of crack ratio, the flutter frequency keeps reducing, which allows more time for the structure to oscillate. Next, for $\eta = 0.2$ in Figure 4.16 (b), the flutter response is the same mode as $\eta = 0.0$, with the deflection a little bit release. This behaviour made the structure be able to stand more load as the rigidity is now increased with the existence of small crack (0.02 m). Thus, it causes an increment of flutter speed compared to the undamaged specimen. The same behaviour of flutter response is seen until $\eta = 0.4$.

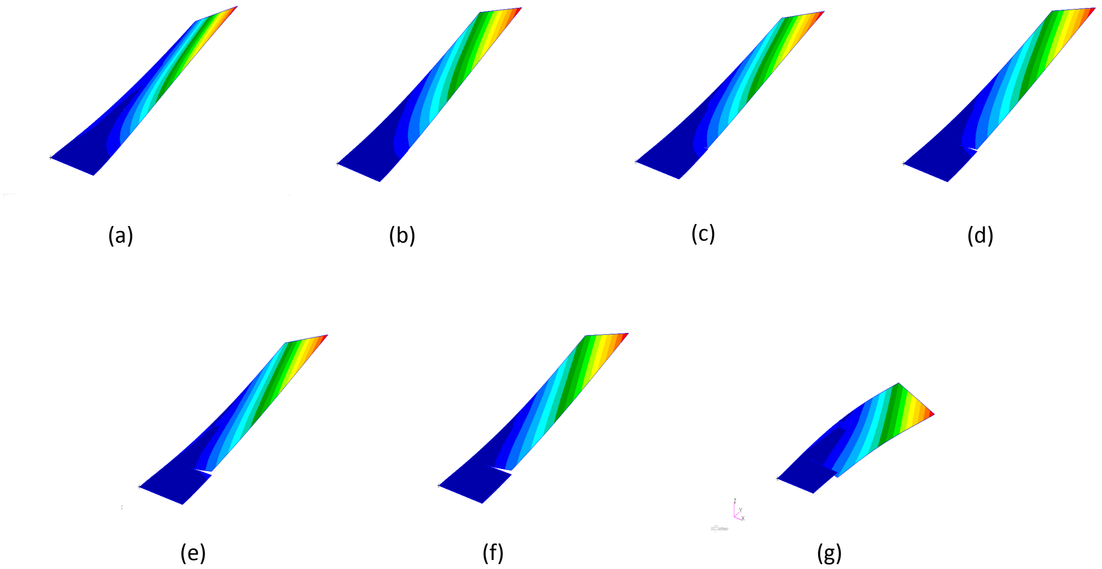

Figure 4.16: Flutter response modes for case $\theta = 0°$ with variation of crack ratio where (a) $\eta = 0.0$, $f_F = 37.37$ Hz, (b) $\eta = 0.2$, $f_F = 34.75$ Hz, (c) $\eta = 0.25$, $f_F = 34.42$ Hz, (d) $\eta = 0.4$, $f_F = 32.75$ Hz, (e) $\eta = 0.5$, $f_F = 31.15$ Hz, (f) $\eta = 0.6$, $f_F = 29.74$ Hz, and (g) $\eta = 0.75$, $f_F = 26.85$ Hz

In Figure 4.16 (e) where $\eta = 0.5$, the flutter speed is now reduced about 3.77 % compared to the undamaged specimen, but the flutter response mode is maintained. With further crack ratio increment, the flutter response mode has switched to the mixture between torsion and bending mode as shown in Figure 4.16 (g) for $\eta = 0.75$. For this case, the flutter speed has reduced to about 15.4 %.

4.5.3.1 Analysis of the flutter speed increment for crack ratio of 0.2

DLM is applicable for interfering the lift distribution on flying surface in subsonic flow. It was developed based on the linearised aerodynamic potential theory. Thus, this method establishes a uniform undisturbed flow either in a steady flow or unsteady flow (with existence of gust) harmonically.

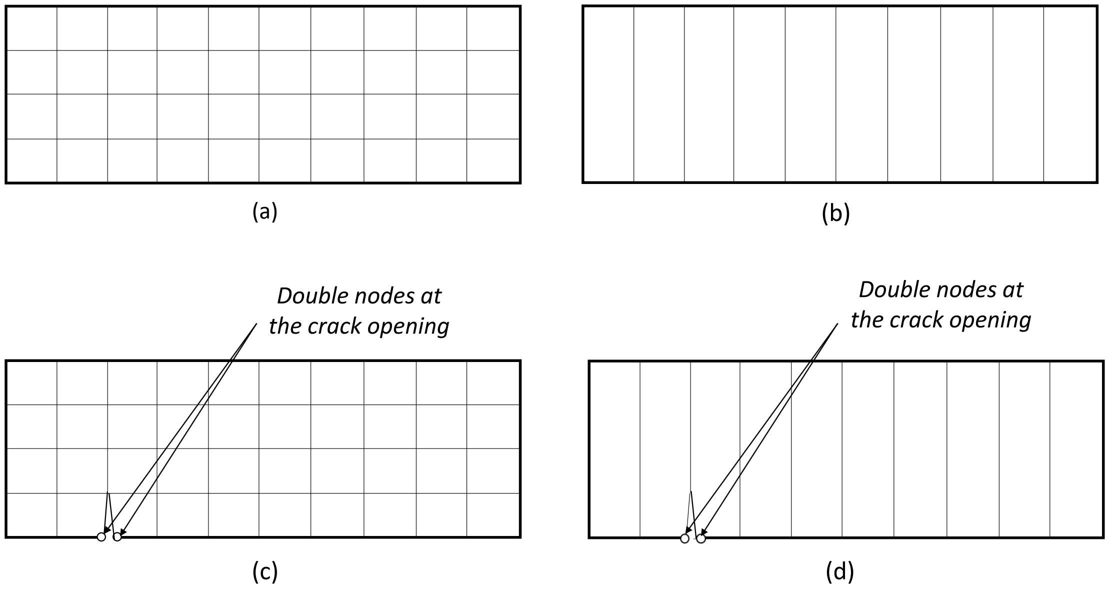

Figure 4.17: Comparison of aerodynamic modelling technique between Doublet Lattice Method and Strip theory for without crack and with crack specimen, where (a) Doublet Lattice Method - without crack, (b) Strip theory - without crack, (c) Doublet Lattice Method - with crack, and (d) Strip theory - with crack

Aerodynamics modelling technique of DLM used in this work is much more advanced than Strip theory since it considers the structural panels, which allows the lifting surface to be divided into small trapezoidal lifting elements called as 'aerodynamic boxes'. As the lifting surfaces are assumed to be almost parallel to the freestream flow (refer Figure 4.5), thus the arranged aerodynamic boxes also aligned in strip direction to be parallel to the airflow.

It is a different situation with strip theory modelling technique. The load at each spanwise station of a wing is assumed to be depending only on the motion of the station when flutter solution is computed. The lifting surface is divided into a set number of strips, and the aerodynamic loads are estimated based on two-dimensional coefficients evaluated at the centreline of the strip.

The comparison using both techniques is illustrated in Figure 4.17. For this reason, the aerodynamics modelling accuracy using Strip theory is lower than DLM where the aerodynamic is consider strip by strip from the root to the tip of the composite plate, including the crack surface. The intention of computing the flutter speed based on Strip theory is to validate the work using DLM, which is not done by Wang et al [35].

Thus, it is believed that the aerodynamic modelling for the crack ratio of 0.2 is more reliable to be modelled with DLM.

To clarify this statement, the real and imaginary parts of the aerodynamic matrices for crack ratio = 0.2 are computed. Aerodynamic matrices of $\boldsymbol{Q}_{hh}$ in Equation 4.42 shows the aerodynamic matrices computed for both real and imaginary parts where $h = 1$ and $h = 2$ are referred to the bending mode and torsion mode, respectively. In this case, Q_{11}, Q_{12}, Q_{21} and Q_{22} refer to the aerodynamic parameters for both real and imaginary parts in bending-bending, bending-torsion, torsion-bending and torsion-torsion, respectively.

$$\boldsymbol{Q}_{hh}(real\&imaginary) = \begin{bmatrix} Q_{11} & Q_{12} \\ Q_{21} & Q_{22} \end{bmatrix} \tag{4.42}$$

Both DLM and Strip theory computational aerodynamic matrices results are presented in Table 4.4.

Table 4.4: Aerodynamic matrices data comparison between DLM and Strip theory for crack ratio 0.2

Aerodynamic parameter	Doublet Lattice Method	Strip Theory
Q_{11}	$2.47\text{x}10^1 - 8.68\text{x}10^2 i$	$-1.94\text{x}10^2 - 1.12\text{x}10^3 i$
Q_{12}	$-1.32\text{x}10^4 - 6.43\text{x}10^2 i$	$1.96\text{x}10^4 + 1.91\text{x}10^3 i$
Q_{21}	$8.58\text{x}10^1 + 8.13\text{x}10^2 i$	$2.22\text{x}10^2 + 8.99\text{x}10^2 i$
Q_{22}	$1.29\text{x}10^4 - 1.57\text{x}10^3 i$	$1.70\text{x}10^4 - 3.53\text{x}10^3 i$

Referring to Equation 4.37, the real and imaginary parts of the aerodynamic matrices are contributed to the aerodynamics stiffness system and aerodynamic damping system, respectively. The negative sign value in Table 4.4 means the addition in the damping or stiffness system while the positive sign means the reduction to the damping of stiffness system. By analysing the data, the real part of the aerodynamic matrices using DLM is higher than the value computed using Strip theory. Thus, it means that the stiffness system estimated using DLM is less than strip theory.

The same analysing procedure is applied in evaluating the damping system. For this case, the imaginary values computed using DLM is less than the value estimated using strip theory. In this case, the lesser values of imaginary aerodynamic matrices have increased the damping system of DLM compared to Strip theory. For this case, the higher damping system has led to the stability of the cracked composite plate with the crack ratio of 0.2 to be increased; thus the flutter speed computed also has increased. This is the reason why the flutter speed of the composite plate with 0.2 is estimated to be higher using DLM compared to the flutter speed computed using strip theory.

4.5.4 Section b: Influence of crack location on flutter speed

The objective of this section is to study the effects of the flutter speed when the location of the crack is changing from the root to the tip of the composite plate. For this part; the crack length, $a = 0.02\ m$ is fixed for each case is validated with work done in [35]. Figure 4.18 shows the results of normalised flutter speeds of V_F/V_R versus the crack location denoted as ξ_c for the unidirectional composites of 0°, 90° and 135° orientations.

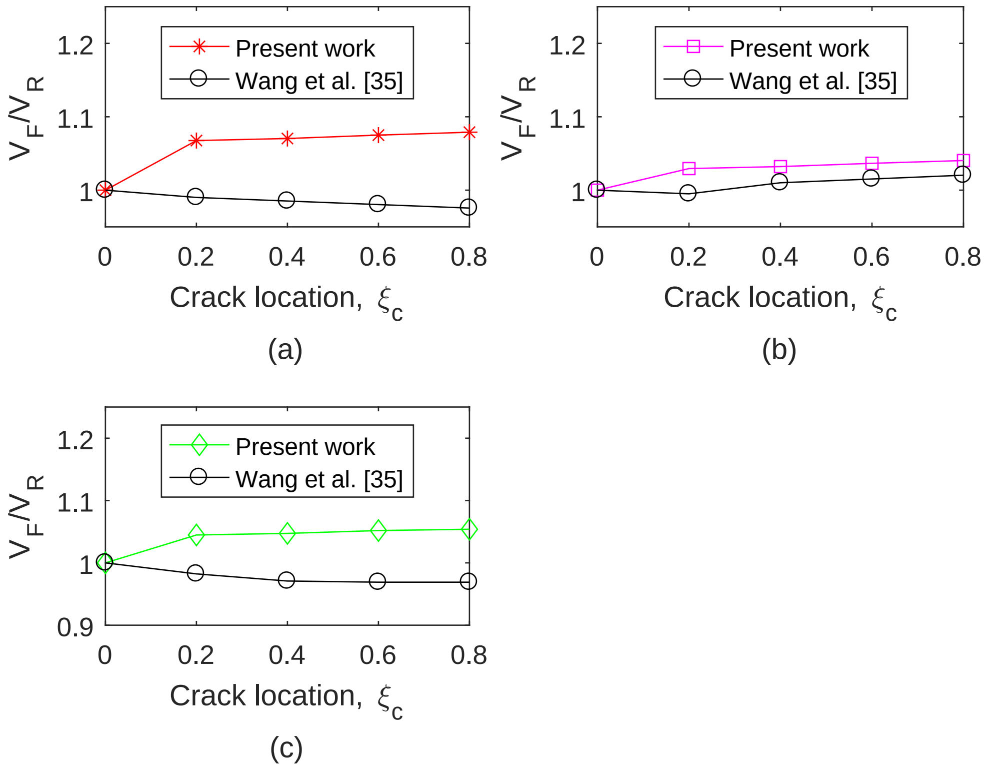

(a) (b) (c)

Figure 4.18: Normalised flutter speeds with respect to the crack location ($\eta = 0.2$) for case (a) $\theta = 0°$, (b) $\theta = 90°$ and (c) $\theta = 135°$

For the same analysed cases, the aerodynamics modelling for the specimens using DLM is repeated by changing it using Strip theory. The comparison results of normalised flutter speeds with respect to the crack location for case $\theta = 0°$, $\theta = 90°$ and $\theta = 135°$ orientations using DLM and Strip theory ($\eta = 0.2$) are shown in Figure 4.19.

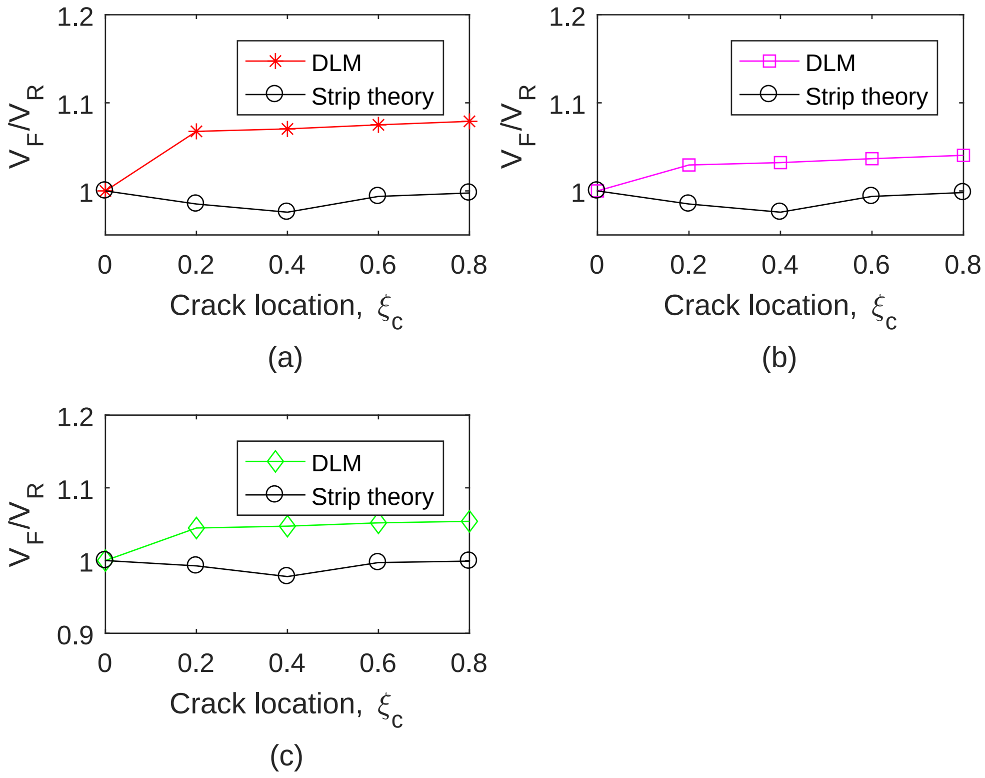

Figure 4.19: Comparison of DLM and Strip theory ($\eta = 0.2$) for normalised flutter speeds with respect to the crack location for case (a) $\theta = 0°$, (b) $\theta = 90°$ and (c) $\theta = 135°$

In this case, V_F/V_R approximation using DLM seems to be higher than the estimation by using Strip theory. There is a significant part of this case where V_F/V_R at $\xi_c = 0.2$ is found to be slightly higher than V_F/V_R at $\xi_c = 0.4$. V_F/V_R are found to have increased after $\xi_c = 0.4$ till near the tip. Hence, the case of $\eta = 0.2$ is much complicated where the V_F/V_R is increased due to the crack ratio, as it is shown in the Section 4.5.3.

Thus, to check the effect of the flutter speed when the location of the crack is changing from the root to the tip, the procedure is repeated using a different crack ratio which is $\eta = 0.6$. It stems from the fact of the consistency shows for the case $\eta = 0.6$ when the crack ratio is constructed in the Section 4.5.3. V_F/V_R results for this case are shown in Figure 4.20.

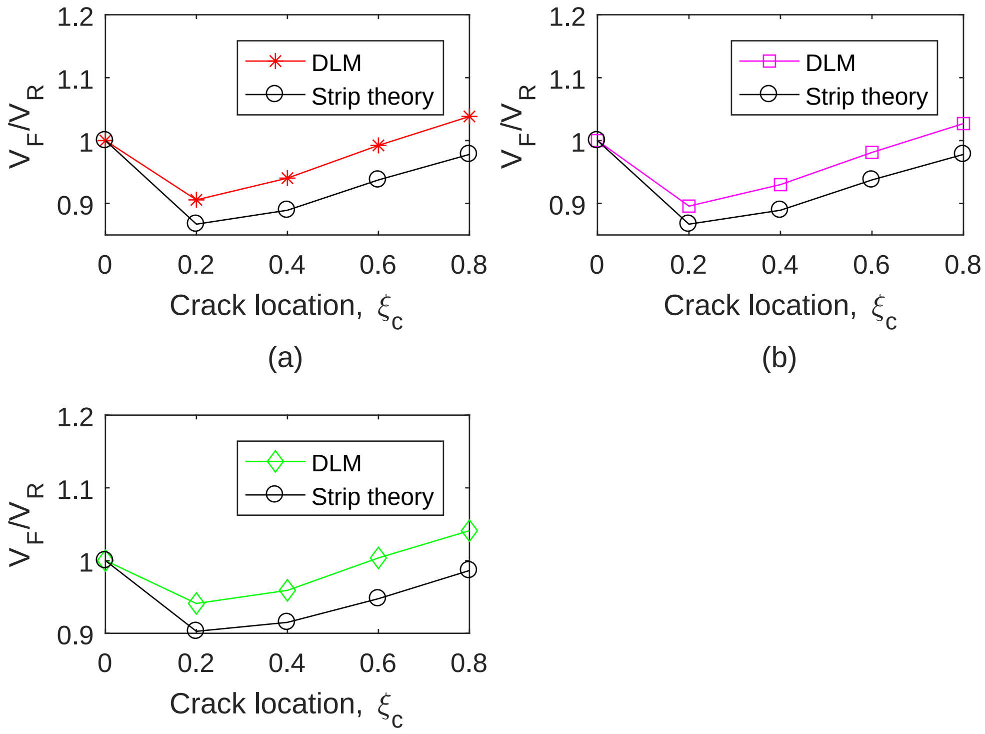

(a)

(b)

(c)

Figure 4.20: Comparison of DLM and Strip theory ($\eta = 0.6$) for normalised flutter speeds with respect to the crack location for case (a) $\theta = 0°$, (b) $\theta = 90°$ and (c) $\theta = 135°$

In Figure 4.20, it turns out that the V_F/V_R plot shows consistency for all unidirectional composite plates of 0°, 90° and 135° orientations. The result indicates that the V_F/V_R increases as the crack location moves from root to tip, as expected. This outcome is explained in Figure 4.21. The flutter responses for unidirectional composite plate of $\theta = 0°$ are plotted; the flutter frequency trend is found to have dropped as the crack location moves from root to tip. The reduction of flutter frequency allocates more time for the structure to swing, thus increase the flutter speed.

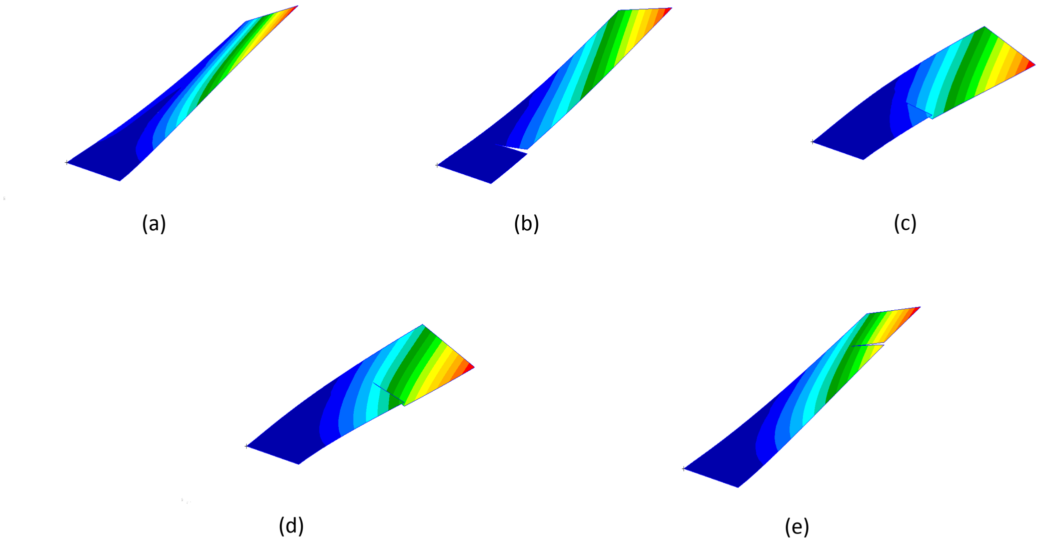

Figure 4.21: Flutter response modes for case $\theta = 0°$ with variation of crack location where (a) $\xi_c = 0.0$, $f_F = 37.37$ Hz, (b) $\xi_c = 0.2$, $f_F = 29.74$ Hz, (c) $\xi_c = 0.4$, $f_F = 31.13$ Hz, (d) $\xi_c = 0.6$, $f_F = 33.84$ Hz, and (e) $\xi_c = 0.8$, $f_F = 35.39$ Hz,

4.6 Summary

This chapter presents the flutter estimation modelling using coupled Finite Elements and Doublet Lattice Method on a cracked unidirectional composite plate. Several cases were discussed that studied the effect of crack ratio and the crack location. The computational results were validated with previous literature. Mori-Tanaka homogenisation model is applied to obtain the effective composite constitutive properties as the function of fibre and matrix volume fraction. Doublet Lattice Method (DLM) was used to calculate the unsteady aerodynamic forces, i.e., lift distributions. It was found that the existence of small crack ratio on the composite plate (less than 0.4) has triggered an increment of the flutter speed. To support this statement, flutter response modes for each crack ratio were plotted, where the structure appeared to be more stiffened than the undamaged plate. However, the crack results in the reduction of flutter speed when the crack ratio reached 0.5. For the crack location assessment, the flutter speed kept increasing as the crack location moved from the root to the tip due to the reduction of flutter frequency. The results show a good agreement with the validation using Strip Theory considering unsteady aerodynamics.

Further analysis is necessary for the results rather than take the results as it is. For example, when a large crack occurs, the plate is almost completely different from the baseline without crack. The dominant modes used for flutter analysis of the baseline plate are likely to change. However, the only two modes taken for V_F calculation in the baseline were kept the same for the cases of different crack ratio. This may lead to a different flutter mode and higher speed. Since no modes are presented and analysed for the plates of different crack ratio, the true reason may not be found. For a thorough study, a more extensive range of modes (> 4) should be included in the flutter speed to ensure the V_F fundamental is determined.

Chapter 5

Structural Integrity of Cracked Composite Plate Subjected to Gust Loads using XFEM

"When everything seems to be going against you, remember that the airplane takes off against the wind, not with it."
- Henry Ford (American captain of industry and a business magnate, the founder of the Ford Motor Company, 1863 – 1947).

This chapter offers an investigation of the cracked composite plate presented in Chapter 4 subjected to the aerodynamic loads to assess the structural integrity of the plate based on the fibre orientation. In the circumstance, flight conditions and the propulsion engines cause some vibrations on the aircraft structure during its cruising [137]. At some point, the aircraft vibration has raised concern to the breaking or cracking of the fuel cell that would trigger any possible internal leakage. An exposed wing could experience the same consequence during the flight condition. To continue this investigation, a novel computational scheme is proposed in this chapter.

5.1 Proposed research flow

The numerical results by [35] and the flutter results presented in Chapter 4 have brought new observations in the aeroelastic field, but somehow the computational results should be rectified since the crack on the unidirectional composite was considered as a static crack. Hence, both works did not attempt to evaluate the possibility of crack propagations when the structure interacts with the aerodynamic loads. This assumption could be fit only if the material strength is higher than the imposed loads on the structure. In general understanding, with the increment of speed, the aerodynamic loads will also increase.

The computational fracture modelling under aerodynamic loads is proposed in this section as displayed in Figure 5.1. The flowchart explains the research flow for modelling the fracture/ crack under aerodynamic loads, where the gust is estimated through the aero-static analysis to compute the aerodynamic load distribution on the present composite plate.

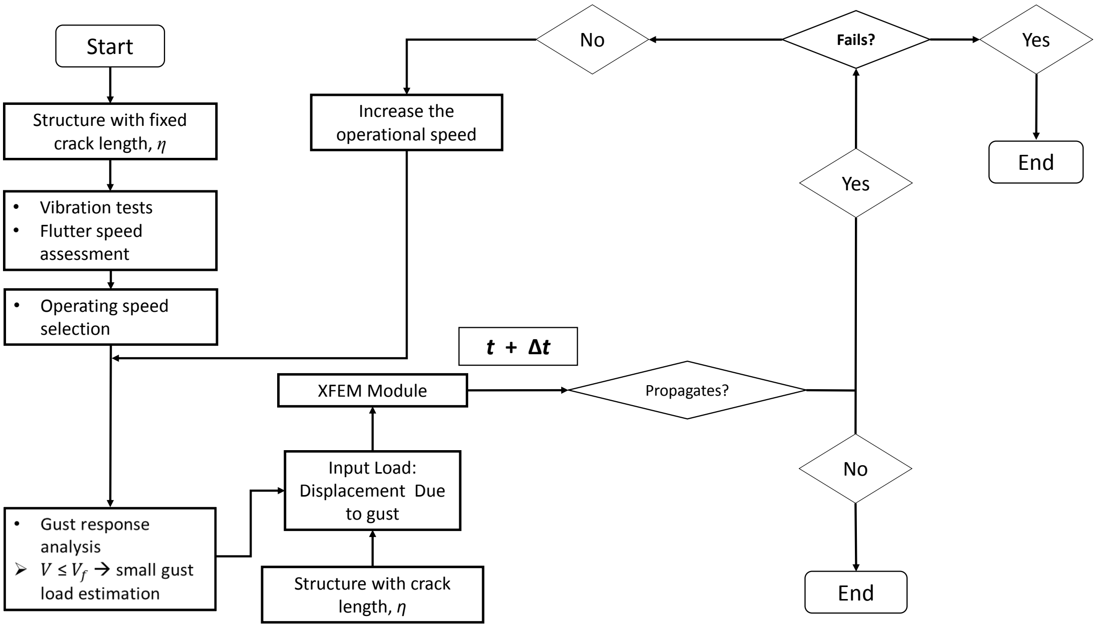

Figure 5.1: Research diagram for the present work

In this section, the structural model and the aerodynamic model of the wing are validated through the flutter analysis. The *pk* - method is applied to estimate the flutter speed based on both structural model and aerodynamic model, and the flutter computational result is compared with the experimental result. From here, the structural and aerodynamic models both are verified when the flutter result is in a good agreement. In that sense, the same structural and aerodynamic model of the wing can be used for analysing the gust response.

As the gust is estimated through the aero-static load at cruise speed condition, the gust distribution is assumed from the '1-cosine' discrete gust approximation. The wing displacements varying with time due to the gust load are intercorrelated by using Fourier Series Function to represent a periodic motion of vibration. Through this approach, the periodic motion is assigned to the cracked composite plate, and the fracture modelling method of XFEM is activated to demonstrate the crack propagation. Hence, the same approach of modelling the crack propagations presented in Chapter 3 is applied in this chapter. Since the evolution used in this approach is based on the energy release rate, it is aware that there crack might not propagate if the loads applied to the structure are not enough to make it fails; hence the structure will be safe.

Prior to this objective, several damaged planforms or surfaces could experience severe destruction after interacted with any dynamic loading. In that sense, it is unusual to maintain the original form for a cracked composite structure analysed in this study. In the event of this matter, an extended investigation is significantly applied for any cracked structure to observe the propagations possibility. In this chapter, the cracked unidirectional composite plates failure subjected to the aerodynamic loads has been investigated. The designed flight manoeuver envelopes (TAS- True Airspeed and EAS- Equivalent Airspeed) for each case are constructed based on regulatory guidance provided by FAR 23 [14] prior to the flutter assessment results in Chapter 4.

5.1.1 FAR 23 Regulations

FAR 23 [14] has provided several guidelines in determining the flight condition considering the airworthiness. In this section, the regulations are used to monitor the operational speed that should be applied to the composite plate.

The dive speed to cruise and flutter to dive relations are written in Equation 5.1 and Equation 5.2.

$$V_{Dive} = 1.25 V_{Cruise} \tag{5.1}$$

$$V_{Flutter} = 1.20 V_{Dive} \tag{5.2}$$

5.2 Computational gust loads

Figure 5.2 which is illustrated by Wright and Cooper [56] shows the representation of an aircraft when it encounters a 1-cosine gust. Equation 5.3 expressed the gust speed, w_g, in terms of '1-cosine' function of the distance, x_g. The gust length and maximum gust speed are denoted by L_g and w_{g0}, respectively.

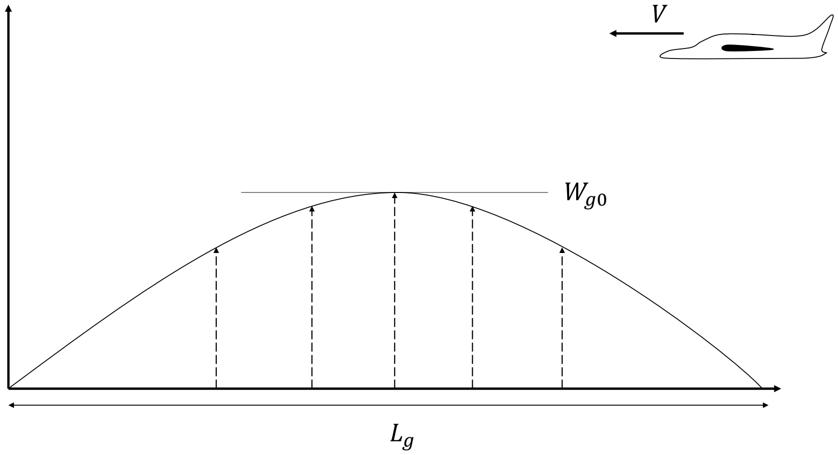

Figure 5.2: Gust load diagram encountered by an aircraft [56]

$$w_g(x_g) = \frac{w_{g0}}{2}(1 - cos\frac{2\pi x_g}{L_g}), 0 \leq x_g \leq L_g \tag{5.3}$$

In this chapter, the same aerostructure coupling expressed in Equation 5.7 is utilised. In the gust load evaluation, an aerodynamic matrix which is used to compute the forces on the aerodynamic elements (boxes) due to an applied downwash at any other element is needed. The aerodynamic distributions on a lifting surface divided into k × j elements, $\boldsymbol{Q}_{kj}$, can be computed by the multiplication of Kernel function, $\boldsymbol{S}_{kj}$ and aerodynamic coefficient, $\boldsymbol{A}_{jj}$ as shown in Equation 5.4.

$$\boldsymbol{Q}_{kj} = \boldsymbol{S}_{kj}\boldsymbol{A}_{jj} \tag{5.4}$$

For instance, Equation 5.4 can be transformed into the modal coordinates using Equation 5.5.

$$\boldsymbol{Q_{ij}} = \Phi_{ai}^T \boldsymbol{G}_{ak}\boldsymbol{Q}_{kj} \tag{5.5}$$

5.2.1 Computational of aerodynamic loads subjected to gust loads

In the present analysis, the total lift acting on the plate is summed as in Equation 5.6, where $L(V_\infty)$ is the lift due to the aerodynamic distributions and $\Delta L(V_g, t)$ is the lift generated by the gust load. The aerodynamic load, $L(V_\infty)$, is transferred into the left side, and form the standard flutter solution. The $\Delta L(V_g, t)$ remains at the right-hand side can also be denoted as $P(\omega)$ in the frequency domain, to represents the gust load in the form of pressure.

$$L_{Total} = L(V_\infty) + \Delta L(V_g, t) \tag{5.6}$$

In the frequency domain, gust load can be modelled as the additional load from external disturbance, i.e., atmospheric turbulence. Thus, the gust response equation may be expressed similarly to Equation 4.37 with an additional gust load as shown in Equation 5.7. This new expression applied the external loads, $P(\omega)$ in the relationship to solve the dynamic response problem, where $\boldsymbol{M}_{hh}$ is the mass matrices, $\boldsymbol{B}_{hh}$ is the damping matrices, $\boldsymbol{K}_{hh}$ is the stiffness matrices, $\boldsymbol{Q}_{hh}^{I}$ is and $\boldsymbol{Q}_{hh}^{R}$ are respectively the imaginary and real parts of $\boldsymbol{Q}_{hh}(m, k)$ in the function of mass, m, and reduced frequency, k.

$$[-\boldsymbol{M}_{hh}\omega^2 + i(\boldsymbol{B}_{hh}\omega - \frac{1}{2}\rho V^2 \boldsymbol{Q}_{hh}(m,k)^I) + (\boldsymbol{K}_{hh} - \frac{1}{2}\rho V^2 \boldsymbol{Q}_{hh}(m,k)^R)]u_h = P(\omega) \tag{5.7}$$

However, in this work, the gust load is considered to be compared with aerodynamic loads. Hence, it can be assumed; the structural response is dominated by the freestream. Moreover, it is relevant to observe the response for various speed, i.e., from cruise speed to near critical flutter speed. Fourier transformation is applied to convert the response in the frequency domain into the time domain.

5.2.2 Periodic motion via Fourier Series Function (FSF)

Prior to the reason mentioned in the Section 5.1, the fracture modelling mechanism has been introduced herein. There is a difficulty that should be worked out since the structure will deform in the interest of aerodynamic loads interactions. In the situation that the material properties of the structure have been identified, an important technique to model the fracture should be imposed. In this work, an advanced/ artificial numerical technique known as Extended Finite Element Method (XFEM) has been implemented to establish the fracture mechanism. XFEM has a capability in determining the crack propagation direction and path since it was developed based on the level set method as discussed in Chapter 3, Section 3.1.1.

XFEM has widely used since it was implemented with Abaqus commercial software [138]. Although XFEM within Abaqus has contributed to many research, it has certain limitations where only general static and implicit dynamic analysis in modelling the fracture can be performed [15]. For that reason, this study has revealed a novel transformation technique from the frequency response to the time-domain representation.

As XFEM used in this research is within the Abaqus commercial software, the response in the time domain of FSF can also be compared with the parameters shown in Equation 5.8. It is significant form modelling the aerodynamic load through this process, where A_0 is the initial amplitude, and n is the periodic oscillation step to compute the Fourier Series Function.

$$u = A_0 + \sum_{n=1}^{N} [A_n cos n\omega(t - t_0) + B_n sin n\omega(t - t_0)]; t \geq t_0 \tag{5.8}$$

5.3 Benchmarking and Validations

In this section, the same unidirectional composite plates that were analysed by [35] and presented in Chapter 4 are examined which is illustrated in Figure 4.6. There are two types of the composite fibre angles shown here, 0° and 135°(−45°), which are significantly having different strength due to the fibre orientation.

5.3.1 Aero-static analysis on unidirectional composite plate

In this section, undamaged specimen (without crack) was modelled and tested under static loading at the specific cruise speed. For this composite plate, the cruise speed is determined through the flutter regulation guided by FAR 23, which is 71.89 m/s (for 0° fibre direction) and 61.51 m/s (for 135° fibre direction). The plate lift distributions on the composite plate at that speed was analytically computed using lifting line theory, where the plate was divided into 10 segments. The results of the lift coefficients and the lift distributions acting on each segment are shown in Figure 5.3 and Figure 5.4, respectively.

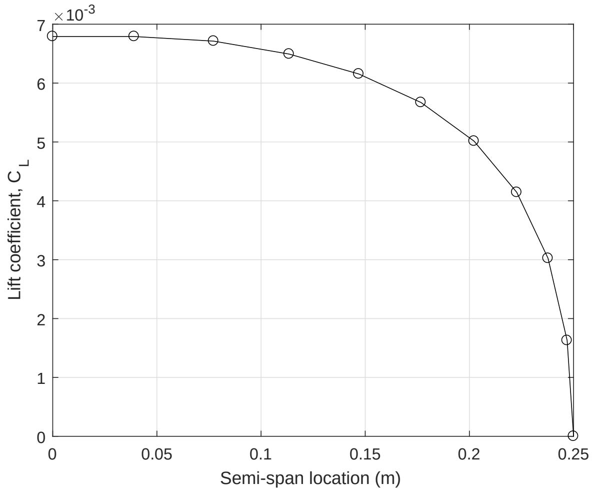

Figure 5.3: Unidirectional composite plate for 0° fibre direction: Lift coefficients for 10 segments on the plate at cruise = 71.89 m/s

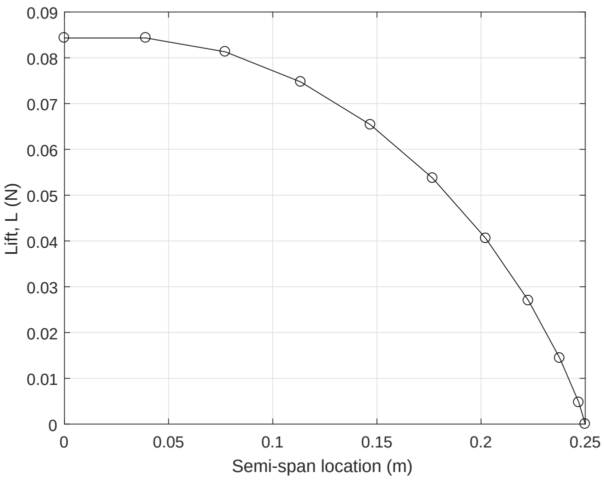

Figure 5.4: Unidirectional composite plate for 0° fibre direction: Lift distributions for 10 segments on the plate at cruise = 71.89 m/s

What can be seen in both Figure 5.3 and Figure 5.4 are the general pattern of lift distributions where the highest loads are acting at the wing root while the lowest loads at the wing tip. The lift distributions data were obtained for each segment and assigned to the composite plate for the aerostatic deformation analysis. Figure 5.5 depicts the results obtained via this approach. From here, the result is implemented as the benchmark deformations in estimating the gust loads acting on the plate, which is expected to give similar deflections on the analysed plate.

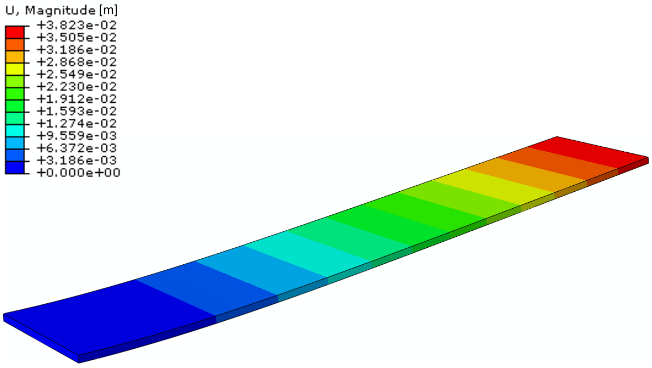

Figure 5.5: Unidirectional composite plate for 0° fibre direction: Displacement plots on cracked composite under aerostatic load cruise = 71.89 m/s

In Figure 5.5, the maximum displacement at the specific speed is found to be 38.23 mm. Hence, it is a necessity to acquire an approximate small percentage of gust implementation to compute the same level of displacement of 38.23 mm.

The same procedures were repeated for 135°(−45°) unidirectional composite plate. Figure 5.8 presents the aerostatic result of this composite plate, which is computed through the obtained lift distributions plotted in Figure 5.6 and Figure 5.7. Here, the maximum displacement plotted for this specimen is 25.72 mm, which is used to estimate the applicable gust in the next section.

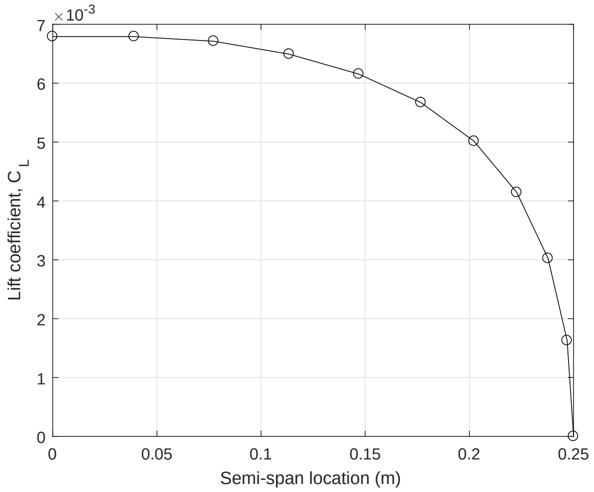

Figure 5.6: Unidirectional composite plate for 135° fibre direction: Lift coefficients for 10 segments on the plate at cruise = 61.51 m/s

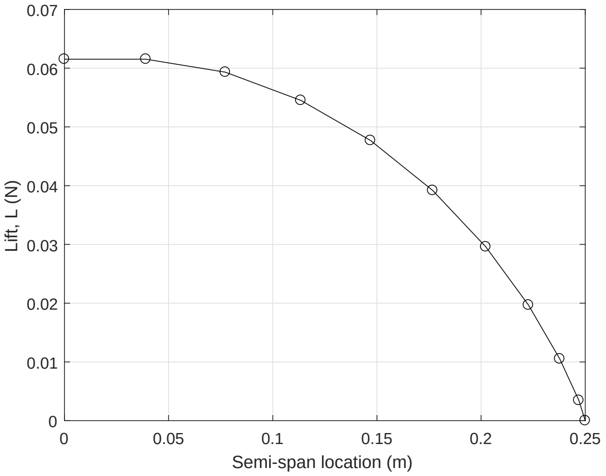

Figure 5.7: Unidirectional composite plate for 135° fibre direction: Lift distributions for 10 segments on the plate at cruise = 61.51 m/s

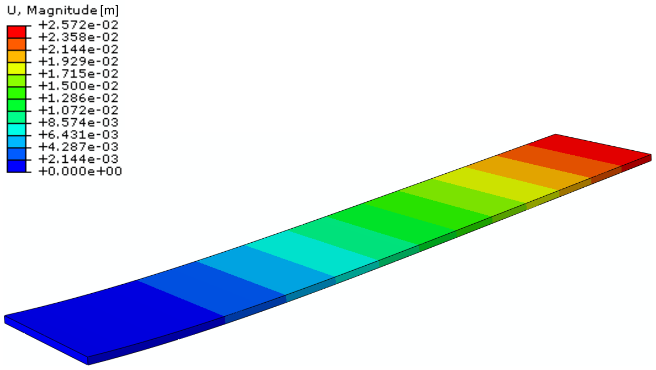

Figure 5.8: Unidirectional composite plate for 135° fibre direction: Displacement plots on cracked composite under aerostatic load cruise = 61.51 m/s

5.3.2 Numerical time domain transformation via gust load response on unidirectional composite plate for 0° fibre direction

For the unidirectional composite at 0° fibre direction, the undamaged specimen was modelled and was tested under several gust loads distribution. Figure 5.9 presents the structural displacement of the unidirectional composite plate 0° where the gust loads were estimated through the percentage of the cruise speed.

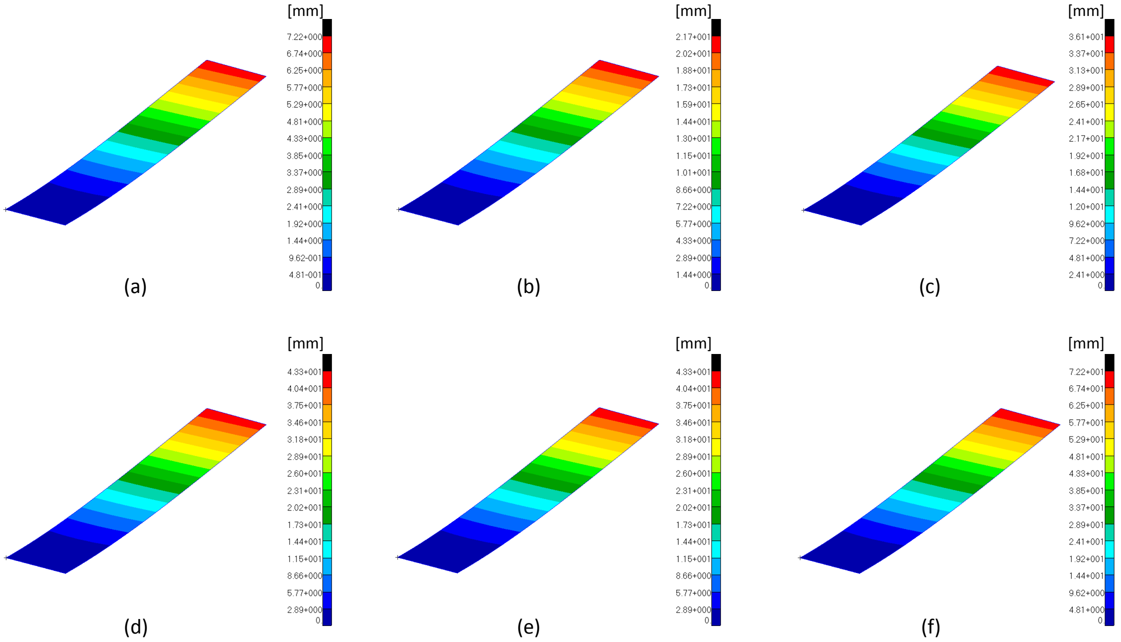

Figure 5.9: Displacement plots under gust on unidirectional cracked composite plate 0° at 71.89 m/s where (a) Gust = 0.1 % of V_c, (b) Gust = 0.3 % of V_c, (c) Gust = 0.5 % of V_c, (d) Gust = 0.6 % of V_c, (e) Gust = 0.8 % of V_c, and (f) Gust = 1.0 % of V_c

Here, the gust loads have been imposed to transform the frequency domain to the time domain. According to the result, the predicted gust load; in this case, gust = 0.5 % of the cruise speed is found to provide the same level of maximum displacement with static cruise load considered at a steady aerodynamic condition in Figure 5.5. With the minimal error of 5.57 % compared for both maximum displacement in aero-static analysis and gust response at 0.5 % for unidirectional composite plate 0°, it is verified that both results are in agreement.

5.3.3 Numerical time domain transformation via gust load response on unidirectional composite plate for $135°$ $(-45°)$ fibre direction

By using the same approach, the procedures were repeated for unidirectional composite plate 135°. Figure 5.10 depicts the gust loads estimation acting on the cracked composite plate for 135° fibre direction. In this case, the estimated gust is found to be acting at 0.9 % of the cruise speed, resulting in a minimal error of 2.96 % with the result of obtained via aero-static analysis. Thus it is comparable with the deflection result illustrated in the aero-static analysis.

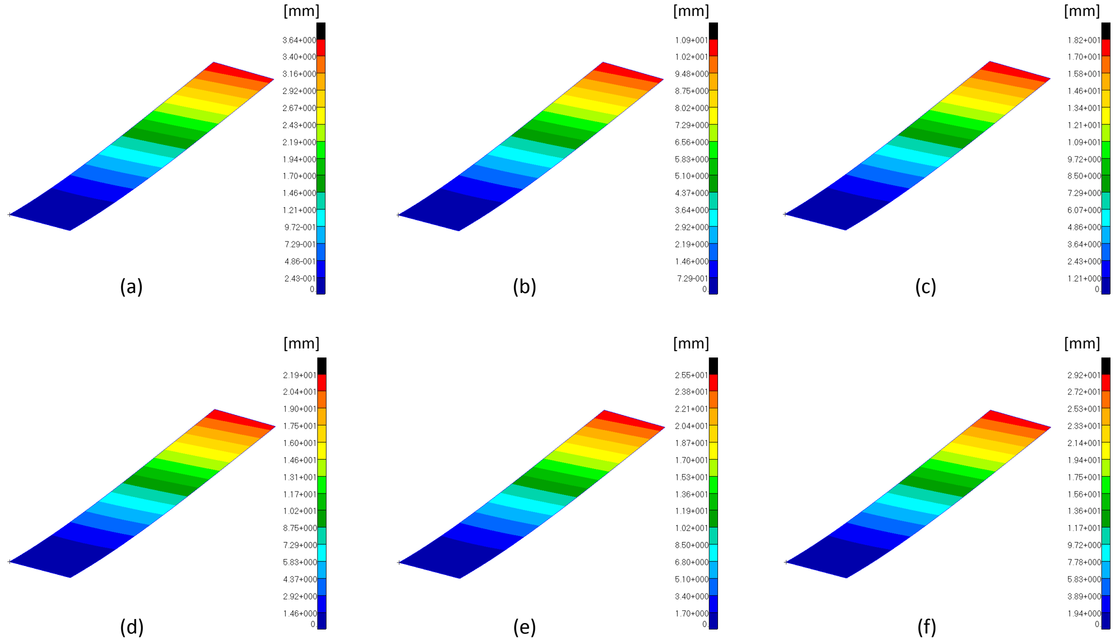

Figure 5.10: Displacement plots under gust on unidirectional cracked composite plate 135° at 61.5 m/s where (a) Gust = 0.1 % of V_c, (b) Gust = 0.3 % of V_c, (c) Gust = 0.5 % of V_c, (d) Gust = 0.6 % of V_c, (e) Gust = 0.7 % of V_c, and (f) Gust = 0.8 % of V_c

5.4 Numerical Results: Unidirectional cracked composite plate 0°

5.4.1 Deflection due to gust: 0.5% of cruise speed

Figure 5.11 presents the designed flight envelope for the cracked composite plate 0°. The flight envelope was estimated through the flutter assessment results provided in Chapter 4, Section 4.5.3, in which the flutter assessment was repeated for several altitudes evaluation. Here, the true airspeed (TAS) of cruise speed and dive speed have been computed based on the regulation guided by FAR 23 shown in Table 5.1. Important to note, in this chapter, the composite plate is applied to the gust response analysis as a proof of concept for the proposed scheme in Figure 5.1. A small disturbance is applied in term of gust thus the dominant force acting on the plate is the unsteady aerodynamic load due to freestream flow.

Table 5.1: Operational speed (TAS) for cracked composite plate 0° based on FAR 23

	Operational Flight Speed		
Altitude (ft)	Cruise Speed (m/s)	Dive Speed (m/s)	Flutter Speed (m/s)
-7943	64.12	80.15	96.18
0	71.89	89.87	107.84
10000	83.86	104.83	125.79
20000	98.75	123.44	148.13
30000	118.05	147.56	177.07

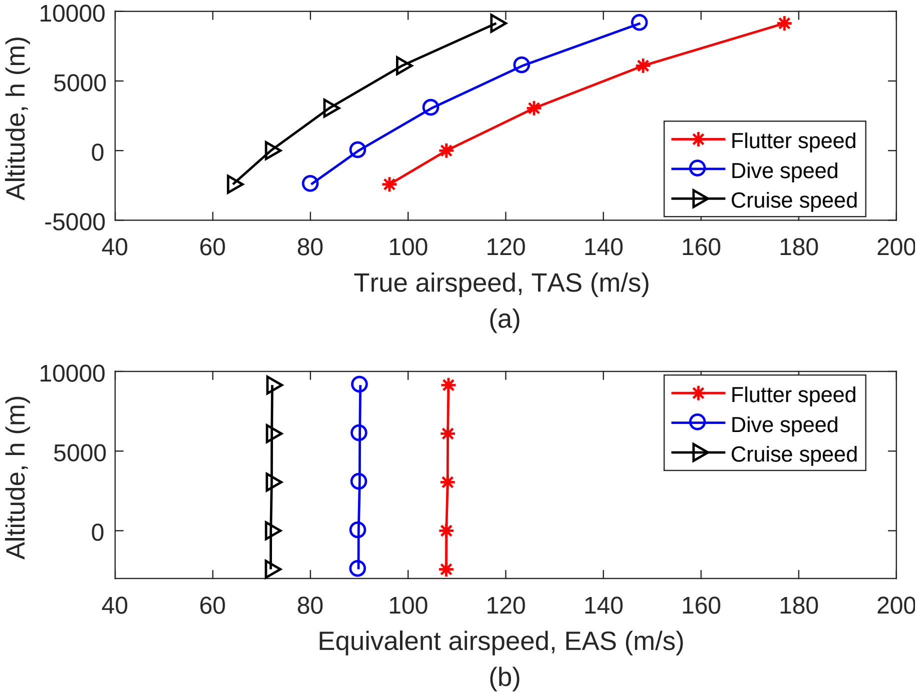

Figure 5.11: Designed flight envelope based on FAR 23 for the unidirectional cracked composite plate 0° where (a) for True airspeed (TAS) and (b) for Equivalent airspeed (EAS)

Figure 5.12 shows the displacement plots of the cracked composite plate at the designed cruise speed of 71.89 m/s. The displacements obtained through this plot are intercorrelated into a periodic motion equation via Fourier Series Transform (FSF).

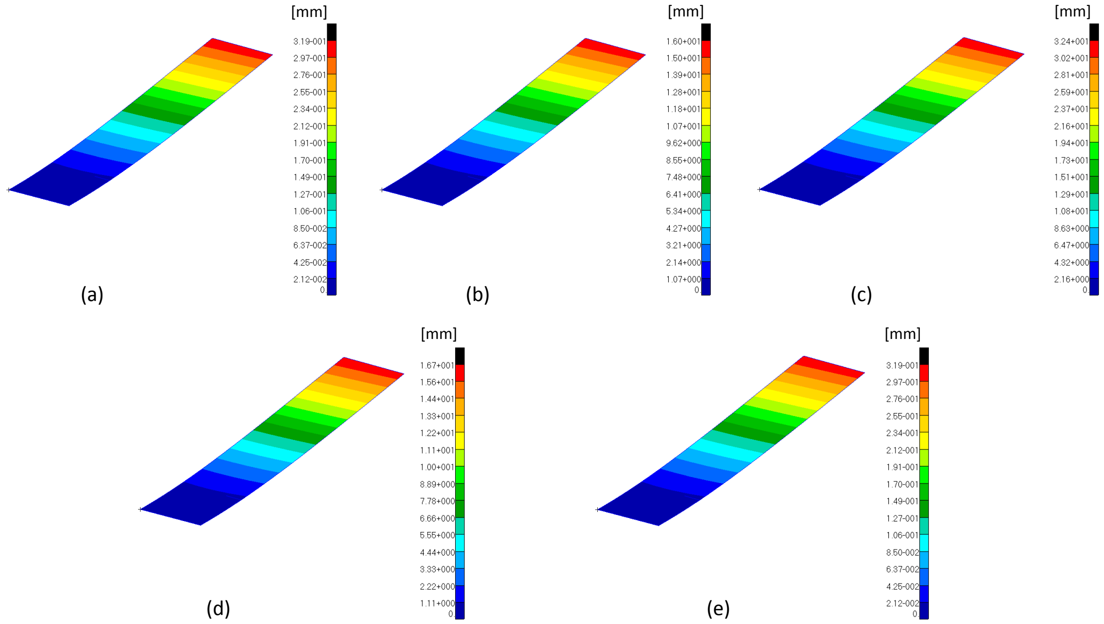

Figure 5.12: Displacement plots on cracked composite at 71.89 m/s where (a) t = 0 s, (b) t = 1.25 s, (c) t = 2.5 s, (d) t = 3.75 s, and (e) t = 5.0 s

The stress tensors for this case is presented in Figure 5.13. In this figure, the stress distributions are found to be concentrated at the crack tip. This observation may support the hypothesis that if the stress concentration is exceeding the maximum material principal stress, the crack might propagate. Unfortunately, this problem is never been discussed by any published research yet.

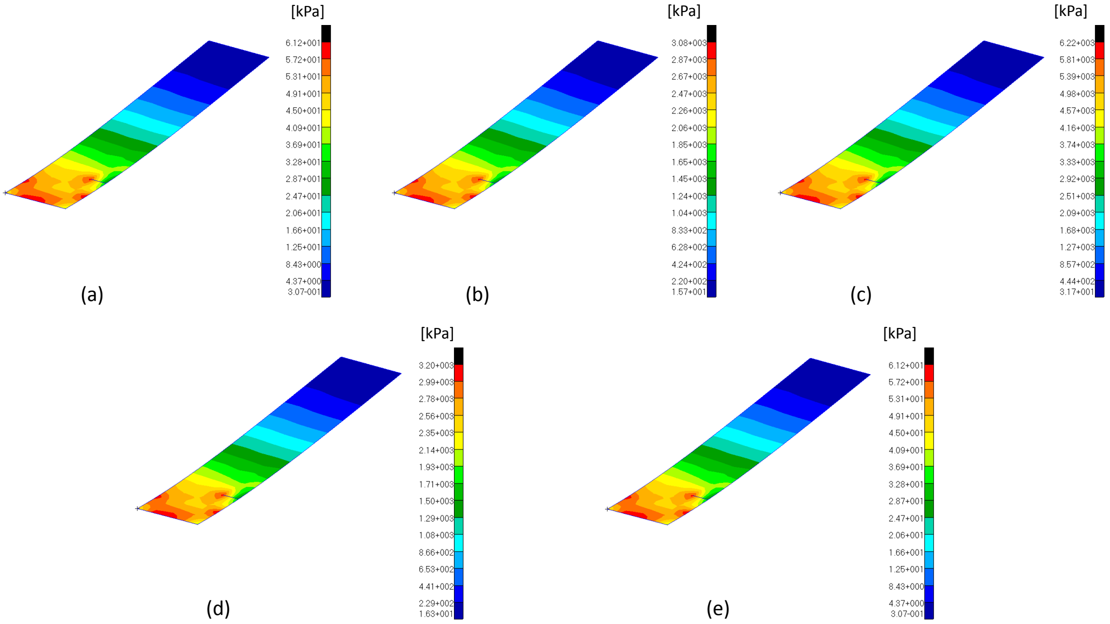

Figure 5.13: Stress tensor plots on cracked composite at 71.89 m/s where (a) t = 0 s, (b) t = 1.25 s, (c) t = 2.5 s, (d) t = 3.75 s, and (e) t = 5.0 s

The same patterns are found when evaluating the stress tensors for the cracked composite plate at 89.97 m/s and 107.84 m/s. For this reason, a fracture analysis is required to investigate this matter since the displacement of the plate subjected to the aerodynamic loads has produced higher stress than the maximum material principal stress.

5.4.2 Periodic motion via Fourier Series Function (FSF)

The periodic motion acting on the structure were computed based on the operational speeds shown in 5.11. For example, at the cruise speed of 71.89 m/s, the displacement plot in Figure 5.12 are extracted, and the maximum displacement at each time is combined to form a periodic motion via FSF presented in Figure 5.14.

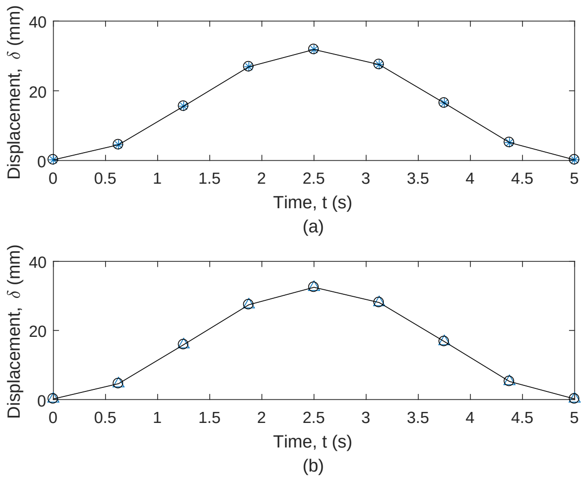

Figure 5.14: Time-domain periodic motion for 5 seconds intercorrelated via Fourier Series Function at operating speed 71.89 m/s where (a) for lower-rear node, and (b) for lower-front node

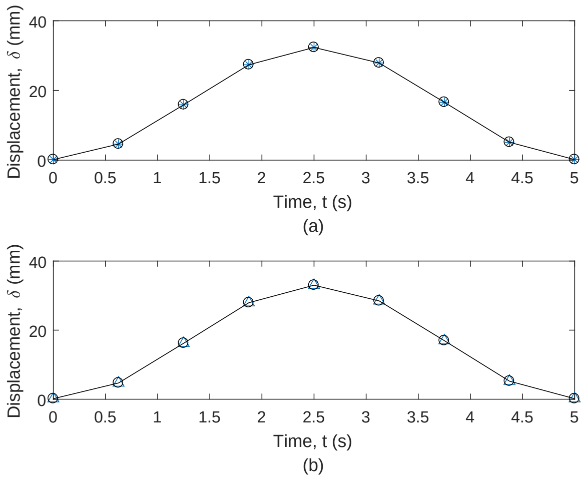

Figure 5.15: Time-domain periodic motion for 5 seconds intercorrelated via Fourier Series Function at operating speed 89.97 m/s where (a) for lower-rear node, and (b) for lower-front node

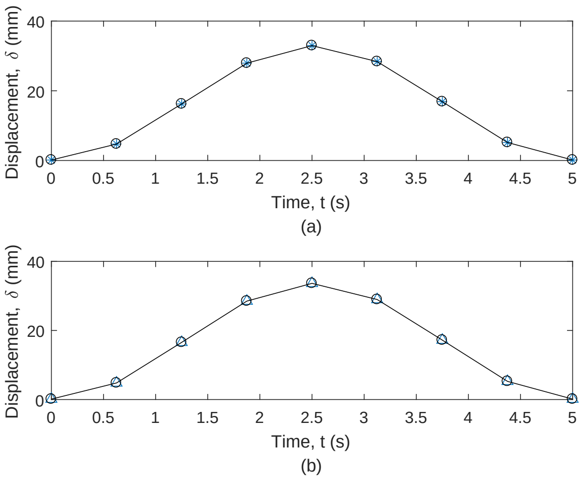

Figure 5.16: Time-domain periodic motion for 5 seconds intercorrelated via Fourier Series Function at operating speed 107.84 m/s where (a) for lower-rear node, and (b) for lower-front node

The periodic motion parameters computed via FSF computed via Equation 5.8 are summarised in Table 5.2.

Table 5.2: Periodic motion via FSF in Abaqus for 0° direction

		Periodic motion parameters			
Speed (m/s)	Node	Initial Amp.	A_1	B_1	Circular Frequency ω(rad/s)
71.89	lower-rear	16.013	-15.833	-0.429	1.2561
	lower-front	16.344	-16.158	-0.446	1.2565
89.87	lower-rear	16.247	-16.095	-0.364	1.2566
	lower-front	16.583	-16.428	-0.371	1.2566
107.84	lower-rear	16.548	-16.416	-0.317	1.2566
	lower-front	16.889	-16.755	-0.323	1.2566

5.4.3 Fracture under gust loads by means of XFEM

The damage criterions for fracture analysis of the composite structures used in this research are presented in Table 5.3, taken from [139].

Table 5.3: Damage criterion of graphite polyimide composite

Maximum principal stress, 0°	$\sigma = 4$ MPa
Maximum principal stress, 135°	$\sigma = 28$ MPa
Fracture toughness	$G_{lc} = 162\ kJ/m^2$

The crack propagations of the cracked composite plate at the cruise speed, 71.89 m/s are shown in Figure 5.17.

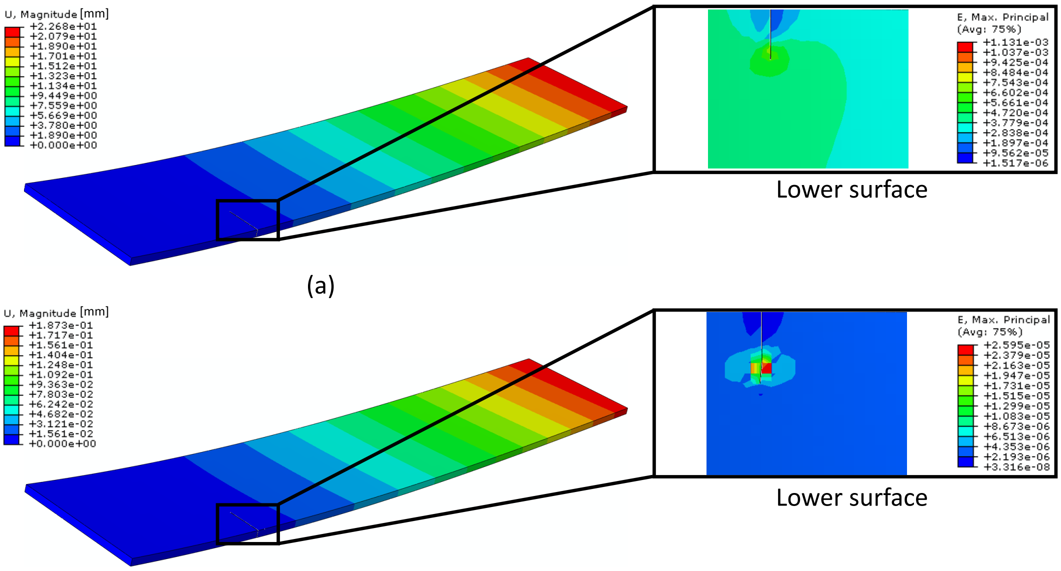

(a)

(b)

Figure 5.17: Crack modelling by means of XFEM at 71.89 m/s where (a) t = 1.59 s and (b) t = 5.0 s

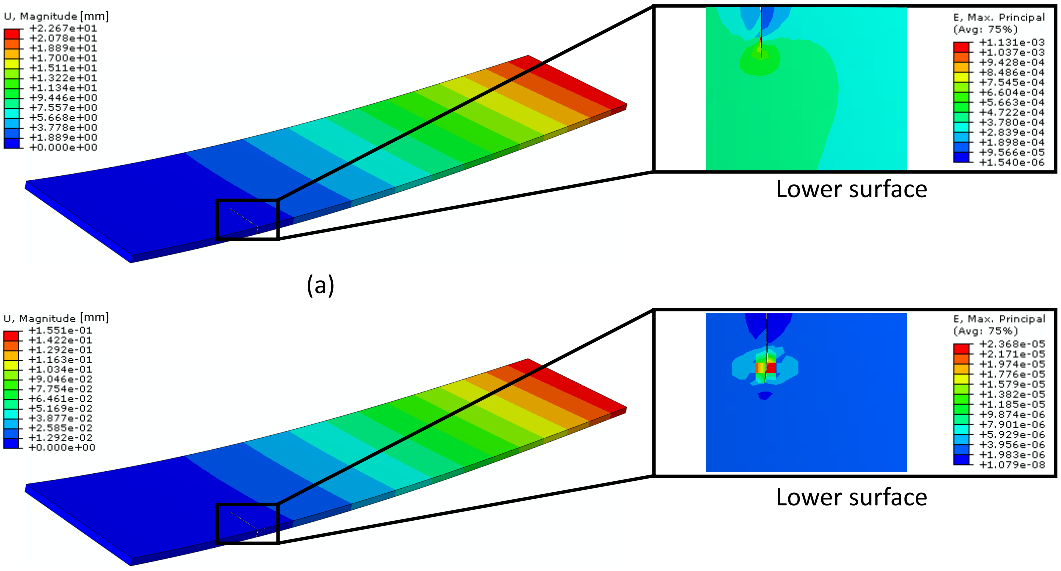

(a)

(b)

Figure 5.18: Crack modelling by means of XFEM at 89.97 m/s where (a) t = 1.57 s and (b) t = 5.0 s

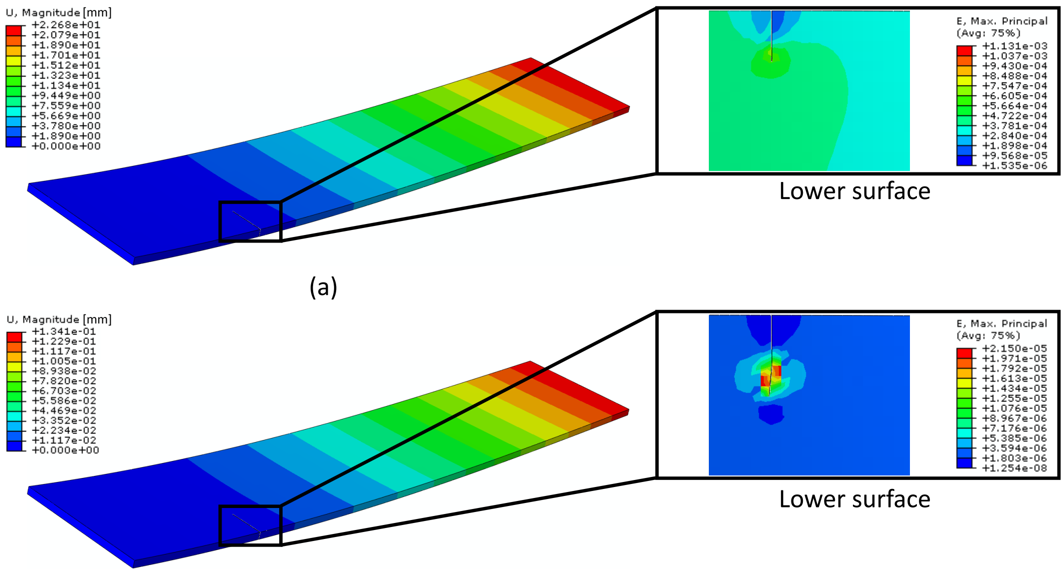

(a)

(b)

Figure 5.19: Crack modelling by means of XFEM at 107.84 m/s where (a) t = 1.55 s and (b) t = 5.0 s

The numerical errors for all cases are plotted in Figure 5.20, which are conferring the convergence of the plot.

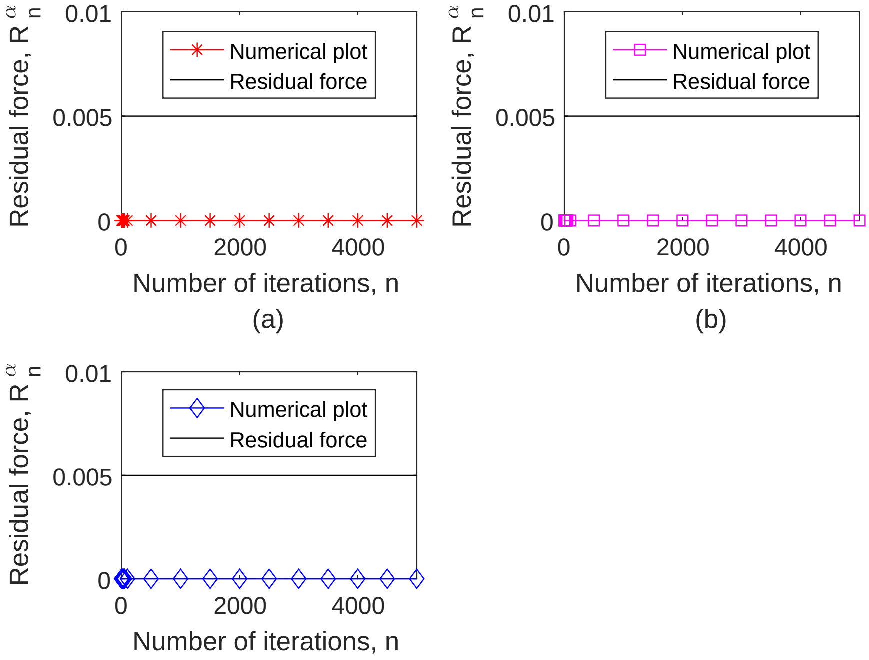

(a)

(b)

(c)

Figure 5.20: Numerical iterations plot of convergence for unidirectional composite plate plate 0° where (a) at 71.89 m/s, (b) at 89.97 m/s, and (c) at 107.84 m/s

In this part, the fracture/ crack modelling has been performed using XFEM, where the damage is expected to evolve through the assignment of the material damage evolution. Based on the results in Figure 5.17, the crack has slightly propagated due to the aerodynamic forces developed at 71.89 m/s. However, the structure has undergone a bending mode, where the lower surface has stretched due to the tension forces, while the upper surface in compression. From the results, the crack propagation has stopped at 5.0 seconds.

At the end of the analysis, the crack at the lower surface found did not propagate until it reached the other plate, which could make the plate to be cut off into two pieces. This finding was unexpected and suggests that the compression on the upper surface did not trigger any crack on the surface. Hence, it could conceivably be hypothesised the possible reason that cracks at the lower surface will stop before it reaches the half of the structure in chordwise direction.

The same modelled plate has also been tested for the higher speeds analysis, in this case, dive speed at 89.97 m/s and flutter speed at 107.84 m/s that were obtained from the flight envelope diagram in Figure 5.11. With the increment of speed, the aerodynamic forces also increase. In this case, the load increment has increased the structural deformation. As can be seen in Figures 5.17(a), 5.18(a), and 5.19(a), the crack at the lower surface has propagated slightly faster when operating at higher speed.

One of the issues that emerge from these findings is which failure comes first when the damaged structure interacts with the aerodynamic loads. These findings raise intriguing curiosity regarding the nature and extent of flutter damage or fracture damage on cracked composite plate. Although the plate seems not propagated until it splits into two parts, it will be a serious matter in the case of load incrementations.

5.5 Numerical Results: Unidirectional cracked composite plate 135° (-45°)

5.5.1 Deflection due to gust: 0.7% of cruise speed

The same procedures were repeated in determining the flight envelope based on the regulation guided by FAR 23 for the cracked composite plate 135°. The true airspeed results for the corresponding structure is shown in Table 5.4. The flight envelope for the cracked composite plate 135° is presented in Figure 5.21.

Table 5.4: Operational speed (TAS) for cracked composite plate 135° based on FAR 23

Altitude (ft)	Operational Flight Speed		
	Cruise Speed (m/s)	Dive Speed (m/s)	Flutter Speed (m/s)
-7943	54.79	68.49	82.19
0	61.51	76.89	92.27
10000	71.71	89.63	107.56
20000	84.56	105.70	126.84
30000	101.13	126.41	151.69

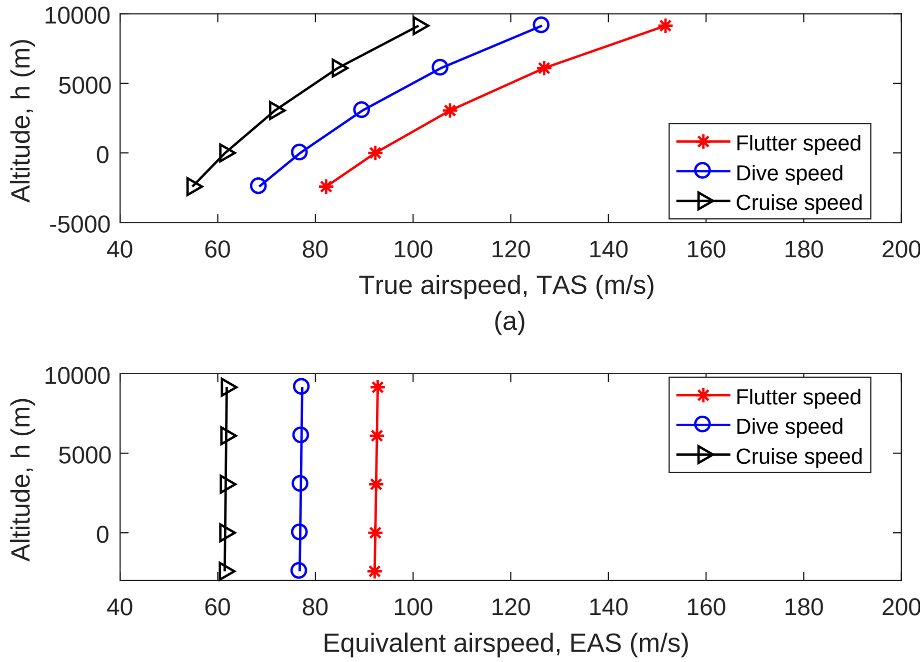

(a)

(b)

Figure 5.21: Designed flight envelope based on FAR 23 for the unidirectional cracked composite plate 135° where (a) for True airspeed (TAS) and (b) for Equivalent airspeed (EAS)

The displacement for the present cracked composite plate is shown in Figure 5.22.

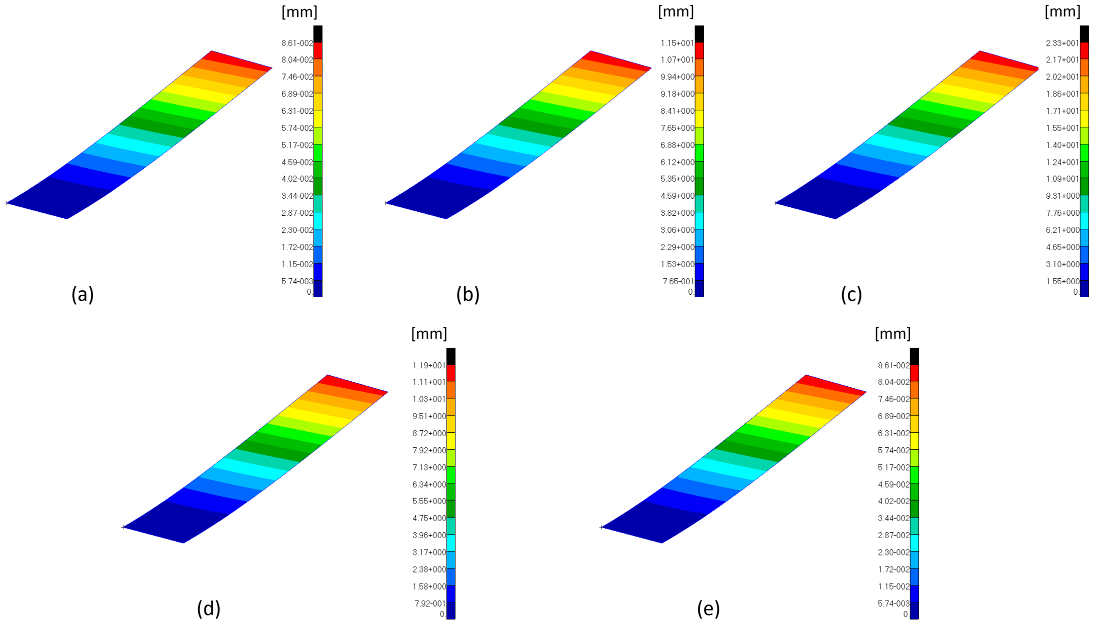

Figure 5.22: Displacement plots on cracked composite at 61.51 m/s where (a) t = 0 s, (b) t = 1.25 s, (c) t = 2.5 s, (d) t = 3.75 s, and (e) t = 5.0 s

Figure 5.23 depicts the stress tensor plot of the unidirectional cracked composite plate at 135°. The results of these plots indicate that the stress distributions are concentrated at the root, instead of at the crack tip. Contrary to expectations from the previous case of 0°, this fibre direction has eliminated the potential of crack propagations since the stress at crack tip is lower than the maximum material principal stress.

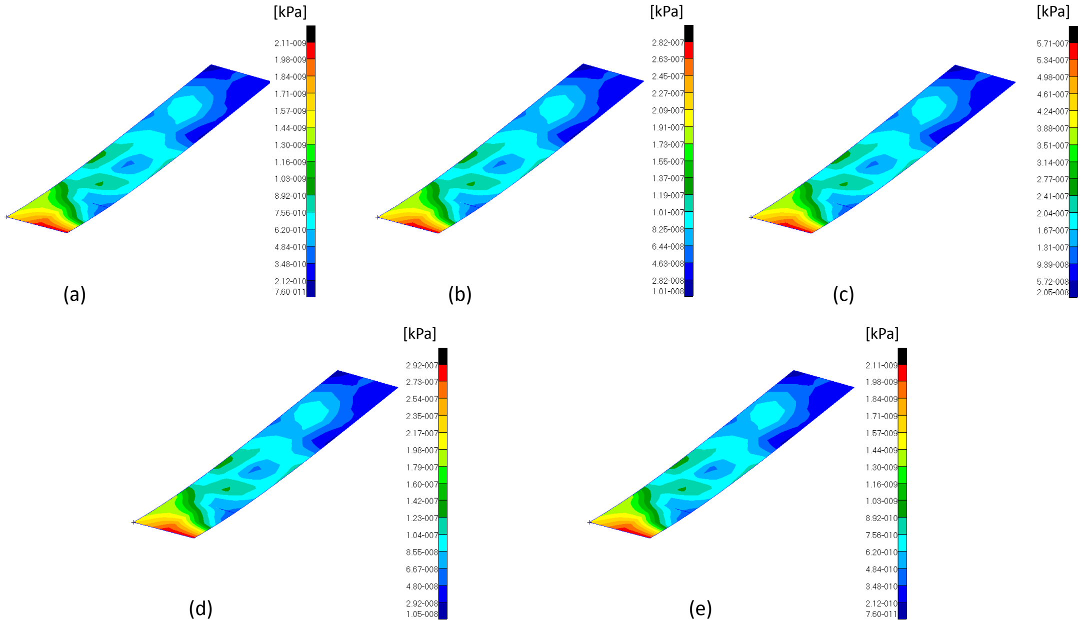

Figure 5.23: Stress tensor plots on cracked composite at 61.51 m/s where (a) t = 0 s, (b) t = 1.25 s, (c) t = 2.5 s, (d) t = 3.75 s, and (e) t = 5.0 s

The same stress concentration plots trends are identified for speeds at 76.89 m/s and at 92.27 m/s, where the stress distribution are concentrated at the root.

5.5.2 Periodic motion via Fourier Series Function (FSF)

In this part, the same procedures of predicting the discrete gust loads on the cracked composite plate of 135° have been applied for all conditions. The discrete gust loads acting on the plate are presented in Figures 5.24, 5.25 and 5.26. The periodic motion of the wing tip displacement via FSF are summarised in Table 5.5.

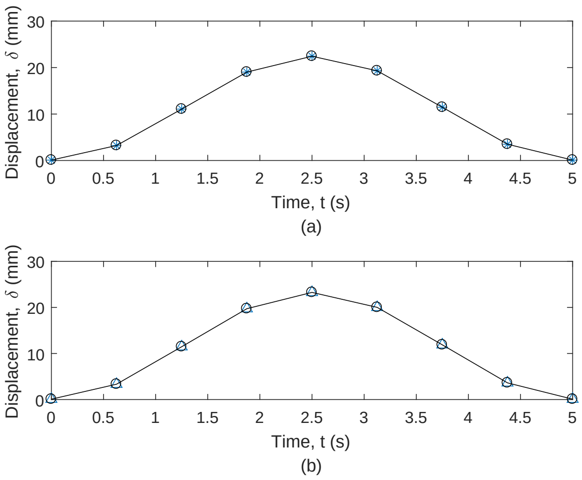

Figure 5.24: Time-domain periodic motion for 5 seconds intercorrelated via Fourier Series Function at operating speed 61.51 m/s where (a) for lower-rear node, and (b) for lower-front node

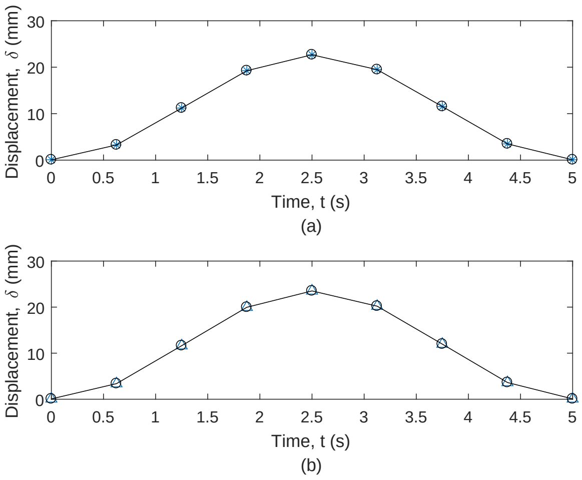

Figure 5.25: Time-domain periodic motion for 5 seconds intercorrelated via Fourier Series Function at operating speed 76.89 m/s where (a) for lower-rear node, and (b) for lower-front node

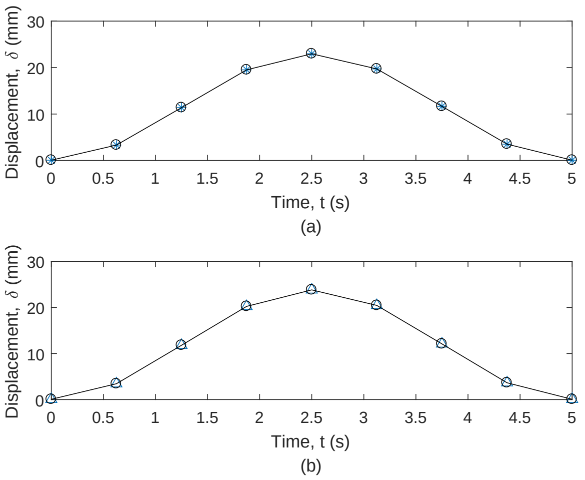

Figure 5.26: Time-domain periodic motion for 5 seconds intercorrelated via Fourier Series Function at operating speed 92.27 m/s where (a) for lower-rear node, and (b) for lower-front node

Table 5.5: Periodic motion via FSF in Abaqus for 135° direction

		Periodic motion parameters			
Speed (m/s)	Node	Initial Amp.	A_1	B_1	Circular Frequency ω(rad/s)
61.51	lower-rear	11.261	-11.177	-0.197	1.2566
	lower-front	11.678	-11.592	-0.204	1.2566
76.89	lower-rear	11.372	-11.302	-0.163	1.2566
	lower-front	11.794	-11.722	-0.169	1.2566
92.27	lower-rear	11.513	-11.451	-0.140	1.2566
	lower-front	11.939	-11.877	-0.145	1.2566

5.5.3 Fracture under gust loads by means of XFEM

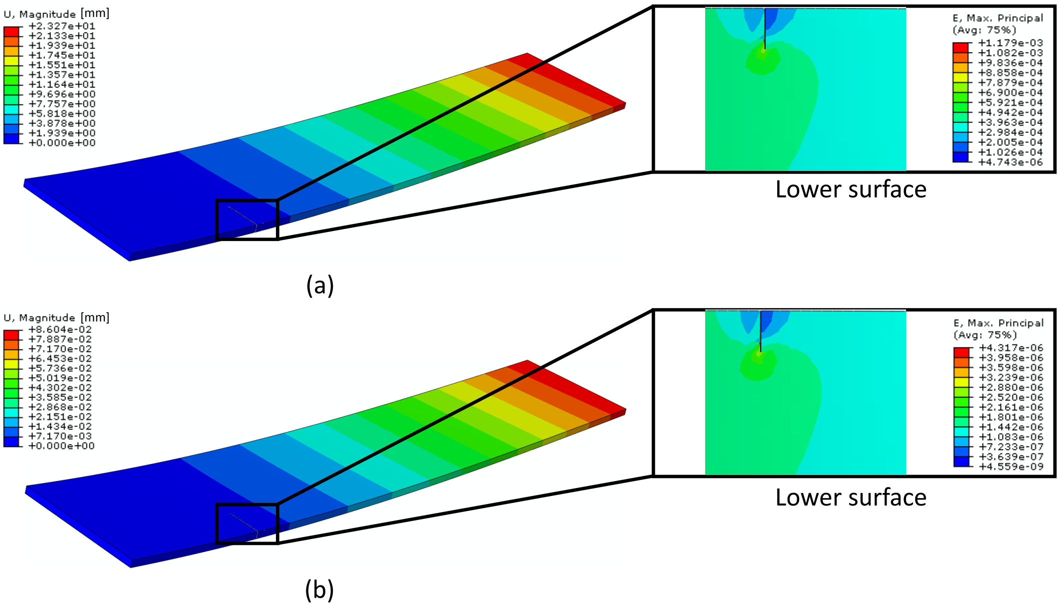

Figure 5.27: Crack modelling by means of XFEM at 61.51 m/s where (a) t = 2.5 s and (b) t = 5.0 s

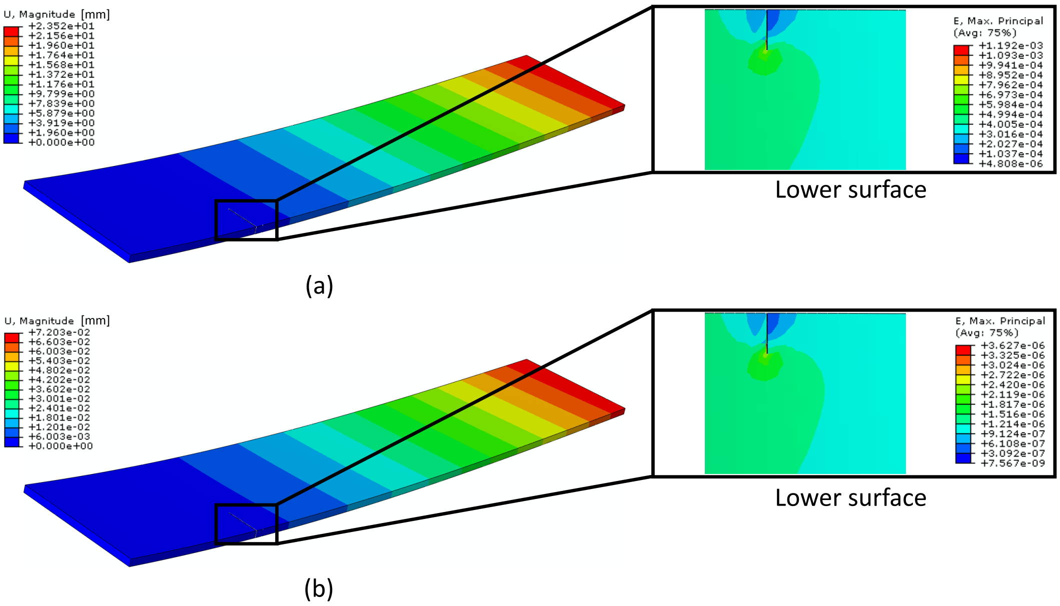

Figure 5.28: Crack modelling by means of XFEM at 76.89 m/s where (a) t = 2.5 s and (b) t = 5.0 s

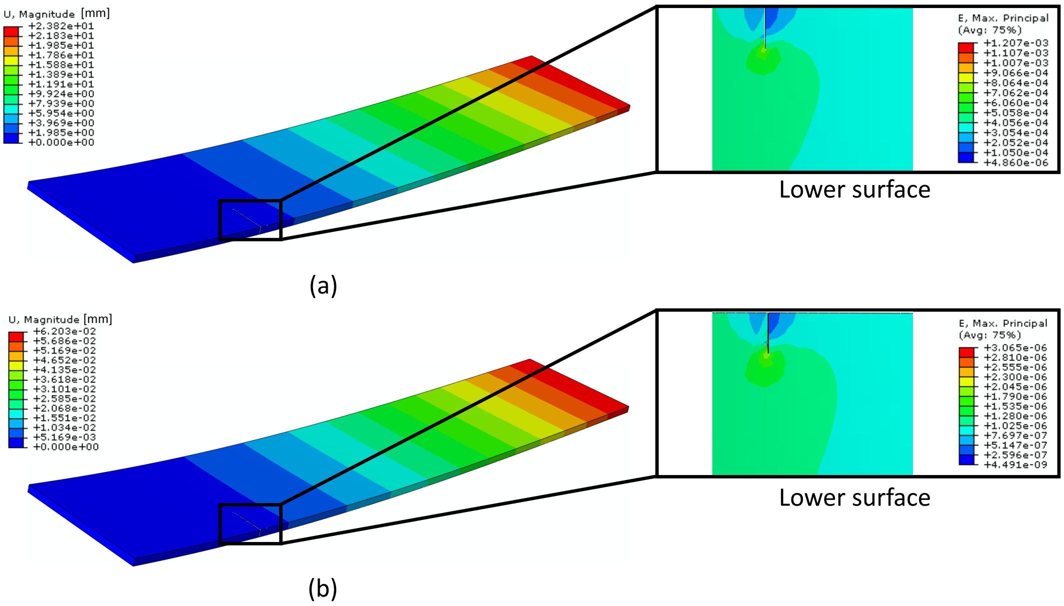

Figure 5.29: Crack modelling by means of XFEM at 92.27 m/s where (a) t = 2.5 s and (b) t = 5.0 s

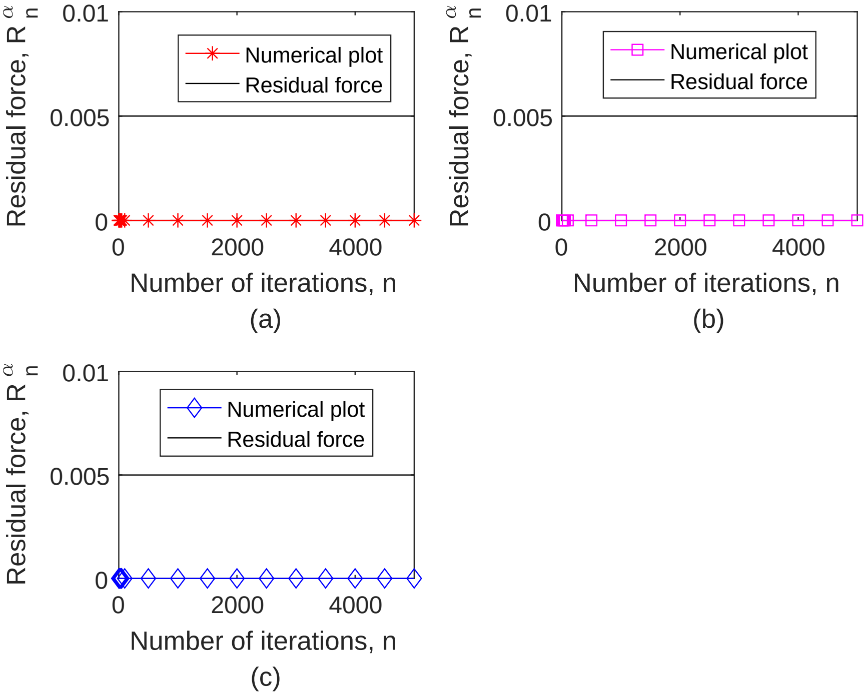

Figure 5.30: Numerical iterations plot of convergence for unidirectional composite plate plate 135° where (a) at 61.51 m/s, (b) at 76.89 m/s, and (c) at 92.27 m/s

These results may be explained by the fact that the maximum material stress for this specimen is higher than the stress developed due to the aerodynamic load. Maximum principal stress theory or normal stress theory suggests that yielding occurs at a point in a body when principle stress (maximum normal stress) in a biaxial system reaches limiting yield value of that material under simple tension test [140]. Rankine has introduced the maximum normal stress theory which ignores the possibility of yielding under shear. In that sense, Rankine's theory is only applicable to material which very strong in shear. Technically, the brittle material is strong in shear, weak in tension or compression. For that reason, this theory is preferred for brittle materials such as to analyse fracture or crack on the composite structure under tensile load. Meanwhile, maximum shear stress theory considers yielding of material occur under shear. Hence Tresca's maximum shear stress theory applied for ductile material, which weak in shear. Thus, maximum principal stress theory is used for brittle materials, which fails by brittle fracture and does not undergo yielding.

As all samples have been evaluated through several aerodynamic speed using XFEM, there is no indication that showing any crack propagation for 135° composite plate. The maximum principal stress for the 135° composite plate is 28 MPa, mentioned in Table 5.3. To have the crack initiation on the plate to propagate, the plate deflection subjected to the flying aerodynamic loads should produce a concentrated stress more than the maximum principal stress at the crack tip.

The stress distributions subjected to the aerodynamic loads are presented in Figure 5.23 for this plate. Based on the plot, the stress concentrations on the cracked plate are deficient and concentrated at the root, leaving the stress at the crack tip minimal. For that reason, no crack propagation is observed for the presented composite plate in this section.

Hence, this observation may support the hypothesis that the cracked specimen of 135° composite plate can sustain the aerodynamics load until it reached the flutter speed. It is concluded that this finding supports the results published by [35] and flutter results in Section 4.5.3 for the cracked specimen of 135° composite plate. However, the crack direction might affect the stress distributions, where it is significant to choose a correct fibre/ ply direction in designing the composite structure. For some reasons, the idea of having a laminated composite plate might assist the cracked composite plate to sustain the aerodynamic loads since the laminates consist of different fibre angle.

5.6 Summary

In this chapter, a novel iterative approach in assessing the structural integrity of cracked composite plate was presented. In this chapter, the flutter evaluation result was revised to estimate the maximum operational speed based on the guidance provided by Federal Aviation Regulations (FAR 23). The dynamics responses were plotted to explain the mode behaviour when the structure interacts with the aerodynamics load at that condition. This is the first time that aerodynamics load (assessed via FE-DLM) is coupled in XFEM to model the crack propagations of the composite plate. The proposed method was used to solve the limitation of XFEM within Abaqus that only general static and implicit dynamic analysis can be performed. Here, the structure is assumed to interact with gust load, and the deflections by the time were expressed in an equation of periodic motion based on Fourier Series Function (FSF). This research focused on determining the first failure experienced by the cracked composite plate, either the crack will propagate and fails, or the composite plate will fail due to flutter. The results show that once the damaged composite plate was deformed due to the dynamics load at dive speed, it has partially failed due to crack propagation first instead of the flutter failure for the 0° cracked composite plate. However, a contradict observation was found for the 135° composite plate where it failed due to the flutter.

Chapter 6

Structural Integrity of Wing Box Dominated by Aeroelastic Gust Loads

"When a gust of wind hits a broken bone, you feel it."
- Shia LaBeouf (American actor, performance artist, and film maker, 1986).

This chapter presents the crack propagation behaviour of wing box under gust loads. Several validation tests including vibration and flutter have been experimentally and numerically performed. The idea of this research is to simulate and to detect the critical point on the aluminum wing box when it interacts with gust loads. Here, an advanced numerical modelling technique called Extended Finite Element Method (XFEM) has been implemented to model the crack propagation. Since gust loads will deform the wing, and create stress concentration at the critical point, XFEM was used to predict the crack initiation point based on the energy release rate of the material. In this research, the crack propagations results performed via XFEM have been demonstrated in Chapter 3 and Chapter 5. For that reason, the same technique in modelling the crack propagations is applied in this chapter. The gust loads initially computed based on the requirement provided by FAR 23 since the aircraft wing is technically designed for the commuter aircraft purpose. The wing tip deflections due to the gust loads are expressed in an equation based on Fourier series periodic function.

6.1 Benchmarking and Validations

In this section, several tests been performed experimentally and computationally including vibration tests, flutter test and gust loads tests on the presented wing box commuter aircraft. Figure 6.1 depicts the wing box prototype developed under the joint program of Indonesian Aerospace, National Institute of Aeronautics and Space of Indonesia and Agency for Assessment and Application of Technology of Indonesia. The basic geometry of the presented wing is summarised in Table 6.1.

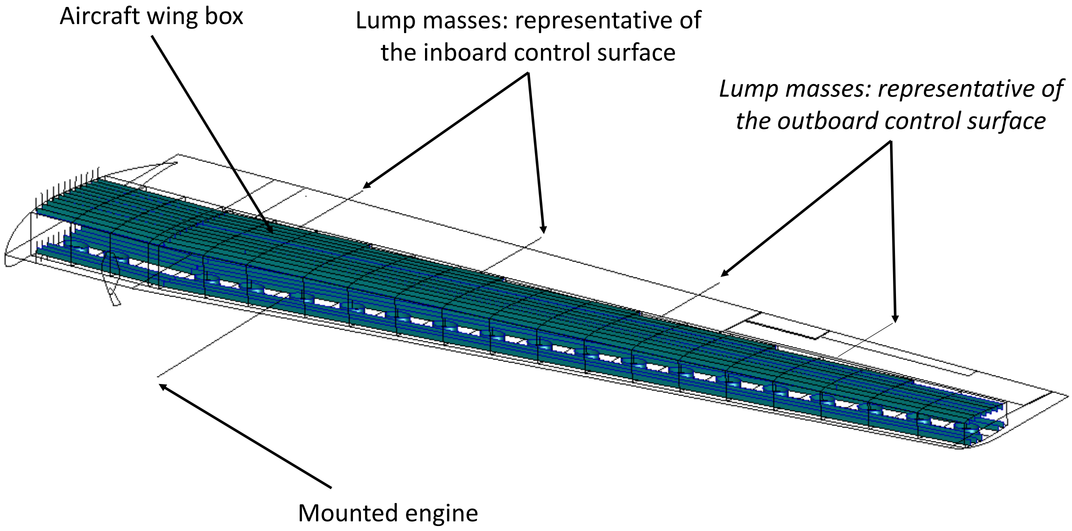

Figure 6.1: Presented aircraft wing box structure

Table 6.1: Basic geometry of the presented wing box

Wing area, S (m^2)	41.5
Aspect ratio, AR	9.16
Taper ratio, λ	0.52
Root chord, C_R (m)	2.8
Tip chord, C_T (m)	1.456
Wing span, b (m)	19.5

The wing is modelled as an Aluminum 6061-T6 wing where the material properties are shown in Table 6.2 taken from [141] and the fracture toughness of the material is presented in Table 6.3, obtained from [142].

Table 6.2: Material properties of Aluminum 6061-T6

Modulus of elasticity	$E = 68.9$ GPa
Poisson's ratio	$\nu = 0.33$
Maximum principal stress	$\sigma_{max} = 186$ MPa
Mass density	$\rho = 2710\ kg/m^3$

Table 6.3: Fracture toughness value of Aluminum 6061-T6

layer	G_{lc} (kJ/m^2)
Aluminum 6061- T6	34.2

6.1.1 Validation: wing box structural vibration test

The first test which is the vibration test made a significant finding when the results for the solid elements model is compared with another model, such that stick model and shell elements model. In this part, the same wing box model that was implemented in the vibration analysis is presented in this section. Table 6.4 presents the scaled model of the given wing box has been verified based on the ground vibration tests and validated using stick model in the modal analysis by [143]. The first vibration analysis used the wing box modelled as the shell element and the second model used the 3D solid component for the skin.

Table 6.4: Vibration test results on the commuter aircraft wing box

Vibration test results comparison - (ground level)				
Mode	Experimental (Ground vibration test)	Stick model (Beam elements)	Present work (Shell plate)	Present work (3D solid elements)
1	2.49	2.47	2.595	2.61
2	4.65	4.58	5.580	5.581
3	8.40	8.28	8.737	8.958
4	11.62	11.56	12.76	14.346
5	17.05	16.38	15.569	16.743

Technically, the stick model is presenting the simplified model of the wing by extracting the stiffness properties of the main structure as a set of beam elements extending along the structure's elastic axis [144]. In Table 6.4, the stick model represented as beam elements show the nearest value to the experimental modal analysis results since it has been analysed with smaller meshing compared to both 3D elements (shell elements and solid elements). Thus, the finite element mesh has been refined in this case of 1D stick element that has led to the accurate values when it is compared to the experimental results. In another perspective, both 3D wing models (shell elements and solid elements) also show an excellent agreement with the results by [143]. In that case, the same mesh refinement can be applied to the 3D model, but it will increase the computational time and cost due to the complexity of the wing geometry. Figure 6.2 illustrates the vibration modes modelled as the 3D solid elements.

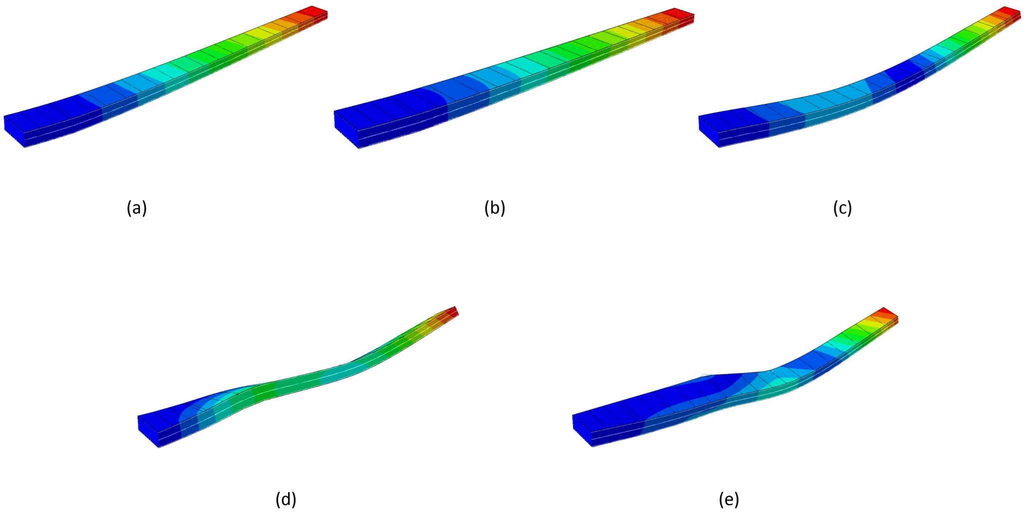

Figure 6.2: Modal vibration results on the wing box (solid element); (a) 1st mode: 2.61 Hz, (b) 2nd mode: 5.581 Hz, (c) 3rd mode: 8.958 Hz, (d) 4th mode: 14.346 Hz, and (e) 5th mode: 16.743 Hz

The same wing box (modelled as solid elements) is used in analysing the fracture behaviour through XFEM since XFEM has a limitation on shell elements model. Thus, it is not possible to investigate the significant wing box fracture modelling subjected to the gust loads because of this limitation. In that case, as the presented wing box that was remodelled as 3D solid elements shows compliance results with other vibrational tests, this model is reliable to be used in fracture analysis.

6.1.2 Validation: wing box aeroelastic flutter test

The flutter test of the presented wing box has been performed in the wind tunnel with the scale of 1:10 from the true scale at National Institute of Aeronautics and Space of Indonesia. Initially, the flutter test has been computationally validated by stick model, presented in [145]. In the present work, the same model is modelled with an enhancement of computational method by using finite element method coupled with the doublet lattice method in MSC Nastran, where the wing box is modelled as the shell element. The results comparison is shown in Table 6.5. The plots are used to determine the flutter speed as explained by Figure 4.1 in Section 4.1.

Figure 6.3 depicts the V-g plot for estimating the flutter speed of the presented wing. Based on this plot, the flutter speed found to have happened at 400 m/s, represented by Mode 4. This result shows a good match with the velocity - frequency (V-f) plot as shown in Figure 6.4 where both Mode 4 and Mode 3 have moved closer to each other.

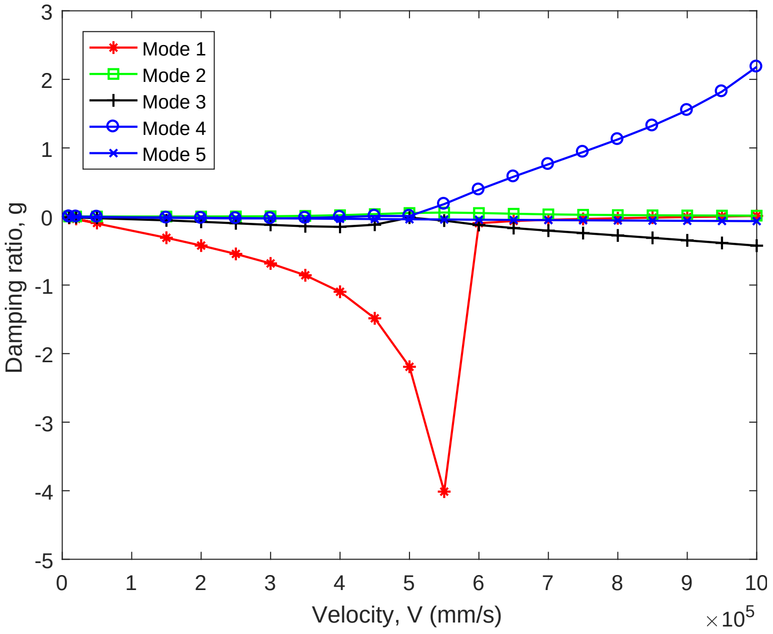

Figure 6.3: V-g plot of the commuter aircraft wing

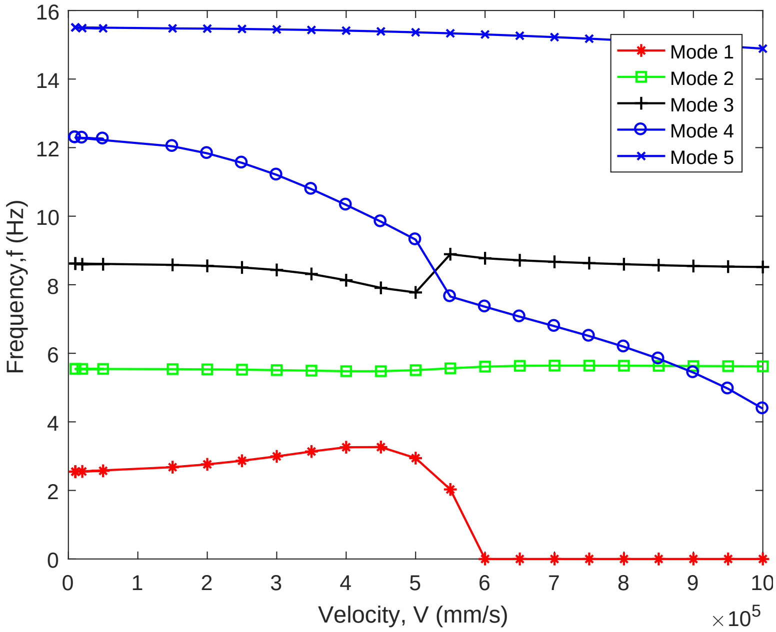

Figure 6.4: V-f plot of the commuter aircraft wing

The present wing set-up inside the wind tunnel conducted by National Institute of Aeronautics and Space of Indonesia is demonstrated in Figure 6.5.

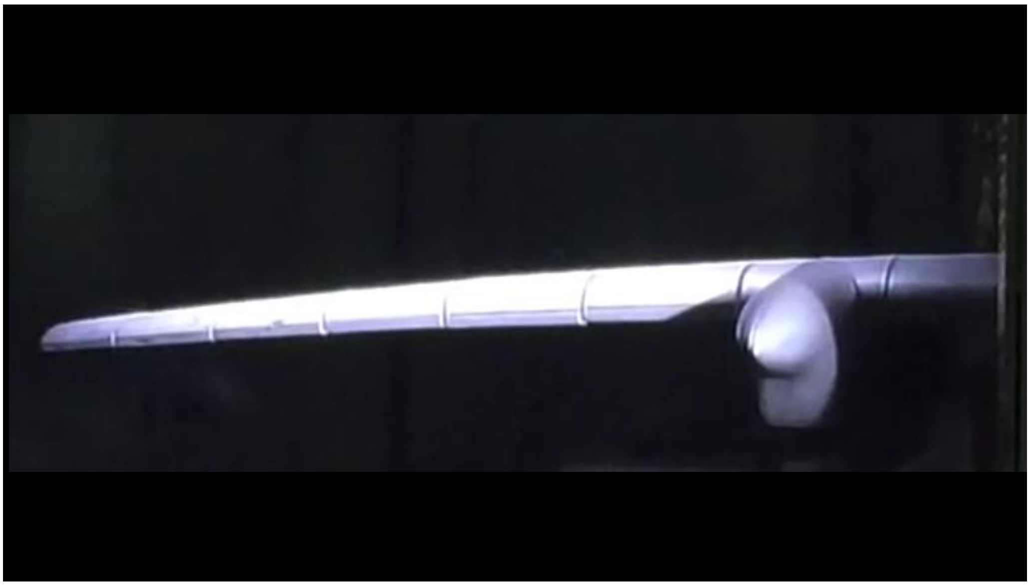

Figure 6.5: Front view: Present wing set-up in a wind tunnel as the right wing [145]

Table 6.5: Flutter test results on the commuter aircraft wing box at H = 10000 ft, M = 0.346

	Flutter results (Maximum take-off weight configuration)		
Parameter	Experimental (wind tunnel test)	Stick model (FE-Strip)	Shell plate (FE-DLM)
Vibration Mode	Torsion	Mode 4 Wing torsion	Mode 4 Wing torsion
Flutter speed	40 m/s (1:10 true scale)	767 KTAS (395 m/s)	400 m/s

As the present flutter result which is using shell elements wing box shows a good agreement with the experimental and numerical (stick model), the current model (solid elements) is acceptable with a low relative error. The numerical flutter mode is shown in Figure 6.6, where the mode is wing torsional mode.

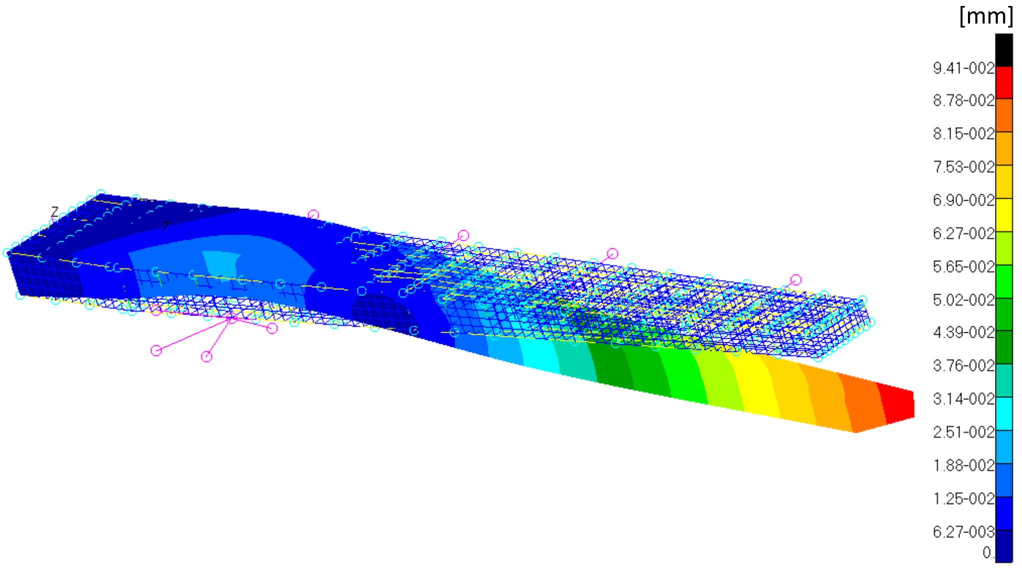

Figure 6.6: Front view: Flutter response on torsional mode modelled as the left wing at $f_F = 10.5$ Hz

6.1.3 Benchmark: wing structural deflection subjected to the gust loads

This section presents the gust loads implementation on the present wing box. As the wing box was designed for the multi-purpose commuter aircraft, the gust loads interaction is conducted based on the guideline provided by CASR Part 23 derived from FAR 23 in [146].

As the computational vibration modes are validated with the experimental in Section 6.1.1, the validations on flutter test tests also performed as presented in Section 6.1.2. Here, the wing box gust responses are computed from the FE-DLM coupling presented in Table 6.5.

The gust responses for the presented wing box are shown in Figure 6.7 where the analysed wing is operated at the breaking speed , $V_B = 140$ KEAS (83.652 m/s at 10000 ft).

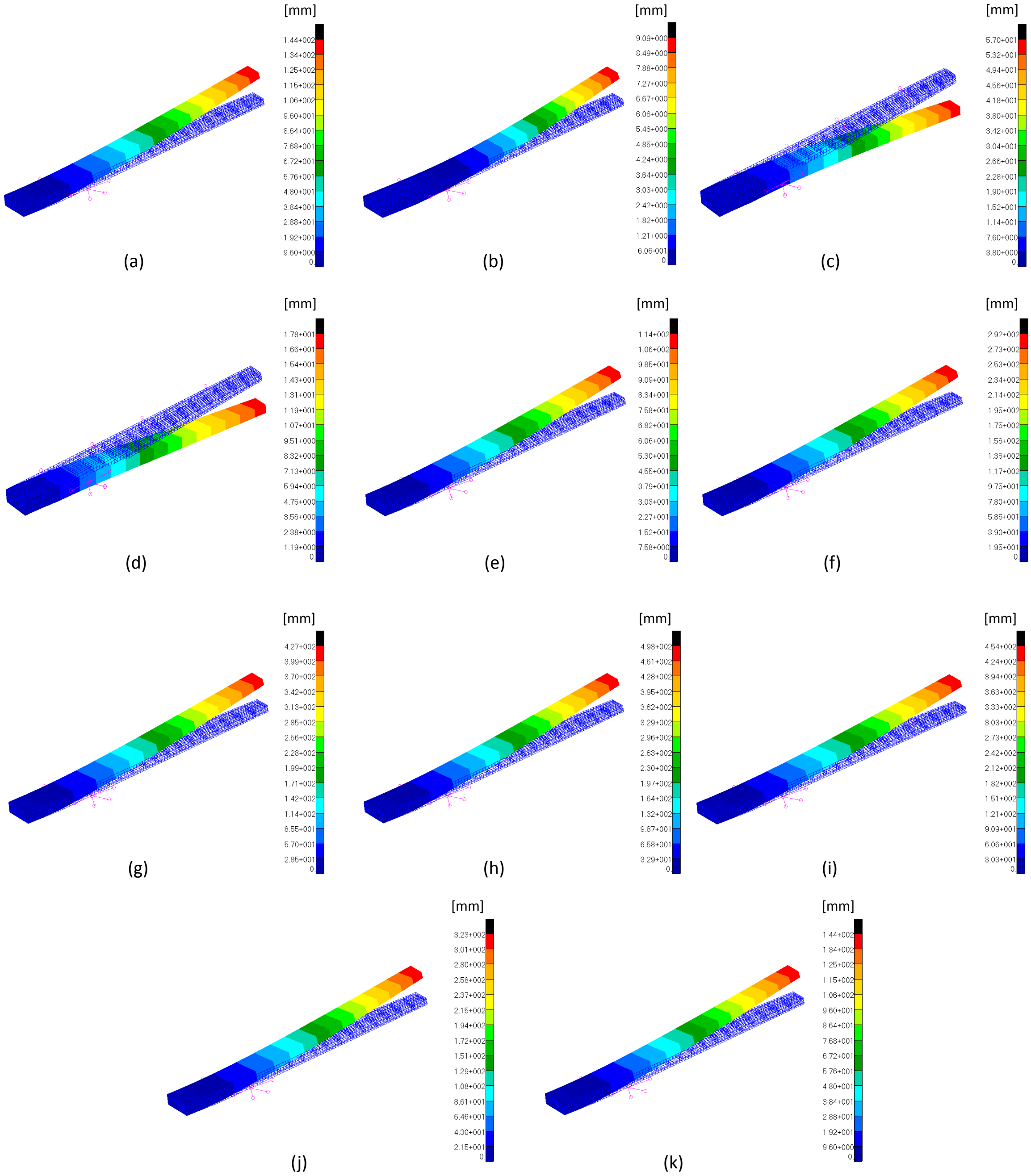

Figure 6.7: Displacement responses on the present wing box from t = 0 s to t = 0.580 s at V_B = 140 KEAS; where (a) t = 0 s, (b) t = 0.058 s, (c) t = 0.116 s, (d) t = 0.174 s, (e) t = 0.232 s, (f) t = 0.290 s, (g) t = 0.348 s, (h) t = 0.406 s, (i) t = 0.464 s, (j) t = 0.522 s, and (k) t = 0.580 s

The stress tensor plotted are shown in Figure 6.8. The plots are significant in determining the critical location where the crack is expected to happen. In general, if the stress acted upon the spot has exceeded the principal material stress, the material will fail. For that case, the relevant computational method will be imposed here to demonstrate the fracture behaviour.

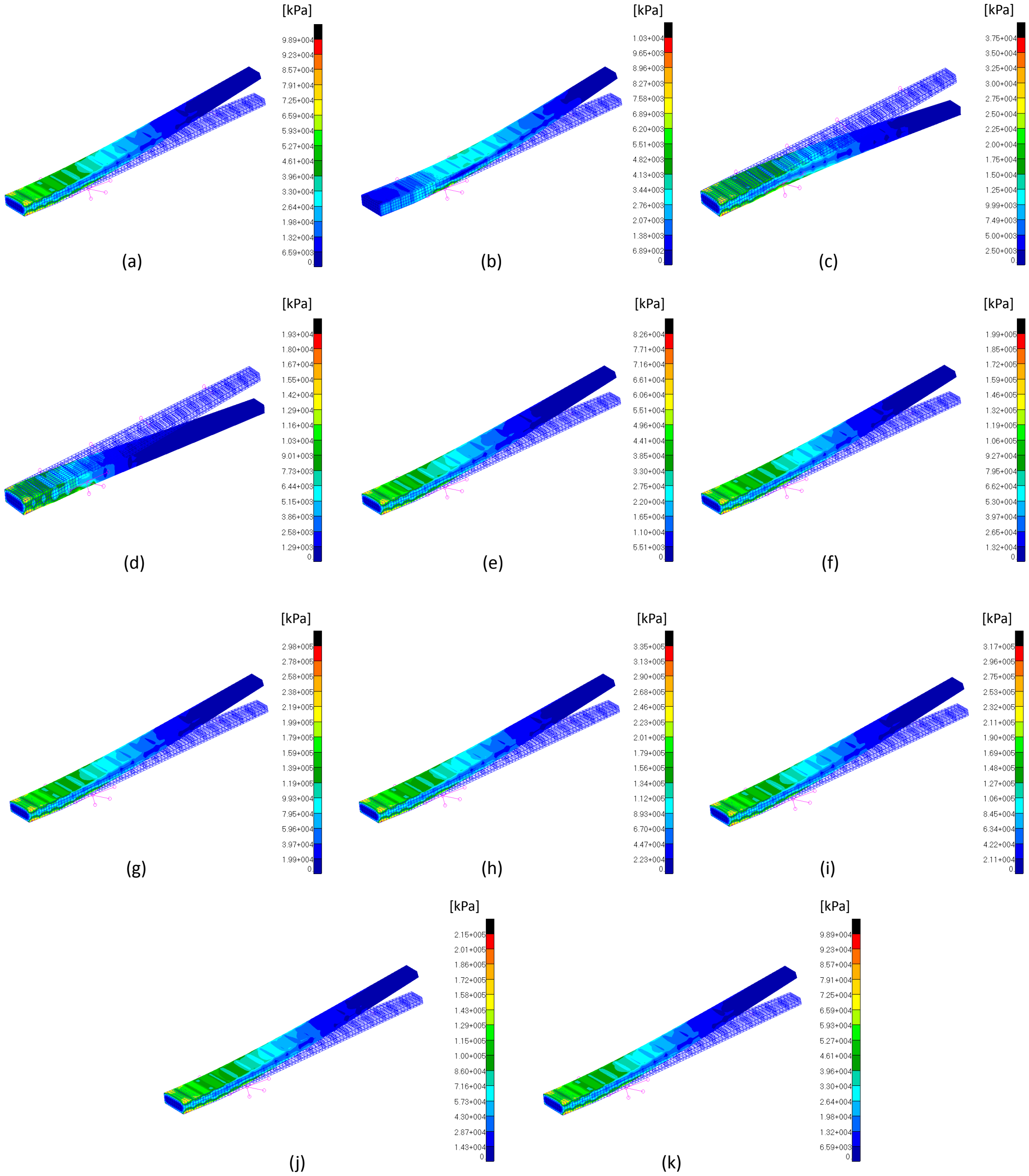

Figure 6.8: Stress tensor on the present wing box from t = 0 s to t = 0.580 s at $V_B = 140$ KEAS; where (a) t = 0 s, (b) t = 0.058 s, (c) t = 0.116 s, (d) t = 0.174 s, (e) t = 0.232 s, (f) t = 0.290 s, (g) t = 0.348 s, (h) t = 0.406 s, (i) t = 0.464 s, (j) t = 0.522 s, and (k) t = 0.580 s

In Figure 6.9, the stress tensor found to be high near to the wing root at the lower-front spar, which has exceeded the material maximum principal stress. In common sense, this area has failed when it has reached the breaking point of the stress-strain plot. In this analysis, since the wing root is fixed, similar to the condition where the wing is attached to an aircraft fuselage. The critical state at this point has triggered a curiosity in this research either there a crack propagation subjected to the gust loads will be developed in due to this situation.

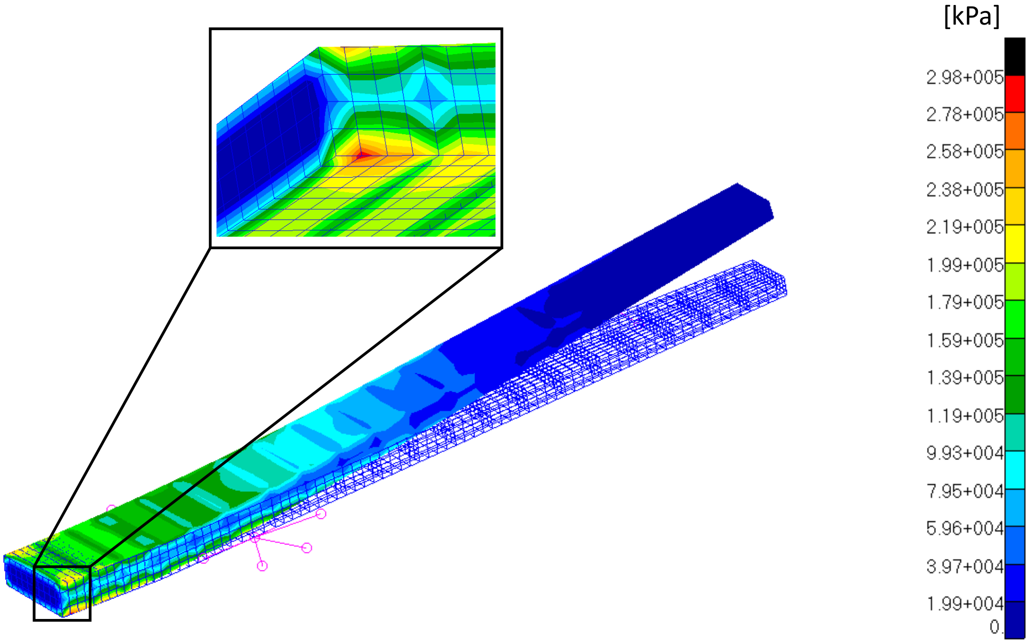

Figure 6.9: Focus view: stress tensor under gust loads for $V_B = 140$ KEAS (83.652 m/s at 10000 ft)

To figure out the failure condition, a fracture analysis should be conducted in this case. To do this, the displacement/deflection data for the present wing box are combined and expressed through an equation based on the Fourier Series Function to represent a periodic motion of vibration as in the sum of sine and cosine functions. The function expressions for this series plots are shown in Figure 6.10. The mechanism of modelling the fracture mechanism is based on the numerical modelling by means of XFEM.

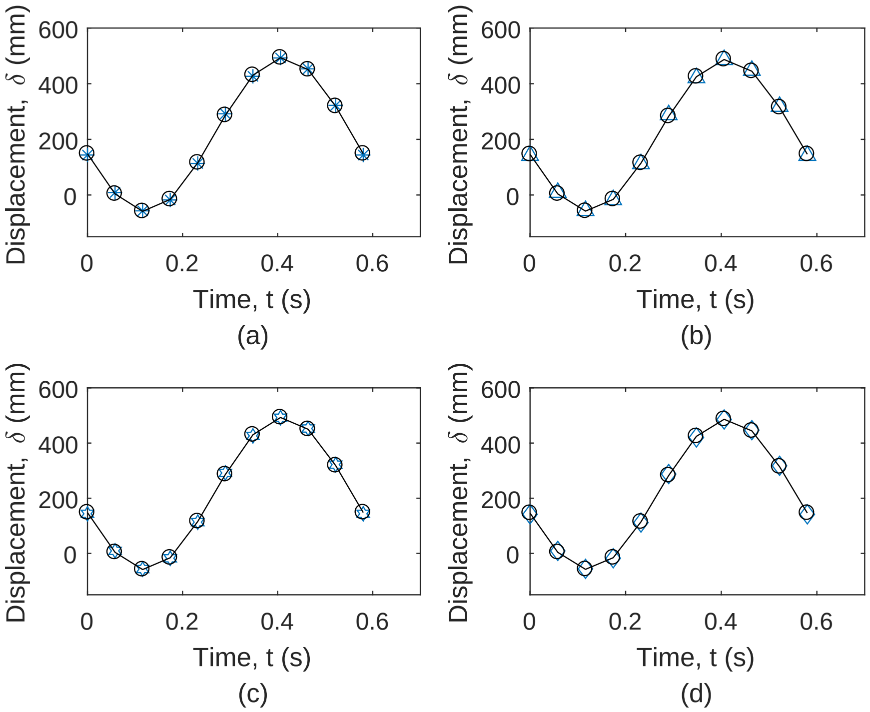

Figure 6.10: Wing tip periodic motions represent via Fourier Series Function at $V_B = 140$ KEAS (83.652 m/s at 10000 ft) where (a) for rear-lower node, (b) for front-lower node, (c) for rear-upper node, and (d) for front-upper node

6.2 Fracture Behaviour via Numerical Modelling using XFEM

In this section, the fracture mechanism on the present wing box subjected to the gust loads using XFEM is explored. Figure 6.11 demonstrates the full wing configuration under the gust loads. The plots show that the wing has deflected subjected to the computation gust loads, which has triggered a critical location under stress near to the wing root. The wing has endured several structural deformations before the crack near at the wing root appears to propagate.

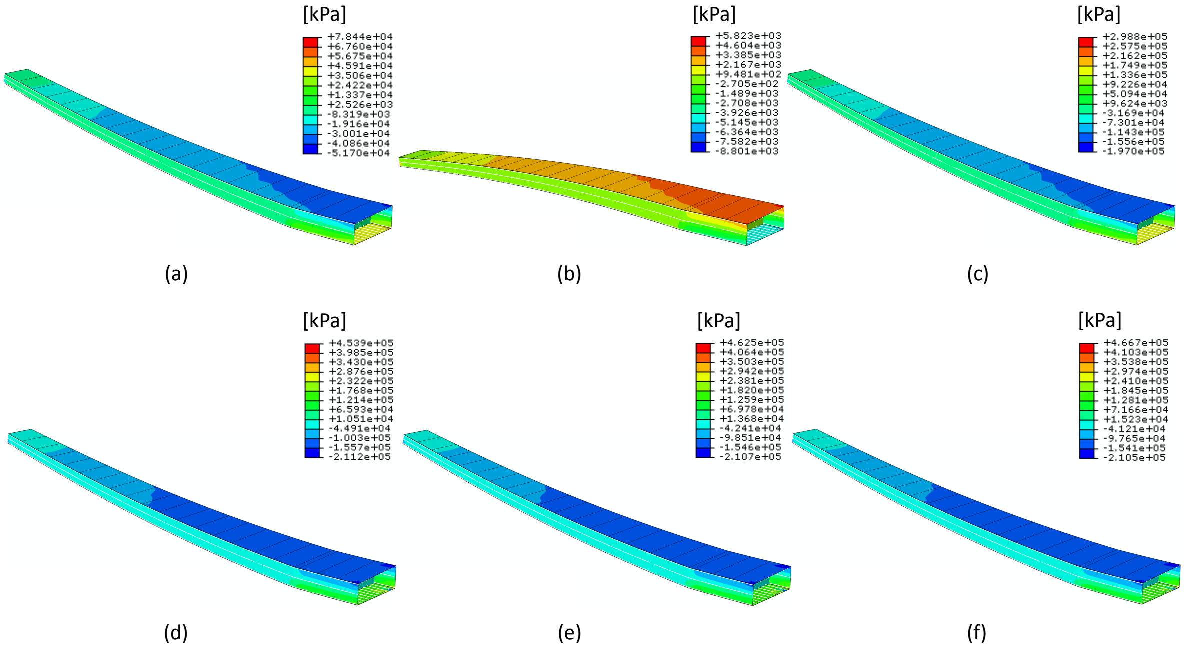

Figure 6.11: Stress plot: full wing results on fracture behaviour via XFEM where (a) t = 0.001 s, (b) t = 0.16 s, (c) t = 0.41 s, (d) t = 0.46 s, (e) t = 0.51 s, and (f) t = 0.58 s

The numerical convergence plot for this analysis is plotted in Figure 6.12. Here, the residual force gained from the computational modelling has achieved the convergence state below the benchmark line of residual force, $R_n^\alpha = 0.005$. Hence, the analysis fracture analysis using XFEM under the gust loads influence on the wing is acceptable.

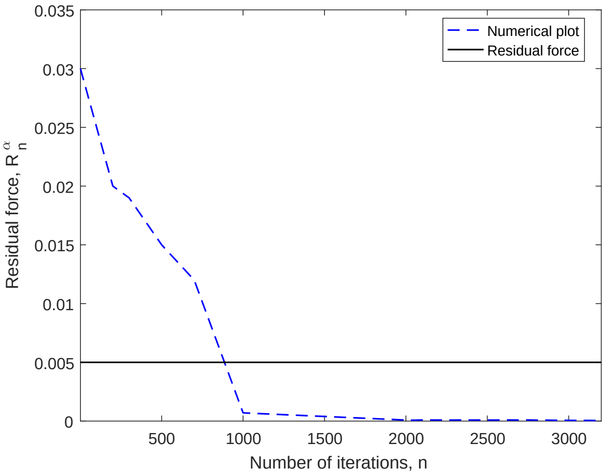

Figure 6.12: Numerical iterations plot of convergence

Figure 6.13 depicts the focus view of the plots in Figure 6.11, where the crack has happened when the operating wing interacts with the gust loads. It is observed that the stress distributions around the crack initiation have increased with the increment of time. Referring to the hypothesis mentioned before, the crack on the surface might propagate if the stress concentration at the crack tip is higher than the principal material stress. In this case, the stress distributions subjected to the wing deflection under the influence of gust loads have triggered the crack initiation to propagate with the increment of time.

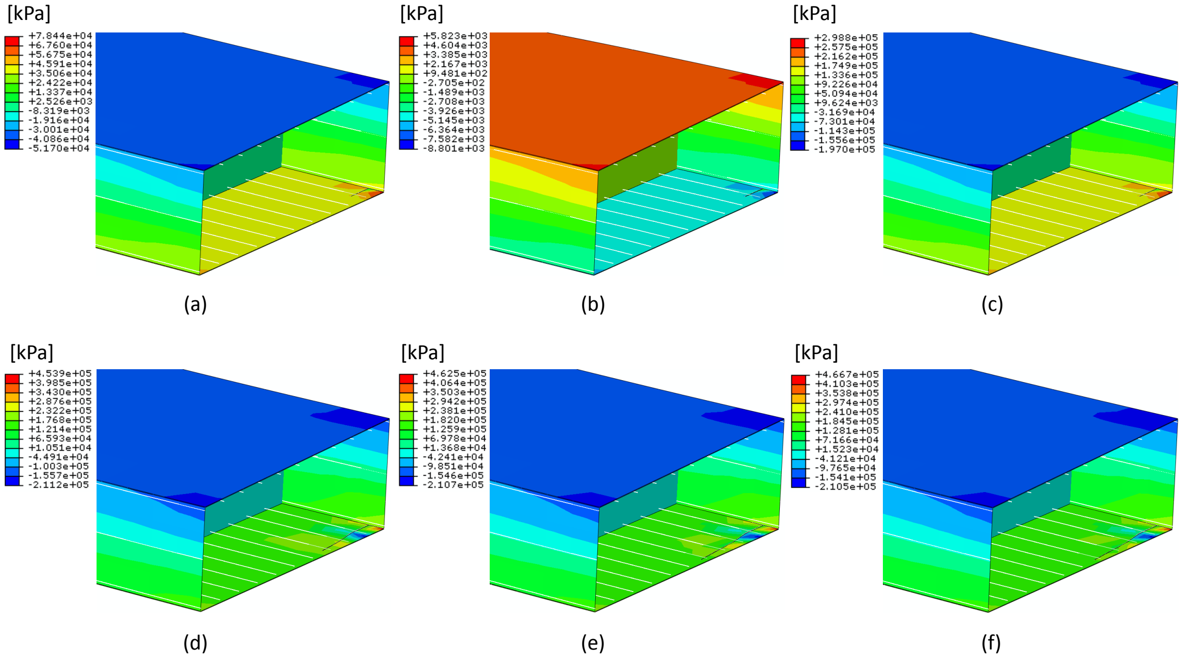

Figure 6.13: Stress plot: near wing root (lower-front skin) results on fracture behaviour via XFEM where (a) t = 0.001 s, (b) t = 0.16 s, (c) t = 0.41 s, (d) t = 0.46 s, (e) t = 0.51 s, and (f) t = 0.58 s

In both Figures 6.11 and 6.13, it is observed that the crack not propagating at t = 0.16 s where the gust loads was has deflected down the wing box. Since the critical crack is locating at the lower wing surface, the skin definitely in compression, while the upper wing skin is in the state of tension. Thus, this situation did not give any serious state to the crack initiation at the lower surface. However, with the increment of time, the gust loads has increased following the discrete gust '1-cosine' shape. The crack is observed to slightly propagated with the gust loads increment between that period until it reached t = 0.41 s.

Although the wing tip deflection is found to be at the highest point at t = 0.4 s as depicted in Figure 6.10, the crack has drastically propagated. It seems possible that these results are due to the crack has propagated before it could reach the highest value of wing deflection. This result may be explained by the fact that the wing strength has reduced once the crack propagated, which results in the more extended crack propagations when it reaches the highest peak of the wing tip deflection. Since the area has weakened by the crack propagations, it is discovered that the crack has severely propagated at t = 0.51 s and remain until the analysis finished at t = 0.58 s. Figure 6.14 provided the focus view of the upper and lower surface of the crack location on the skin near to the wing root where the crack has stopped propagating at that length.

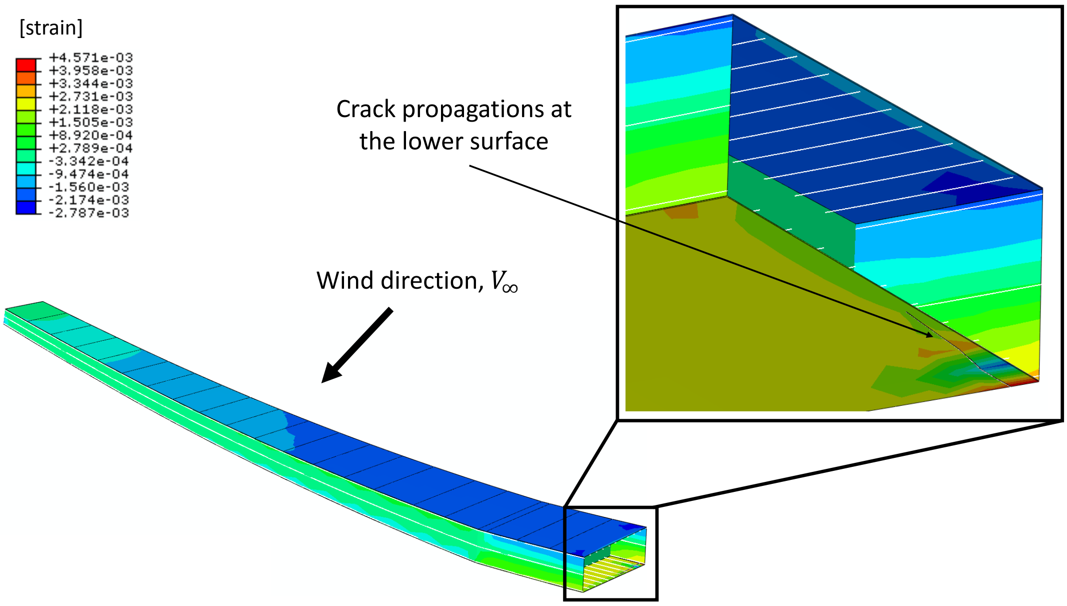

Figure 6.14: Final state: near wing root (lower-front skin) results on fracture behaviour via XFEM

However, with the increment of time, crack is found to stop propagating since the wing deflection subjected to the gust loads has reduced. Since the crack existence has affected the flying safety envelope of an aircraft, it is doubtful that the wing can sustain for a longer time since it might encounter several loads during cruising at high altitude.

These results provide further support for the hypothesis that the existence of discrete gust loads might increase the wing deflections and hence will increase the stress concentration at the weak wing spot. For instance, the since the structure could not sustain the loads developed by the gust, the crack will appear. One of the issues that emerge from these findings is the possible solutions that could be applied to reduce the stress concentration at the wing root.

6.3 Summary

This chapter presents the crack propagation behaviour of wing box under gust loads. Several validation tests including vibration and flutter have been experimentally and numerically performed. The idea of this research is to simulate and detect the critical point on the aluminum wing box when it interacts with gust loads. Here, an advanced numerical modelling technique called Extended Finite Element Method (XFEM) has been implemented to model the crack propagation. Since gust loads will deform the wing, and create stress concentration at the critical point, XFEM was used to predict the crack initiation point based on the energy release rate of the material. The gust loads initially were computed based on the requirement provided by FAR 23 since the aircraft wing was technically designed for the commuter aircraft purpose. The wing tip deflections subjected to the gust loads were expressed in an equation based on Fourier series periodic function.

Chapter 7

Conclusions

"A conclusion is the place where you get tired of thinking."
- Arthur Bloch (American physician and author, 1897 - 1962).

This chapter presents the conclusion for all investigations conducted in this research.

7.1 Conclusions

1. **Transversal crack and delamination of laminates using XFEM.**
   - This work offers a new insight on the computational modelling of crack and delamination of carbon fibre composite. Transversal crack and delamination have been assessed using XFEM validated against experimental and analytical data. Both transversal crack and delamination analysis were simulated using XFEM for a composite structure. The carbon fibre composite lay-up of $(45/90/-45/0)_s$ XFEM fracture simulation shows a significant result, wherein the failure strength renders 0.2% of difference compared with the experimental results (21.6%).
   - The good correlation of results in investigating the size effect modelling has been presented in this report. The results are in close agreement between the experimental and analytical data of each specimen modelled based on the size of the carbon fibre composite volume.

2. **Aeroelastic assessment of cracked composite plate by means of fully coupled Finite Element and Doublet Lattice Method.**

   - This work offers a new investigation of the computational flutter estimation on a cracked composite plate. The study is divided into two sections; Section a: Flutter effects on the crack ratio and Section b: Flutter effects on crack location.
   - This is the first time that the flutter on a cracked composite plate is assessed using the coupled FEM-DLM method. The variation of unidirectional angle led to different flutter speed obtained for each composite structures. Using FEM-DLM approach, the crack ratio initiated until 0.4 has increased the flutter speed for all unidirectional composite plate of 0°, 90° and 135°. The existence of crack on the structure results in a reduction of flutter speed from the crack ratio of 0.4 until the structure about to break.
   - The crack ratio effect on flutter speed needs more rational analyses since the only and same 2 modes as the baseline case were used for cracked plates. It may be possible that small crack would lead to higher V_F, but crack ratio 0.2 to 0.4 of the dimension and through the thickness is not a small crack if the plate is scaled up to a wing box.
   - The flutter analysis of cracked unidirectional composite plate due to the different crack location by fixing the crack length, η were performed. For this part, the analysis was performed where the crack location has been varied from the root to the tip of the plate. It was found that there is no consistency for the crack ratio against the flutter speed. In that sense, more investigations are needed in exploring this issue.
   - As a concluding remark, the same investigation conducted by Wang et al. [35] was explored where the flutter on the cracked composite structure has been assessed using an advanced computational technique of *pk*- method by coupling the 2D structures using finite element (structural) and doublet lattice method (unsteady aerodynamic). The flutter assessment results presented in this chapter shows a good agreement with results presented by

[35]. In addition to that compliance, an exciting discovery was found where the critical flutter speed may increase due to the small crack appearance, supported by the flutter responses and the aerodynamics insight.

3. **Structural Integrity on Crack Propagations of Cracked Composite Plate Subjected to Aerodynamic Loads using XFEM.**

    - This research presents a novel technique in developing a fracture mechanism on a cracked composite plate under aerodynamic loads by means of XFEM. This study provides new insights into airworthiness evaluation of an aircraft wing when there is an existence of crack.
    - In this research, two type of cracked composite plates were studied, such that 0° and 135° fibre angle orientations. The flutter boundary of the specimens initially predicted through the coupling of FE-DLM presented in Chapter 4 using *pk*-method of flutter condition.
    - The most crucial limitation lies in the fact that XFEM in Abaqus can only be used in general static and implicit dynamic analysis when modelling the fracture. Therefore, this study makes a significant contribution to research on unidirectional cracked composite by demonstrating the fracture mechanism of crack under the computed aerodynamic load, by the implementation of gust loads. The results are in good agreement when compared with the steady flight condition.
    - Using this approach, the deflection/ displacement at the specific time has successfully computed. The loads were intercorrelated using the Fourier Series Function to represent the periodic motion of vibration function.

4. **Structural Integrity of Wing Box Dominated by Aeroelastic Gust Loads.**

    - The maximum stress is successfully determined based on an advanced computational method called XFEM based on the energy release rate. For the present wing box, the crack propagation near to the wing root under gust loads has been detected when the stress concentration is larger than the maximum material principal of stress. In future, this procedure might be performed to evaluate the crack emerging on composite wing box under the gust loads.

- This research presents a novel insight in fracture mechanics where the computational fracture analysis has been performed by considering the gust loads acted on present wing box. Initially, the gust loads analytically computed via '1-cosine' of gust estimation.
- As the gust loads affecting the aircraft wing displacement/deflection, at several moments the wing might meet the breaking point of fracture. In that sense, the wing is computationally analysed in term of the fracture perspective when the stress imposed on the wing has exceeded the maximum material principal stress. An advanced computational technique, called XFEM has been imposed to locate the weak fracture point, and determine the fracture behaviour of crack. It is concluded that the crack has influenced the wing structural integrity.
- This is the first time that the crack propagation has been successfully modelled under the aeroelastic loads, focusing on gust loads. As the fracture mechanism implemented via an advanced numerical method, called XFEM, the fracture criteria depend on the maximum material stress and the evolution criterion by energy release rate.

7.2 Future works/ Recommendations

1. **Flutter assessment on a laminated cracked composite plate**
    - The presented flutter assessment approach has been discussed in Chapter 4 on the cracked unidirectional composite plate. Since the sample is only considered a different type of unidirectional composite plate, the evaluated procedure could be applied to assess a influence of crack on flutter for the laminated composite presented in Chapter 3. However, several considerations should be highlighted, such as crack location and crack direction. The crack initiation might be defined in a different manner because the laminates have different ply angle, and the crack might randomly appear.

2. **Fracture analysis using different fracture modelling approach.**

    - In recent day, there are several numerical techniques in fracture mechanics have been well developed. For example, VCCT that has widely known has a capability to model crack and delamination. Hence, this technique could be implemented in investigating the cracked composite plate as highlighted in Chapter 5.
    - At the same time, the analysed composite plate presented in Chapter 4 and Chapter 5 can be replaced by a laminated composite plate. The different results might be obtained from laminated composite could exhibit higher strength and stiffness compared to the presented unidirectional composite.

3. **Fracture modelling via fluid-structure interactions.**

    - As discussed in Chapter 2, Section 2.4.1, the computation of FSI in fracture mechanic might requires very high computational cost. However, this procedure is still could be implemented providing the research is well performed with a longer time required. A preliminary results could be presented on 2D isotropic material first in reducing the computational cost.
    - In Chapter 6, the main dynamic loads computed is prior due to the gust loads. In another situation, the present investigation can be repeated by considering different dynamic loads such as impact loads. One of the example subjected to the impact is bird strike. The new analysis could be studied if both loads, gust and impact happen at the same time.

Author Publications To Date

JOURNALS

Abdullah, N.A, Curiel-Sosa, J.L, Taylor, Z.A, Tafazzolimoghaddam, B., Martinez Vicente, J.L., Chao Zhang, ”Transversal crack and delamination of carbon fiber composite laminates using XFEM”, Composite Structures 2017; 173: 78-85.

Abdullah, N.A, Curiel-Sosa, J.L, Akbar, M., ”Aeroelastic assessment of cracked composite plate by means of fully coupled finite element and Doublet Lattice Method”, Composite Structures 2018; 202: 151-161.

CONFERENCES

Jose L. Curiel-Sosa, B. Tafazzolimoghaddam, J. Navarro-Zafra, M. Akbar, **N.A Abdullah**, MIM. Ahmad, "Modelling techniques for delamination and fracture", 7th International Conference on Mechanics and Materials in Design(M2D 2017), 11-15 June 2017, Albufeira/Algarve, Portugal.

Abdullah, N.A, Curiel-Sosa, J.L, Taylor, Z.A, Tafazzolimoghaddam, B., Martinez Vicente, J.L., Chao Zhang, "Modelling of transversal crack and delamination under traction with XFEM", 3rd International Conference on Mechanics of Composites (MECHCOMP3), 4-7 July 2017, Bologna, Italy.

Abdullah, N.A, Curiel-Sosa, J.L, Akbar, M., " Flutter assessment on composite plate with crack by means of fully coupled Finite Element and Doublet Lattice Method", 3rd International Conference on Mechanics of Composites (MECHCOMP3), 4-7 July 2017, Bologna, Italy.

Abdullah, N.A, Curiel-Sosa, J.L, Wirawan, N., Akbar, M., "Structural integrity assessment on cracked composite plate under aeroelastic loading by means of XFEM", 6th International Conference Integrity-Reliability-Failure (IRF2018), 22-26 July 2018, Lisbon, Portugal.

Abdullah, N.A, Wirawan, N., Curiel-Sosa, J.L, Akbar, M., "Aerofracturelastic on wing box of multi-purpose commuter aircraft under gust load by means of XFEM", 6th International Conference Integrity-Reliability-Failure (IRF2018), 22-26 July 2018, Lisbon, Portugal.

Wirawan, N., **Abdullah, N.A**, Curiel-Sosa, J.L, Akbar, M., "Analysis on cracked commuter aircraft wing under dynamic cruise load by means of XFEM", Modern Practice in Stress and Vibration Analysis (MPSVA 2018), 2-4 July 2018, Cambridge, UK.

Ahmad, M.I.M., Curiel-Sosa, J.L., Akbar, M. and **Abdullah, N.A**. "Numerical Inspection based on Quasi-Static Analysis using Rousselier Damage Model for Aluminium Wingbox Aircraft Structure", Modern Practice in Stress and Vibration Analysis (MPSVA 2018), 2-4 July 2018, Cambridge, UK.

Bibliography

[1] D. H. Hodges and G. A. Pierce, *Introduction to Structural Dynamics and Aeroelasticity.* Cambridge University Pres, 2 ed., 2006.

[2] R. Bisplinghoff, H. Ashley, and R. Halfman, *Aeroelasticity.* Dover Books on Aeronautical Engineering Series, Dover Publications, 1996.

[3] A. B. Rostami and M. Armandei, "Renewable energy harvesting by vortex-induced motions: Review and benchmarking of technologies," *Renewable and Sustainable Energy Reviews*, vol. 70, pp. 193 – 214, 2017.

[4] "Flutter analysis of light aircraft," *Acta Mechanica*, vol. 62, no. Supplement C, pp. 105 – 112, 1986.

[5] G. Williams, *Biplanes and Bombsights: British Bombing in World War I.* Air University Press, 1999.

[6] C. A. Board, "File no. 1-006c aircraft accident report," tech. rep., Civil Aeronautics Board, 1959.

[7] P. Hylton, "Analyzing a simple prop-whirl-flutter model using modern analysis tools," in *Proceedings of The 2006 IJME – INTERTECH Conference*, session ENG 204-005, 2006.

[8] D. of Transportation Australia (DOTA), "Report on investigation of tailplane flutter : Special investigation report 77-1," tech. rep., Department of Transportation Australia, 1977.

[9] BFU, "Investigation report," tech. rep., German Federal Bureau of Aircraft Accident Investigation (BFU), 2010.

[10] S. A. C. A. Authority, “Aircraft accident report and executive summary,” tech. rep., South African Civil Aviation Authority, 2010.

[11] NTSB, “Aircraft accident brief - pilot/race 177, the galloping ghost, north american p-51d, n79111, reno, nevada, september 16, 2011. ntsb/aab-12/01.,” Tech. Rep. 2, National Transportation Safety Board, 490 L’Enfant Plaza, S.W. Washington, D.C. 20594, 2012.

[12] “Collapse of the tacoma narrows bridge.” www.youtube.com/watch?v=3mclp9QmCGs, 1999. urldate: 2006-09-23.

[13] M. O. W. Wolfe, “Aeronautical research council reports current papers: Vibration and flutter flight testing,” tech. rep., Ministry of Supply, 1955.

[14] FAA, “Advisory circular (u. s. d. o. transportation, trans.: 23.629-1b - means of compliance with title 14 cfr, part 23, § 23.629, flutter,” tech. rep., United States Department of Transportation, U.S.A, 2004.

[15] L. Gigliotti, *Assessment of the applicability of XFEM in Abaqus for modelling crack growth in rubber*. PhD thesis, KTH School of Engineering Sciences, Sweden, 2012.

[16] A. de Morais, M. de Moura, A. Marques, and P. de Castro, “Mode-i interlaminar fracture of carbon/epoxy cross-ply composites,” *Composites Science and Technology*, vol. 62, no. 5, pp. 679 – 686, 2002.

[17] P. P. Camanho, “Advances in the simulation of damage and fracture of composite structures,” X Reunión de Usuarios de ABAQUS, (Madrid, Spain), Springer, 2005.

[18] M. Rathinasabapathy, “The application of vcct for abaqus to prediction and simulation of delamination growth in composite structures,” in *Aerospace Technology Conference and Exposition*, SAE International, oct 2005.

[19] O. Allix and P. Ladevèze, “Interlaminar interface modelling for the prediction of delamination,” *Composite Structures*, vol. 22, no. 4, pp. 235 – 242, 1992.

[20] J. Schellekens and R. D. Borst, “Free edge delamination in carbon-epoxy laminates: a novel numerical/experimental approach,” *Composite Structures*, vol. 28, no. 4, pp. 357 – 373, 1994.

[21] R. B. Pipes and N. Pagano, “Interlaminar stresses in composite laminates under uniform axial extension,” *Journal of Composite Materials*, vol. 4, no. 4, pp. 538–548, 1970.

[22] T. Kim, S. N. Atluri, O. Kravchenko, and R. B. Pipes, “Interlaminar stresses in composite laminates under out-of-plane shear/bending,” *AIAA Journal*, vol. 32, no. 8, pp. 1700–1708, 1994.

[23] J. Goodsell, N. J. Pagano, O. Kravchenko, and R. B. Pipes, “Interlaminar stresses in composite laminates subjected to anticlastic bending deformation,” *Journal of Applied Mechanics*, vol. 80, no. 4, 2013.

[24] T. Kim and S. N. Atluri, “Analysis of edge stresses in composite laminates under combined thermo-mechanical loading, using a complementary energy approach,” *Computational Mechanics*, vol. 16, pp. 83–97, Mar 1995.

[25] C. A. E. Associates, “Using composites analysis to predict interlaminar stresses,” 2017.

[26] C.-H. Chue and C.-I. Liu, “Disappearance of free-edge stress singularity in composite laminates,” *Composite Structures*, vol. 56, no. 1, pp. 111 – 129, 2002.

[27] J. Schijve, “Effect of load sequences on crack propagation under random and program loading,” *Engineering Fracture Mechanics*, vol. 5, no. 2, pp. 269 – 280, 1973.

[28] J. Schijve, A. Vlutters, Ichsan, and J. ProvóKluit, “Crack growth in aluminium alloy sheet material under flight-simulation loading,” *International Journal of Fatigue*, vol. 7, no. 3, pp. 127 – 136, 1985.

[29] S. Odahara, Y. Murakami, M. Inoue, and A. Sueoka, “Fatigue failure by in-line flow-induced vibration and fatigue life evaluation,” *Transactions of the Japan Society of Mechanical Engineers Series A*, vol. 70, no. 690, pp. 212–220, 2004.

[30] G. Dong and J. Chen, “Vibration analysis and crack identification of a rotor with open cracks,” *Japan Journal of Industrial and Applied Mathematics*, vol. 28, pp. 171–182, Apr 2011.

[31] F. Magi, D. D. Maio, and I. Sever, “Validation of initial crack propagation under vibration fatigue by finite element analysis,” *International Journal of Fatigue*, vol. 104, pp. 183 – 194, 2017.

[32] X. Zhang, H. Xiang, and B. Sun, “Nonlinear aerostatic and aerodynamic analysis of long-span suspension bridges considering wind-structure interactions,” *Journal of Wind Engineering and Industrial Aerodynamics*, vol. 90, no. 9, pp. 1065 – 1080, 2002.

[33] A. Sengupta, F. L. Haan, P. P. Sarkar, and V. Balaramudu, “Transient loads on buildings in microburst and tornado winds,” *Journal of Wind Engineering and Industrial Aerodynamics*, vol. 96, no. 10, pp. 2173 – 2187, 2008.

[34] E. E. Theotokoglou and G. A. Balokas, “Computational analysis and material selection in cross-section of a composite wind turbine blade,” *Journal of Reinforced Plastics and Composites*, vol. 34, no. 2, pp. 101–115, 2015.

[35] K. Wang, D. J. Inman, and C. R. Farrar, “Crack-induced changes in divergence and flutter of cantilevered composite panels,” *Structural Health Monitoring*, vol. 4, no. 4, pp. 377–392, 2005.

[36] F. Holzinger, F. Wartzek, M. Nestle, H. Schiffer, and S. Leichtfuß, “Self-excited blade vibration experimentally investigated in transonic compressors: Acoustic resonance,” in *ASME Turbo Expo 2015: Turbine Technical Conference and Exposition*, vol. 7B, 2015.

[37] R. E. Kielb, K. C. Hall, M. Spiker, and J. P. Thomas, “Non-synchronous vibration of turbomachinery airfoils,” tech. rep., Duke University, 2006.

[38] D. Moxon, “Aeronautical research council reports and memoranda: Flexible mass-balance arms and control-surface flutter,” tech. rep., Ministry of Aviation, 1958.

[39] W. G. Molyneux, "Aeronautical research council reports and memoranda: The flutter of swept and unswept :'wings with fixed-root conditions part i,part ii, part iii," tech. rep., Ministry of Supply, 1950.

[40] J. G. Barmby, H. J. Cunningham, and I. E. Garrick, "Report 1014: Study of effects of sweep on the flutter of cantilever wings," tech. rep., 1955.

[41] W. G. Molyneux and F. Ruddlesden, "Aeronautical research council reports and memoranda: Some flutter tests on swept-back wings using ground-launched rockets," tech. rep., Ministry of Supply, 1953.

[42] F. A. Johnsen, *Sweeping forward : developing and flight testing the Grumman X-29A forward swept wing research aircraft.* National Aeronautics and Space Administration, 2013.

[43] N. J. Krone, "Divergence elimination with advanced composites," in *Aircraft Systems and Technology Meeting*, AIAA, 1975.

[44] T. J. Hertz, M. H. Shirk, R. H. Ricketts, and T. A. Weisshaar, "Aeroelastic tailoring with composites applied to forward swept wings," tech. rep., Air Force Wright Aeronautical Laboratories NASA Langley Research Center and Purdue University, 1981.

[45] T. A. Weisshaar, "Aeroelastic tailoring of forward swept composite wings," *Journal of Aircraft*, vol. 18, no. 8, pp. 669–676, 1981.

[46] J. Dillinger, M. Abdalla, T. Klimmek, and Z. Gürdal, "Static aeroelastic stiffness optimization and investigation of forward swept composite wings," in *10th World Congress on Structural and Multidisciplinary Optimization*, 2013.

[47] A. Manan, G. A. Vio, M. Y. Harmin, and J. E. Cooper, "Optimization of aeroelastic composite structures using evolutionary algorithms," *Engineering Optimization*, vol. 42, no. 2, pp. 171–184, 2010.

[48] S. Guo, D. Li, and Y. Liu, "Multi-objective optimization of a composite wing subject to strength and aeroelastic constraints," *Proceedings of the Institution of*

Mechanical Engineers, Part G: Journal of Aerospace Engineering, vol. 226, no. 9, pp. 1095–1106, 2012.

[49] N. A. Abdullah and E. Sulaeman, "Aeroelastic tailoring of oscillating supersonic wing with external stores," in *Intelligent Materials and Mechatronics*, vol. 464 of *Applied Mechanics and Materials*, pp. 110–115, Trans Tech Publications, 2014.

[50] P. Jin, B. Song, X. Zhong, T. Yu, and F. Xu, "Aeroelastic tailoring of composite sandwich panel with lamination parameters," *Proceedings of the Institution of Mechanical Engineers, Part G: Journal of Aerospace Engineering*, vol. 230, no. 1, pp. 105–117, 2016.

[51] G. A. A. Thuwis, R. De Breuker, M. M. Abdalla, and Z. Gürdal, "Aeroelastic tailoring using lamination parameters," *Structural and Multidisciplinary Optimization*, vol. 41, pp. 637–646, Apr 2010.

[52] C. D. Marqui, W. G. R. Vieira, A. Erturk, and D. J. Inman, "Modeling and analysis of piezoelectric energy harvesting from aeroelastic vibrations using the doublet-lattice method," *Journal of Vibration and Acoustics*, vol. 133, no. 1, 2011.

[53] M. Akbar and J. Curiel-Sosa, "Piezoelectric energy harvester composite under dynamic bending with implementation to aircraft wingbox structure," *Composite Structures*, vol. 153, no. Supplement C, pp. 193 – 203, 2016.

[54] Z. Zhang, H. Xiang, and Z. Shi, "Mechanism exploration of piezoelectric energy harvesting from vibration in beams subjected to moving harmonic loads," *Composite Structures*, vol. 179, pp. 368 – 376, 2017.

[55] C. Bruni, J. Gibert, G. Frulla, E. Cestino, and P. Marzocca, "Energy harvesting from aeroelastic vibrations induced by discrete gust loads," *Journal of Intelligent Material Systems and Structures*, vol. 28, no. 1, pp. 47–62, 2017.

[56] J. R. Wright and J. E. Cooper, *Introduction to Aircraft Aeroelasticity and Loads.* American Institute of Aeronautics Astronautics, 1 ed., 2007.

[57] D. W. Camp, "Wind velocity measurements of low level wind gust amplitude and duration and statistical gust shape characteristics," tech. rep., National Aeronautics and Space Administration, 1968.

[58] F. Verheij, J. Cleijne, and J. Leene, "Gust modelling for wind loading," *Journal of Wind Engineering and Industrial Aerodynamics*, vol. 42, no. 1, pp. 947 – 958, 1992.

[59] C. Knigge and S. Raasch, "Improvement and development of one- and two-dimensional discrete gust models using a large-eddy simulation model," *Journal of Wind Engineering and Industrial Aerodynamics*, vol. 153, pp. 46 – 59, 2016.

[60] T.-U. Kim and I. H. Hwang, "Reliability analysis of composite wing subjected to gust loads," *Composite Structures*, vol. 66, no. 1, pp. 527 – 531, 2004.

[61] L. Wang, Y. Dai, and C. Yang, "Gust response analysis for helicopter rotors in the hover and forward flights," *Shock and Vibration*, vol. 2017, 2017.

[62] X. Zhou, Z. Han, M. Gu, A.-a. Zhang, W. Zhang, and W. Fang, "Research on wind-induced responses of a large-scale membrane structure," *Earthquake Engineering and Engineering Vibration*, vol. 12, no. 2, pp. 297–305, 2013.

[63] S. A. Fazelzadeh and H. Sadat-Hoseini, "Nonlinear flight dynamics of a flexible aircraft subjected to aeroelastic and gust loads," *Journal of Aerospace Engineering*, vol. 25, no. 1, pp. 51–63, 2012.

[64] R. G. Cook, R. Palacios, and P. Goulart, "Robust gust alleviation and stabilization of very flexible aircraft," *AIAA Journal*, vol. 51, no. 2, pp. 330–340, 2013.

[65] L. Yagil, D. E. Raveh, and M. Idan, "Deformation control of highly flexible aircraft in trimmed flight and gust encounter," *AIAA Journal*, 2017.

[66] Y. Wang and D. J. Inman, "Simultaneous energy harvesting and gust alleviation for a multifunctional composite wing spar using reduced energy control via piezoceramics," *Journal of Composite Materials*, vol. 47, no. 1, pp. 125–146, 2013.

[67] J. Xiang, Y. Wu, and D. Li, “Energy harvesting from the discrete gust response of a piezoaeroelastic wing: Modeling and performance evaluation,” *Journal of Sound and Vibration*, vol. 343, pp. 176 – 193, 2015.

[68] Y. Chen, J. Zhan, J. Wu, and J. Wu, “A fully-activated flapping foil in wind gust: Energy harvesting performance investigation,” *Ocean Engineering*, vol. 138, pp. 112 – 122, 2017.

[69] S. Guo, J. De Los Monteros, and Y. Liu, “Gust alleviation of a large aircraft with a passive twist wingtip,” *Aerospace*, vol. 2, no. 2, p. 135–154, 2015.

[70] R. J. H. Wanhill, “Gust spectrum fatigue crack propagation in candidate skin materials,” *Fatigue & Fracture of Engineering Materials & Structures*, vol. 1, no. 1, pp. 5–19, 1979.

[71] M. S. Tajabadi, “Metallurgical failure analysis of a cracked aluminum 7075 wing internal angle,” *Case Studies in Engineering Failure Analysis*, vol. 7, pp. 9 – 16, 2016.

[72] G. Georgiou, A. Manan, and J. Cooper, “Modeling composite wing aeroelastic behavior with uncertain damage severity and material properties,” *Mechanical Systems and Signal Processing*, vol. 32, pp. 32 – 43, 2012. Uncertainties in Structural Dynamics.

[73] R. H. Ricketts, “Structural testing for static failure, flutter and other scary things,” tech. rep., National Aeronautics and Space Administration, 1981.

[74] G. Hou, J. Wang, and A. Layton, “Numerical methods for fluid-structure interaction — a review,” *Communications in Computational Physics*, vol. 12, no. 2, p. 337–377, 2012.

[75] C. Michler, S. Hulshoff, E. van Brummelen, and R. de Borst, “A monolithic approach to fluid–structure interaction,” *Computers Fluids*, vol. 33, no. 5, pp. 839 – 848, 2004.

[76] P. B. Ryzhakov, R. Rossi, S. R. Idelsohn, and E. Oñate, “A monolithic lagrangian approach for fluid–structure interaction problems,” *Computational Mechanics*, vol. 46, pp. 883–899, Nov 2010.

[77] L. Yin, J.-c. Jiang, and L.-x. Zhang, “Monolithic approach to thermal fluid-structure interaction with nonconforming interfaces,” *Applied Mathematics and Mechanics*, vol. 33, pp. 211–222, Feb 2012.

[78] D. Forti, M. Bukac, A. Quaini, S. Canic, and S. Deparis, “A monolithic approach to fluid–composite structure interaction,” *Journal of Scientific Computing*, vol. 72, pp. 396–421, Jul 2017.

[79] K. Park, C. A. Felippa, and R. Ohayon, “Partitioned formulation of internal fluid–structure interaction problems by localized lagrange multipliers,” *Computer Methods in Applied Mechanics and Engineering*, vol. 190, no. 24, pp. 2989 – 3007, 2001.

[80] J. Vierendeels, L. Lanoye, J. Degroote, and P. Verdonck, “Implicit coupling of partitioned fluid–structure interaction problems with reduced order models,” *Computers Structures*, vol. 85, no. 11, pp. 970 – 976, 2007. Fourth MIT Conference on Computational Fluid and Solid Mechanics.

[81] J. Degroote, K.-J. Bathe, and J. Vierendeels, “Performance of a new partitioned procedure versus a monolithic procedure in fluid–structure interaction,” *Computers Structures*, vol. 87, no. 11, pp. 793 – 801, 2009. Fifth MIT Conference on Computational Fluid and Solid Mechanics.

[82] H. Baek and G. E. Karniadakis, “A convergence study of a new partitioned fluid–structure interaction algorithm based on fictitious mass and damping,” *Journal of Computational Physics*, vol. 231, no. 2, pp. 629 – 652, 2012.

[83] J. Donea, A. Huerta, J. Ponthot, and A. RodríguezFerran, *Arbitrary Lagrangian–Eulerian Methods*, ch. 14. American Cancer Society, 2004.

[84] F. Sturla, E. Votta, M. Stevanella, C. A. Conti, and A. Redaelli, “Impact of modeling fluid–structure interaction in the computational analysis of aortic root

biomechanics," *Medical Engineering Physics*, vol. 35, no. 12, pp. 1721 – 1730, 2013.

[85] K. G. Wang, P. Lea, and C. Farhat, "A computational framework for the simulation of highspeed multimaterial fluid–structure interaction problems with dynamic fracture," *International Journal for Numerical Methods in Engineering*, vol. 104, no. 7, pp. 585–623, 2015.

[86] V. I. Kushch, I. Sevostianov, and L. Mishnaevsky, "Effect of crack orientation statistics on effective stiffness of mircocracked solid," *International Journal of Solids and Structures*, vol. 46, no. 6, pp. 1574 – 1588, 2009.

[87] E. J. Barbero and D. H. Cortes, "A mechanistic model for transverse damage initiation, evolution, and stiffness reduction in laminated composites," *Composites Part B: Engineering*, vol. 41, no. 2, pp. 124 – 132, 2010.

[88] W. T. Thompson, "Vibration periods at tacoma narrows," *Engineering News Record*, vol. P477, no. 1, pp. 61 – 62, 1941.

[89] K. Y. Billah and R. H. Scanlan, "Resonance, tacoma narrows bridge failure," *American Journal of Physics*, vol. 59, no. 2, pp. 118 – 124, 1991.

[90] S. C. Castravete and R. A. Ibrahim, "Effect of stiffness uncertainties on the flutter of a cantilever wing," *AIAA Journal*, vol. 46, no. 4, pp. 925 – 935, 2008.

[91] V. Birman and L. Librescu, "Supersonic flutter of shear deformable laminated composite flat panels," 1990.

[92] R. M. V. Pidaparti, "Free vibration and flutter of damaged composite panels," *Composite Structures*, vol. 38, no. 1, pp. 477 – 481, 1997.

[93] R. M. V. Pidaparti and C. C. Chang, "Finite element supersonic flutter analysis of skewed and cracked composite panels," *Computers Structures*, vol. 69, no. 2, pp. 265 – 270, 1998.

[94] S. Natarajan, G. Manickam, and S. Bordas, "Supersonic flutter analysis of functionally graded material plates with cracks," *Frontiers in Aerospace Engineering*, vol. 2, no. 2, pp. 91–97, 2013.

[95] I. E. Reimanis, “Functionally graded materials,” in *The Handbook of Advanced Material: Enabling New Designs* (J. K. Wessel, ed.), ch. 10, pp. 465–486, New Jersey: John Wiler & Sons, 2004.

[96] E. Viola, A. Marzani, and N. Fantuzzi, “Interaction effect of cracks on flutter and divergence instabilities of cracked beams under subtangential forces,” *Engineering Fracture Mechanics*, vol. 151, pp. 109 – 129, 2015.

[97] B. J. Ryu, K. Katayama, and Y. Sugiyama, “Dynamic stability of timoshenko columns subjected to subtangential forces,” *Computers Structures*, vol. 68, no. 5, pp. 499 – 512, 1998.

[98] Y. Sugiyama, K. Katayama, K. Kiriyama, and B.-J. Ryu, “Experimental verification of dynamic stability of vertical cantilevered columns subjected to a subtangential force,” *Journal of Sound and Vibration*, vol. 236, no. 2, pp. 193 – 207, 2000.

[99] A. V. Styuart, E. Livne, L. Demasi, and M. Mor, “Flutter failure risk assessment for damage-tolerant composite aircraft structures,” *AIAA Journal*, vol. 49, no. 3, pp. 655 – 669, 2011.

[100] J. Curiel-Sosa and N. Karapurath, “Delamination modelling of {GLARE} using the extended finite element method,” *Composites Science and Technology*, vol. 72, no. 7, pp. 788 – 791, 2012.

[101] L. S. Al-ansari, H. N. Al-mahmud, and S. K. Al-raheem, “Calculating stress intensity factor {Mode I} for composite plate with central crack,” *International Journal of Computer Applications*, vol. 75, no. 15, pp. 1–10, 2013.

[102] S. Lecheb, A. Nour, A. Chelli, H. Mechakra, N. Hamad, and H. Kebir, “Stress intensity factor for dynamic cracking of composite material by x-fem method,” *International Journal of Mathematical, Computational, Physical, Electrical and Computer Engineering*, vol. 8, no. 5, pp. 809–815, 2014.

[103] L. M. Zhou, G. W. Meng, X. L. Li, and F. Li, “Analysis of dynamic fracture parameters in functionally graded material plates with cracks by graded finite

element method and virtual crack closure technique," *Advances in Materials Science and Engineering*, 2016.

[104] T. Belytschko and T. Black, "Elastic crack growth in finite elements with minimal remeshing," *International Journal for Numerical Methods in Engineering*, vol. 45, no. 5, pp. 601 – 620, 1999.

[105] D. B. P. Huynh and T. Belytschko, "The extended finite element method for fracture in composite materials," *International Journal for Numerical Methods in Engineering*, vol. 77, no. 2, pp. 214–239, 2009.

[106] G. Golewski, P. Golewski, and T. Sadowski, "Numerical modelling crack propagation under mode {II} fracture in plain concretes containing siliceous fly-ash additive using {XFEM} method," *Computational Materials Science*, vol. 62, pp. 75 – 78, 2012.

[107] M. S. Moreno, J. Curiel-Sosa, J. Navarro-Zafra, J. M. Vicente, and J. L. Cela, "Crack propagation in a chopped glass-reinforced composite under biaxial testing by means of {XFEM}," *Composite Structures*, vol. 119, pp. 264 – 271, 2015.

[108] J. Navarro-Zafra, J. L. Curiel-Sosa, and M. C. Serna Moreno, "Three-dimensional static and dynamic analysis of a composite cruciform structure subjected to biaxial loading: A discontinuum approach," *Applied Composite Materials*, vol. 23, no. 2, pp. 139–154, 2016.

[109] D. Grogan, C. . Brádaigh, and S. Leen, "A combined {XFEM} and cohesive zone model for composite laminate microcracking and permeability," *Composite Structures*, vol. 120, pp. 246 – 261, 2015.

[110] S. Yazdani, W. J. Rust, and P. Wriggers, "An {XFEM} approach for modelling delamination in composite laminates," *Composite Structures*, vol. 135, pp. 353 – 364, 2016.

[111] X. Hu, B. Chen, M. Tirvaudey, V. Tan, and T. Tay, "Integrated xfem-ce analysis of delamination migration in multi-directional composite laminates," *Composites Part A: Applied Science and Manufacturing*, vol. 90, pp. 161 – 173, 2016.

[112] Z. Wang, T. Yu, T. Q. Bui, S. Tanaka, C. Zhang, S. Hirose, and J. L. Curiel-Sosa, “3-d local mesh refinement (xfem) with variable-node hexahedron elements for extraction of stress intensity factors of straight and curved planar cracks,” *Computer Methods in Applied Mechanics and Engineering*, vol. 313, pp. 375 – 405, 2017.

[113] S. R. Hallett, W.-G. Jiang, B. Khan, and M. R. Wisnom, “Modelling the interaction between matrix cracks and delamination damage in scaled quasi-isotropic specimens,” *Composites Science and Technology*, vol. 68, no. 1, pp. 80 – 89, 2008.

[114] D. Rabinovich, D. Givoli, and S. Vigdergauz, “Xfembased crack detection scheme using a genetic algorithm,” *International Journal for Numerical Methods in Engineering*, vol. 71, no. 9, pp. 1051–1080, 2007.

[115] D. Rabinovich, D. Givoli, and S. Vigdergauz, “Crack identification by ’arrival’ time using xfem and a genetic algorithm,” *International Journal for Numerical Methods in Engineering*, vol. 77, no. 3, pp. 337–359, 2009.

[116] S. Mohammadi, *EXTENDED FINITE ELEMENT METHOD for Fracture Analysis of Structures.* Blackwell Publishing Ltd, 2008.

[117] M. Stolarska, D. L. Chopp, N. Moës, and T. Belytschko, “Modelling crack growth by level sets in the extended finite element method,” *International Journal for Numerical Methods in Engineering*, vol. 51, no. 8, pp. 943–960, 2001.

[118] M. N. Nasr, E.-G. Ng, and M. Elbestawi, “A modified time-efficient {FE} approach for predicting machining-induced residual stresses,” *Finite Elements in Analysis and Design*, vol. 44, no. 4, pp. 149 – 161, 2008.

[119] J. Rice and G. Rosengren, “Plane strain deformation near a crack tip in a power-law hardening material,” *Journal of the Mechanics and Physics of Solids*, vol. 16, no. 1, pp. 1 – 12, 1968.

[120] L. O. Jernkvist, “Fracture of wood under mixed mode loading: I. derivation of fracture criteria,” *Engineering Fracture Mechanics*, vol. 68, no. 5, pp. 549 – 563, 2001.

[121] M. Wisnom, B. Khan, and S. Hallett, "Size effects in unnotched tensile strength of unidirectional and quasi-isotropic carbon/epoxy composites," *Composite Structures*, vol. 84, no. 1, pp. 21 – 28, 2008.

[122] J. M. Corum, R. L. Battiste, K. C. Liu, and M. B. Ruggles, "Basic properties of reference crossply carbon-fiber composite," tech. rep., Lockheed Martin Energy Research Corporation, 2000.

[123] S. Pinho, P. Robinson, and L. Iannucci, "Fracture toughness of the tensile and compressive fibre failure modes in laminated composites," *Composites Science and Technology*, vol. 66, no. 13, pp. 2069 – 2079, 2006.

[124] Ibtihal-Al-Namie, A. A. Ibrahim, and M. F. Hassan, "Study the mechanical properties of epoxy resin reinforced with silica (quartz) and alumina particles," *The Iraqi Journal For Mechanical And Material Engineering*, vol. 11, no. 3, pp. 486 – 5069, 2011.

[125] M. Kehoe, "A historical overview of flight flutter: Testing nasa technical memorandum 4720," tech. rep., National Aeronautics and Space Administration, Edwards, California, 1995.

[126] E. Nissim and G. B. Gilyard, "Method for experimental determination of flutter speed by parameter identification," tech. rep., National Aeronautics and Space Administration, Ames Research Center Dryden Flight Research Facility Edwards, Calfornia, 1989.

[127] J. D. Eshelby, "The determination of the elastic field of an ellipsoidal inclusion, and related problems," *Proceedings. Mathematical, Physical, and Engineering Sciences*, vol. 241, no. 1226, pp. 376–396, 1957.

[128] G. Z. Voyiadjis and P. I. Kattan, *Mechanics of Composite Materials with MATLAB*. Springer, 2005.

[129] T. Mori and K. Tanaka, "Average stress in matrix and average elastic energy of materials with misfitting inclusions," *Acta Metallurgica*, vol. 21, no. 5, pp. 571 – 574, 1973.

[130] Y. Benveniste, “A new approach to the application of mori-tanaka’s theory in composite materials,” *Mechanics of Materials*, vol. 6, no. 2, pp. 147 – 157, 1987.

[131] E. Albano and W. P. Rodden, “A doublet-lattice method for calculating lift distributions on oscillating surfaces in subsonic flows,” *AIAA Journal*, vol. 7, no. 2, pp. 279–285, 1969.

[132] M. K. Abbas, H. M. Negm, and M. A. Elshafei, “Flutter and divergence characteristics of composite plate wing,” *International Journal of Innovative Science Engineering and Technology*, vol. 4, no. 2, pp. 105 – 115, 2014.

[133] J. L. Curiel-Sosa and A. J. Gil, “Analysis of a continuum-based beam element in the framework of explicit-fem,” *Finite Elements in Analysis and Design*, vol. 45, no. 8, pp. 583 – 591, 2009.

[134] M. S. C. Corporation, *MSC.Nastran Version 68. In Aeroelastic Analysis User’s Guide.* M.S.C. Software Corporation, 2014.

[135] K. Nikpur and A. Dimarogonas, “Local compliance of composite cracked bodies,” *Composites Science and Technology*, vol. 32, no. 3, pp. 209 – 223, 1988.

[136] O. Song, T.-W. Ha, and L. Librescu, “Dynamics of anisotropic composite cantilevers weakened by multiple transverse open cracks,” *Engineering Fracture Mechanics*, vol. 70, no. 1, pp. 105 – 123, 2003.

[137] V. Rouss, P. Lesage, S. Bégot, D. Candusso, W. Charon, F. Harel, X. François, V. Selinger, C. Schilo, and S. Yde-Andersen, “Mechanical behaviour of a fuel cell stack under vibrating conditions linked to aircraft applications part i: Experimental,” *International Journal of Hydrogen Energy*, vol. 33, no. 22, pp. 6755 – 6765, 2008.

[138] Abaqus, “Abaqus analysis user’s guide documentation,” *Dassault Systemes Simulia Corp, Abaqus 6.14-2*, 2014.

[139] L. Zhao, N. Warrior, and A. Long, “A micromechanical study of residual stress and its effect on transverse failure in polymer–matrix composites,” *International Journal of Solids and Structures*, vol. 43, no. 18, pp. 5449 – 5467, 2006.

[140] D. W. A. Rees, "Yield, strength, and failure criteria," in *The Mechanics Of Engineering Structures*, ch. 12, pp. 487–534, London: Imperial College Press, 2015.

[141] R. Hibbeler, *Mechanics of Materials.* Singapore: Pearson, 9 ed., 2013.

[142] F. MacMaster, K. Chan, S. Bergsma, and M. Kassner, "Aluminum alloy 6069 part ii: fracture toughness of 6061-t6 and 6069-t6," *Materials Science and Engineering: A*, vol. 289, no. 1, pp. 54 – 59, 2000.

[143] K. Abdurohman, R. Bayu, and P. W. P. Silitonga, "Normal mode analysis of n219 wing for b-11 configuration," in *International Seminar on Aerospace Science and Technology*, (Bali, Indonesia), ISAST 2015, 2015.

[144] M. S. A. Elsayed, R. Sedaghati, and M. Abdo, "Accurate stick model development for static analysis of complex aircraft wing-box structures," *AIAA Journal*, vol. 47, pp. 2063 – 2075, 2009.

[145] S. Syamsuar, T. Sasongko, N. Kartika, A. Suksmono, M. Saputro, and D. Eskayudha, "Half wing n219 aircraft model clean configuration for flutter test on low speed wind tunnel," in *International Seminar on Aerospace Science and Technology*, (Medan, Indonesia), ISAST 2017, 2017.

[146] CASR23, "CASR Part 23 Amdt. 2, Part 23. Airworthiness Standards: Normal, Utility, Acrobatic, and the Commuter Category Airplanes," tech. rep., Ministry of Transportation, Republic of Indonesia, 09 2014.

APPENDIX A

Numerical Code for Mean Field Homogenisation (MFH) via Mori-Tanaka Method

```
close all;
clear all;
clc;

%% Input fiber & matrix properties

% Fiber

E_p = 275.6e9;
NU_p = 0.2;

C_p = inv([1/E_p -NU_p/E_p -NU_p/E_p 0 0 0 ; -NU_p/E_p 1/E_p -NU_p/E_p 0 0 0 ;...
-NU_p/E_p -NU_p/E_p 1/E_p 0 0 0 ; 0 0 0 2*(1+NU_p)/E_p 0 0 ;...
0 0 0 0 2*(1+NU_p)/E_p 0 ; 0 0 0 0 0 2*(1+NU_p)/E_p]);

C11_p = C_p(1,1);% Pa
C12_p = C_p(1,2);% Pa
C13_p = C_p(1,3);% Pa
C21_p = C_p(2,1);% Pa
C22_p = C_p(2,2);% Pa
C23_p = C_p(2,3);% Pa
C31_p = C_p(3,1);% Pa
C32_p = C_p(3,2);% Pa
C33_p = C_p(3,3);% Pa
C44_p = C_p(4,4);% Pa
C55_p = C_p(5,5);% Pa
C66_p = C_p(6,6);% Pa

% C_p = [C11_p C12_p C13_p 0     0     0;...
%       C21_p C22_p C23_p 0     0     0;...
%       C31_p C32_p C33_p 0     0     0;...
%       0     0     0     C44_p 0     0;...
%       0     0     0     0     C55_p 0;...
%       0     0     0     0     0     C66_p ;];
```

```
 S_p = inv(C_p);

e15_p = 0.0001;% C/m2
e31_p = 0.0001;% C/m2
e32_p = 0.0001;% C/m2
e33_p = 0.0001; % C/m2

e_p = [0     0     0     0     e15_p 0;...
      0     0     0     e15_p 0     0;...
      e31_p e32_p e33_p 0     0     0;];

d_p = e_p*S_p;


EiJMn_p = [C_p, -e_p';...
         e_p, k_p;];


% Matrix

E_m = 2.76e9;
NU_m = 0.33;

C_m = inv([1/E_m -NU_m/E_m -NU_m/E_m 0 0 0 ; -NU_m/E_m 1/E_m -NU_m/E_m 0 0 0 ;...
-NU_m/E_m -NU_m/E_m 1/E_m 0 0 0 ; 0 0 0 2*(1+NU_m)/E_m 0 0 ;...
0 0 0 0 2*(1+NU_m)/E_m 0 ; 0 0 0 0 0 2*(1+NU_m)/E_m]);

C11_m = C_m(1,1);% Pa
C12_m = C_m(1,2);% Pa
C13_m = C_m(1,3);% Pa
C21_m = C_m(2,1);% Pa
C22_m = C_m(2,2);% Pa
C23_m = C_m(2,3);% Pa
```

```
C31_m = C_m(3,1);% Pa
C32_m = C_m(3,2);% Pa
C33_m = C_m(3,3);% Pa
C44_m = C_m(4,4);% Pa
C55_m = C_m(5,5);% Pa
C66_m = C_m(6,6);% Pa

S_m = inv(C_m);

e15_m = 0.0;% C/m2
e31_m = 0.0;% C/m2
e32_m = 0.0;% C/m2
e33_m = 0.0;% C/m2

e_m = [0    0    0    0    e15_m 0;...
      0    0    0    e15_m 0    0;...
      e31_m e32_m e33_m 0    0    0;];


EiJMn_m = [C_m, -e_m';...
          e_m, k_m;];

EiJMn_pm = EiJMn_p - EiJMn_m;
invEiJMn_m=inv(EiJMn_m);

eta = (EiJMn_p-EiJMn_m)./(EiJMn_p+EiJMn_m);

for ii=1:9
   for jj=1:9
      if isnan(eta(ii,jj))== 1
         eta(ii,jj)=0;
      end
   end
end
```

```
%% Geometry of inclusion (fiber in the matrix) & concentration tensor

alfa = 1;% long-infinite cylindrical inclusion
V_p = 0.01:0.01:0.99;% volume fraction of fiber

% Concentration/Eshelby Tensor of the inclusion as the function of Matrix
% properties (EiJMn_m) and inclusion geometry/shape (alfa),
% in this case only long-infinite cylindrical inclusion (alfa = 1)
SMnAb_p = zeros(9,9);
if alfa == 1
  % Original Dunn-Taya Concentration Tensor
  S1111_p = ((5*C11_m)+C12_m)/(8*C11_m);
  S2222_p = S1111_p;

  S1212_p = ((3*C11_m)-C12_m)/(8*C11_m);
  S2121_p = S1212_p;
  S1221_p = S1212_p;
  S2112_p = S1212_p;

  S1313_p = 1/4;
  S3131_p = S1313_p;
  S1331_p = S1313_p;
  S3113_p = S1313_p;
  S2323_p = S1313_p;
  S3232_p = S1313_p;
  S2332_p = S1313_p;
  S3223_p = S1313_p;

  S1122_p = ((3*C12_m)-C11_m)/(8*C11_m);
  S2211_p = S1122_p;

  S1133_p = C13_m/(2*C11_m);
  S2233_p = S1133_p;
```

```
    S1143_p = e31_m/(2*C11_m);
    S2243_p = S1143_p;
    S4141_p = 1/2;
    S4242_p = S4141_p;

    SMnAb_p(1,1) = S1111_p;
    SMnAb_p(1,2) = S1122_p;
    SMnAb_p(1,3) = S1133_p;
    SMnAb_p(1,9) = S1143_p;

    SMnAb_p(2,1) = S2211_p;
    SMnAb_p(2,2) = S2222_p;
    SMnAb_p(2,3) = S2233_p;
    SMnAb_p(2,9) = S2243_p;

    SMnAb_p(4,4) = S2323_p;
    SMnAb_p(5,5) = S1313_p;
    SMnAb_p(6,6) = S1212_p;

    SMnAb_p(7,7) = S4141_p;
    SMnAb_p(8,8) = S4242_p;

end

% Odegard reference material properties function
for i=1:numel(V_p)
    EiJMn_0(:,:,i)=EiJMn_m.*(1+(V_p(i)*eta))./(1-(V_p(i)*eta));
end


SMnAb_p0 = zeros(9,9,numel(V_p));
for i=1:numel(V_p)
```

```
SMnAb_p0 = zeros(9,9,numel(V_p));
for i=1:numel(V_p)
   % Modified Dunn-Taya/Odegard Concentration Tensor
   S1111_p0(i) = ((5*EiJMn_0(1,1,i))+EiJMn_0(1,2,i))/(8*EiJMn_0(1,1,i));
   S2222_p0(i) = S1111_p0(i);

   S1212_p0(i) = ((3*EiJMn_0(1,1,i))-EiJMn_0(1,2,i))/(8*EiJMn_0(1,1,i));
   S2121_p0(i) = S1212_p0(i);
   S1221_p0(i) = S1212_p0(i);
   S2112_p0(i) = S1212_p0(i);

   S1313_p0(i) = 1/4;
   S3131_p0(i) = S1313_p0(i);
   S1331_p0(i) = S1313_p0(i);
   S3113_p0(i) = S1313_p0(i);
   S2323_p0(i) = S1313_p0(i);
   S3232_p0(i) = S1313_p0(i);
   S2332_p0(i) = S1313_p0(i);
   S3223_p0(i) = S1313_p0(i);

   S1122_p0(i) = ((3*EiJMn_0(1,2,i))-EiJMn_0(1,1,i))/(8*EiJMn_0(1,1,i));
   S2211_p0(i) = S1122_p0(i);

   S1133_p0(i) = EiJMn_0(1,3,i)/(2*EiJMn_0(1,1,i));
   S2233_p0(i) = S1133_p0(i);

   S1143_p0(i) = EiJMn_0(9,1,i)/(2*EiJMn_0(1,1,i));
   S2243_p0(i) = S1143_p0(i);

   S4141_p0(i) = 1/2;
   S4242_p0(i) = S4141_p0(i);
```

```
   SMnAb_p0(1,1,i) = S1111_p0(i);
   SMnAb_p0(1,2,i) = S1122_p0(i);
   SMnAb_p0(1,3,i) = S1133_p0(i);
   SMnAb_p0(1,9,i) = S1143_p0(i);

   SMnAb_p0(2,1,i) = S2211_p0(i);
   SMnAb_p0(2,2,i) = S2222_p0(i);
   SMnAb_p0(2,3,i) = S2233_p0(i);
   SMnAb_p0(2,9,i) = S2243_p0(i);

   SMnAb_p0(4,4,i) = S2323_p0(i);
   SMnAb_p0(5,5,i) = S1313_p0(i);
   SMnAb_p0(6,6,i) = S1212_p0(i);

   SMnAb_p0(7,7,i) = S4141_p0(i);
   SMnAb_p0(8,8,i) = S4242_p0(i);
end

I = eye(9,9);
A_dil=inv(I+((SMnAb_p*invEiJMn_m*EiJMn_pm))); % Dilute Concentration Tensor

for i=1:numel(V_p)

V_m(i) = 1-V_p(i);% volume fraction of matrix

EiJMn(:,:,i) = EiJMn_m(:,:) + V_p(i)*(EiJMn_pm(:,:))*A_dil(:,:);

A_MT_m(:,:,i)=I*inv((V_m(i)*I)+(V_p(i)*A_dil));% Mori-Tanaka Concentration Tensor - matrix
A_MT_p(:,:,i)=A_dil*inv((V_m(i)*I)+(V_p(i)*A_dil));% Mori-Tanaka Concentration Tensor - fiber
EiJMn_MT(:,:,i)=(V_m(i)*EiJMn_m(:,:)*A_MT_m(:,:,i))+(V_p(i)*EiJMn_p(:,:)*A_MT_p(:,:,i));

EiJMn_pm0(:,:,i) = EiJMn_p(:,:) - EiJMn_0(:,:,i);
invEiJMn_0(:,:,i)=inv(EiJMn_0(:,:,i));
```

```
A_0(:,:,i)=inv(I+((SMnAb_p0(:,:,i)*invEiJMn_0(:,:,i)*EiJMn_pm0(:,:,i))));% Odegard Concentration Tensor
EiJMn_OD(:,:,i) = EiJMn_0(:,:,i) + V_p(i)*(EiJMn_pm0(:,:,i))*A_0(:,:,i);

C(:,:,i)=EiJMn(1:6,1:6,i);
e(:,:,i)=EiJMn(7:9,1:6,i);
S(:,:,i)=inv(C(:,:,i));
d(:,:,i)=e(:,:,i)*S(:,:,i);

C_MT(:,:,i)=EiJMn_MT(1:6,1:6,i);
e_MT(:,:,i)=EiJMn_MT(7:9,1:6,i);
S_MT(:,:,i)=inv(C_MT(:,:,i));
d_MT(:,:,i)=e_MT(:,:,i)*S_MT(:,:,i);

C_OD(:,:,i)=EiJMn_OD(1:6,1:6,i);
e_OD(:,:,i)=EiJMn_OD(7:9,1:6,i);
S_OD(:,:,i)=inv(C_OD(:,:,i));
d_OD(:,:,i)=e_OD(:,:,i)*S_OD(:,:,i);

% Chan & Unsworth Model (1989)
cv(i) = C_p(1,1)+C_p(1,2)+((V_p(i)*(C_m(1,1)+C_m(1,2)))/(1-V_p(i)));
sv(i) =(V_p(i)*S_m(1,1))+ ((1-V_p(i))*(S_p(3,3)));

c33v(i) = (V_p(i)*(C_p(3,3)-(2*((C_p(1,3)-C_m(1,2))^2)/cv(i))))+((1-V_p(i))*C_m(1,1));
e33v(i) = V_p(i)*(e_p(3,3)-(2*e_p(3,1)*(C_p(1,3)-C_m(1,2))/cv(i)));
c31v(i) = ((C_m(1,2)*(C_p(1,1)+C_p(1,2)))+(V_p(i)*C_p(1,3)*(C_m(1,1)+C_m(1,2))/(1-V_p(i))))/cv(i);
e31v(i) = e_p(3,1)*(1-((C_p(1,1)+C_p(1,2))/cv(i)));
s31v(i) = ((S_p(3,3)*S_m(1,2)*(1-V_p(i)))+(V_p(i)*S_m(1,1)*S_p(1,3)))/sv(i);
s33v(i) = S_m(1,1)*S_p(3,3)/sv(i);
d33v(i) = V_p(i)*S_m(1,1)*d_p(3,3)/sv(i);
d31v(i) = (V_p(i)*d_p(3,1))-((V_p(i)*(1-V_p(i))*d_p(3,3)*(S_p(1,3)-S_m(1,2)))/sv(i));

end
```

```
for i=1:numel(V_p)
   C33(i)=C(3,3,i);
   C31(i)=C(3,1,i);
   e33(i)=e(3,3,i);
   e31(i)=e(3,1,i);
   d33(i)=d(3,3,i);
   d31(i)=d(3,1,i);
   S33(i)=S(3,3,i);
   S31(i)=S(3,1,i);

   C33_MT(i)=C_MT(3,3,i);
   C31_MT(i)=C_MT(3,1,i);
   e33_MT(i)=e_MT(3,3,i);
   e31_MT(i)=e_MT(3,1,i);
   d33_MT(i)=d_MT(3,3,i);
   d31_MT(i)=d_MT(3,1,i);
   S33_MT(i)=S_MT(3,3,i);
   S31_MT(i)=S_MT(3,1,i);

   C33_OD(i)=C_OD(3,3,i);
   C31_OD(i)=C_OD(3,1,i);
   e33_OD(i)=e_OD(3,3,i);
   e31_OD(i)=e_OD(3,1,i);
   d33_OD(i)=d_OD(3,3,i);
   d31_OD(i)=d_OD(3,1,i);
   S33_OD(i)=S_OD(3,3,i);
   S31_OD(i)=S_OD(3,1,i);
end
```

```
figure (1)
plot (V_p,C33_MT*1E-10,'bo',V_p,c33v*1E-10,'k-')
xlabel('\it\bf\fontsize{12}Volume Fraction of Fiber');
ylabel('\it\bf\fontsize{12}C_{33} (10^{10} N/m^{2})');
title('\bf\fontsize{12} Stiffness C_{33} vs Volume Fraction of Fiber');
legend('Present Code - Mori Tanaka','Chan-Unsworth Model')
print(figure(1), '-depsc2', 'MTC33')

figure (2)
plot (V_p,C31_MT*1E-10,'bo',V_p,c31v*1E-10,'k-')
xlabel('\it\bf\fontsize{12}Volume Fraction of Fiber');
ylabel('\it\bf\fontsize{12}C_{31} (10^{10} N/m^{2})');
title('\bf\fontsize{12} Stiffness C_{31} vs Volume Fraction of Fiber');
legend('Present Code - Mori Tanaka','Chan-Unsworth Model')
print(figure(2), '-depsc2', 'MTC31')

figure (3)
plot (V_p,S33_MT*1E12,'bo',V_p,s33v*1E12,'k-')
xlabel('\it\bf\fontsize{12}Volume Fraction of Fiber');
ylabel('\it\bf\fontsize{12}S_{33} (10^{-12} m^{2}/N)');
title('\bf\fontsize{12} Compliance S_{33} vs Volume Fraction of Fiber');
legend('Present Code - Mori Tanaka','Chan-Unsworth Model')
print(figure(7), '-depsc2', 'MTS33')

figure (4)
plot (V_p,S31_MT*1E12,'bo',V_p,s31v*1E12,'k-')
xlabel('\it\bf\fontsize{12}Volume Fraction of Fiber');
ylabel('\it\bf\fontsize{12}S_{31} (10^{-12} m^{2}/N)');
title('\bf\fontsize{12} Compliance S_{31} vs Volume Fraction of Fiber');
legend('Present Code - Mori Tanaka','Chan-Unsworth Model')
print(figure(8), '-depsc2', 'MTS31')
```

```
%% Output 2D Plane Stress Constitutive

for i=1:numel(V_p)
    C11_2D(i) = C(1,1,i) - ((C(1,3,i)^2)/C(3,3,i));
    C12_2D(i) = C(1,2,i) - ((C(1,3,i)*C(2,3,i))/C(3,3,i));
    C22_2D(i) = C(2,2,i) - ((C(2,3,i)^2)/C(3,3,i));
    C66_2D(i) = C(6,6,i);

    C_2D(:,:,i) = [C11_2D(i) C12_2D(i) 0;...
        C12_2D(i) C22_2D(i) 0;...
        0 0 C66_2D(i);];

    S_2D(:,:,i) = inv(C_2D(:,:,i));

    e31_2D(i) = e(3,1,i) - ((C(1,3,i)*e(3,3,i))/C(3,3,i));
    e32_2D(i) = e(3,2,i) - ((C(2,3,i)*e(3,3,i))/C(3,3,i));

    e_2D(:,:,i) = [e31_2D(i) e32_2D(i) 0];

    d_2D(:,:,i) = e_2D(:,:,i)*S_2D(:,:,i);

    k3_2D(i) = k(3,3,i) +((e(3,3,i)^2)/C(3,3,i));
    k_2D(i) = k3_2D(i);

    EiJMn_2D(:,:,i) = [C_2D(:,:,i), -e_2D(:,:,i)';...
          e_2D(:,:,i), k_2D(i);];
end
```

APPENDIX B

Sample of Flutter Speed Computational Code for Cracked Composite Plate via Coupling of FEM-DLM

```
SOL 145
CEND
$ Direct Text Input for Global Case Control Data
TITLE = TESTPLATE_FLUTTER
SUBTI = CANTILEVERED, DOUBLET-LATTICE AERODYNAMICS AT MACH NO. 0.0
LABEL = PK FLUTTER METHOD
ECHO  = BOTH
SPC   = 1 $ FUSELAGE CONSTRAINT
SDAMP = 2000 $ STRUCTURAL DAMPING
METHOD= 1 $ LANCZOS METHOD
SVEC  = NONE $ PRINT VIBRATION MODES
SET 999 = 1,3
MODESELECT = 999
FMETHOD = 40 $ PK-FLUTTER METHOD
DISP  = ALL $ PRINT FLUTTER MODES
BEGIN BULK
$ Direct Text Input for Bulk Data
PARAM   GRDPNT   0
PARAM    POST    1
PARAM   PRTMAXIM YES
$              * * STRUCTURAL DAMPING * *                    $
$                                       $
$       THE PARAMETER KDAMP DETERMINES THE MANNER OF INCLUSION        $
$       OF STRUCTURAL DAMPING IN EQUATIONS OF MOTION (SEE HANDBOOK    $
$       FOR DYNAMIC ANALYSIS, SECT. 3.2.2).  IF SET TO -1, MODAL      $
$       DAMPING IS PUT INTO COMPLEX STIFFNESS MATRIX AS STRUCTURAL    $
$       DAMPING.                                $
$                                       $
$      N      V1     V2
PARAM   KDAMP   +1
$                                       $
$       THE TABDMP1 ENTRY DEFINES MODAL DAMPING AS A TABULAR          $
$       FUNCTION OF FREQUENCY.  THE DAMPING LEVELS ARE LINEAR         $
$       BETWEEN THE FREQUENCY AND DAMPING PAIRS AND ARE EXTRAP-       $
$       OLATED OUTSIDE THE TABULATED FREQUENCY RANGE.                 $
$                                       $
$      ID                                +TDP
TABDMP1 2000                                    +T2000
$      F1     G1     F2     G2     ETC           ENDT
+T2000  0.0     0.00    1000.   0.00    ENDT
```

```
$                  * * * AERODYNAMIC DATA * * *                  $
$                                                    $
$                     (SNAIL-IN-SEC SYSTEM)                  $
$                                                    $
$                   * * ELEMENT GEOMETRY * *                  $
$                                                    $
$       THE AERO ENTRY SPECIFIES THE AERO COORDINATE SYSTEM, THE       $
$       VELOCITY (USED FOR DATA RECOVERY), THE REFERENCE CHORD        $
$       AND FLUID DENSITY, PLUS SYMMETRY KEYS.  SYMXZ=1 INDICATES      $
$       THAT THE MODEL IS MOUNTED WITH A ROOT REFLECTION PLANE;        $
$       SYMXY = 0 INDICATES THAT THE MODEL IS MOUNTED FAR ENOUGH       $
$       FROM THE FLOOR SO THAT REFLECTION EFFECTS ARE NEGLIGIBLE.      $
$
$234567 1234567 1234567 1234567 1234567 1234567 1234567
$       ACSID   VELOCITY REFC   RHOREF  SYMXZ   SYMXY
AERO    0       100000. 100     1.225E-9  1

$       THE CAERO1 ENTRY IS USED FOR DOUBLET-LATTICE AERODYNAMICS.     $
$       LISTED ARE ITS PAERO ENTRY ID AND THE COORDINATE SYSTEM        $
$       FOR LOCATING THE INBOARD AND OUTBOARD LEADING EDGE POINTS      $
$       (1 AND 4).  NSPAN AND NCHORD, OR LSPAN AND LCHORD, ARE         $
$       USED TO PARTITION THE WING INTO AERODYNAMIC BOXES, THE         $
$       FORMER FOR UNIFORMLY SPACED BOXES AND THE LATTER FOR           $
$       NON-UNIFORMLY SPACED BOXES.  IGID IS THE ID OF ITS             $
$       ASSOCIATED INTERFERENCE GROUP.  THE CONTINUATION ENTRY         $
$       DEFINES POINTS 1 AND 2, THE ROOT CHORD AND THE TIP CHORD.      $
$       THE BOXES FORMED BY THE GRID LINES WILL BE NUMBERED            $
$       BEGINNING WITH EID, SO A NUMBER SHOULD BE CHOSEN THAT IS       $
$       UNIQUE, AND IS GREATER THAN ALL STRUCTURAL GRID, SCALAR        $
$       AND EXTRA POINT IDS.                                 $
$
$234567 1234567 1234567 1234567 1234567 1234567 1234567 1234567 1234567 $
$       EID     PID     CP      NSPAN   NCHORD  LSPAN   LCHORD  IGID
CAERO1  3001    1000    0       4       5                       1       +CC1
$234567 1234567 1234567 1234567 1234567 1234567 1234567 1234567 1234567
$       (FWD INBOARD POINT)     ROOTCHORD  (FWD OUTBOARD POINT) TIP CHORD
+CC1    0.0     0.0     0.0     100.    0.0     100.    0.0     100.
$
```

```
$      EID     PID     CP      NSPAN   NCHORD  LSPAN   LCHORD  IGID
CAERO1  5001    1000    0       16      5                       1       +CC2
$234567 1234567 1234567 1234567 1234567 1234567 1234567 1234567 1234567
$      (FWD INBOARD POINT)   ROOTCHORD  (FWD OUTBOARD POINT) TIP CHORD
+CC2    0.0     100.0   0.0     100.    0.0     500.    0.0     100.
$                                                 $
$       THE PAERO ENTRY IS REQUIRED EVEN THOUGH IT IT NON-FUNCTIONAL   $
$       (BECAUSE THERE ARE NO ASSOCIATED BODIES IN THIS EXAMPLE).      $
$                                                 $
PAERO1  1000


$            * * SPLINE FIT ON THE LIFTING SURFACES * *              $
$                                                 $
$               * LINEAR SPLINE FIT ON THE WING *                 $
$                                                 $
$       THE SPLINE2 ENTRY SPECIFIES A BEAM SPLINE FOR INTERPOLAT-      $
$       ION OVER THE REGION OF THE CAERO ENTRY (ID1 AND ID2 ARE        $
$       THE FIRST AND LAST BOXES IN THIS REGION).  SETG REFERS         $
$       TO A SET1 ENTRY WHERE THE STRUCTURAL GRID POINTS ARE           $
$       DEFINED.  DZ AND DTOR ARE SMOOTHING CONSTANTS FOR LINEAR       $
$       ATTACHMENT AND TORSIONAL FLEXIBILITIES.  DTHX AND DTHY         $
$       ARE ROTATIONAL ATTACHMENT FLEXIBILITIES. CID IDENTIFIES        $
$       THE  SPLINE AXIS.                                $
$
$234567 1234567 1234567 1234567 1234567 1234567 1234567 1234567 1234567 $
$****************    Aerodynamics Model******************************$
$      EID     CAERO   BOX1    BOX2    SETG    DZ      METH    USAGE
SPLINE1 3001    3001    3001    3020    3001    0.0
SET1    3001    1       THRU    30
$
$      EID     CAERO   BOX1    BOX2    SETG    DZ      METH    USAGE
SPLINE1 5001    5001    5001    5080    5001    0.0
SET1    5001    36      THRU    132
```

```
$              * * * SOLUTION SPECIFICATIONS * * *              $
$                                          $
$               * VIBRATION SOLUTION PARAMETERS *               $
$                                          $
$       THE EIGR ENTRY SPECIFIES THE METHOD OF EXTRACTING THE EIGEN-   $
$       SOLUTIONS OF THE STRUCTURE IN A VACUUM, IN THIS CASE THE       $
$       LANCZOS METHOD.  TEN MODES ARE DESIRED, NORMALIZED     $
$       ON THE MAXIMUM DISPLACEMENTS.                          $
$                                          $
$     SID       V1      V2      ND                             $
EIGRL    1                    10


$                  * AERODYNAMIC CONDITIONS *                   $
$                                          $
$       ALL COMBINATIONS OF MACH NUMBER AND REDUCED FREQUENCY LISTED   $
$       ON THE MKAERO1 ENTRY AND ITS CONTINUATION CARD WILL BE USED    $
$       TO GENERATE GENERALIZED AERO FORCE MATRICES.  IF MORE THAN     $
$       EIGHT MACH NO.S OR REDUCED FREQUENCIES ARE REQUIRED A SECOND   $
$       MKAERO1 ENTRY IS NECESSARY.                            $
$                                          $
$234567 1234567 1234567 1234567 1234567 1234567 1234567 1234567 1234567 $
$       M1     M2      M3      ETC
MKAERO1  0.0                                       +MK
$234567 1234567 1234567 1234567 1234567 1234567 1234567 1234567 1234567 $
$       K1     K2      K3      K4      K5      ETC
+MK      0.001  0.01    0.3     0.6    1.1                   2.2     3.3           10.1


$                 *FLUTTER SOLUTION PARAMETERS *                $
$                                          $
$       THE FLUTTER ENTRY DEFINES THE METHOD OF SOLUTION, IDENTIFIES   $
$       THE FLFACT ENTRIES THAT FOLL0W, SPECIFIES THE INTERPOLATION    $
$       METHOD, THE NUMBER OF ROOTS DESIRED IN THE OUTPUT AND THE      $
$       CRITERION FOR CONVERGENCE (DEFAULT IS 10-3).           $
$                                          $
$     SID    METHOD  DENS    MACH    VEL    IMETH   NVALUE  EPS     $
FLUTTER 40      PK      1       2       4       L
```

```
$       FLFACT ENTRIES ARE USED TO SPECIFY DENSITY RATIOS, MACH NO.S   $
$       AND REDUCED FREQUENCIES/VELOCITIES FOR FLUTTER ANALYSES.       $
$       NEGATIVE VELOCITIES ARE SIGNALS TO COMPUTE AND PRINT EIGEN-    $
$       VECTORS.                                            $
$                                                   $
$234567 1234567 1234567 1234567 1234567 1234567 1234567 1234567 1234567 $
$     SID    F1     F2     F3     F4     F5     F6     F7     $
FLFACT  1      1.00                                    DENSITY
FLFACT  2      0.0                                     MACH NO
FLFACT  4      50000.         55000.       60000.       65000.       70000.       75000.       80000.       +VV
+VV     85000.  90000.  95000.  100000. 105000. 110000. 115000. 120000. VELOCITY
$                                                   $
$       THE PARAM,LMODES,N ENTRY SPECIFIES THAT N MODES ARE TO BE      $
$       USED IN THE FLUTTER ANALYSIS.                         $
$                                                   $
PARAM   LMODES  10
PARAM   VREF    1.

$ Elements and Element Properties for region : plate
$ Composite Property Reference Material: plate
$ Composite Material Description :
PCOMP   1
        1       5.      0.      YES

$ Pset: "plate" will be imported as: "pcomp.1"
CQUAD4  1       1       1       2       8       7
CQUAD4  2       1       2       3       9       8
CQUAD4  3       1       3       4       10      9
CQUAD4  4       1       4       5       11      10
CQUAD4  5       1       5       6       12      11
CQUAD4  6       1       7       8       14      13
CQUAD4  7       1       8       9       15      14
CQUAD4  8       1       9       10      16      15
CQUAD4  9       1       10      11      17      16
CQUAD4  10      1       11      12      18      17
CQUAD4  11      1       13      14      20      19
CQUAD4  12      1       14      15      21      20
CQUAD4  13      1       15      16      22      21
CQUAD4  14      1       16      17      23      22
CQUAD4  15      1       17      18      24      23
```

```
CQUAD4  16  1  19  20  26  25
CQUAD4  17  1  20  21  27  26
CQUAD4  18  1  21  22  28  27
CQUAD4  19  1  22  23  29  28
CQUAD4  20  1  23  24  30  29
CQUAD4  21  1  25  26  38  37
CQUAD4  22  1  26  27  39  38
CQUAD4  23  1  27  28  40  39
CQUAD4  24  1  28  29  41  40
CQUAD4  25  1  29  36  42  41
CQUAD4  26  1  37  38  44  43
CQUAD4  27  1  38  39  45  44
CQUAD4  28  1  39  40  46  45
CQUAD4  29  1  40  41  47  46
CQUAD4  30  1  41  42  48  47
CQUAD4  31  1  43  44  50  49
CQUAD4  32  1  44  45  51  50
CQUAD4  33  1  45  46  52  51
CQUAD4  34  1  46  47  53  52
CQUAD4  35  1  47  48  54  53
CQUAD4  36  1  49  50  56  55
CQUAD4  37  1  50  51  57  56
CQUAD4  38  1  51  52  58  57
CQUAD4  39  1  52  53  59  58
CQUAD4  40  1  53  54  60  59
CQUAD4  41  1  55  56  62  61
CQUAD4  42  1  56  57  63  62
CQUAD4  43  1  57  58  64  63
CQUAD4  44  1  58  59  65  64
CQUAD4  45  1  59  60  66  65
CQUAD4  46  1  61  62  68  67
CQUAD4  47  1  62  63  69  68
CQUAD4  48  1  63  64  70  69
CQUAD4  49  1  64  65  71  70
CQUAD4  50  1  65  66  72  71
CQUAD4  51  1  67  68  74  73
CQUAD4  52  1  68  69  75  74
CQUAD4  53  1  69  70  76  75
CQUAD4  54  1  70  71  77  76
CQUAD4  55  1  71  72  78  77
```

```
CQUAD4  56   1   73   74   80   79
CQUAD4  57   1   74   75   81   80
CQUAD4  58   1   75   76   82   81
CQUAD4  59   1   76   77   83   82
CQUAD4  60   1   77   78   84   83
CQUAD4  61   1   79   80   86   85
CQUAD4  62   1   80   81   87   86
CQUAD4  63   1   81   82   88   87
CQUAD4  64   1   82   83   89   88
CQUAD4  65   1   83   84   90   89
CQUAD4  66   1   85   86   92   91
CQUAD4  67   1   86   87   93   92
CQUAD4  68   1   87   88   94   93
CQUAD4  69   1   88   89   95   94
CQUAD4  70   1   89   90   96   95
CQUAD4  71   1   91   92   98   97
CQUAD4  72   1   92   93   99   98
CQUAD4  73   1   93   94   100   99
CQUAD4  74   1   94   95   101   100
CQUAD4  75   1   95   96   102   101
CQUAD4  76   1   97   98   104   103
CQUAD4  77   1   98   99   105   104
CQUAD4  78   1   99   100   106   105
CQUAD4  79   1   100   101   107   106
CQUAD4  80   1   101   102   108   107
CQUAD4  81   1   103   104   110   109
CQUAD4  82   1   104   105   111   110
CQUAD4  83   1   105   106   112   111
CQUAD4  84   1   106   107   113   112
CQUAD4  85   1   107   108   114   113
CQUAD4  86   1   109   110   116   115
CQUAD4  87   1   110   111   117   116
CQUAD4  88   1   111   112   118   117
CQUAD4  89   1   112   113   119   118
CQUAD4  90   1   113   114   120   119
CQUAD4  91   1   115   116   122   121
CQUAD4  92   1   116   117   123   122
CQUAD4  93   1   117   118   124   123
CQUAD4  94   1   118   119   125   124
CQUAD4  95   1   119   120   126   125
```

```
CQUAD4   96     1      121    122    128    127
CQUAD4   97     1      122    123    129    128
CQUAD4   98     1      123    124    130    129
CQUAD4   99     1      124    125    131    130
CQUAD4   100     1      125    126    132    131


$ Referenced Material Records
$ Material Record : comp
$ Description of Material : Date: 10-Aug-17          Time: 18:19:54
MAT2     1      6.8503+63.1437+6 0.    6.8503+6 0.    2.646+6 1.75-6
$ Nodes of the Entire Model
GRID     1             0.     0.     0.
GRID     2            20.     0.     0.
GRID     3            40.     0.     0.
GRID     4            60.     0.     0.
GRID*    5                         79.9999923706055 0.
*        0.
GRID     6            100.    0.     0.
GRID     7             0.    25.     0.
GRID     8            20.    25.     0.
GRID     9            40.    25.     0.
GRID     10            60.    25.     0.
GRID*    11                         79.999992370605525.
*        0.
GRID     12            100.   25.     0.
GRID     13             0.    50.     0.
GRID     14            20.    50.     0.
GRID     15            40.    50.     0.
GRID     16            60.    50.     0.
GRID*    17                         79.999992370605550.
*        0.
GRID     18            100.   50.     0.
GRID     19             0.    75.     0.
GRID     20            20.    75.     0.
GRID     21            40.    75.     0.
GRID     22            60.    75.     0.
GRID*    23                         79.999992370605575.
```

```
GRID    24              100.    75.     0.
GRID    25              0.      100.    0.
GRID    26              20.     100.    0.
GRID    27              40.     100.    0.
GRID    28              60.     100.    0.
GRID*   29                              79.9999923706055100.
*       0.
GRID    30              100.    100.    0.
GRID    36              100.    100.    0.
GRID    37              0.      125.    0.
GRID*   38                              19.9999980926514125.
*       0.
GRID*   39                              39.9999961853027125.
*       0.
GRID*   40                              59.9999961853027125.
*       0.
GRID*   41                              79.9999923706055125.
*       0.
GRID    42              100.    125.    0.
GRID    43              0.      150.    0.
GRID*   44                              19.9999980926514150.
*       0.
GRID*   45                              39.9999961853027150.
*       0.
GRID*   46                              59.9999961853027150.
*       0.
GRID*   47                              79.9999923706055150.
*       0.
GRID    48              100.    150.    0.
GRID    49              0.      175.    0.
GRID*   50                              19.9999980926514175.
*       0.
GRID*   51                              39.9999961853027175.
*       0.
GRID*   52                              59.9999961853027175.
*       0.
GRID*   53                              79.9999923706055175.
*       0.
GRID    54              100.    175.    0.
GRID    55              0.      200.    0.
```

```
GRID*   56                      19.9999980926514200.
*       0.
GRID*   57                      39.9999961853027200.
*       0.
GRID*   58                      59.9999961853027200.
*       0.
GRID*   59                      79.9999923706055200.
*       0.
GRID    60              100.    200.    0.
GRID    61              0.      225.    0.
GRID*   62                      19.9999980926514225.
*       0.
GRID*   63                      39.9999961853027225.
*       0.
GRID*   64                      59.9999961853027225.
*       0.
GRID*   65                      79.9999923706055225.
*       0.
GRID    66              100.    225.    0.
GRID    67              0.      250.    0.
GRID*   68                      19.9999980926514250.
*       0.
GRID*   69                      39.9999961853027250.
*       0.
GRID*   70                      59.9999961853027250.
*       0.
GRID*   71                      79.9999923706055250.
*       0.
GRID    72              100.    250.    0.
GRID    73              0.      275.    0.
GRID*   74                      19.9999980926514275.
*       0.
GRID*   75                      39.9999961853027275.
*       0.
GRID*   76                      59.9999961853027275.
*       0.
GRID*   77                      79.9999923706055275.
*       0.
GRID    78              100.    275.    0.
GRID    79              0.      300.    0.
```

```
GRID*   80                      19.9999980926514300.
*       0.
GRID*   81                      39.9999961853027300.
*       0.
GRID    82              60.     300.    0.
GRID*   83                      79.9999923706055300.
*       0.
GRID    84              100.    300.    0.
GRID    85               0.     325.    0.
GRID    86              20.     325.    0.
GRID    87              40.     325.    0.
GRID    88              60.     325.    0.
GRID*   89                      79.9999923706055325.
*       0.
GRID    90              100.    325.    0.
GRID    91               0.     350.    0.
GRID    92              20.     350.    0.
GRID    93              40.     350.    0.
GRID    94              60.     350.    0.
GRID*   95                      79.9999923706055350.
*       0.
GRID    96              100.    350.    0.
GRID    97               0.     375.    0.
GRID    98              20.     375.    0.
GRID    99              40.     375.    0.
GRID    100             60.     375.    0.
GRID*   101                     79.9999923706055375.
*       0.
GRID    102             100.    375.    0.
GRID    103              0.     400.    0.
GRID    104             20.     400.    0.
GRID    105             40.     400.    0.
GRID    106             60.     400.    0.
GRID*   107                     79.9999923706055400.
*       0.
GRID    108             100.    400.    0.
GRID    109              0.     425.    0.
GRID    110             20.     425.    0.
GRID    111             40.     425.    0.
GRID    112             60.     425.    0.
```

```
GRID*   113                     79.9999923706055425.
*       0.
GRID    114         100.    425.    0.
GRID    115         0.      450.    0.
GRID    116         20.     450.    0.
GRID    117         40.     450.    0.
GRID    118         60.     450.    0.
GRID*   119                     79.9999923706055450.
*       0.
GRID    120         100.    450.    0.
GRID    121         0.      475.    0.
GRID    122         20.     475.    0.
GRID    123         40.     475.    0.
GRID    124         60.     475.    0.
GRID*   125                     79.9999923706055475.
*       0.
GRID    126         100.    475.    0.
GRID    127         0.      500.    0.
GRID    128         20.     500.    0.
GRID    129         40.     500.    0.
GRID    130         60.     500.    0.
GRID*   131                     79.9999923706055500.
*       0.
GRID    132         100.    500.    0.
$ Loads for Load Case : Default
SPCADD  2       1
$ Displacement Constraints of Load Set : fix
SPC1    1       123456  1       2       3       4       5       6
$ Referenced Coordinate Frames
ENDDATA 2c8acab6
```

APPENDIX C

Sample of Computational Gust Response on the Presented Commuter Aircraft

```
$ AEROELASTIC DYNAMIC RESPONSE

SOL 146
CEND
$ Direct Text Input for Global Case Control Data
TITLE = N219_GUST
SUBTI = B11 MC01
LABEL = SQUARE-EDGED GUST
ECHO  = BOTH
SPC   = 1 $ FUSELAGE CONSTRAINT
SDAMP = 2000 $ STRUCTURAL DAMPING
METHOD= 1 $ LANCZOS METHOD
SVEC  = NONE $ PRINT VIBRATION MODES
SDAMP = 2000          $ STRUCTURAL DAMPING (2 PERCENT)
GUST  = 1000          $ AERODYNAMIC LOADING (SQUARE GUST)
DLOAD = 1001          $ REQUIRED
FREQ = 40             $ FREQUENCY LIST
TSTEP = 41            $ SOLUTION TIME STEPS (1 PERIOD)
SET 999 = 1, 3
MODESELECT = 999
DISP  = ALL $ PRINT DYNAMIC RESPONSES
STRESS(SORT1,REAL,VONMISES,BILIN)= ALL

BEGIN BULK
$ Direct Text Input for Bulk Data
PARAM   GRDPNT   0
PARAM    POST    1
PARAM   PRTMAXIM YES

$               * * STRUCTURAL DAMPING * *                    $
$                                        $
$       THE PARAMETER KDAMP DETERMINES THE MANNER OF INCLUSION        $
$       OF STRUCTURAL DAMPING IN EQUATIONS OF MOTION (SEE HANDBOOK    $
$       FOR DYNAMIC ANALYSIS, SECT. 3.2.2).  IF SET TO -1, MODAL      $
$       DAMPING IS PUT INTO COMPLEX STIFFNESS MATRIX AS STRUCTURAL    $
$       DAMPING.                                 $
$                                        $
```

```
$      N      V1     V2
PARAM   KDAMP   +1
$                                               $
$       THE TABDMP1 ENTRY DEFINES MODAL DAMPING AS A TABULAR          $
$       FUNCTION OF FREQUENCY.  THE DAMPING LEVELS ARE LINEAR         $
$       BETWEEN THE FREQUENCY AND DAMPING PAIRS AND ARE EXTRAP-       $
$       OLATED OUTSIDE THE TABULATED FREQUENCY RANGE.                 $
$                                               $
$      ID                                        +TDP
TABDMP1 2000                                            +T2000
$      F1     G1     F2     G2     ETC           ENDT
+T2000  0.0     0.02    1000.   0.02    ENDT


$                   * * * AERODYNAMIC DATA * * *                    $
$                                               $
$                      (SNAIL-IN-SEC SYSTEM)                    $
$                                               $
$                    * * ELEMENT GEOMETRY * *                    $
$                                               $
$       THE AERO ENTRY SPECIFIES THE AERO COORDINATE SYSTEM, THE      $
$       VELOCITY (USED FOR DATA RECOVERY), THE REFERENCE CHORD        $
$       AND FLUID DENSITY, PLUS SYMMETRY KEYS.  SYMXZ=1 INDICATES     $
$       THAT THE MODEL IS MOUNTED WITH A ROOT REFLECTION PLANE;       $
$       SYMXY = 0 INDICATES THAT THE MODEL IS MOUNTED FAR ENOUGH      $
$       FROM THE FLOOR SO THAT REFLECTION EFFECTS ARE NEGLIGIBLE.     $
$
$234567 1234567 1234567 1234567 1234567 1234567 1234567
$      ACSID   VELOCITY REFC   RHOREF  SYMXZ   SYMXY
AERO    0       83652.  1937    .9065E-9  1
```

```
$       THE CAERO1 ENTRY IS USED FOR DOUBLET-LATTICE AERODYNAMICS.     $
$       LISTED ARE ITS PAERO ENTRY ID AND THE COORDINATE SYSTEM        $
$       FOR LOCATING THE INBOARD AND OUTBOARD LEADING EDGE POINTS      $
$       (1 AND 4).  NSPAN AND NCHORD, OR LSPAN AND LCHORD, ARE         $
$       USED TO PARTITION THE WING INTO AERODYNAMIC BOXES, THE         $
$       FORMER FOR UNIFORMLY SPACED BOXES AND THE LATTER FOR           $
$       NON-UNIFORMLY SPACED BOXES.  IGID IS THE ID OF ITS             $
$       ASSOCIATED INTERFERENCE GROUP.  THE CONTINUATION ENTRY         $
$       DEFINES POINTS 1 AND 2, THE ROOT CHORD AND THE TIP CHORD.      $
$       THE BOXES FORMED BY THE GRID LINES WILL BE NUMBERED            $
$       BEGINNING WITH EID, SO A NUMBER SHOULD BE CHOSEN THAT IS       $
$       UNIQUE, AND IS GREATER THAN ALL STRUCTURAL GRID, SCALAR        $
$       AND EXTRA POINT IDS.                                           $
$
$234567 1234567 1234567 1234567 1234567 1234567 1234567 1234567 1234567 $
$      EID     PID     CP      NSPAN   NCHORD  LSPAN   LCHORD  IGID
CAERO1  3001    9999    0       48      20                      1       +CC1
$234567 1234567 1234567 1234567 1234567 1234567 1234567 1234567 1234567
$      (FWD INBOARD POINT)   ROOTCHORD  (FWD OUTBOARD POINT) TIP CHORD
+CC1    6625    0.0     4001.06 2614.42 6625    -9511.3 4322.82 1259.59

$       THE PAERO ENTRY IS REQUIRED EVEN THOUGH IT IT NON-FUNCTIONAL   $
$       (BECAUSE THERE ARE NO ASSOCIATED BODIES IN THIS EXAMPLE).      $
$                                                                      $
PAERO1  9999
$                                                                      $
$             * * SPLINE FIT ON THE LIFTING SURFACES * *               $
$                                                                      $
$                 * LINEAR SPLINE FIT ON THE WING *                    $
$                                                                      $
$       THE SPLINE2 ENTRY SPECIFIES A BEAM SPLINE FOR INTERPOLAT-      $
$       ION OVER THE REGION OF THE CAERO ENTRY (ID1 AND ID2 ARE        $
$       THE FIRST AND LAST BOXES IN THIS REGION).  SETG REFERS         $
$       TO A SET1 ENTRY WHERE THE STRUCTURAL GRID POINTS ARE           $
$       DEFINED.  DZ AND DTOR ARE SMOOTHING CONSTANTS FOR LINEAR       $
$       ATTACHMENT AND TORSIONAL FLEXIBILITIES.  DTHX AND DTHY         $
$       ARE ROTATIONAL ATTACHMENT FLEXIBILITIES. CID IDENTIFIES        $
$       THE  SPLINE AXIS.                                              $
$
```

```
$****************   Aerodynamics Model*******************************$
$     EID    CAERO   BOX1    BOX2    SETG    DZ     METH    USAGE
SPLINE1 3001    3001    3001    3960    3001    0.0
SET1    3001    4012    THRU    4044    4067    THRU    4099    4122    +SE
+SE     THRU    4154    4199    THRU    4231    4254    THRU    4286    +SE1
+SE1    4309    THRU    4341    4364    THRU    4396    4419    THRU    +SE2
+SE2    4451    4474    THRU    4506    4529    THRU    4561    4584    +SE3
+SE3    THRU    4616    4639    THRU    4671    4694    THRU    4726    +SE4
+SE4    4749    THRU    4781    4804    THRU    4836    4859    THRU    +SE5
+SE5    4891    4914    THRU    4946    4969    THRU    5001    5024    +SE6
+SE6    THRU    5056    5079    THRU    5111

$              * * * SOLUTION SPECIFICATIONS * * *               $
$                                              $
$               * VIBRATION SOLUTION PARAMETERS *                 $
$                                              $
$       THE EIGR ENTRY SPECIFIES THE METHOD OF EXTRACTING THE EIGEN-   $
$       SOLUTIONS OF THE STRUCTURE IN A VACUUM, IN THIS CASE THE       $
$       LANCZOS METHOD.  TEN MODES ARE DESIRED, NORMALIZED     $
$       ON THE MAXIMUM DISPLACEMENTS.                            $
$                                              $
$      SID       V1      V2      ND                          $
EIGRL    1                  5
$                                              $
$                  * AERODYNAMIC CONDITIONS *                    $
$                                              $
$       ALL COMBINATIONS OF MACH NUMBER AND REDUCED FREQUENCY LISTED   $
$       ON THE MKAERO1 ENTRY AND ITS CONTINUATION CARD WILL BE USED    $
$       TO GENERATE GENERALIZED AERO FORCE MATRICES.  IF MORE THAN     $
$       EIGHT MACH NO.S OR REDUCED FREQUENCIES ARE REQUIRED A SECOND   $
$       MKAERO1 ENTRY IS NECESSARY.                             $
$                                              $
$234567 1234567 1234567 1234567 1234567 1234567 1234567 1234567 1234567 $
$       M1      M2      M3      ETC
MKAERO1  0.255                                          +MK
$234567 1234567 1234567 1234567 1234567 1234567 1234567 1234567 1234567 $
$       K1      K2      K3      K4      K5      ETC
+MK     0.023   0.1     0.5     1.0     2.0             3.0     4.0     5.0     +MK1
+MK1    10.0    15.0    20.0    25.0    34.542
```

```
$            * * DYNAMIC LOAD AND RESPONSE DATA * *
$
$       GUST DEFINES A STATIONARY VERTICAL GUST.  LISTED ARE T/RLOAD ENTRY
$       ID, GUST ANGLE OF ATTACK (I.E., THE RATIO OF GUST VELOCITY TO THE
$       VEHICLE VELOCITY), LOCATION OF THE GUST WITH RESPECT TO THE ORIGIN
$       OF THE AERO COORDINATE SYSTEM, AND THE VEHICLE VELOCITY.
$234567 1234567 1234567 1234567 1234567 1234567 1234567 1234567 1234567 $
$      SID     DLOAD   WG      X0      V
GUST    1000    1001    0.24    0.      83652.
$
$       TLOAD1 DEFINES A TIME DEPENDENT DYNAMIC LOAD OR ENFORCED MOTION.
$       LISTED ARE THE ID, DAREA ID, DELAY ID, TYPE OF DYNAMIC EXCITATION,
$       AND TABELDi ID.
$
$      SID     DAREA   DELAY   TYPE    TID
TLOAD1  1001    1002                    1003
$
$       DAREA DEFINES THE DOF WHERE THE LOAD IS APPLIED AND A SCALE FACTOR.
$       NOTE: THIS IS JUST DUMMY CARD REQUIRED BY TLOAD CARD BUT
$           NOT AFFECTING THE ACTUAL LOAD
$
$      SID     P       C       A
DAREA   1002    11      1       0.

$       TABLED1 DEFINES A TABULAR FUNCTION OF A TIME-DEPENDENT LOAD.
$
$      SID
TABLED1 1003                                                    +TAB1
$      X1      Y1      X2      Y2      X3      Y3      X4      Y4
+TAB1   0.      0.      0.145   0.5     0.29    1.      0.435   0.5     +TAB2
$      X5      Y5
+TAB2   0.58    0.      ENDT

$      PARAM,GUSTAERO,-1 IS REQUIRED IF GUST LOADS ARE TO BE COMPUTED.
$
PARAM   GUSTAERO -1
$
$      PARAM,MACH SPECIFIES MACH NUMBER.
$
PARAM   MACH    0.255
```

```
$     PARAM,Q SPECIFIES DYNAMIC PRESSURE.
$
PARAM   Q      3.17169
$
$      PARAM,LMODES,N SPECIFIES THAT N MODES ARE TO BE USED IN
$      THE GUST ANALYSIS.
$
$ PARAM   LMODES  3
$
$      FREQ1 DEFINES THE SET OF FREQUENCIES USED TO OBTAIN
$      THE FREQUENCY RESPONSE SOLUTION. LISTED ARE THE STARTING
$      FREQUENCY, FREQUENCY INCREMENT AND NUMBER OF INCREMENTS.
$
$234567 1234567 1234567 1234567 1234567 1234567 1234567 1234567 1234567 $
$     SID    F1     DF     NDF
FREQ1   40     0.     1.72413810
$
$      TSTEP DEFINES TIME STEP INTERVALS AT WHICH THE TRANSIENT
$      RESPONSES ARE DESIRED.  LISTED ARE  THE NUMBER OF STEPS,
$      THE TIME INTERVAL AND SKIP FACTOR FOR OUTPUT.
$      T = 1/DF
$     SID    N      DT     NO
TSTEP   41     10     0.058   1
$

$ Elements and Element Properties for region : Rib
PSHELL  1      1     1.6     1            1
$ Pset: "Rib" will be imported as: "pshell.1"
CQUAD4  1      1      1      2      13     12
CQUAD4  2      1      2      3      14     13
CQUAD4  3      1      3      4      15     14
CQUAD4  4      1      4      5      16     15
CQUAD4  5      1      5      6      17     16
CQUAD4  6      1      6      7      18     17
CQUAD4  7      1      7      8      19     18
CQUAD4  8      1      8      9      20     19
CQUAD4  9      1      9      10     21     20
CQUAD4  10     1      10     11     22     21
CQUAD4  11     1      12     13     24     23
CQUAD4  12     1      13     14     25     24
```

Elements and Element Properties for region : Rib

```
CQUAD4  7285  3    1013  7447  7452  1024
CQUAD4  7286  3    7447  7448  7453  7452
CQUAD4  7287  3    7448  7449  7454  7453
CQUAD4  7288  3    7449  1068  1079  7454
CQUAD4  7289  3    1024  7452  4969  1035
CQUAD4  7290  3    7452  7453  4980  4969
CQUAD4  7291  3    7453  7454  4991  4980
CQUAD4  7292  3    7454  1079  1090  4991
CQUAD4  7293  3    1046  3024  7467  1057
CQUAD4  7294  3    3024  3035  7468  7467
CQUAD4  7295  3    3035  3046  7469  7468
CQUAD4  7296  3    3046  1101  1112  7469
CQUAD4  7297  3    1057  7467  7472  1068
CQUAD4  7298  3    7467  7468  7473  7472
CQUAD4  7299  3    7468  7469  7474  7473
CQUAD4  7300  3    7469  1112  1123  7474
CQUAD4  7301  3    1068  7472  7477  1079
CQUAD4  7302  3    7472  7473  7478  7477
CQUAD4  7303  3    7473  7474  7479  7478
CQUAD4  7304  3    7474  1123  1134  7479
CQUAD4  7305  3    1079  7477  5024  1090
CQUAD4  7306  3    7477  7478  5035  5024
CQUAD4  7307  3    7478  7479  5046  5035
CQUAD4  7308  3    7479  1134  1145  5046
CQUAD4  7309  3    1101  3079  7492  1112
CQUAD4  7310  3    3079  3090  7493  7492
CQUAD4  7311  3    3090  3101  7494  7493
CQUAD4  7312  3    3101  1156  1167  7494
CQUAD4  7313  3    1112  7492  7497  1123
CQUAD4  7314  3    7492  7493  7498  7497
CQUAD4  7315  3    7493  7494  7499  7498
CQUAD4  7316  3    7494  1167  1178  7499
CQUAD4  7317  3    1123  7497  7502  1134
CQUAD4  7318  3    7497  7498  7503  7502
CQUAD4  7319  3    7498  7499  7504  7503
CQUAD4  7320  3    7499  1178  1189  7504
CQUAD4  7321  3    1134  7502  5079  1145
CQUAD4  7322  3    7502  7503  5090  5079
CQUAD4  7323  3    7503  7504  5101  5090
CQUAD4  7324  3    7504  1189  1200  5101
```

End of Elements and
Element Properties for
region : Rib

```
$ Elements and Element Properties for region : Skin_Upper
PSHELL   4      1     2.5     1            1
$ Pset: "Skin_Upper" will be imported as: "pshell.4"
CQUAD4  4001   4      45     46     4013   4012
CQUAD4  4002   4      46     47     4014   4013
CQUAD4  4003   4      47     48     4015   4014
CQUAD4  4004   4      48     49     4016   4015
CQUAD4  4005   4      49     50     4017   4016
CQUAD4  4006   4      50     51     4018   4017
CQUAD4  4007   4      51     52     4019   4018
CQUAD4  4008   4      52     53     4020   4019
CQUAD4  4009   4      53     54     4021   4020
CQUAD4  4010   4      54     55     4022   4021
CQUAD4  4011   4      4012   4013   4024   4023
CQUAD4  4012   4      4013   4014   4025   4024
CQUAD4  4013   4      4014   4015   4026   4025
CQUAD4  4014   4      4015   4016   4027   4026
CQUAD4  4015   4      4016   4017   4028   4027
CQUAD4  4016   4      4017   4018   4029   4028
CQUAD4  4017   4      4018   4019   4030   4029
```

Elements and Element Properties for region : Skin Upper Surface

```
CQUAD4  4794   4      5093   5094   5105   5104
CQUAD4  4795   4      5094   5095   5106   5105
CQUAD4  4796   4      5095   5096   5107   5106
CQUAD4  4797   4      5096   5097   5108   5107
CQUAD4  4798   4      5097   5098   5109   5108
CQUAD4  4799   4      5098   5099   5110   5109
CQUAD4  4800   4      5099   5100   5111   5110
CQUAD4  4801   4      5101   5102   1201   1200
CQUAD4  4802   4      5102   5103   1202   1201
CQUAD4  4803   4      5103   5104   1203   1202
CQUAD4  4804   4      5104   5105   1204   1203
CQUAD4  4805   4      5105   5106   1205   1204
CQUAD4  4806   4      5106   5107   1206   1205
CQUAD4  4807   4      5107   5108   1207   1206
CQUAD4  4808   4      5108   5109   1208   1207
CQUAD4  4809   4      5109   5110   1209   1208
CQUAD4  4810   4      5110   5111   1210   1209
```

End of Elements and Element Properties for region : Skin Upper Surface

```
$ Elements and Element Properties for region : Skin_Lower
PSHELL  5     1     2.     1           1
$ Pset: "Skin_Lower" will be imported as: "pshell.5"
CQUAD4  2001  5     1     2     2013  2012
CQUAD4  2002  5     2     3     2014  2013
CQUAD4  2003  5     3     4     2015  2014
CQUAD4  2004  5     4     5     2016  2015
CQUAD4  2005  5     5     6     2017  2016
CQUAD4  2006  5     6     7     2018  2017
CQUAD4  2007  5     7     8     2019  2018
CQUAD4  2008  5     8     9     2020  2019
CQUAD4  2009  5     9     10     2021  2020
CQUAD4  2010  5     10     11     2022  2021
CQUAD4  2011  5     2012  2013  2024  2023
CQUAD4  2012  5     2013  2014  2025  2024
CQUAD4  2013  5     2014  2015  2026  2025
CQUAD4  2014  5     2015  2016  2027  2026
CQUAD4  2015  5     2016  2017  2028  2027
CQUAD4  2016  5     2017  2018  2029  2028
```

Elements and Element Properties
for region : Skin Lower Surface

```
CQUAD4  2794  5     3093  3094  3105  3104
CQUAD4  2795  5     3094  3095  3106  3105
CQUAD4  2796  5     3095  3096  3107  3106
CQUAD4  2797  5     3096  3097  3108  3107
CQUAD4  2798  5     3097  3098  3109  3108
CQUAD4  2799  5     3098  3099  3110  3109
CQUAD4  2800  5     3099  3100  3111  3110
CQUAD4  2801  5     3101  3102  1157  1156
CQUAD4  2802  5     3102  3103  1158  1157
CQUAD4  2803  5     3103  3104  1159  1158
CQUAD4  2804  5     3104  3105  1160  1159
CQUAD4  2805  5     3105  3106  1161  1160
CQUAD4  2806  5     3106  3107  1162  1161
CQUAD4  2807  5     3107  3108  1163  1162
CQUAD4  2808  5     3108  3109  1164  1163
CQUAD4  2809  5     3109  3110  1165  1164
CQUAD4  2810  5     3110  3111  1166  1165
```

End of Elements and Element
Properties for region : Skin Lower
Surface

```
$ Elements and Element Properties for region : mass_ribs1
CONM2    100101  100101        100.
$ Elements and Element Properties for region : mass_engine1
CONM2    100001  100001        200.
$ Elements and Element Properties for region : mass_engine2
CONM2    100002  100002        200.
$ Elements and Element Properties for region : mass_0
CONM2    100200  100200        .01
CONM2    100201  100201        .01
CONM2    100202  100202        .01
CONM2    100203  100203        .01
CONM2    100204  100204        .01

$ Elements and Element Properties for region : Spar_upperZ1
PBAR     6       1      64.32   5713.34 3542.95 31.0511
         0.      0.      0.      0.      0.      0.      0.      0.
        .405018 .362354 -3075.25

$ Pset: "Spar_upperZ1" will be imported as: "pbar.6"
CBAR     600001  6       45      4012    0.      0.      1.
                 0.      0.      -10.42  0.      0.      -10.42
CBAR     600002  6       4012    4023    0.      0.      1.
                 0.      0.      -10.42  0.      0.      -10.42
CBAR     600003  6       4023    4034    0.      0.      1.
                 0.      0.      -10.42  0.      0.      -10.42
CBAR     600004  6       4034    100     0.      0.      1.
                 0.      0.      -10.42  0.      0.      -10.42
CBAR     600005  6       46      4013    0.      0.      1.
                 0.      0.      -10.42  0.      0.      -10.42
CBAR     600006  6       4013    4024    0.      0.      1.
                 0.      0.      -10.42  0.      0.      -10.42
CBAR     600007  6       4024    4035    0.      0.      1.
                 0.      0.      -10.42  0.      0.      -10.42

CBAR     600008  6       4035    101     0.      0.      1.
                 0.      0.      -10.42  0.      0.      -10.42
CBAR     600009  6       47      4014    0.      0.      1.
                 0.      0.      -10.42  0.      0.      -10.42
CBAR     600010  6       4014    4025    0.      0.      1.
                 0.      0.      -10.42  0.      0.      -10.42
```

Sample of concentrated mass applied to represent the aircraft engines

Sample of upper wing surface spars